Study of High-harmonic Gyro-devices in the THz Range

By

Xiang Li

A thesis submitted to the University of London for partial fulfilment of the requirements for the degree of Doctor of Philosophy

School of Electronic Engineering and Computer Science

Queen Mary University of London

United Kingdom

May 2016

I, Xiang Li, confirm that the research included within this thesis is my own work or that where it has been carried out in collaboration with, or supported by others, that this is duly acknowledged below and my contribution indicated. Previously published material is also acknowledged below.

I attest that I have exercised reasonable care to ensure that the work is original, and does not to the best of my knowledge break any UK law, infringe any third party's copyright or other Intellectual Property Right, or contain any confidential material.

I accept that the College has the right to use plagiarism detection software to check the electronic version of the thesis.

I confirm that this thesis has not been previously submitted for the award of a degree by this or any other university.

Signature: Xiang Li

Date: 31 May 2016

Details of collaboration and publications:

Please refer to section "7.4 List of Publications" on page 168-171.

To My Family

Abstract

In the terahertz (THz) band, high-harmonic operations of gyro-devices are attractive for the great potential to reduce the required external magnetic field strength, which is proportional to the oscillation frequency but inversely proportional to the operational harmonics. This thesis focuses on the study of high-harmonic operation of the gyro-devices. Specifically, a high-harmonic large-orbit gyrotron (LOG) and the output system for a gyro-multiplier will be investigated.

Firstly, the complex-cavity gyrotron, which is the foundation of the gyro-multiplier scheme, is studied by programming and computer simulation. The computer code and the complex-cavity operation are then verified by three-dimensional (3D) Particle-In-Cell (PIC) simulation. The code can be used as a preliminary design tool of the beam-wave interaction cavity for both the LOG and the gyro-multiplier.

Secondly, a high-harmonic LOG operating with the $TE_{m,1,1}$ modes (m=4-9) has been designed and investigated. It is shown that by proper choice of the operation parameters, selective excitation of oscillation from the fourth to the ninth harmonic of the electron cyclotron resonance can be achieved with kW-level output power from 230 GHz to 465 GHz. By enabling the high-harmonics operation, the required external magnetic field strengths are reduced to the range between 2.6 T to 3.1 T. The parameter variation study is also performed to provide a general conclusion of the high-harmonic LOGs operation.

Thirdly, this thesis presents the investigation of a quasi-optical output system for a fourth-harmonic gyro-multiplier in the THz band. A dual-harmonic quasi-optical mode converter (DQMC) and a frequency selective surface (FSS) are employed within this system. It is shown that the optimal design of the DQMC requires a special mode selection in the gyro-multiplier. The high-pass FSS is designed, fabricated and experimentally verified by a THz-TDS system. It is demonstrated that the designed FSS is capable of handling the high-power output from the gyro-multiplier.

Acknowledgements

I would like to express my sincere gratitude to my supervisor Prof. Xiaodong Chen for his guidance and full support during my PhD study. I have benefited a lot from his serious attitude, extraordinary motivation and professional work. I have also learned a lot from him about time managing and health keeping which will have essential impact on my future career. Special thanks go to my second supervisor Dr. Yasir Alfadhl for his professional training since the beginning of my PhD study and endless support for my ambitions.

I am greatly indebted to Dr. Robert Donnan for his examination work and kind help in the experimental part of the thesis work. I would also like to thank Prof. Clive Parini for his guidance and support. A number of senior colleagues, Dr. Massimo Candotti, Dr. Max Torrico, Mr. Kok Ho Huen, Dr. Daohui Li, Dr. Oluyemi Falade, Dr. Oleksandr Sushko, Dr. Lei Li, Dr. Min Zhou, Dr. Zhijiao Chen, Dr. Manmohan Sharma, Dr. Ke Yang and Mr. Jiandong Lang have offered valuable help and suggestions to me during my PhD study. Many thanks to Mr. Guangwei Jiang, Mr. Yang Zeng, Miss. Zhijin Qin, Mr. Deepak Nagarkoti, Mr. Min Zhou (Kevin), Miss. Yuan Ma, Mr. Xingjian Zhang, Miss. Qianyun Zhang, Mr. Biyi Wu, Mr. Peter Alizadeh, Mr. Shaker Alkaraki, Mr. Andre Andy, Mr. Li Cheng, Miss. Jia Ran, Mr. Muhammad Qureshi, Mr. Mingtuan Lin and Mr. Ju Gao for always being there in tough times. The supports from all other members of the antenna group at Queen Mary University of London are appreciated.

My warm gratitude also goes to Prof. Sheng Yu in University of Electronic Science and Technology of China (UESTC), who encouraged me to do PhD abroad. It was also him who introduced me to the field of vacuum electronic science and technologies. Prof. Hongfu Li, Dr. Xinjian Niu and Dr. Yinghui Liu in UESTC also helped me a lot during the early stage of study in gyro-devices. The sweet memories that I share with Dr. Jianhua Guo, Dr. Tianzhong Zhang, Mrs. Yunfei Qian, Mr. Qixiang Zhao, Dr. Guo Liu, Dr. Yanyan Zhang, Dr. Chaojun Lei, Dr. Shengyong Hou, Mr. Chen Chen, Mr. Xiangke Gao, Mr. Youwei Yang, Mr. Keyong Zhang, Mr. Bin Huang, Mr. Jun Liang, Mr. Yusheng Zhao, Mr. Kai Li, Mr. Lifei Pang in UESTC are always motivating me.

I deeply appreciate the valuable help from Dr. Xiaoming Liu in Beijing University of Posts and Telecommunications (BUPT) in the design, fabrication and test of the frequency selective surfaces (FSSs) in this thesis. Prof. Junsheng Yu in BUPT has offered thought-provoking instructions on how to do effective research. Dr. Cheng Yang in BUPT also shared his expertise in the quasi-optical systems design, simulation and test. Mr. Xiaohang Cao in BUPT has offered indispensible help during the fabrication process of the FSS.

My deepest love goes to my family. Many thanks and gratitude go to my parents, Mr. Jian Li and Mrs. Deying Zeng for educating and encouraging me all these years with ever-lasting support. My lovely, smart and diligent wife, Mrs. Xuejiao Huang, is always standing by me during the tough times. A warm and faithful huge from my aunt, Mrs Rui Li had helped me out of the lowest period of my life.

Table of Contents

List of Figures

List of Tables

List of Abbreviations

3D	Three-Dimensional
AC	Alternating-Current
BWOs	Backward-wave Oscillators
CNC	Computer Numerically Controlled
COBE	Cosmic Background Explorer
CW	Continuous-Wave
DC	Direct-Current
DFG	Difference-frequency Generation
DNP	Dynamic Nuclear Polarisation
DQMC	Dual-Harmonic Quasi-Optical Mode Converter
ECH	Electron Cyclotron Heating
ECM	Electron Cyclotron Maser
EM	Electromagnetic
FELs	Free Electron Lasers
FFT	Fast Fourier Transformation
FIRI	Far Infra-Red Interferometer
FSS	Frequency Selective Surface
GO	Geometric Optics
GMR	Guided Mode Resonance
HF	High-Frequency
LF	Low-Frequency
LOG	Large-Orbit Gyrotron
MFEF	Maximum Field Enhancement Factor
NMR	Nuclear Magnetic Resonance
PDs	Photonic Devices
PIC	Particle-In-Cell
QCL	Quantum Cascade Lasers
QMC	Quasi-optical Mode Converter
RCS	Radar Cross Section

SDs	Solid-state Devices
SDW	Single Disc Window
THz	Terahertz
THz-TDS	Terahertz Time Domain Spectroscopy
TWTs	Travelling-wave Tubes
VEDs	Vacuum Electronic Devices
WMC	Waveguide Mode Converter

Chapter 1 Introduction

1.1 Overview

The terahertz (THz) frequency range spans from 0.1 THz to 10 THz in the electromagnetic spectrum. It is between the microwave band and the infrared region, as shown in Figure 1-1. Although the scientists' attention had been paid to the THz radiation from at least 1920s [1], this part of electromagnetic spectrum had been poorly explored until recent years. In the past decades, the technology innovations in photonics and progress in the traditional microwave electronics have enabled the THz research to be expanded to many more sectors [2].

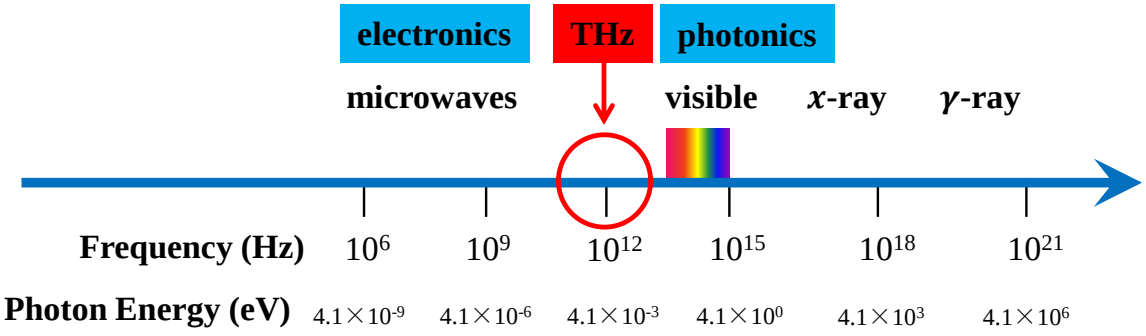

Figure 1-1: Schematic of the electromagnetic spectrum showing the location of THz band. (Reproduced from [3])

1.1.1 Properties of THz Radiation

THz radiation has unique penetration properties. It is capable of penetrating a wide variety of visually opaque and non-conducting materials, such as ceramics, clothing, wood and plastic [4]. The penetration is non-ionizing since the photon energy of THz wave is four orders of magnitude smaller than that of X-rays [5]. Thus a THz probe can be non-destructive and non-invasive.

THz radiation also has unique propagation characteristics. Unlike X-rays, it can be focused and manipulated in optics fashion by quasi-optical mirrors. And it has higher

spatial resolution and signal-to-noise ratio than the microwave due to the stronger interaction with materials [6].

THz radiation can interact with matters via a number of mechanisms. In the material science, the electromagnetic wave has much stronger interaction with the molecular rotations in the THz band than that in the neighbouring bands [7]. For the biology science, the wavelengths in the THz band are very close to the bio-molecular vibrations. This property can be used to characterise the bio-molecular vibrations and obtain better understanding of such systems [8]. For the chemical science, the internal change of the chemical composition and material bond can impart information to the THz signal, and be detected by the phase and amplitude variations [9].

1.1.2 THz Applications

In the past two to three decades, numerous applications of the THz wave have emerged due to its unique properties.

The THz radiation plays an essential part in the space and earth science. It can be seen from the Cosmic Background Explorer (COBE) spacecraft measurements that approximately one-half of the luminosity and 98% of the photons emitted since the Big Bang lie in the far-infrared region [2], within which the THz band is included. The photons in the THz frequency range provide important information about the formation of galaxies and new stars. For instance, Figure 1-2 is a schematic view of the collection telescope configuration used in a space-based far infra-red interferometer (FIRI) [10]. The light from the target is collected by the telescope and transmitted to the cold optics module, in which the frequency bands of interest are extracted to generate the interferograms. The obtained interferograms can be post-processed and cleaned to give the spectral information and data cube of the target. Other application of this category includes atmospheric observations, environmental monitoring [11], planetary and small-body observations [2], and portable THz spectrometers [12].

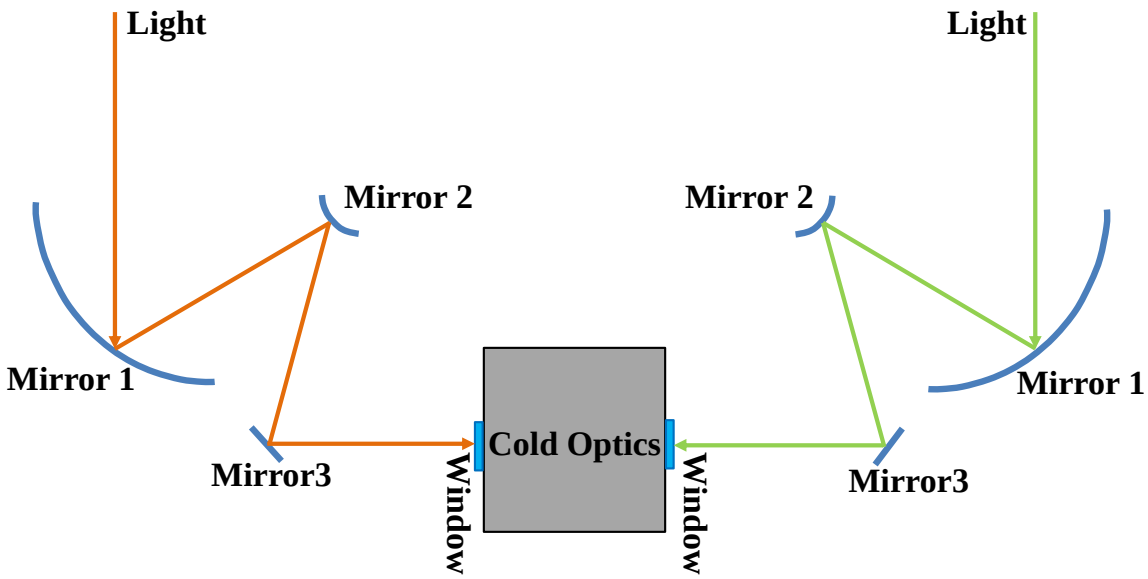

Figure 1-2: The collection telescope scheme used in a space-based FIRI. The collected light from the target is directed to the cold optics module to obtain the interferograms. (Reproduced from [10])

The THz radiation has indispensible applications in the spectroscopy and imaging. The THz pulse generated by the photo-conductive antenna or crystal is widely used in the THz Time Domain Spectroscopy (THz-TDS) systems, which allows for the characterisation of devices such as frequency selective surfaces (FSS), dielectric mirrors, artificial THz materials and modulators [13]. Furthermore, many materials can be examined using the THz emission spectroscopy [11] since they can emit THz waves by ultrafast modulation of the photo-excited carriers. As for the THz imaging, the THz wave has been applied in the holographic imaging [14], electro-optic imaging [15], near-field imaging [16] and dark-field imaging [17]. The THz-TDS and imaging techniques find their applications in security, material science, electronic engineering, biology and chemistry. For example, L-3 communications is cooperating with the Pacific Northwest National Laboratory of the United States to develop THz imaging systems in the frequency range from 30 GHz to 350 GHz [18]. Figure 1-3 shows one of the commercial personnel screening systems developed by L-3 communications for aviation security check [19]. The system is free of health risk to the passengers because no ionising radiation is involved. The imaging data is analysed automatically by software to determine if any threats are presented, which is also a favourable factor to protect the passenger privacy. If no threats are detected, the green screen as shown in Figure 1-3 (b)

will be displayed and the individual can be cleared. When potential threats are detected, their locations will be mapped onto the generic mannequin image, as shown in Figure 1-3 (c).

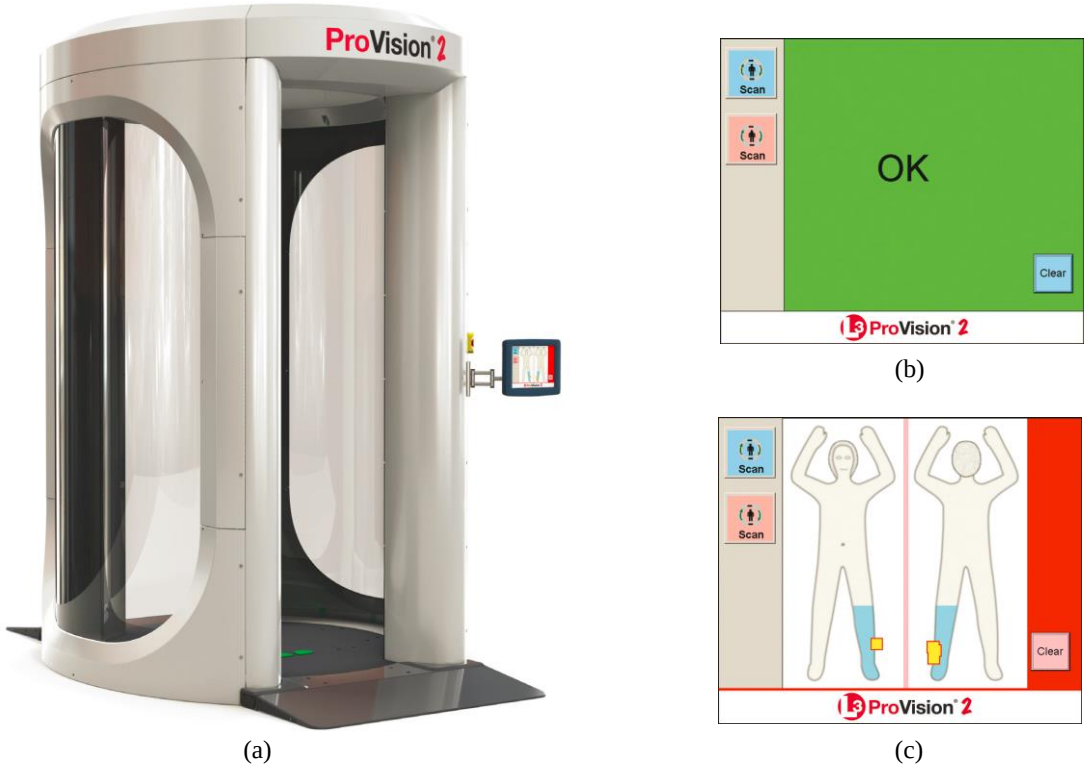

(a) (b) (c)

Figure 1-3: The personnel screening system developed by L-3 Communications for aviation security check. (a) The system profile; (b) The screen shown to the operator when no threats are detected; (c) The detected threats are marked accordingly on a generic mannequin image instead of showing a real image. (Reproduced from [19])

The THz radiation has found important applications in the basic science. The sensitivity of modern nuclear magnetic resonance (NMR) for spectroscopy has been improved by about a factor of 100, using the microwave-driven dynamic nuclear polarisation (DNP) technology. And it has been demonstrated that by adopting high power THz radiation, the NMR could be extended to even higher magnetic fields, resulting much better spectral resolution [20]. Another well-known application of the high-power THz wave is the creation of megawatt-level continuous-wave (CW) radiation at frequencies between 70 GHz and 240 GHz for electron cyclotron heating (ECH) in Tokamak as well as stellarator plasmas. Figure 1-4 shows the layout of the ECH system used in the ITER Tokamak [21]. The high-power THz radiation at 170 GHz is generated by gyrotrons which are located at

B15. The radiation is then directed by the transmission lines to the Tokamak building (B11) for heating of the plasma to the fusion-required temperature. Other basic research that requires high-power coherent THz radiation includes plasma diagnostics, electron-spin resonance spectroscopy, atmospheric monitoring and so on [22].

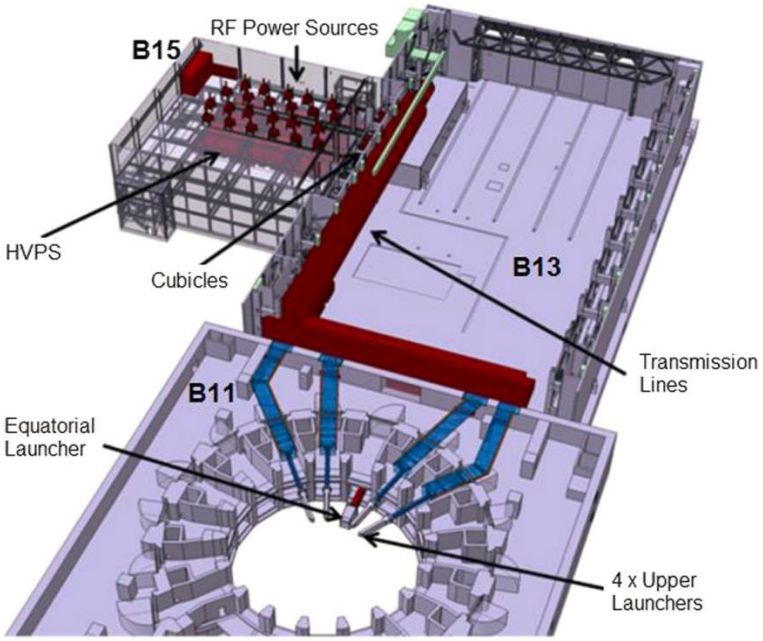

Figure 1-4: Layout of the Electron Cyclotron Heating (ECH) system in the ITER Tokamak [21]. HVPS is short for high-voltage power supplies.

For the field of biology and medicine, the THz radiation can be used for disease detection, tissue identification, protein states and molecular signatures, monitoring of receptor binding, performing label-free DNA sequencing visualizing, and radiation effects on biological samples and biological processes [23]. Figure 1-5 introduces an interesting non-destructive approach for monitoring changes in the coffee leaf water content using THz waves [24]. Two CW lasers with very similar wavelengths and equal output power are employed to generate the beat frequency between 0 to 2 THz. The beat is then partly used for the excitation of a THz antenna and partly transmitted directly to the detector as reference signal. The THz radiation generated by the antenna, after going through the coffee leaf, is changed both in phase and amplitude due to the interaction with the water content. The phase and amplitude variation can then be used to determine the water content change of the leaf.

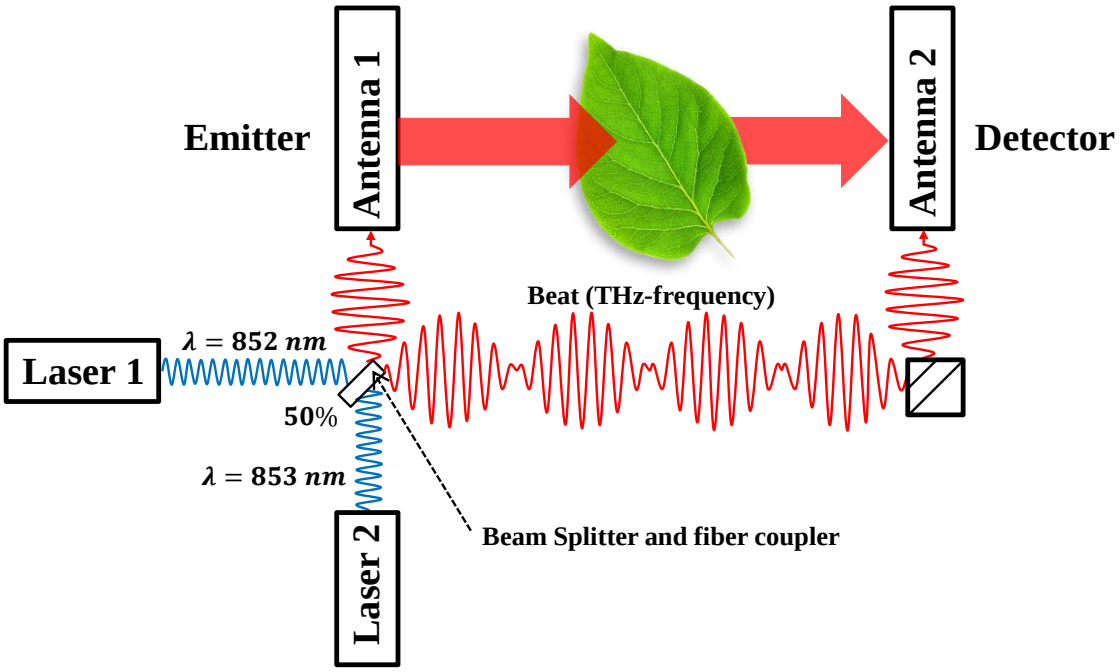

Figure 1-5: Schematic view of the THz-based approach for monitoring the water content changes in the coffee leaf. (Reproduced from [24])

The THz communication has also been enabled by the advances of compact and stable sources. It is recognised as one of the most promising methods to meet the increasing demand for the high data rate communications [25]. Although such demand can be temporally accommodated with the advanced modulation schemes and signal processing techniques, to achieve data rates of or beyond 10 Gb/s seems challenging due to limited bandwidth in the microwave region. To explore more spectral resources in the future wireless communications, the THz band, especially the frequency band between 275 GHz and 3000 GHz which has not been allocated for specific uses, has attracted considerable attention. Besides being promising for indoor communications, the THz wave is also seen applicable in the secured wireless communication on battle field and deep-space communication [26]. Figure 1-6 is a proposed scheme for a hidden THz communication link based on the ultrawide bandwidth [27]. By encrypting a 1 Mb/s data signal using a long code sequence at a chip rate of 100 Gb/s, the decoder can describe a rejection ratio of about 40 dB for the jamming attached. Thus a potential adversary should possess several orders of magnitude more power to overwhelm the receiver.

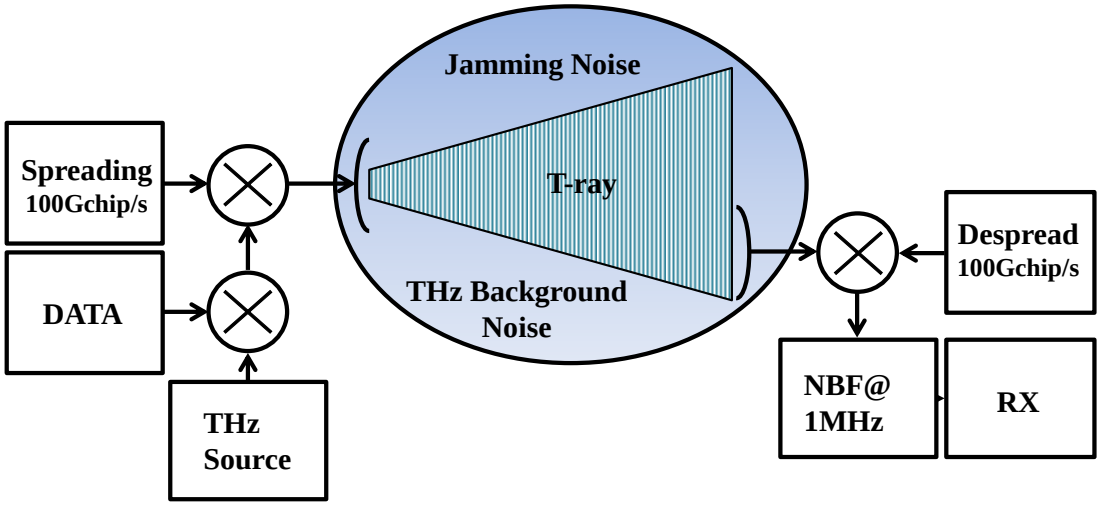

Figure 1-6: Schematic of view of a hidden THz communication link based on the ultrawide bandwidth. The spreading factor is 10^5 (100 Gb/s:1 Mb/s). T-ray means THz radiation. NBF is short for noise band filter, RX represents the receiver. (Reproduced from [27])

1.1.3 THz Sources

The above applications can only be realised based on the successful development of reliable THz sources. There are numerous developed THz radiation sources as candidates for the above applications. These sources can be classified into three groups as Photonic Devices (PDs), Solid-state Devices (SSDs) and Vacuum Electronic Devices (VEDs). The output power variation with the operation frequency for a number of typical THz sources is summarised in Figure 1-7.

1.1.3.1 Photonic Devices

The PDs has served for a few decades as the pioneering THz sources. They are optical and laser devices that employ the frequency down-conversion techniques to generate THz radiation. The PDs can be divided into two types: the optical THz generators and the quantum cascade lasers (QCL) in the THz regime.

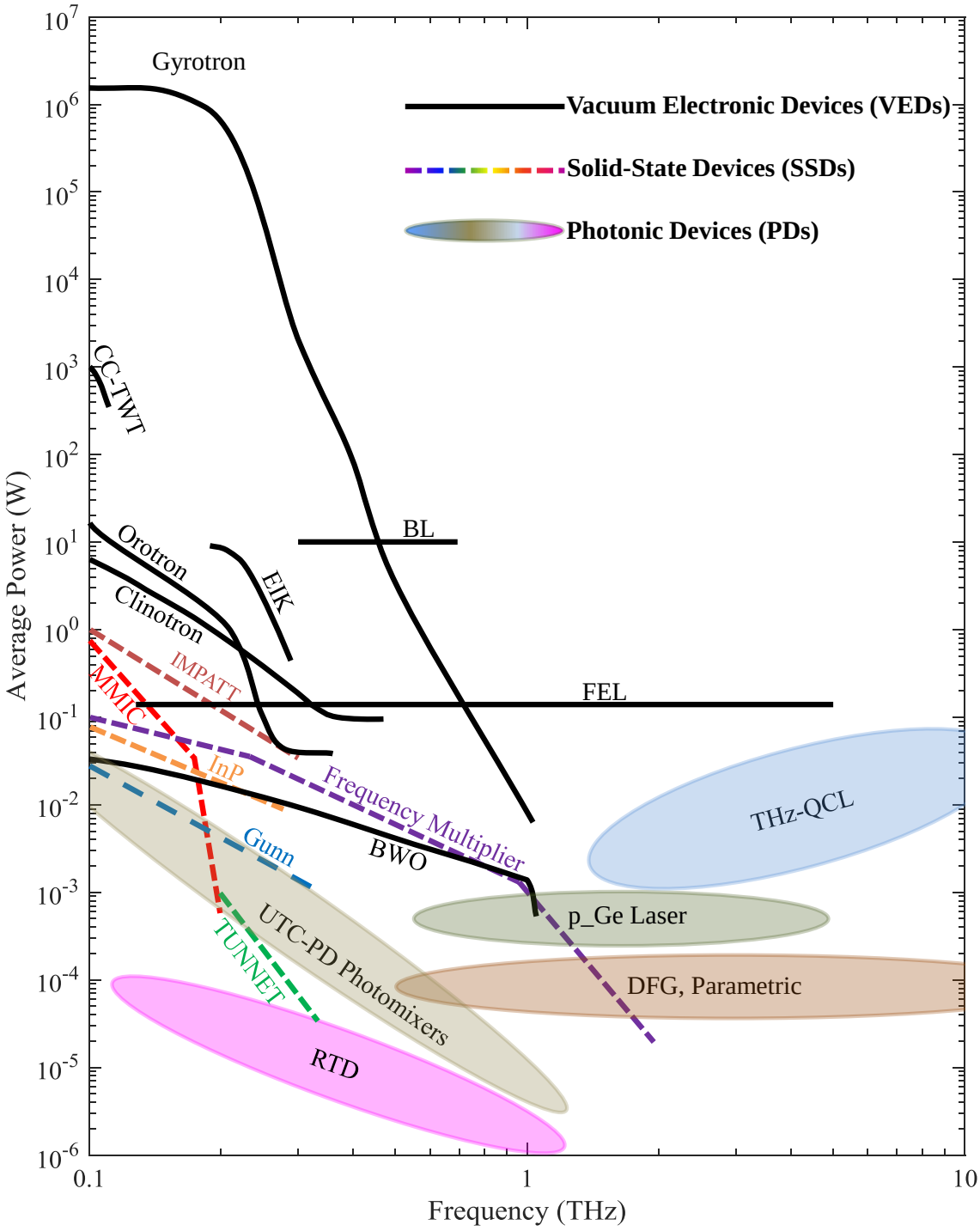

Figure 1-7: The average output power of THz sources as a function of the frequency. This plot is based on the summary of a number of previous publications of overview [11, 28-33] and the recent literature reports [22, 34, 35]. CC-TWT stands for the coupled cavity travelling-wave tubes. BL refers to the beamline sources. EIK is short for the extended-interaction klystron. IMPATT is short for impact ionization avalanche transit-time diode. MMIC represents microwave monolithic integrated circuit. TUNNET means tunnel injection transit time. InP stands for InP power amplifier. RTD stands for resonant tunneling diode. UTC-PD is short for uni-travelling-carrier photodiode. DFG is short for difference-frequency generation.

In the optical THz generators, the ultrafast modulated photocurrent is generated in a semiconductor or a photoconductive switch, using the photo-Dember effect or the electric-field carrier acceleration. Some other optical THz generator also utilises the nonlinear optical effects, such as the optical parametric oscillation, the optical rectification and difference-frequency generation (DFG), to generate THz emissions [11].

The QCL has been firstly demonstrated at a lasing frequency of about 70 THz in 1994. The THz waves are emitted by means of electron streaming down between subbands of quantum wells [36]. After that, continuous effort has been devoted to lower the emission frequency of such device by means of resonant-photon assistance, external magnetic field, and new designs of gratings. The future development of QCL involves the reduction of the lasing frequency and the starting current, the increase of the operation temperatures, and the improvement of the quality of the THz beams [11].

It can be seen from Figure 1-7 that the PDs, while being able to cover the frequency band between 0.1 THz and 10 THz, have limited output power capabilities.

1.1.3.2 Solid-state Devices

The SSDs are microwave electronic devices that transfer the kinetic energy of the conduction current in semiconductors to electromagnetic field energy. Typical SSDs include high frequency IMPATT, Gunn and TUNNET diodes [37]. They are compact and stable source capable of CW operation at room temperature. Starting from the millimetre wave band, the development of the solid-state devices has reached the low frequency end of the THz regime, and is progressing towards even higher frequency band [11], as shown in Figure 1-7.

The operation frequencies of SSDs are generally limited by the effect of high frequency roll-off, which is caused by the finite transit time of carriers across the semiconductor junctions. Typically a CW operation at around 100 GHz can be obtained with output power of about 100 mW. Beyond 200 GHz, frequency multiplications with two or more diodes are usually adopted. Thus, between 100 GHz and 200 GHz, the output power is

inversely proportional with the square of the operation frequency, while above 200 GHz, the former is inversely proportional with the cube of the latter [38].

1.1.3.3 Vacuum Electronic Devices

The VEDs also belong to the microwave electronic devices. However, they are designed to transfer the kinetic or potential energy of the convection current in vacuum to THz emissions. Since these devices are based on the free electrons, they have the potential to deliver high-power THz emissions, which can also be seen from Figure 1-7. Thus, development of VEDs for THz radiation is useful in applications calling for high-power usually with considerably high efficiency. The VEDs include backward-wave oscillators (BWOs) [39], travelling wave tubes (TWTs) [40], klystrons [41], Smith-Purcell radiation devices [42], magnetrons [43], free electron lasers (FELs) [44], gyro-devices [45] and so on. After the development of more than a century, the VED family now covers over 12 orders of magnitude in power and more than three orders of magnitude in frequency, while further advances are still foreseeable and anticipated.

In the linear type of VEDs, electron beams are emitted by cathodes and accelerated by applied direct-current (DC) or pulsed voltage to gain longitudinal momentum and transit through the devices. External magnetic fields are usually employed to guide the electron beam and counterbalance the repulsive forces among electrons. At the entrance of the beam-wave interaction region, the electrons are uniformly distributed in a specified region and generate noise-level electromagnetic radiation. Then, due to the special interaction structure or external input signal, a preferred electromagnetic mode will be established and interact with the electron beam. The result of interaction is that some of the electrons are accelerated while others are decelerated and hence the electron bunching might be formed. The bunched electrons contain an alternating-current (AC) component which enables coherent radiation. As long as most of the electrons stay in the decelerating phase of the electromagnetic field, they will lose energy to the field which will in turn be amplified. After the process of beam-wave interaction, the spent electrons are collected by the collector and their kinetic energy is thermally dissipated [46].

To enable the beam-wave interaction in the linear type of VEDs, the synchronism condition should be fulfilled:

$$\omega - k_{\parallel} v_{\parallel} = s\Omega \tag{1.1}$$

where ω represents angular frequency of the wave, $k_{\parallel}$ is the wavenumber of the wave in the z direction, $v_{\parallel}$ is the electron axial velocity, s denotes the harmonic number and Ω represents the gyrating frequency of electron oscillations due to the external magnetic or electric field. The derivation of (1.1) can be found in the Appendix-I. In (1.1), $k_{\parallel} v_{\parallel}$ is called the Doppler term. The changes of the energy of the electron during the process of beam-wave interaction may have two consequences. One is the longitudinal bunching of the electron due to the changes of $v_{\parallel}$ values. The other one is the orbital bunching due to the dependence of Ω on the energy of the electron.

When the transverse motion of the electron beam is negligible compared with the Doppler term, the synchronism condition can be simplified into

$$v_{ph} = \frac{\omega}{k_{\parallel}} \approx v_{\parallel} < c \tag{1.2}$$

where v_{ph} and c represent the phase velocity of the wave and the speed of light, respectively. This synchronism condition implies that only waves with v_{ph} less than c can interact with the electrons. To realise this particular condition, the slow-wave structures are usually used to decrease the phase velocity of the electromagnetic (EM) wave. The corresponding devices are called slow-wave devices, such as TWTs and BWOs. Figure 1-8 shows a typical TWT configuration where a helical structure is used as the slow-wave circuit. Since the dimension of a slow-wave structure is usually a fraction of the operation wavelength, the operation of slow-wave device will inevitably encounter the fabrication difficulties and high-power breakdown problem in the THz frequency range.

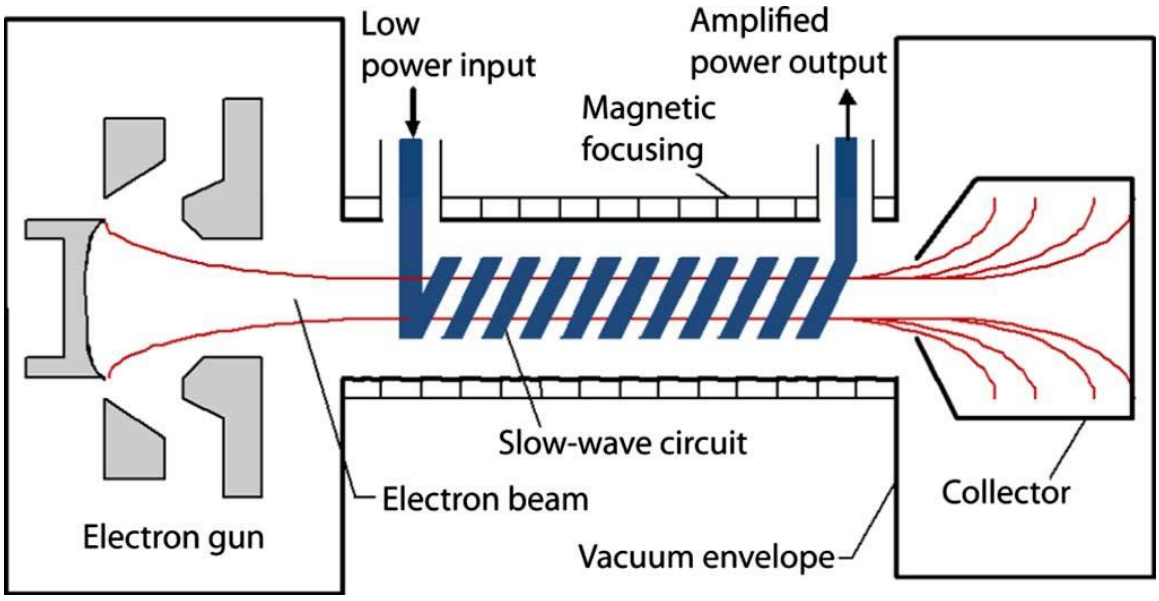

Figure 1-8: Schematic view of a TWT [28].

Then, if Ω has a finite value, the synchronism condition stated in (1.1) will allows the electrons to interact with the fast wave, the phase velocity of which is larger than c. In gyro-devices, an external magnetic field (B_0) in the axial direction guides the gyrating movement of the electrons with a cyclotron frequency of Ω:

$$\Omega = \frac{eB_0}{m_e\gamma} \tag{1.3}$$

in which e and m_e are the charge and rest mass of single electron, respectively. γ represents the relativistic factor which is related to the beam accelerating voltage (V_b) as

$$\gamma = 1 + \frac{eV_b}{m_e c^2}. \tag{1.4}$$

As the fast-wave devices employ the waveguides with smooth wall, whose transverse dimensions could be larger than the wavelength when operating with the high-order waveguide modes, they are not dimensionally confined by the operating frequencies. This in turn gives rise to overmoded smooth wall waveguide's application in THz band operations, offering considerable convenience in fabrication and impressive capacity for high power handling. In factor, the adoption of overmoded waveguides has enabled the

gyrotrons to deliver unprecedented high power in the THz band. This also explains the superior output power capabilities of the gyrotrons, as illustrated in Figure 1-7.

1.2 Research Motivation

A number of the applications, such as the dynamic nuclear polarisation enhanced nuclear magnetic resonance (DNP-NMR) [20], electron-cyclotron resonance heating (ECRH), current drive in tokamak and stellarator plasmas [21], plasma diagnostics [47], and electron-spin resonance spectroscopy [48], will depend on the availability of high-power THz radiations. From Figure 1-7, not all the sources are capable of high-power THz radiation generation. The output powers of devices such as the BWOs, TWTs, SDs and PDs are not yet sufficient for the above applications. Thus, this thesis is focused on the study of gyro-devices, which can generate impressively high-power radiation from 0.1 THz to 1 THz.

Despite the great potential of producing high power, the development of gyrotrons in the THz band is limited by the requirement of intense external magnetic field (B_0), which can be expressed as [49-51]

$$B_0 \cong \frac{\gamma m_e}{e} \cdot \frac{2\pi f}{s}. \tag{1.5}$$

Here f represents the oscillation frequency of the electromagnetic field. It can be seen that for high frequency oscillation, one needs high external magnetic field. For example, the 1.022 THz gyrotron operating at the fundamental harmonic requires a B_0 value as high as 38.5 T, which can only be provided by a pulsed magnet currently [34]. This problem could be eased by enabling harmonic operations ($s > 1$) because the required B_0 magnitude is inversely proportional to s, as described in (1.5). However, under the traditional small-orbit gyrotron configuration as shown in Figure 1-9 (a), a harmonic operation will inevitably encounter serious mode competition due to the high density of the mode spectrum. When simultaneous resonant interaction between several modes and the electron beam takes place, the device operation may be unstable. In addition, multimode oscillation causes a deterioration of the coherence and directivity of the generated radiation, gives rise to trapped modes and, in general, decreases the device

efficiency. As a result, the harmonic operations at or beyond the third harmonic are rarely reported for the small-orbit gyrotron [35].

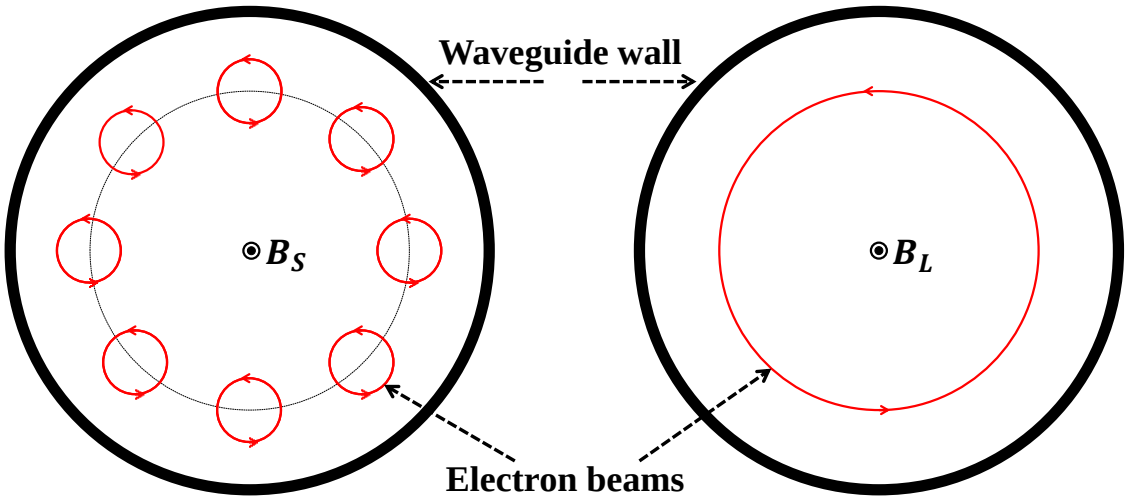

(a) (b)

Figure 1-9: Transverse view of the trajectory of the gyrating electrons: (a) Small orbit electron beam with the external magnetic field of B_S; (b) Large-orbit electron beam with the external magnetic field of B_L. B_S is larger than B_L.

To enable high-harmonic operations of gyrotrons, electro-dynamic systems with effective selectivity and discrimination of the cavity modes should be considered. There are several promising ways to be chosen from, such as the large-orbit gyrotron (LOG) scheme [52-59], the gyro-multiplier scheme [60-65], the planar gyrotrons [66] and the coaxial gyrotron scheme [67]. This thesis focuses on the LOG and gyro-multiplier.

In a LOG, the guiding centre of the gyrating electron beam coincides with the axis of the axisymmetric waveguide, as shown in Figure 1-9 (b). In such a configuration, the excitation factor of $TE_{m,n}$ mode at the sth harmonic is simplified as [51]:

$$G_{m,n} = \frac{J_{m-s}^2(0)}{\left(\mu_{m,n}'^2 - m^2\right)J_m^2\left(\mu_{m,n}'\right)} \tag{1.6}$$

where J_m is the mth order Bessel Function and $\mu_{m,n}'$ is the nth root of its derivative. m and n can also be interpreted as the azimuthal and radial indexes of the $TE_{m,n}$ mode. To maintain a non-zero value of $G_{m,n}$, m must be equal to s. This means only the modes with m equal to s can be excited, which will greatly alleviate the problem of mode competition. In fact, this feature has led to a number of experimental demonstrations of LOGs mainly

within the first five harmonics [6, 22, 58, 59, 68-70]. For example, researchers in University of Fukui [59] have demonstrated the fifth harmonic operation of a LOG at 138 GHz with the beam voltage U=40 kV. Also researchers in Institute of Applied Physics [70] and University of California, Los Angles [53] have achieved the fifth harmonic LOG operations at 75 GHz (U=250 kV) and 38 GHz (U=500 kV), respectively. However, in the development of THz LOGs where significant reduction of the external magnetic fields is required, even higher harmonic operations ($s > 5$) should be considered. In the THz LOG, new challenges such as the choice of the electron beam source, the separation between neighbouring harmonics, the influence of Ohmic loss and the impact of electron velocity spread should be carefully examined.

As for the gyro-multiplier, a relatively low-frequency (LF) signal provides electron modulation and bunching at the frequency of the operating wave and also simultaneously at its harmonics, which occurs due to the nonlinear properties of the electron beam. Because of this preferential frequency imposed on the electron beam, high-frequency (HF) radiation at a high electron cyclotron harmonic can be selectively excited, as shown in Figure 1-10 for the case of the sectioned-cavity gyro-multiplier.

Based on [65], the beam-wave interaction cavity can be divided into three parts: Cavity 1, 2 and 3, as shown in Figure 1-10. Cavity 1 and 3 are tuned to be resonant for $TE_{1,2}$ and $TE_{1,3}$ modes operating at fundamental low frequency (LF), respectively. The electron beam, being modulated by the LF wave, can excite harmonic high frequency (HF) waves in the middle cavity (Cavity 2). $TE_{1,2}$ and $TE_{1,3}$ modes are designed to be oscillating at the fundamental LF of 342 GHz, while Cavity 2 is designed to be suitable for excitation of $TE_{4,9}$ mode operating at the fourth harmonic HF of 1368 GHz. The output power at LF and HF is simulated to be 2 kW and 0.12 kW, respectively. The component of the output wave is summarised in Table 1-1.

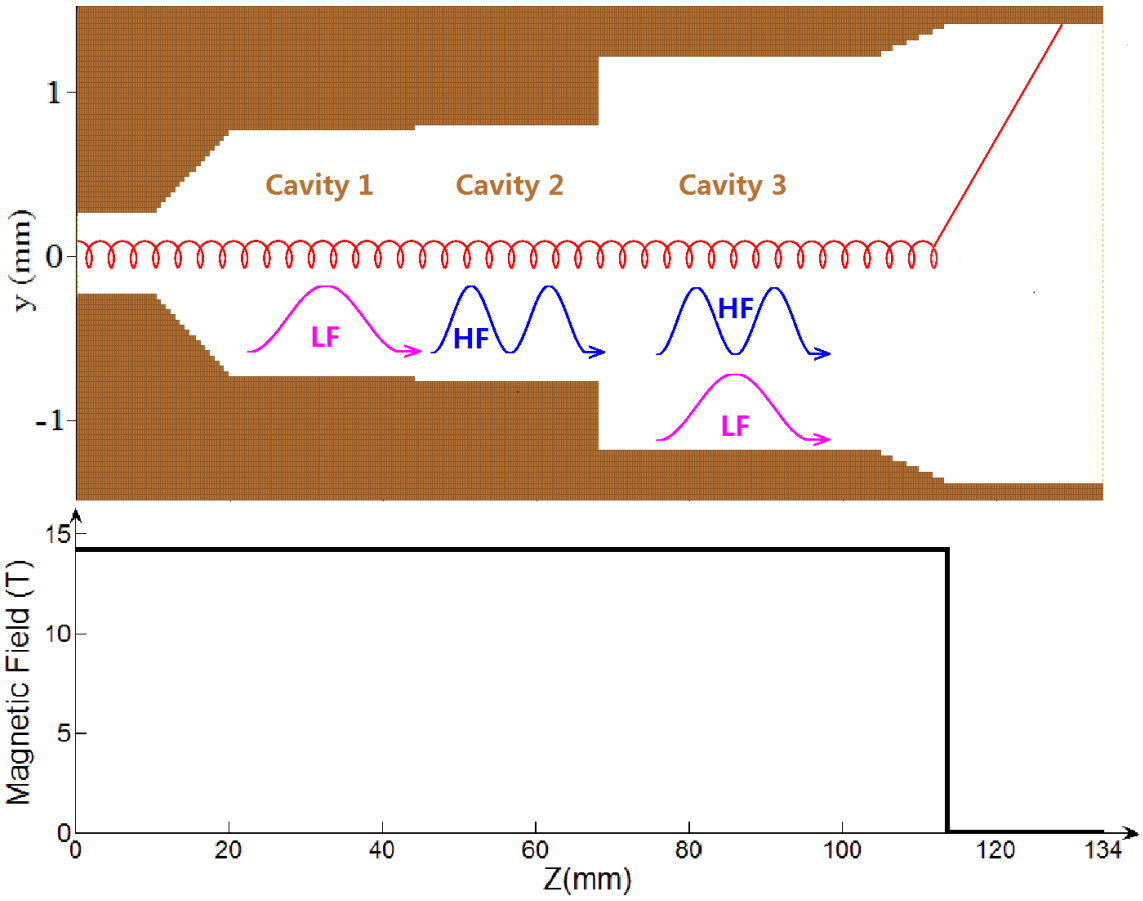

Figure 1-10: Schematic view of the sectioned-cavity gyro-multiplier.

Table 1-1: Summary of the component in the output wave.

	LF	HF
s	1	4
Frequency (GHz)	342	1368
Power, P_0 (kW)	2	0.12
Mode content	$TE_{1,3}$	$TE_{4,9}$

However, in most of the applications of gyro-devices, a single frequency radiation as well as quasi-Gaussian output is required. Thus at the output of the gyro-multiplier, an effective system must be adopted to separate the high frequency from the low frequency wave and converter the high-order waveguide modes into quasi-Gaussian beams. Besides, the reflection of the output wave back into the beam-wave interaction system of the gyro-multiplier should be minimised. And an acceptable efficiency of the power transportation should also be maintained.

Although the operation of the gyro-multiplier has been studied extensively in theory [63, 64, 71, 72] and demonstrated successfully in experiments [62, 65] in recent years, the investigation of a proper output system for such device has not been discussed in the literature. Unlike the traditional gyrotrons of single mode operation, the output of a gyro-multiplier contains two modes with one operating at the fundamental electron cyclotron resonance and the other one being excited at one of the harmonics. A proper output system for the gyro-multiplier is in need to not only convert the generated wave to quasi-Gaussian beams, but also separate the two modes in two frequency bands.

1.3 Aim and Objectives

The above analysis justifies the overall objective of this thesis, which is to study the high-harmonic gyro-device in the THz band. Specifically, this thesis work involves the theoretical study and tool development, the insight into the operation of high-harmonic THz gyrotrons and the design as well as fabrication of key components for a THz gyro-multiplier output system.

As the gyro-multiplier with sectioned cavity is essentially based on the traditional complex-cavity gyrotron, the study of the latter will be helpful for the future development of the former. At THz frequencies, the commercial software (such as CST [73], HFSS [74] and MAGIC [75]) typically takes extensive computational time and resource for either the cold cavity analysis or the hot cavity simulation of gyro-devices, despite of their adorable numerical accuracy. Thus this thesis will start with the development and verification of an in-house analysis code for the study of the complex-cavity gyrotron. The Fortran-based code will also be made to be applicable in the cold cavity analysis of the high-harmonic LOG.

This thesis will then characterise the operation of a high-harmonic LOG in the THz range. The study will aim at significantly reducing the required external magnetic field by enabling high-harmonics operation of the device. Using the linear analysis and three-dimensional (3D) Particle-In-Cell (PIC) simulations, a LOG capable of operation at up to the 9^{th} electron cyclotron harmonic will be designed and simulated. With the assistance of

3D PIC software, the starting oscillation process and the beam-wave interaction scenario will be demonstrated. Based on the simulation model developed, the competition among neighbouring harmonics will be studied. The methods that can be used to alleviate the mode competition and enable single mode operation will be investigated. Some key issues in THz LOGs, such as the Ohmic loss, the influence of the electron beams and the multi-modes, multi-harmonics behaviour will be characterised.

A considerable portion of effort in this thesis will be devoted to investigate an effective output system for the gyro-multiplier which is capable of not only extracting the high frequency content from the beam-wave interaction, but also transforming it into quasi-Gaussian beams. To do so, a dual-harmonic quasi-optical mode converter (DQMC) and a frequency selective surface (FSS) will be integrated in the output system. The traditional quasi-optical mode converter (QMC) has been successfully utilised in gyrotrons for the conversion of the single mode output into quasi-Gaussian beam [76]. It has also been optimised for the frequency tunable gyrotrons operating with a number of neighbouring modes at the fundamental harmonic [77]. In the case of the gyro-multiplier, however, the fundamental and harmonic modes are distantly separated in the spectrum. The traditional geometrical optics analysis needs to be modified in the design of a DQMC by taking into consideration of the propagation properties of both modes to enable the simultaneous transformation of both contents into quasi-Gaussian beams. For the separation of the two frequencies, a FSS is employed. The FSS has been widely used in the low-power range as an effective filter [78]. It has also been shown as operable with high-power microwave radiation [79]. Nevertheless, its operation with high-power THz radiation has not been considered elsewhere. In this work, a high-pass FSS formed by periodic circular perforations on a metal plate will be designed, fabricated and tested.

1.4 Organization of the Thesis

The remaining part of this thesis is organized as follows:

Chapter 2 begins with the introduction to the fundamentals of the beam-wave interaction principle in all the gyro-devices: electron cyclotron maser (ECM). The family of gyro-

devices are reviewed. Following that, the operation principle and the configuration requirement of the gyro-multiplier is analysed. Then, the quasi-optical mode converters, as commonly used in traditional gyrotrons with high-order waveguide modes, are introduced. The launchers and mirrors, as the essential constitutions of a quasi-optical mode converter, are summarised and analysed in detail. At the end, the FSS and the possible cooperation with high-power THz devices are reviewed.

Chapter 3 presents the steady-state nonlinear theory of the gyrotron and the development of an in-house analysis tool for gyrotrons. A complex-cavity gyrotron, which also forms the foundation of the gyro-multiplier scheme discussed in this thesis, is studied by both the in-house code and 3D PIC simulations. A comparison between the results will also be conducted, showing reasonable agreement.

Chapter 4 provides the design and simulation of a high-harmonic large-orbit gyrotron. The choice of the electron beam source, the cold cavity analysis and the hot cavity simulation will be described. A number of key issues such as the competition between neighbouring harmonics, the beam-wave interaction scenario and the Ohmic loss will be discussed. The multi-modes, multi-harmonics behaviour will also be characterised.

Chapter 5 presents the investigation of a quasi-optical output system for a fourth-harmonic gyro-multiplier in the THz band through geometric optic analysis and 3D full-wave simulation. The output system of the gyro-multiplier needs not only to transfer two high-order waveguide modes into the quasi-Gaussian beams, but also to separate the two beams. A DQMC and a FSS are employed to achieve both goals within this system. It is shown that the optimal design of the DQMC requires a special mode selection in the gyro-multiplier. The FSSs are designed with consideration of the fabrication error. It is also demonstrated that the designed FSS is capable of handling the high-power output from the gyro-multiplier.

Chapter 6 illustrates the fabrication and experimental test of the high-pass FSS. The comparison of the simulation result and experimental outcomes will be conducted. Some methods to improve the performance of the FSS will be demonstrated in theory and tested in experiments.

Chapter 7 concludes this thesis, summarises the key contributions and suggests the future work as well as possible improvements. The author's publications during the doctoral research are also listed.

Chapter 2 Operation of the Gyro-devices

This chapter begins with a brief review of the operation of the traditional gyro-devices and the gyro-multipliers. Following that, the geometrical optics for the quasi-optical mode converters (QMC) is introduced. Finally, an overview of the frequency selective surface (FSS) is given, with attention paid to the recent studies on its high-power applications.

2.1 Electron Cyclotron Maser

The electron cyclotron maser (ECM) is based on a stimulated cyclotron emission process involving energetic electrons in gyration motion. The principle of ECM instability can be illustrated in Figure 2-1.

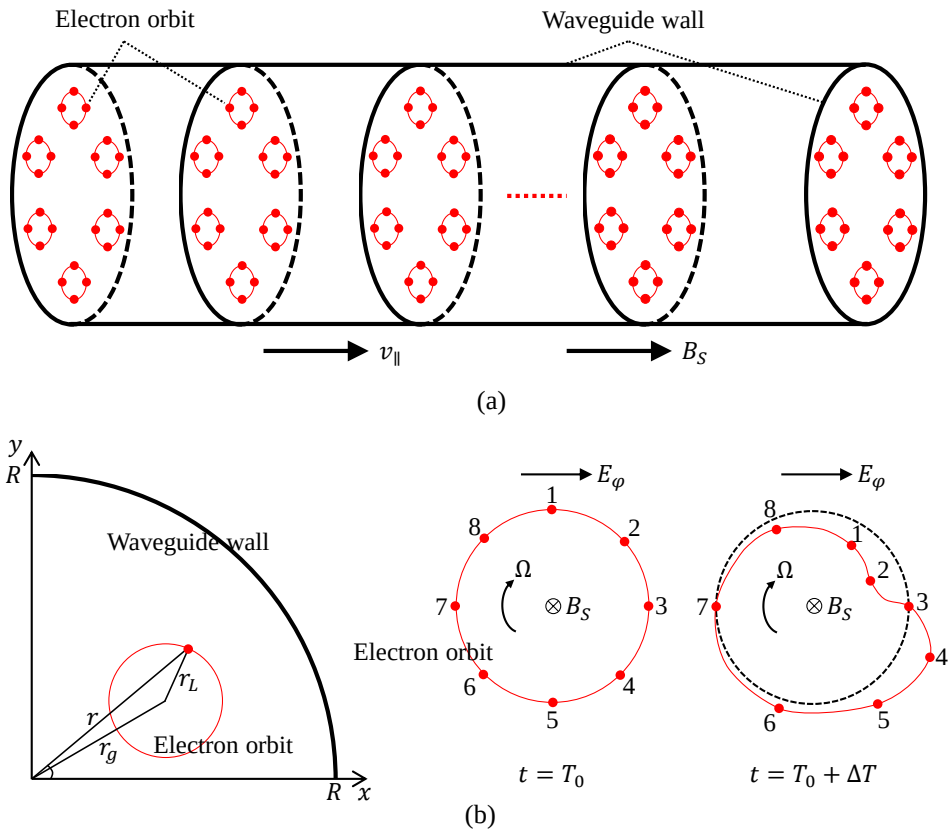

Figure 2-1: The operation principle of ECM. (a) Electrons distribution in the transverse direction; (b) Bunching process of the electrons.

As shown in Figure 2-1 (a), a hollow electron beam is moving through a waveguide with radius of R. The electrons possess an axial velocity of $v_{\parallel}$ and a transverse velocity of $v_{\perp}$ due to the confinement of an external magnetic field (B_s) in the axial direction. The ratio between the two velocities is called the pitch factor (α) and:

$$\alpha = \frac{v_{\perp}}{v_{\parallel}}. \tag{2.1}$$

The process of synchronism and bunching of the electrons can be explained by examining one of the electron orbits, as shown in Figure 2-1 (b), on which eight electrons are initially monoenergetic. r_g denotes the guiding radius of electrons and r_L is the Larmor radius of electron cyclotron movement. $\boldsymbol{E_{\varphi}}$ is the azimuthal electric field vector which modulate the electrons and

$$\boldsymbol{E_{\varphi}} = E_{\varphi}\boldsymbol{e_{\varphi}} \tag{2.2}$$

in which $\boldsymbol{e_{\varphi}}$ is the unit vector in the φ direction of the cylindrical coordinate system (r, φ, z). At the time T when the electrons enter the interaction cavity, they are evenly distributed in phase but gyrating in different directions. Considering the relativistic effect, the radius of the gyrating movement of the electrons (r_L) can be express as:

$$r_L = \frac{v_{\perp}}{\Omega} \tag{2.3}$$

and Ω can be obtained from (1.3).

After entering the interaction structure, the direction of gyration movement of electron No. 3 and No. 7 are perpendicular to $\boldsymbol{E_{\varphi}}$. And their motion will not be disturbed. However, electron No. 1 is gyrating in the same direction with $\boldsymbol{E_{\varphi}}$, whose $v_{\perp}$ as well as γ values will be lowered. Thus its r_L value will become smaller while Ω value will be higher. This means that electron No. 1 will gyrate faster in phase and approach electron No. 3. And the same effect will be induced on electron No. 2 and No. 8. The opposite effect will be laid on electron No. 4, No. 5 and No. 6 by which their $r_L$values will become larger with lower values of Ω. Under this situation, these three electrons will lag behind

in phase and be caught up by electron No. 3. As this process goes on, a phase bunching will be formed around electron No. 3, as shown Figure 2-1 (b) at the time $T + \Delta T$.

Thus, the electrons will form a phase bunch azimuthally due to the interaction with the EM field. In case that ω equals to Ω, there will be no energy exchange between the two as one half of the electrons will be in the accelerating phase while the other half will be in the decelerating phase.

If ω is slightly larger than Ω, the bunching will fall into the decelerating phase of the field, where the electrons will lose energy to the field. As long as the condition of

$$\omega \geq \Omega \tag{2.4}$$

is maintained, this process will go on and the EM field will be amplified. The electrons losing energy will have their Ω values raised until the above condition is dissatisfied. In the reverse case of

$$\omega < \Omega \tag{2.5}$$

, the electrons will gain energy from the EM field.

From the above discussion we can see that the relativistic effect of electrons cyclotron movement forms the basis of ECM. Due to this effect, the electrons gaining energy become heavier in relativistic masses and lag behind in phase, while the ones losing energy acquire phase advances. Such kind of phase bunching imparts an AC component to the electron beam current and thus enables the emission of EM waves.

2.1.1 Traditional Gyro-devices

There are traditionally four types of gyro-devices, whose interaction structures are shown in Figure 2-2. These interaction structures all support fast wave propagation with open ends to enable extraction of the generated wave.

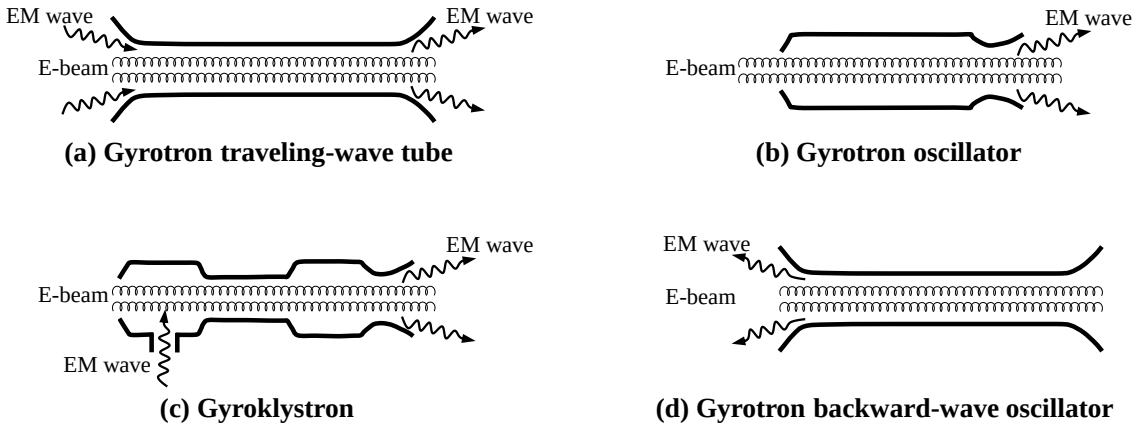

Figure 2-2: Interaction structure of four basic types of gyro-devices. (Reproduced from [80])

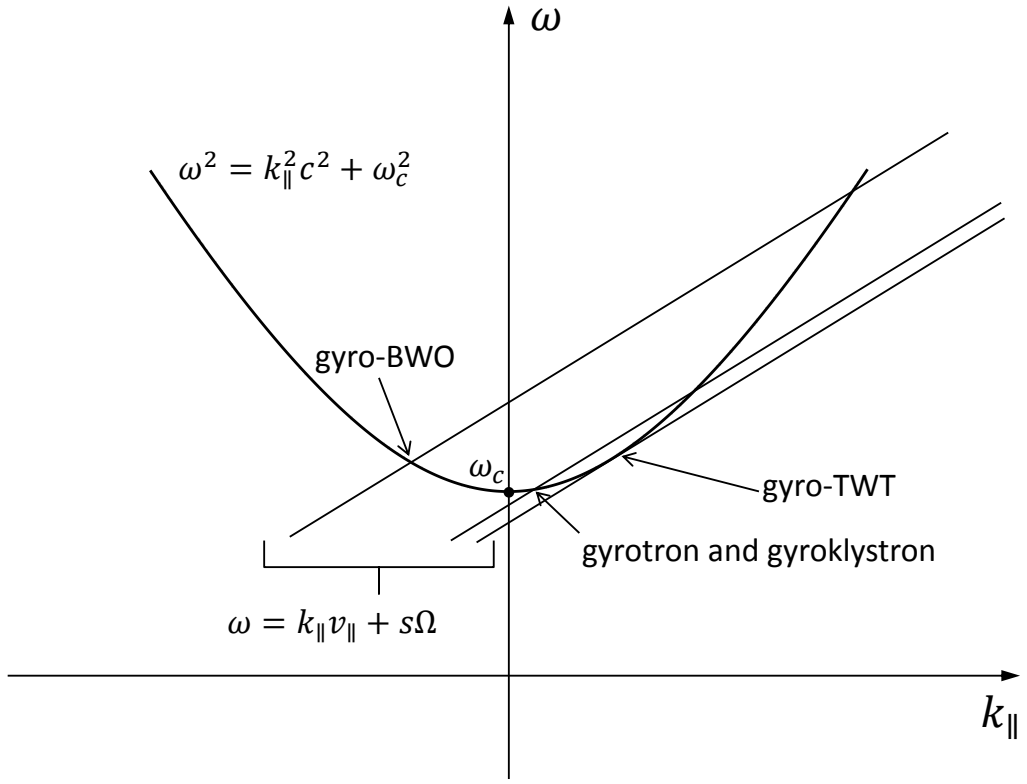

Figure 2-3: Intersection point between the mode line and the beam-wave synchronism lines for different types of gyro-devices. (Reproduced from [80])

The synchronism and resonant interaction between the waveguide mode and the electron beam can be shown in Figure 2-3, in which the hyperbolic line represents the dispersion relation of a typical propagating mode in a waveguide and the straight lines are the synchronism condition for different B_0 values. The cut-off frequency of the waveguide is also shown as ω_c in the figure. In principle, a resonant interaction can take place at any

intersecting point between the mode dispersion curve and the synchronism line. To lower the susceptibility of the operation to the electron velocity spread, all the four devices operate closely to the cut-off frequency of the waveguide, ω_c.

In a gyro-TWT as shown in Figure 2-2 (a), the input wave is amplified while propagating forward with the electron beam. Thus, in the steady state of amplification, the wave amplitude increases along the axial direction of the tube while maintains a constant value at any fixed point in space. When the input driving signal is turn off, there will be no output power.

The gyroklystron amplifier is a narrow band amplifier that commonly employs multiple cavities to increase the gain. The two-cavity example is shown in Figure 2-3 (c). In the first cavity, the electrons are modulated by the input signal enabling azimuthal phase bunching effect. They are continuously bunched when passing the drifting cavity before entering the second cavity, where they drives a larger amplitude oscillation compared to the input signal. The oscillation is then extracted from the output end of the tube.

In a gyrotron oscillator as shown in Figure 2-2 (b), the key principle of operation is reflective feedback. As the EM field oscillates in the cavity, there will be end reflection resulting forward and backward waves. This results a closed loop of continuous wave circulation. When the electron beam interacts with and amplifies the forward wave, a gyrotron is established.

The gyro-BWO, as shown in Figure 2-2 (d), is a device in which the azimuthal bunch of electrons loses energy to the backward wave.

The gyro-TWT amplifier is capable of being tuned over a broad bandwidth. The gyroklystron amplifier has better stability property and greater power capability but narrower bandwidth than gyro-TWT. The gyrotron oscillator provides the highest average power and frequency while the gyro-BWO features continuous and fast frequency tunability by changing the electron beam voltage.

2.1.2 Gyro-multiplier Operation

The operation of a gyro-multiplier is based on the combination of the ECM and the frequency multiplication technique. In a gyro-multiplier, a relatively low-frequency (LF) signal provides electron modulation and bunching at the fundamental harmonic and also at its harmonics, which occurs due to the nonlinear properties of the electron beam [60-65, 71, 81-88]. By special configurations of the beam-wave interaction cavity (such as the sectioned-cavity or the corrugated cavity), one of the high-harmonic contents of the nonlinear transverse movement of the electron beam can be selectively extracted. By avoiding the direct excitation of the high-harmonic oscillation, the required B_0 value is greatly reduced.

The LF wave in a gyro-multiplier may either be induced internally of injected externally. A self-exciting gyro-multiplier, which needs no input, is often more attractive in the THz range. In such a device, the electron beam excites both the LF and HF waves, such as the sectioned-cavity gyro-multiplier in Figure 1-10. In each cavity, the oscillation frequency ω and the cavity radius R are linked by

$$\omega = c \cdot \sqrt{k_{\parallel}^2 + \frac{\mu_{m,n}'^2}{R^2}} \tag{2.6}$$

in which $\mu_{m,n}'$ is the eigenvalue of the oscillation mode. In Cavity 1 and 3, the electron beam is in resonance with the low-frequency wave at the $s_{LF} - th$ electron cyclotron harmonic, meaning

$$\omega_{LF} \approx s_{LF}\Omega + k_{\parallel LF} v_{\parallel}. \tag{2.7a}$$

The radius of Cavity 2 is adjusted to extract the HF content at the $s_{HF} - th$ electron cyclotron harmonic, meaning

$$\omega_{HF} \approx s_{HF}\Omega + k_{\parallel HF} v_{\parallel}. \tag{2.7b}$$

Here ω_{LF} and ω_{HF} are the frequencies of the LF and HF waves, respectively. s_{LF} and s_{HF}represent the harmonic number of the LF and HF waves, respectively. For the gyro-

multiplier studied in this thesis, $s_{LF} = 1$ and $s_{HF} = 4$. $k_{\parallel LF}$ and $k_{\parallel HF}$ are their longitudinal wavenumbers, respectively. Ω can be obtained from (1.3). In Cavity 1 and 3, the electron beam is modulated by the LF wave at the harmonic number of s_{LF}. In Cavity 2, due to the special choice of the radius which satisfies

$$\omega_{HF} \approx \frac{s_{HF}}{s_{LF}} \omega_{LF} \tag{2.8}$$

, the bunched electron beam can excite the HF wave at the $s_{HF} - th$ electron cyclotron harmonic. And it can be derived that

$$k_{HF} = \frac{\omega_{HF}}{c} \approx \frac{s_{HF}}{s_{LF}} \cdot \frac{\omega_{LF}}{c} = \frac{s_{HF}}{s_{LF}} k_{LF}. \tag{2.9}$$

In the case of a uniform B_0, (2.7)-(2.8) automatically make the divisibility of the longitudinal wavenumbers necessary,

$$k_{\parallel HF} \approx \frac{s_{HF}}{s_{LF}} k_{\parallel LF}. \tag{2.10}$$

Knowing that

$$k^2 = k_{\parallel}^2 + k_{\perp}^2 \tag{2.11}$$

, it can be derived that

$$k_{\perp HF} \approx \frac{s_{HF}}{s_{LF}} k_{\perp LF}. \tag{2.12}$$

Considering

$$k_{\perp} = \mu'_{m,n}/R \tag{2.13}$$

, it can be derived that

$$\mu'_{m,nHF} \approx \frac{s_{HF}}{s_{LF}} \cdot \mu'_{m,nLF} \tag{2.14}$$

where $\mu'_{m,nLF}$ and $\mu'_{m,nHF}$ are the eigenvalues of the HF and LF modes, respectively. Like in the traditional gyro-devices, the most evident selectivity and efficient frequency multiplication can be obtained by using large-orbit electron beams. For the designed sectioned-cavity gyro-multiplier, the utilisation of the large-orbit electron beam restricts that

$$s_1 = m_{LF} \tag{2.15a}$$

$$s_2 = m_{HF} \tag{2.15b}$$

where m_{HF} and m_{LF} are the azimuthal index of the HF and LF modes, respectively. The above analysis also justifies the selected operation modes as listed in Table 1-1.

Although both the traditional high-harmonic gyrotrons and the gyro-multipliers adopt the harmonic operation to lower the required external magnetic field, the later describe much lower cavity heating load and starting oscillation current requirement, since only the LF oscillation condition should be fulfilled. Currently, at smaller currents the HF power from the gyro-multipliers will be lower than that from the high-harmonic gyrotrons, but it will be sufficient for a majority of applications. And the advantage of utilising low-current electron beams may often overweighs the disadvantage of low output power.

2.2 Quasi-optical Mode Converters

To reduce the wall loss and avoid breakdown, the waveguide radius of the gyrotron should be much larger than the free-space wavelength of the operation mode. Thus, the waveguide used in a traditional gyrotron is overmoded. The output wave, when being radiated from a truncated waveguide directly as shown in Figure 2-4, appears in a relatively broad circularly asymmetric hollowed cone, with rather complex distribution and polarisation. Such kind of radiated field is not suitable for the aforementioned applications, most of which will require a linearly polarised beam. Besides, these high-order modes are not suitable for driving conventional antennas because of sidelobe generation, gain reduction, and inefficient power loading on the antenna aperture [89]. Thus, the waveguide modes should be transformed into linearly polarised quasi-Gaussian

beams [90]. There are basically two structures which can be used to convert the waveguide modes into quasi-Gaussian beams: the waveguide mode converter (WMC) and the quasi-optical mode (QMC) converter consisting of a launcher and several mirrors.

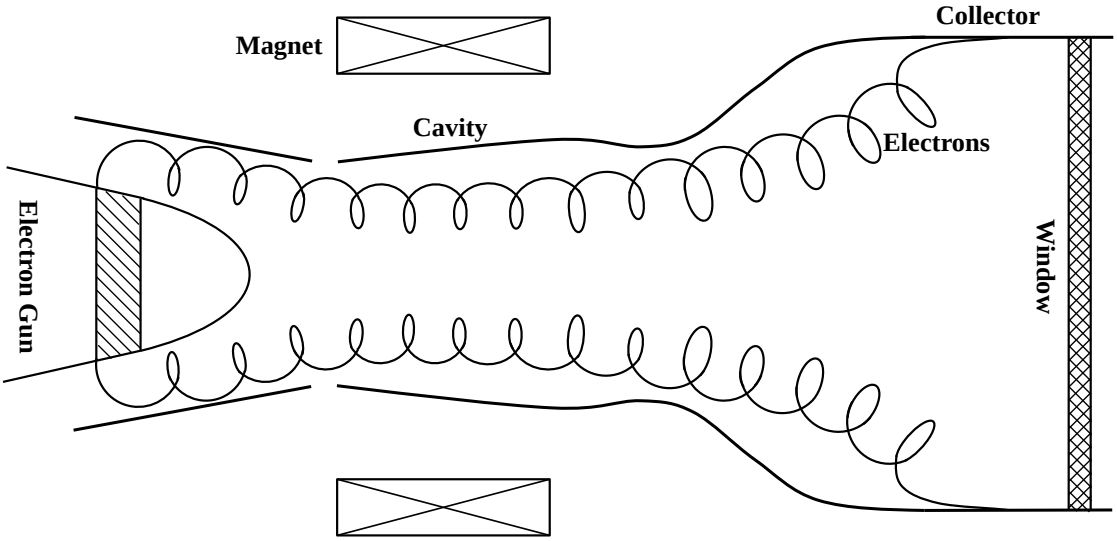

Figure 2-4: Traditional gyrotron scheme with axial wave extraction.

For relatively low-order modes, a typical approach for mode conversion is the adoption of the WMC, especially for the $TE_{0,n}$ modes [91-93]. Figure 2-5 shows a typical configuration of the WMC that is used to convert a TE_{03} mode gyrotron output to TE_{11} mode [93]. An axisymmetric waveguide section is used firstly to convert the TE_{03} mode into the TE_{01} mode. Then, a wiggle waveguide is used to transfer the TE_{01} mode into a TE_{11} mode, which is suitable for transmission or feeding to antennas.

The WMCs describe high efficiency when converting low-order $TE_{0,n}$ modes at low frequency to quasi-Gaussian beams. However, in the above gyro-multiplier design, the operation mode is high-order volume modes with high operation frequency. To convert such modes to quasi-Gaussian beams, the required inner radius of the WMCs will be extremely small and the required length will be incredibly long. This will bring difficulties to the fabrication process and assembly with the gyro-multiplier. What's more, this approach is also complicated by the large number of possible coupled modes during the process of conversion from high-order modes to low-order modes. The above

factors have made traditional WMCs complicated and inefficient for the transformation of high-order waveguide modes. Meanwhile, the QMCs have shown capabilities of transforming the high-order waveguide modes of gyrotrons into quasi-Gaussian beams with relative simplicity as well as high efficiency [90, 94].

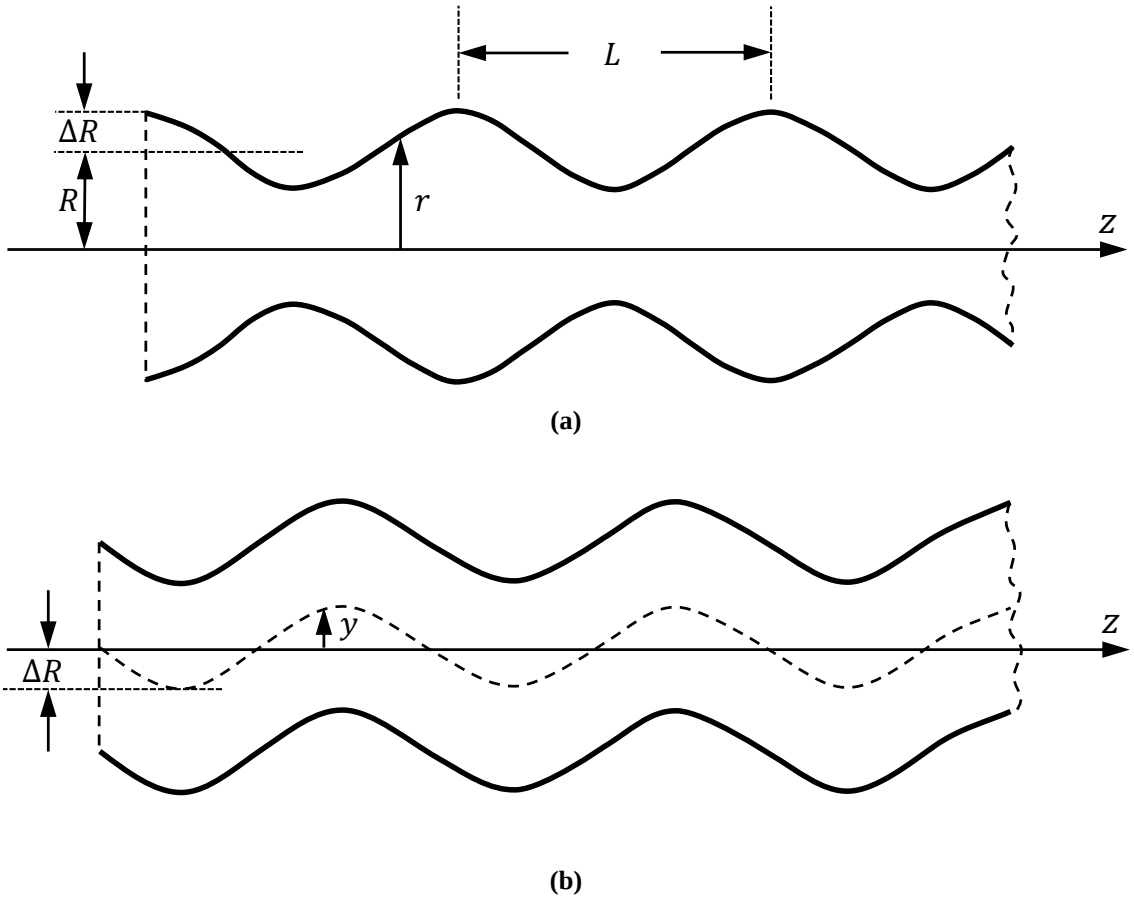

Figure 2-5: (a) An axisymmetric TE_{0n}-TE_{01}, waveguide mode converter; (b) A wiggle waveguide that convert TE_{01} mode to TE_{11} mode. *R* is the unperturbed waveguide radius. Δ*R* is the perturbation of the waveguide radius. *L* is the period of the perturbation. (Reproduced from [93])

A QMC is the combination of an open waveguide antenna (launcher) and a mirror system, as shown in Figure 2-6. The launcher is used to radiate the high-order waveguide mode with directivity. The radiated beam is then corrected in both amplitude and phase by several mirrors to form a quasi-Gaussian beam output. Such kind of converter is simple and compact, which is a favourable factor to reduce the Ohmic loss in the THz regime. The first QMC is proposed and demonstrated by Vlasov et al. in 1975 [95]. To improve the radiation characteristics of the output, several major improvements to the Vlasov launcher have been reported in the literature [91, 94, 96-98].

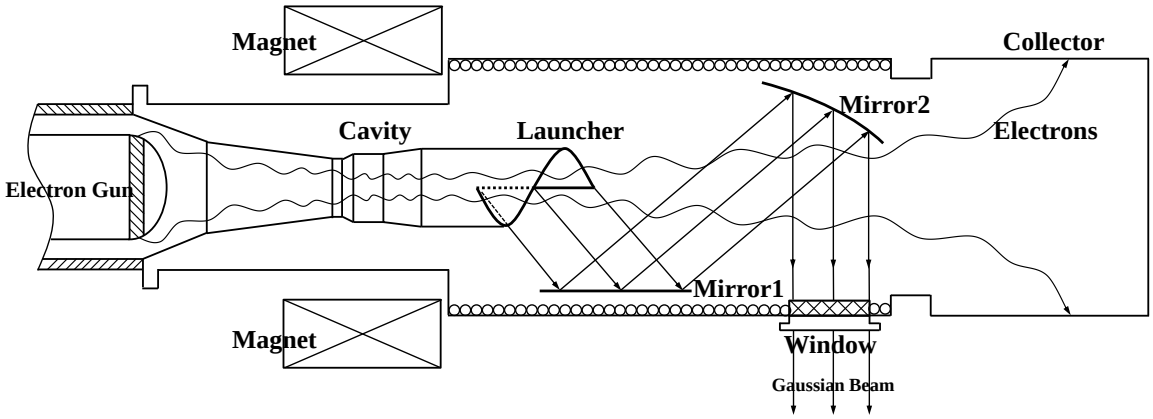

Figure 2-6: Schematic view of the QMC.

The adoption of a QMC has the following advantages. Firstly, the generated microwave can be easily separated from the spent electron beam at the end of the launcher, which allows the incorporation of space extended collectors [99, 100] or distributed collectors [101] for recovering partially the exhausted beam energy and suppression of after cavity interactions [102]. Secondly, the QMCs have more power capacity than the WMCs. Thirdly, the output mode is converted to a collimated beam with large area. In this way, the power intensity loaded on the vacuum window can be lowered.

2.2.1 Geometric Optics Analysis

In the QMC for a high-order mode gyrotron, the propagation of the wave can be described in terms of geometric optics (GO) [95, 98, 103, 104]. The output electromagnetic field from the gyrotron, before propagating to the helical cut of the Vlasov launcher, can be expressed in the cylindrical coordinates system (r, φ, z) as:

$$u(r, \varphi, z) = A_0 J_m(k_\perp r) e^{-jm\varphi} e^{-jk_\parallel z} \tag{2.16}$$

for right-handed rotating $TE_{m,n}$ modes. A_0 is the amplitude of the field.

It can be interpreted from (2.16) that the field in the radial direction is standing wave which varies with the value of the Bessel function. A standing wave can be decomposed into two components: the incident and the reflected travelling waves. The Bessel function

can be represented by the sum of the first kind of Hankel function $H_m^{(1)}(z)$ and the second kind of Hankel function $H_m^{(2)}(z)$, as

$$J_m(k_\perp r) = \frac{H_m^{(1)}(k_\perp r) + H_m^{(2)}(k_\perp r)}{2}. \tag{2.17}$$

The combination of (2.16) and (2.17) yields

$$u(r,\varphi,z) = \frac{A_0}{2}\left(H_m^{(1)}(k_\perp r) + H_m^{(2)}(k_\perp r)\right)e^{-jm\varphi}e^{-jk_\parallel z}. \tag{2.18}$$

Thus the incident and the reflected waves can be expressed by

$$u_{(r,\varphi,z)}^{in} = \frac{A_0}{2}H_m^{(1)}(k_\perp r)e^{-jm\varphi}e^{-jk_\parallel z} \tag{2.19a}$$

$$u_{(r,\varphi,z)}^{re} = \frac{A_0}{2}H_m^{(2)}(k_\perp r)e^{-jm\varphi}e^{-jk_\parallel z} \tag{2.19b}$$

in which $H_m^{(1)}(k_\perp r)$ and $H_m^{(2)}(k_\perp r)$ are conjugate complexes as

$$H_m^{(1)}(k_\perp r) = (H_m^{(2)}(k_\perp r))^*. \tag{2.20}$$

The sign of '$*$' represent the complex conjugate. The value of $k_\perp r$ varies with r as

$$\begin{aligned} &k_\perp r < m \quad for \quad 0 < r < R_c \\ &k_\perp r = m \quad for \quad r = R_c \\ &k_\perp r > m \quad for \quad R_c < r < R \end{aligned} \tag{2.21}$$

in which $R_c = R \cdot m/\mu'_{m,n}$ is the caustic radius of the $TE_{m,n}$ modes. Since the field when $r < R_c$ is evanescent, only the field when $r \geq R_c$ will be considered. Thus $k_\perp r \geq m$. Under this condition, $H_m^{(2)}(k_\perp r)$ can be approximated as

$$H_m^{(2)}(k_\perp r) \approx \sqrt{\frac{2}{\pi\sqrt{(k_\perp r)^2 - m^2}}}e^{j\left(-\sqrt{(k_\perp r)^2-m^2}+m\cdot arccos\left(\frac{m}{k_\perp r}\right)+\frac{\pi}{4}\right)}. \tag{2.22}$$

Substituting (2.22) into (2.19b) yields:

$$u_{(r,\varphi,z)}^{re} \approx \frac{A_0}{2}\sqrt{\frac{2}{\pi\sqrt{(k_\perp r)^2-m^2}}}e^{j\left(-\sqrt{(k_\perp r)^2-m^2}+m\cdot arccos\left(\frac{m}{k_\perp r}\right)+\frac{\pi}{4}-m\varphi-k_\parallel z\right)}. \quad (2.23)$$

Thus the phase of the reflected travelling wave is

$$\Upsilon\left(u_{(r,\varphi,z)}^{re}\right) \approx -\sqrt{(k_\perp r)^2-m^2}+m\cdot arccos\left(\frac{m}{k_\perp r}\right)+\frac{\pi}{4}-m\varphi-k_\parallel z. \quad (2.24)$$

In GO limit, the right-handed rotating travelling wave in the cylindrical waveguide can be decomposed into a continuous flow of rays, the direction of which are along the gradient of the wavefront and can be calculated as

$$\boldsymbol{N}(r,\varphi,z) = \boldsymbol{\nabla}\left(K-\Upsilon\left(u_{(r,\varphi,z)}^{re}\right)\right) \quad (2.25)$$

where K is a phase constant. Taking (2.24) into (2.25) gives

$$\boldsymbol{N}(r,\varphi,z) \approx k_\perp\sqrt{1-\frac{m^2}{k_\perp^2 r^2}}\,\boldsymbol{e_r}+\frac{m}{r}\boldsymbol{e_\varphi}+k_\parallel\boldsymbol{e_z} \quad (2.26)$$

where $\boldsymbol{e_r}$, $\boldsymbol{e_\varphi}$ and $\boldsymbol{e_z}$ are the unit vector in the r, φ and z directions, respectively. Correspondingly, the propagation direction of the incident travelling wave by the ray representation can be written as

$$\boldsymbol{N}(r,\varphi,z) \approx -k_\perp\sqrt{1-\frac{m^2}{k_\perp^2 r^2}}\,\boldsymbol{e_r}+\frac{m}{r}\boldsymbol{e_\varphi}+k_\parallel\boldsymbol{e_z}. \quad (2.27)$$

On the launcher wall where $r = R$, the propagation direction of the rays can be written as

$$\boldsymbol{N}(r,\varphi,z) \approx \frac{\sqrt{\mu_{m,n}'^2-m^2}}{R}\boldsymbol{e_r}+\frac{m}{R}\boldsymbol{e_\varphi}+k_\parallel\boldsymbol{e_z}. \quad (2.28)$$

It can be interpreted that the rays propagates at the Brillouin angle

$$\theta_B = arccos\left(\frac{\boldsymbol{N}(r,\varphi,z)\cdot\boldsymbol{e_z}}{|\boldsymbol{N}(r,\varphi,z)||\boldsymbol{e_z}|}\right) \tag{2.29}$$

as shown in Figure 2-7. Thus θ_B can be obtained as

$$\theta_B = arcsin\left(\frac{\mu'_{m,n}}{R\cdot k}\right) \tag{2.30}$$

where k is the wavenumber and $k = \omega/c$.

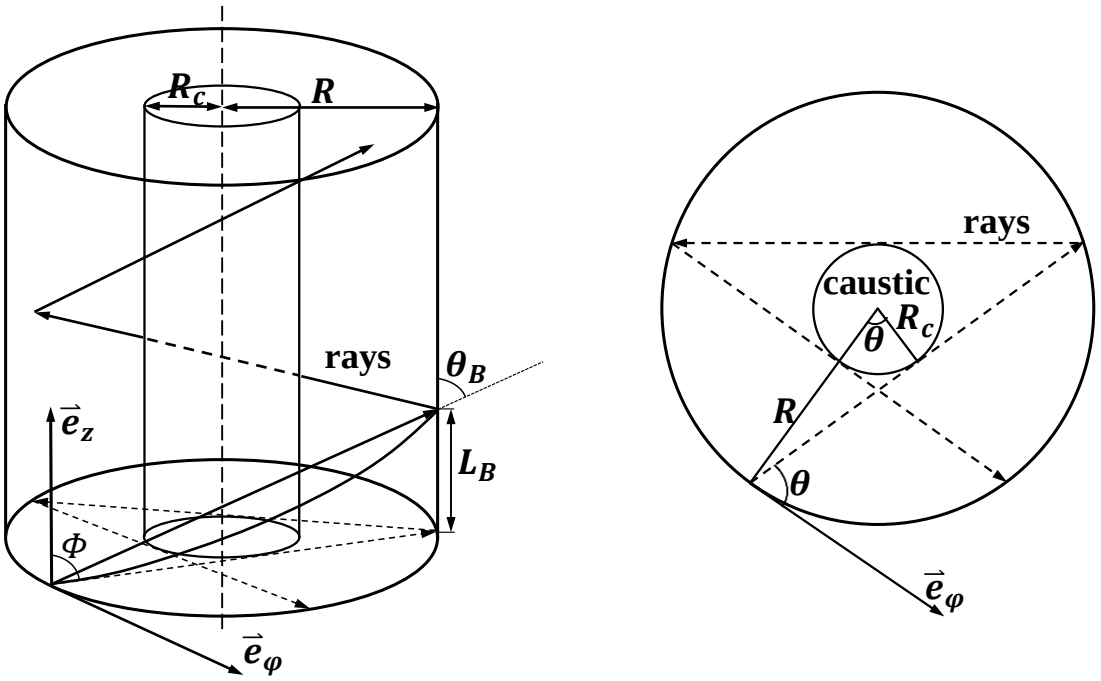

Figure 2-7: Geometric representation of the EM field propagation in a cylindrical waveguide.

The projection of the rays in the transverse plane follows the direction of $\boldsymbol{N_t}(r,\varphi)$ and

$$\boldsymbol{N_t}(r,\varphi) = \frac{\sqrt{\mu'^2_{m,n} - m^2}}{R}\boldsymbol{e_r} + \frac{m}{R}\boldsymbol{e_\varphi}. \tag{2.31}$$

Thus the projection of the rays forms an angle θ with $\boldsymbol{e_\varphi}$ and

$$\theta = arccos\left(\frac{\vec{N}_t(r,\varphi)\cdot\vec{e}_\varphi}{|\vec{N}_t(r,\varphi)||\vec{e}_\varphi|}\right) = arccos\left(\frac{m}{\mu'_{m,n}}\right). \tag{2.32}$$

The reflecting points of individual ray on the waveguide wall form a helical line, which has an inclination angle, Φ, regarding the axial direction. Φ can be calculated by the geometrics in Figure 2-7. From the GO, the axial distance between two subsequent reflection points of one of the rays, L_B, can be expressed as:

$$L_B = R \cdot 2\theta \cdot cot\Phi = 2R \cdot sin\theta \cdot cot\theta_B \tag{2.33}$$

which gives

$$\Phi = arccot\left(\frac{sin\theta \cdot cot\theta_B}{\theta}\right). \tag{2.34}$$

The distance that a ray has propagated in the axial direction, when it complete a full azimuthal turn, can be obtained as

$$L = 2\pi R \cdot cot\Phi = 2\pi R^2 \frac{k_z}{\mu'_{m,n}} \sqrt{1 - \left(\frac{m}{\mu'_{m,n}}\right)^2} \left(arccos\left(\frac{m}{\mu'_{m,n}}\right)\right)^{-1}. \tag{2.35}$$

Considering the rotational nature of the rays' propagation inside the cylindrical waveguide, there will be a series of Brillouin regions on the internal surface of the waveguide, each of which reflects all the rays exactly once. Figure 2-8 shows three representative shapes of Brillouin region on the unfolded inner surface of the cylindrical waveguide, for the case when $\pi/3 < \theta < \pi/2$. The case for other values of θ can be studied in the same manner. Region 1, 2, 3 and 4 represent four Brillouin regions that are connected in series. The rays inside the waveguide, when propagating towards the $+z$ direction, will be sequentially reflected by the four regions. The Brillouin region in Figure 2-8 (b) spans an azimuthal angle of ψ, and

$$\psi = 2\theta. \tag{2.36}$$

Thus the azimuthal length of the Brillouin region in Figure 2-8 can be expressed as

$$L_a = 2\theta R. \tag{2.37}$$

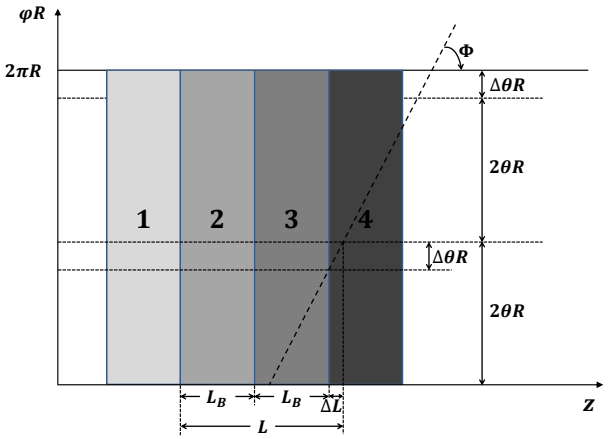

(a)

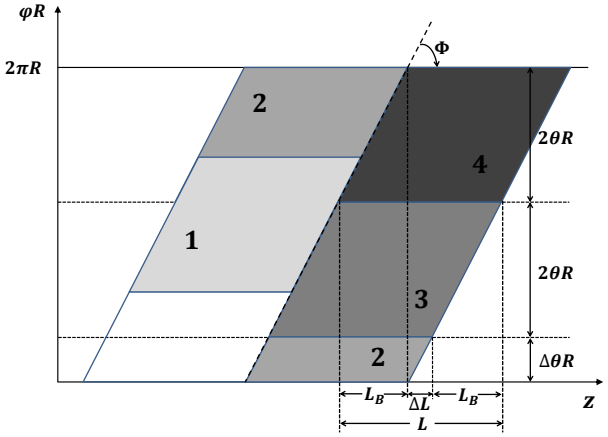

(b)

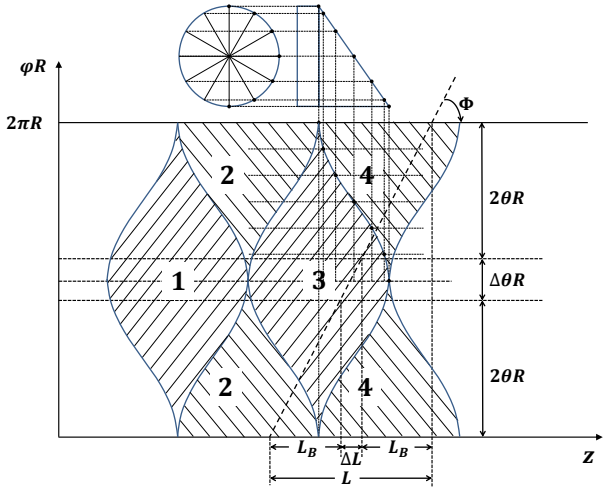

(c)

Figure 2-8: Some typical distribution examples of the Brillouin region inside a cylindrical waveguide.

Although different Brillouin regions describe distinguished shapes, the surface areas of them are identical. $\Delta\theta$ as shown in Figure 2-8 is the residue when 2π is divided by θ, meaning that

$$\Delta\theta = 2\pi \ mod \ \theta. \tag{2.38}$$

Correspondingly, ΔL can be defined as

$$\Delta L = \Delta\theta R \cdot cot\Phi. \tag{2.39}$$

Considering (2.33), (2.35) and (2.39),

$$L = 2L_B + \Delta L. \tag{2.40}$$

If one of these Brillouin regions is removed by cutting the waveguide, all the rays will be radiated into free space through the aperture formed. The theory of the Brillouin regions serves as the basis for analysing the Vlasov launchers in Chapter 5.

2.2.2 Launchers

A launcher is basically an asymmetrically cut waveguide that is capable of radiating the high-order waveguide mode with certain directivity and polarisation.

2.2.2.1 Vlasov Launcher

Traditionally, there are three types of Vlasov launcher: step-cut, bevel-cut and helical-cut. These three types of cut are all based on the analysis of different types of Brillouin region.

1. Step-cut

A typical step-cut Vlasov launcher is shown in Figure 2-9. The step-cut launcher can be derived from Figure 2-8 (a). Here each of the Brillouin regions can be divided into three sections (when $\theta = \pi/3$): Section A, B and C, as shown in Figure 2-10. Here Region 1, Region 2, Region 3 and Region 4 are four Brillouin regions that are connected in series. As the rays propagate, the ones reflected by Section A, B and C of one Brillouin region

will be radiated onto their counterparts of the next Brillouin region, respectively. To allow all the rays to be radiated into the free space, an area should be removed which contains at least a Section A, a Section B and a Section C.

Figure 2-9: The profile of a step-cut Vlasov launcher.

This implies that the cutting edge can be located as being shown by the bold dotted line. The distribution of the radiated field is also shown on the right hand side. As originally proposed by Vlasov, the step-cut Vlasov launcher has sharp edges and hence may suffer from the electric breakdown problem when radiating high-power microwaves [89].

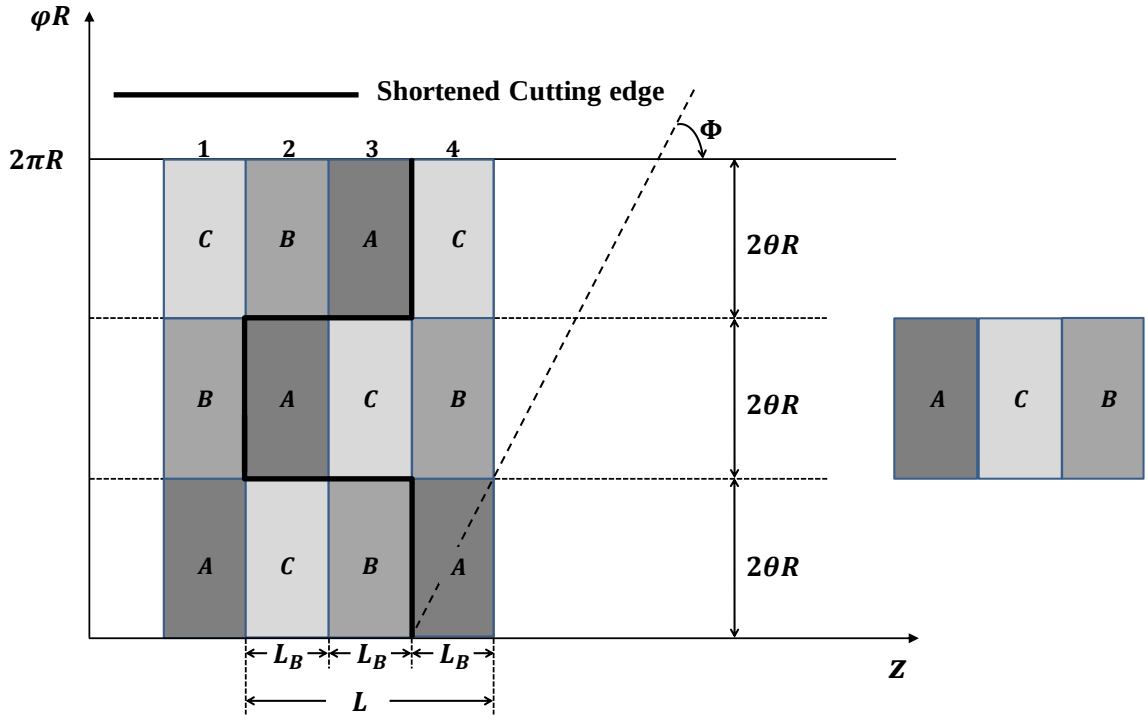

Figure 2-10: The cutting edge for the step-cut Vlasov launcher. The shape of the radiated field is shown in the right-hand side.

2. Bevel-cut

A typical bevel-cut Vlasov launcher is shown in Figure 2-11. The bevel-cut launcher can be derived from Brillouin region analysis shown in Figure 2-8 (c). Through removing the Region 4 by the cut shown in bold solid line in Figure 2-12, all the rays can be radiated into free space. The radiated field distribution is also shown.

Figure 2-11: The profile of a bevel-cut Vlasov launcher.

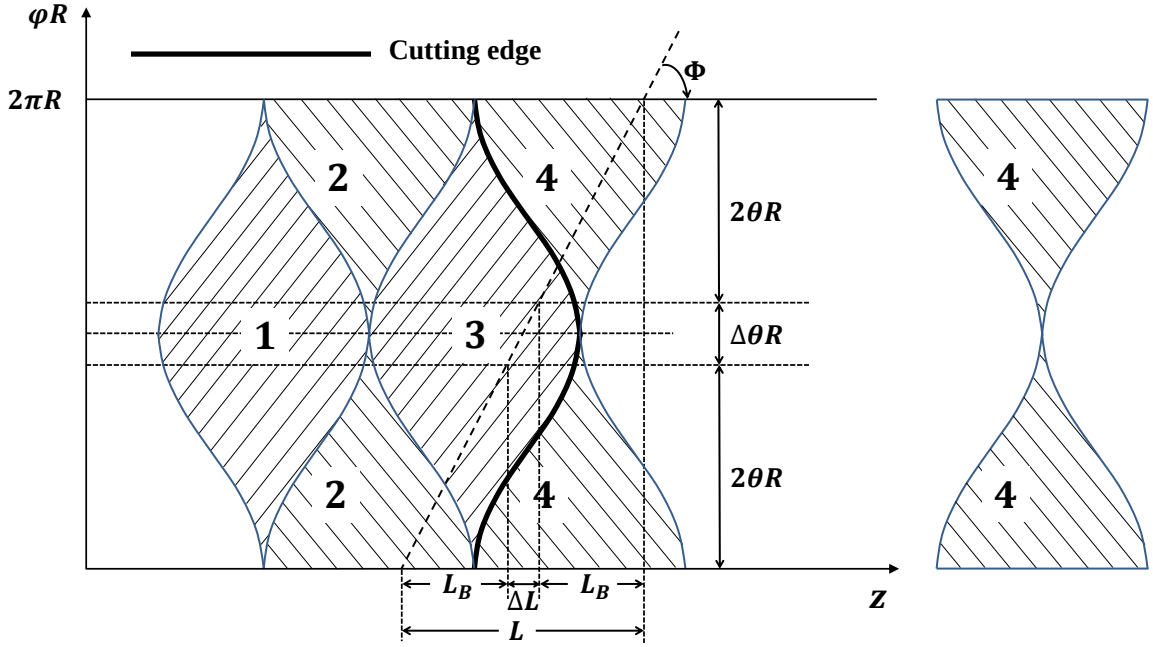

Figure 2-12: The shape of the Bevel-cut in an unfolded waveguide view.

Suppose the angle between the surface of the cut and the z axis is τ, then it can be seen from Figure 2-8 (c) that

$$tan\tau = \frac{2R}{L_B} = \frac{1}{sin\theta} tan\theta_B. \tag{2.41}$$

For $TE_{0,n}$ modes, $\theta = \pi/2$ and

$$tan\tau = tan\theta_B. \tag{2.42}$$

It can be interpreted from Figure 2-12 that, although the bevel-cut eliminates the sharp edges as in the step-cut and reduce the risk of electric breakdown at high power, the directivity of the radiated field is degraded. The radiated field actually spread an angle of 2π in the azimuthal direction, which is not effectively focused.

3. Helical-cut

A typical helical-cut Vlasov launcher is shown in Figure 2-13. The helical-cut Vlasov launcher can be derived from Figure 2-8 (b). By removing the Region 4 by the cut shown in bold solid line in Figure 2-14, all the rays can be radiated to free space. The radiated field distribution is also shown on the right hand side.

Figure 2-13: The profile of a helical-cut Vlasov launcher.

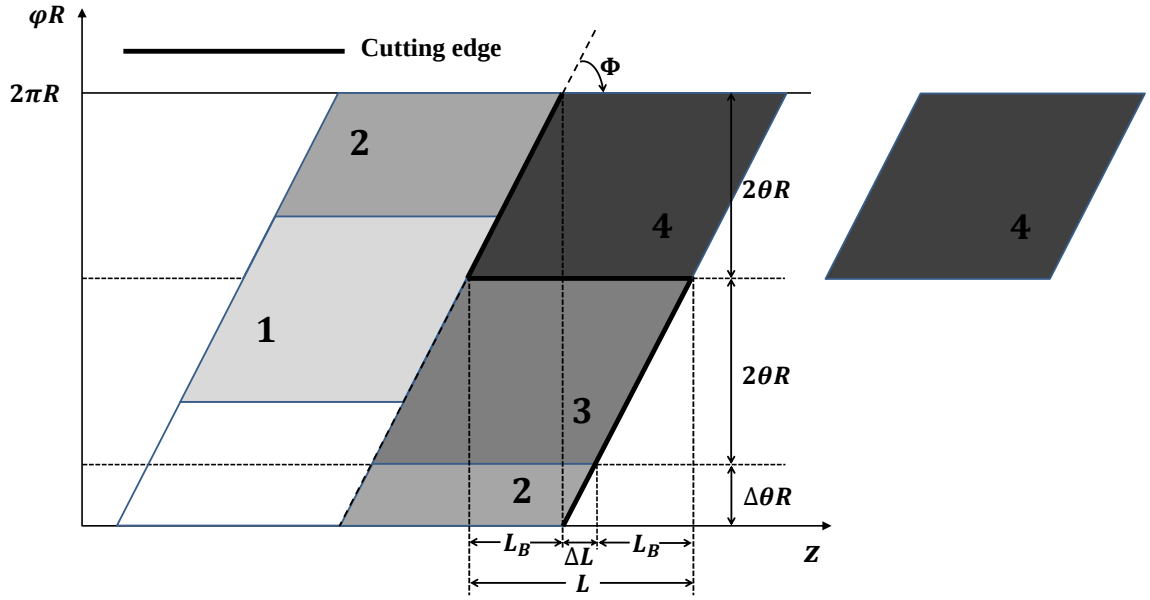

Figure 2-14: An unfolded waveguide wall with the reflection points of the rays and the Brillouin region. The radiation field distribution is also shown as the block on the right-hand side.

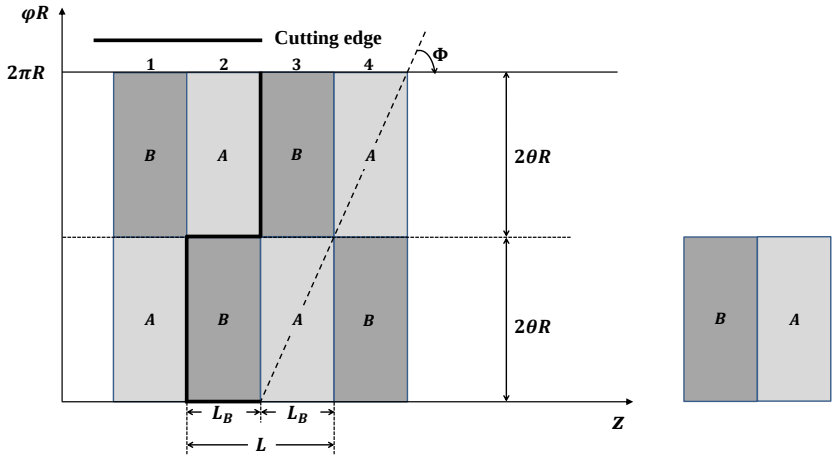

(a)

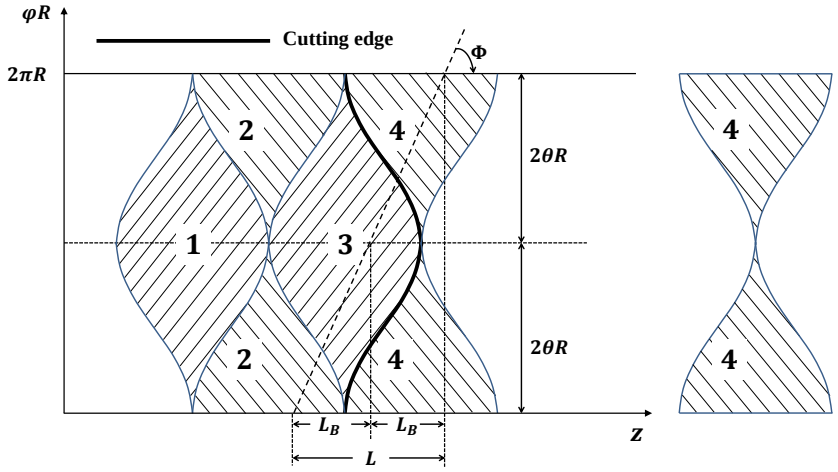

(b)

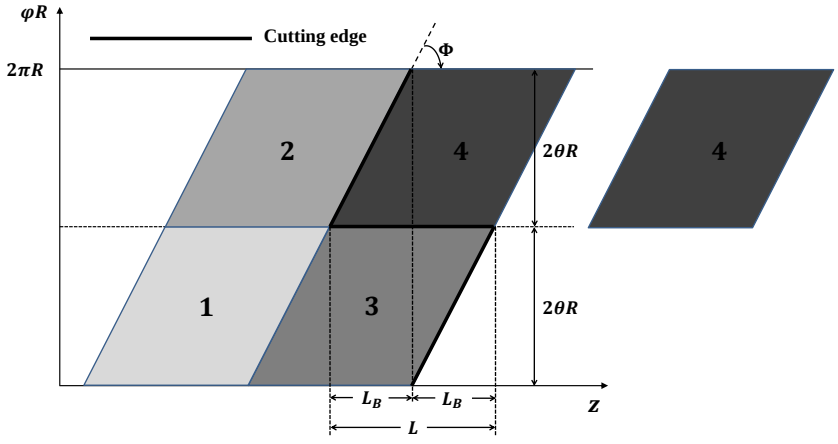

(c)

Figure 2-15: The Brillouin region distribution and cutting edges of the three types of launchers for the $TE_{0,n}$ modes. The radiation field for each type of launcher is shown on the right, respectively. (a) The step-cut launcher; (b) The bevel-cut launcher; (c) The helical-cut launcher. The radiation field distributions are also shown as the blocks on the right-hand side of each figure.

The traditional gyrotrons are operated with $TE_{m,n}$ modes. For $m = 0$ modes, it can be derived from (2.32) and (2.38) that $\theta = \pi/2$ and $\Delta\theta = 0$, respectively. It can also be shown from (2.39) and (2.40) that $\Delta L = 0$ and $L = 2L_B$. Thus the Brillouin region distribution can be simplified as shown in Figure 2-15 for the three types of launchers. It can be seen that for the $TE_{0,n}$ modes, all the three types of launcher can be applied. For the simplicity and to facilitate the design of the subsequent mirrors, the step-cut and bevel-cut are usually used for the modes with $m = 0$ [104].

For the $TE_{m,n}$ $(m \neq 0)$ modes, the radiated fields when using the step-cut or bevel-cut are irregularly distributed, which will introduce additional difficulties to the design of the subsequent mirrors. However, the radiated field of the $TE_{m,n}$ $(m \neq 0)$ modes from a helical-cut launcher is evenly distributed in a rhombic-shaped area as shown in Figure 2-14. Thus the helical-cut can be used for asymmetrical waveguide $TE_{m,n}$ $(m \neq 0)$ modes.

2.2.2.2 Denisov Launcher

From the above geometrical analysis, the EM field strength at the cutting edge of a Vlasov launcher is quite high, which causes diffraction and sidelobes of the radiation. To minimise the fields at the cutting edge, the output waveguide mode, before being emitted from the launcher, can be pre-bunched to form a focused field distribution. The Denisov launcher is an improved version of the Vlasov launcher which, by introducing a pre-defined distortion to the smooth waveguide wall as shown in Figure 2-16, can transform the high-order mode of a gyrotron output to have a Gaussian profile before launching. The distortion of the wall can help to couple the single mode of a gyrotron output into a number of neighbouring modes with matched amplitudes and relative phases. The superposition of these modes at the output aperture of the launcher will form a quasi-Gaussian field distribution [103].

Figure 2-16: The profile of a Denisov launcher [103].

2.2.3 Mirrors

The launcher converts the gyrotron output into a linearly-polarised beam with sidelobes [105]. To improve the beam quality and obtain a quasi-Gaussian field distribution, subsequent mirrors should be used to adjust the amplitude and phase of the beam. The shape of the mirrors depends on the radiated waveform by the launcher.

2.2.3.1 Standard Mirrors

There are a number of standard mirrors that can be used in the QMC, of which the elliptical cylinder mirror, parabolic cylinder mirror and elliptic paraboloid mirror are the most commonly used ones. The choice of these types of mirrors is dependent on the launcher configurations, the operation modes and the focusing requirements.

1. Elliptical Cylinder Mirror

An elliptical cylinder mirror is a kind of bifocal mirror which has two focal lines. The longitudinal and transverse view of an elliptical cylinder mirror is shown in Figure 2-17. It can be viewed as a cylinder in the longitudinal direction, while in the transverse direction, it is a part of an ellipse. The rays radiated from one of the focal line will be focused by the mirror to the other focal line. For a step-cut or bevel-cut Vlasov launcher which operates with TE_{0n} modes, the radiated field can be viewed as rays that come out of the launcher from the axis of the waveguide. If an elliptical mirror is applied with its focal line placed exactly on the axis of the launcher waveguide, all the rays will be focused to another focal line, as shown in Figure 2-17.

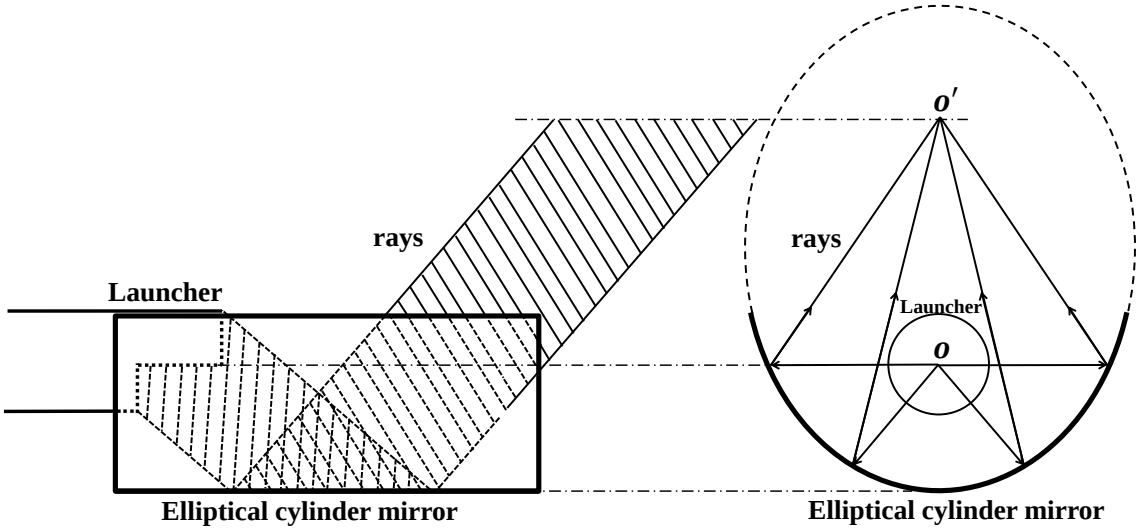

Figure 2-17: The longitudinal and transverse view of an elliptical cylinder mirror.

2. Parabolic Cylinder Mirror

When one of the focal line of the elliptical cylinder mirror is placed infinitely far away, all the rays radiated from the focal line will be reflected by the mirror surface to produce a beam of parallel rays. And the mirror will become a parabolic cylinder mirror, as shown in Figure 2-18. It can be viewed as a cylinder in the longitudinal direction, while in the transverse direction, it is a part of a parabola.

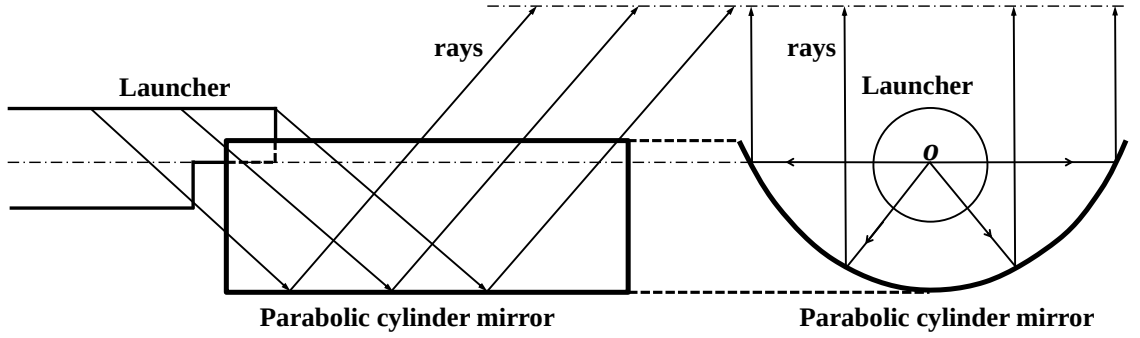

Figure 2-18: The longitudinal and transverse view of a parabolic cylindrical mirror.

For a step-cut or bevel-cut Vlasov launcher which operates with TE_{0n} modes, the radiated field can be viewed as rays that come out of the launcher from the axis of the waveguide. If a parabolic mirror is applied with its focal line placed exactly on the axis of the waveguide, the radiation from the launcher will be reflected to form a beam of parallel rays, as shown in Figure 2-18.

3. Quasi-elliptical Cylinder Mirror

For TE_{mn} ($m \neq 0$) modes, the radiated rays originate from the surface of the caustic area, as shown in the geometrical optics, Figure 2-19. In this case, the transverse shape of the elliptical cylinder mirror should be modified by the geometrical optics in order to focus the rays to a given focal line. The modified elliptical cylinder mirror is called quasi-elliptical cylinder mirror.

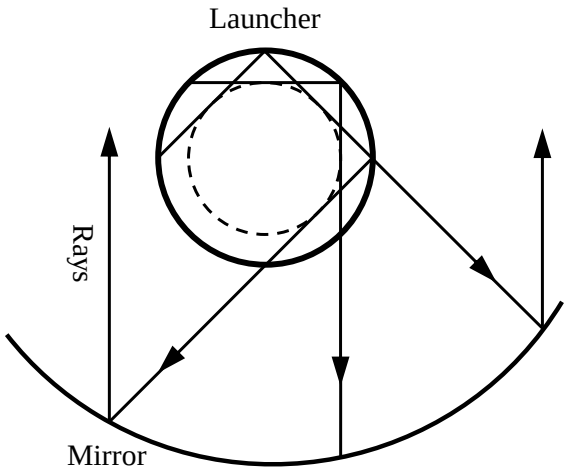

Figure 2-19: Ray representation of the radiation being reflected by a quasi-elliptical cylinder mirror.

The geometric structure of the cross section of the helical-cut launcher and the quasi-elliptical mirror is shown in Figure 2-20. The global coordinate is indicated where the centre of the launcher aperture is set on the x-axis and the launcher axis is arranged along the z-axis. l_1 and $l_1 + l_2$ denote the two focal lengths of the quasi-elliptical mirror. The launcher axis is usually set at one of the focal lines, and then the wave beam radiated from the launcher will be focused by the quasi-elliptical cylinder mirror to the other focal line.

The shape of the mirror is governed by [103]

$$x(\phi) = -(R_c cos\phi + \ l(\phi) sin\phi) \tag{2.43a}$$

$$y(\phi) = R_c sin\phi - \ l(\phi) cos\phi \tag{2.43b}$$

and

$$l(\phi) = \frac{{R_c}^2(1-\pi^2+2\pi\phi-\phi^2)+2R_c\left(l_2 sin\phi+\pi L(\pi)-\phi L(\pi)\right)+{l_2}^2-L(\pi)^2}{2\pi R_c-2R_c\phi-2L(\pi)+2l_2 cos\phi} \tag{2.44}$$

in which

$$L(\pi) = l_1 + \sqrt{(l_1+l_2)^2+{R_c}^2}. \tag{2.45}$$

From (2.43)-(2.45), the coordinates of the points on the quasi-elliptical cylinder mirror surface can be obtained as $(x(\phi), y(\phi), z)$.

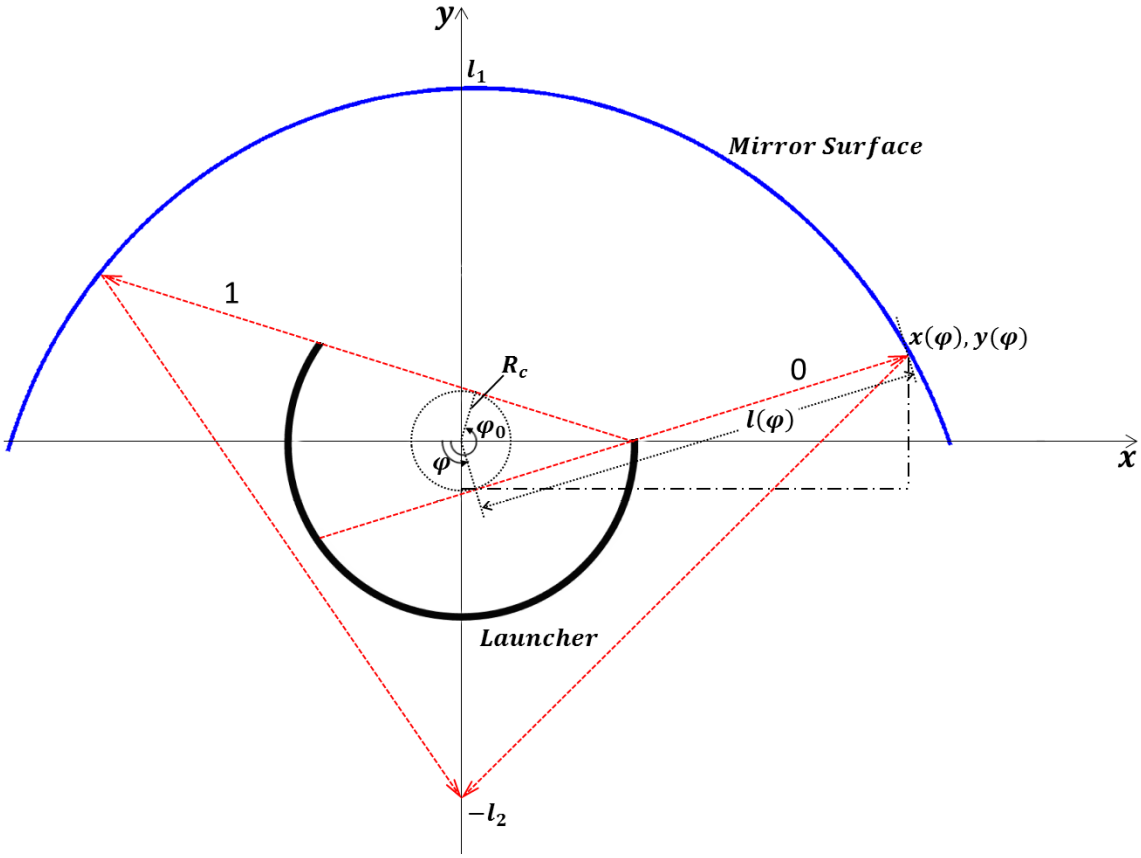

Figure 2-20: The cross-section view of the launcher the quasi-elliptical cylinder mirror.

4. Quasi-parabolic Cylinder Mirror

In case of $l_2 \to \infty$, the quasi-elliptical cylinder mirror becomes a quasi-parabolic cylinder mirror. In this case,

$$l(\phi) = \frac{R_c sin\phi + \pi R_c - R_c\phi - 2l_1}{cos\phi - 1}. \tag{2.46}$$

Then from (2.43)

$$x(\phi) = R_c + \pi R_c cot(\phi/2) - R_c \phi cot(\phi/2) - 2l_1 cot(\phi/2) \quad (2.47a)$$

$$y(\phi) = R_c cot(\phi/2) + (\pi R_c/2 - R_c\phi/2 - l_1)(cot^2(\phi/2) - 1). \quad (2.47b)$$

5. Elliptic Paraboloid Mirror

An elliptic paraboloid mirror is a quadric surface shaped like an oval cup, as shown in Figure 2-21. In the Cartesian coordinate system (x, y, z), an elliptic paraboloid surface with its opening towards the $+z$ direction, can be expressed by the following equation:

$$z = \frac{x^2}{a^2} + \frac{y^2}{b^2} \quad (2.48)$$

where a and b are constants which determine the level of curvatures in the $x - z$ and $y - z$ planes, respectively.

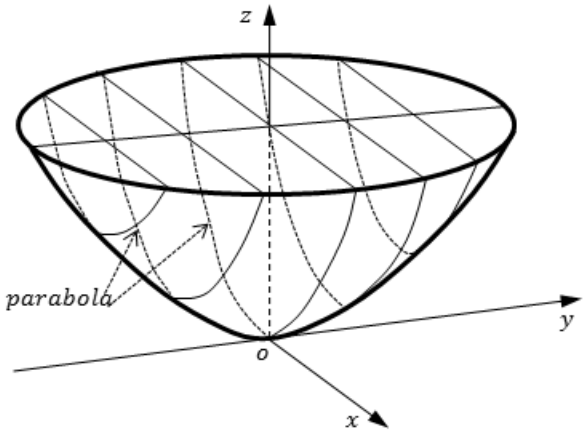

Figure 2-21: The forming of an elliptic paraboloid mirror.

2.2.3.2 Phase Correcting Mirrors

It is noteworthy that the above mirrors are described and analysed mainly in the frame of GO, which usually neglects the effect of diffraction and existence of high-order Gaussian modes. Besides, the wave front of the reflected beam is broadly distributed and the propagation directions at some points form large angles with the transmission line. Thus the surface shape of the standard mirrors should be modified to optimise the phase distribution of the reflected wave on the window area. Figure 2-22 shows an example of

the phase correcting mirror which is modified from the standard parabolic cylinder mirror [90].

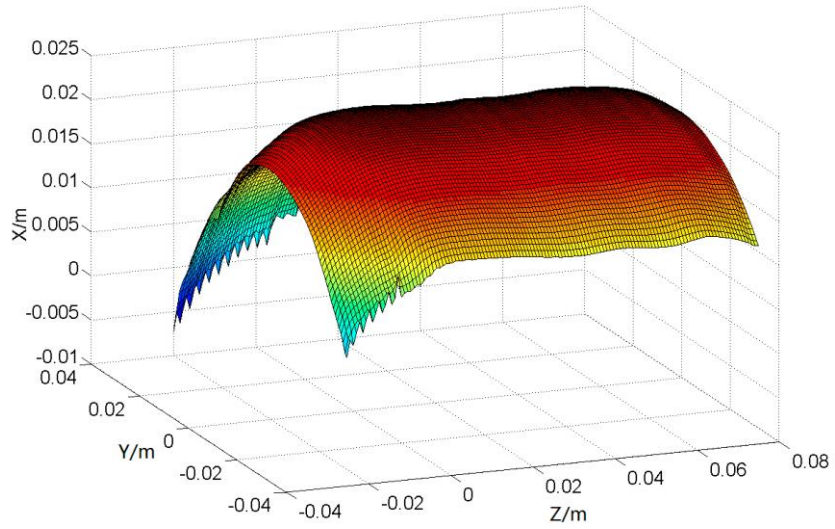

Figure 2-22: The phase correcting mirror based on the shape of a parabolic mirror [90].

2.3 Possible Application of the Frequency Selective Surface

A frequency selective surface (FSS) consists of periodic arrays of usually metallic unit cells on a dielectric substrate. It can also be called a spatial filter for the electromagnetic waves, as a counterpart for the traditional filter used in the RF circuits. Once exposed to the incident electromagnetic waves, a FSS generates a scattered wave. The total field, formed by the superposition of the incident and scattered waves, will have a prescribed frequency response. The overall effect will be the total transmission of some frequency bands and the total reflection in some other frequency bands. The FSSs are typically used as radome to reduce the radar cross section (RCS) [106], the angular filter [107], the diplex splitter [108], metamaterials [109-111], the reflect-array antennas [112], the planar lenses [113, 114], and the dichroic sub-reflector [115].

2.3.1 Overview of the Frequency Selective Surface

FSSs are usually two-dimensional periodic structures, the shape of which does not vary along the third dimension. In recent years, new concept of three-dimensional frequency

selective surface, which usually consists of a two-dimensional periodic array of three-dimensional unit cells, are proposed to improve the performance of such device [116].

Although in different configurations, the conventional FSSs follow the same operation mechanisms that are governed by the phenomenon of resonance. Being exposed to the incident plane wave, the unit cells of a FSS will resonant at frequencies where the effective length of the unit cells is a multiple of the half wavelength, $\lambda/2$.

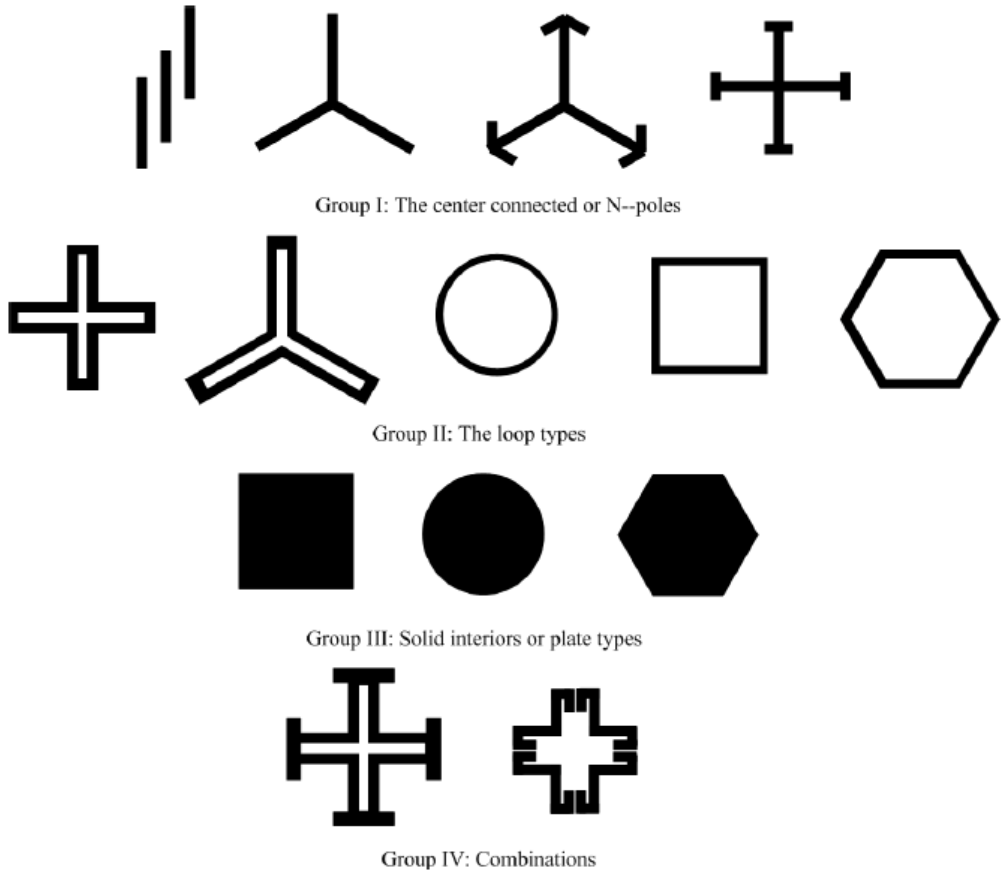

Figure 2-23: The four categories of FSS elements [117].

Since the FSSs have periodic structures, such arrays are usually assumed to be two-dimensionally infinite in the numerical analysis. By assuming the array to be infinite, the whole problem of characterisation can be effectively reduced to calculating the frequency response of a unit cell in the array. Thus the FSS can be classified, summarised and analysed by the styles of the unit cells. Over the years, a number of FSS unit cells have been introduced to the arrays to enable different band-pass and band-stop applications. A complete summary of the unit cells used in FSSs can be found in References [117-119].

Based on the type of the unit cells and the way they are assembled in the periodic arrays, the FSSs are divided into four categories by Munk in his book [117]: the centre connected types, the loop types, the solid-interior types and the hybrid types, as shown in Figure 2-23. In his categorisation, both the FSSs composed of solid plates and slots are included in the 'solid interiors or plate types' category because of their complementarity in shapes. The centre connected and the loop types usually exhibit band-stop performance. The FSSs composed of solid plates generally have band-stop behaviour, while the slot-array FSSs behave like band-pass filters. The hybrid types can be modified with different configurations to have desired characteristics.

The typical behaviour of the above FSS unit cells have been studied extensively and comprehensively by Munk in his book [117]. It is then convenient to pick up one of the configurations from the summary and scale the size of the unit cell to obtain the required frequency response.

2.3.2 Frequency Selective Surfaces for High-power Application

Although the FSS has been invented for nearly a century, its application with high-power microwaves has been rarely reported until recently [79, 120-126]. When operating at the vicinity of high-power microwaves, the power handling capability, heat dissipation ability and the electric breakdown limitations of the FSS become essential factors in determining its usability.

Munk has discussed two types of breakdown in his book [117]: the one caused by heat accumulation due to high average power incident and the one induced by high peak power. The FSSs with wire elements and the ones with slot elements are investigated to check their resistance of high-power breakdown.

In 2011, researchers in University of Wisconsin began to investigate the FSSs for pulsed high-power microwave applications through two approaches [79, 120-125]. On the one hand, a class of miniaturised FSSs composed entirely of non-resonant elements is adopted. The non-resonant elements can reduce the localised electric field intensity of the unit cell, thereby enhance the power handling capability of the FSS. In their experiments,

the FSS unit cell is capable of handling a peak power of 25 kW with a pulse length of 1 μs at 9.832 GHz. And it is predicted in theory that the power handling capability of the designed FSS can surpass 1.0 MW/cm^2. On the other hand, the ε-negative layers sandwiched by double-positive layers are used, which can handle a peak power of 4.2 kW at 9.832 GHz. By increasing the vertical dimension of the slot on the middle layer or by substituting the slot with a number of sub-wavelength perforated holes, the peak power handling capability of the FSS can be increased to over 25 kW.

In 2014, an all-dielectric FSS was also proposed [127]. The design of the FSS is based on guided-mode resonance (GMR). A monolithic construction was adopted to make the FSS more robust to vibration, internal stresses and many other problems that arise from the composite materials. In their experiments, the designed FSS was used mainly as a reflector that reflects an input power of 1.7 GW/m^2 with 3.1 ns pulse length at 10.5 GHz.

Since the dielectrics usually exhibits much weaker interaction with the incident field, an all-dielectric FSS is unsuitable for manipulation of the converted quasi-Gaussian beam from the QMC of a gyro-multiplier, where distinguished reflectivity and transmission properties are required.

Chapter Summary

In this chapter, the theory of the electron cyclotron maser (ECM), the geometric optics for the quasi-optical mode converter (QMC) and the operation of the frequency selective surface (FSS) have been reviewed. The operation principle of the gyro-multiplier, the radiation characteristics of the launchers, the governing equations of different mirrors and the latest development of the high-power frequency selective surface (FSS) have also been summarised. The theory in this chapter serves as the basis for the work in this thesis.

Chapter 3 Complex-cavity Gyrotron

Unlike the traditional gyrotrons where a single mode operation is adopted, the complex-cavity gyrotron incorporates a pair of modes with identical azimuthal index, that is, $TE_{m,n}$ mode and $TE_{m,n+1}$ mode. Correspondingly, the beam-wave interaction cavity is divided into two sections. Within the first section, the $TE_{m,n}$ mode will be excited but the energy exchange between this mode and the electron beam will be weak. The beam-wave interaction in the first section provides an initial azimuthal modulation of the electron beam. Then, in the second section of the cavity, the azimuthally modulated electron beam will favourably excite the $TE_{m,n+1}$ mode. Such mechanism is usually used to alleviate the mode competition problem in traditional gyrotrons.

The study of the complex-cavity gyrotron scheme has additional merits. It has been shown in Chapter 2 that the sectioned-cavity gyro-multiplier is actually based on a complex-cavity gyrotron, while an additional middle cavity is inserted between the original cavities. Thus the study of the complex-cavity scheme will provide a fundamental insight into the mechanism of the gyro-multiplier operation, as well as form a preliminary design tool for the beam-wave interaction cavity of the gyro-multiplier. In addition, the cold cavity theory developed in the process can also be adopted in the calculation of cavity quality factor and resonance frequency for the operation modes in the LOGs.

3.1 Theoretical Analysis

In the development of gyro-devices, the numerical simulation tool plays an important role as it can predict the nonlinear effects of beam-wave interaction which dominates the behaviour of the devices. The numerical simulation tool can be divided into two categories: The general-purpose 3D PIC codes [128-130] and the device-specified codes (see e.g. [131]). With the development of the computer science, a number of PIC codes are widely used to study the nonlinear beam-wave interaction process in the design of gyro-devices. However, the PIC code requires an extensive computation resource and

long simulation time, which is not efficient in the design and optimisation phase of the gyro-devices.

To improve the computation efficiency, a device-specified code for gyrotrons is developed by utilising the steady-state self-consistent nonlinear algorithm [50, 132, 133]. By assuming that the gyrotron being in the steady oscillation state, the beam-wave interaction in the gyrotron cavity can be approximated by the telegraphist's equations together with the Lorentz force equations which characterise the motion of electrons. Then, by incorporating cut-off and open boundary conditions at the input and output ends of the cavity separately, the above differential equations can be solved self-consistently. This algorithm is more computational efficient than the PIC approach as it focuses on the steady state of the gyrotron operation.

The second order telegraphist's equations can be derived from the Maxwell's equation:

$$\nabla \times \boldsymbol{E} = -j\omega\sigma\boldsymbol{H} \tag{3.1a}$$

$$\nabla \times \boldsymbol{H} = \boldsymbol{J} - j\omega\varepsilon\boldsymbol{E} \tag{3.1b}$$

in which $\boldsymbol{E}$ and $\boldsymbol{H}$ are the electric and magnetic field vectors, respectively. $\boldsymbol{J}$ denotes the current density of the electron beam source. σ and ε are the permeability and conductivity of the medium. $\boldsymbol{E}$ and $\boldsymbol{H}$ can be decomposed as

$$\boldsymbol{E} = \boldsymbol{E_t} + E_z\boldsymbol{e_z} \tag{3.2a}$$

$$\boldsymbol{H} = \boldsymbol{H_t} + H_z\boldsymbol{e_z} \tag{3.2b}$$

where $\boldsymbol{E_t}$ and $\boldsymbol{H_t}$ are the transverse electric and magnetic field vectors, respectively. E_z and H_z are the axial electric and magnetic field strength, respectively. $\boldsymbol{e_z}$ is the axial unit vector in the cylindrical coordinate system (r, φ, z). E_z and H_z in a cylindrical waveguide can be expressed as the superposition of a series of $TE_{mn}$and TM_{mn} modes:

$$\boldsymbol{E_t}(r, \varphi, z) = \sum_{i=1}^{2}\sum_{mn} V_{mn}^{(i)}(z)\boldsymbol{e_{mn}^{(i)}}(r, \varphi) \tag{3.3a}$$

$$\boldsymbol{H_t}(r,\varphi,z)=\sum_{i=1}^{2}\sum_{mn} I_{mn}^{(i)}(z)\boldsymbol{h_{mn}^{(i)}}(r,\varphi) \tag{3.3b}$$

in which $i=1$ and $i=2$ denotes the TM and TE modes, respectively. $V_{mn}^{(i)}(z)$ and $I_{mn}^{(i)}(z)$ are the profile functions of the $TE_{mn}$and TM_{mn} modes which vary with z. $\boldsymbol{e_{mn}^{(i)}}$ and $\boldsymbol{h_{mn}^{(i)}}$ are the orthonormal basis function, which are defined as

$$\boldsymbol{e_{mn}^{(1)}}(r,\varphi)=A_{mn}^{(1)}\left[-\boldsymbol{e_r}J_m'\left(k_{\perp mn}^{(1)}r\right)k_{\perp mn}^{(1)}+\boldsymbol{e_\varphi}J_m(k_{\perp mn}^{(1)}r)\frac{jm}{r}\right]e^{-jm\varphi} \tag{3.4a}$$

$$\boldsymbol{e_{mn}^{(2)}}(r,\varphi)=A_{mn}^{(2)}\left[\boldsymbol{e_r}J_m(k_{\perp mn}^{(2)}r)\frac{jm}{r}+\boldsymbol{e_\varphi}J_m'\left(k_{\perp mn}^{(2)}r\right)k_{\perp mn}^{(2)}\right]e^{-jm\varphi} \tag{3.4b}$$

$$\boldsymbol{h_{mn}^{(i)}}(r,\varphi)=\boldsymbol{e_z}\times\boldsymbol{e_{mn}^{(i)}}(r,\varphi) \tag{3.4c}$$

where $\boldsymbol{e_r}$ and $\boldsymbol{e_\varphi}$ are the radial and azimuthal unit vectors, respectively. $k_{\perp mn}^{(i)}$ is the transverse wave number and

$$k_{\perp mn}^{(1)}=\frac{\mu_{mn}}{R} \tag{3.5a}$$

$$k_{\perp mn}^{(2)}=\frac{\mu'_{mn}}{R} \tag{3.5b}$$

where μ_{mn} and μ'_{mn} are the nth roots of the mth order Bessel function and its derivative, respectively. R is the waveguide radius which varies with z for a resonant cavity of gyrotrons. $A_{mn}^{(i)}$ is determined by the following normalisation condition:

$$\iint_S \boldsymbol{e_{mn}^{(1)}}\cdot\boldsymbol{e_{mn'}^{(1)*}}dS=\iint_S \boldsymbol{h_{mn}^{(1)}}\cdot\boldsymbol{h_{mn'}^{(1)*}}dS=\delta_{nn'} \tag{3.6a}$$

$$\iint_S \boldsymbol{e_{mn}^{(2)}}\cdot\boldsymbol{e_{mn'}^{(2)*}}dS=\iint_S \boldsymbol{h_{mn}^{(2)}}\cdot\boldsymbol{h_{mn'}^{(2)*}}dS=\delta_{nn'} \tag{3.6b}$$

$$\iint_S \boldsymbol{e}_{\boldsymbol{mn}}^{(\mathbf{1})} \cdot \boldsymbol{e}_{\boldsymbol{mn'}}^{(\mathbf{2})*} dS = \iint_S \boldsymbol{h}_{\boldsymbol{mn}}^{(\mathbf{1})} \cdot \boldsymbol{h}_{\boldsymbol{mn'}}^{(\mathbf{2})*} dS = 0 \tag{3.6c}$$

in which $*$ denotes the conjugate. S is the transverse area of the waveguide over which the integration is undertaken. $\delta_{nn'} = 0$ if $n \neq n'$ and $\delta_{nn'} = 1$ if $n = n'$. By taking (3.2) and (3.3) into (3.1), the second order telegraphist's equations for the TM_{mn} modes ($i = 1$) and TE_{mn} modes ($i = 2$) can be derived as [50, 132, 133]

$$\frac{d^2 V_{mn}^{(i)}}{dz^2} = \left(\beta_{\|mn}^{(i)}\right)^2 V_{mn}^{(i)} + Z_{mn}^{(i)} \beta_{\|mn}^{(i)} \iint_S \boldsymbol{J_t}(r,\varphi,z) \cdot \boldsymbol{e}_{\boldsymbol{mn}}^{(\boldsymbol{i})*} \, ds$$

$$+ \frac{d\left(lnZ_{mn}^{(i)} \beta_{\|mn}^{(i)}\right)}{dz} \left\{ \frac{dV_{mn}^{(i)}}{dz} - \frac{1}{R}\frac{dR}{dz} \sum_{i'} \sum_{mn'} V_{mn}^{(i')} C_{(mn)(mn')}^{(i)(i')} \right\}$$

$$+ Z_{mn}^{(i)} \beta_{\|mn}^{(i)} \frac{1}{R}\frac{dR}{dz} \sum_{i'} \sum_{mn'} \frac{C_{(mn')(mn)}^{(i')(i)}}{Z_{mn'}^{(i')} \beta_{\|mn'}^{(i')}} \left\{ -\frac{dV_{mn'}^{(i')}}{dz} + \frac{1}{R}\frac{dR}{dz} \sum_{i''} \sum_{mn''} V_{mn''}^{(i'')} C_{(mn')(mn'')}^{(i')(i'')} \right\}$$

$$+ \frac{1}{R}\frac{dR}{dz} \sum_{i'} \sum_{mn'} \frac{dV_{mn'}^{(i')}}{dz} C_{(mn)(mn')}^{(i)(i')} + \left[\frac{1}{R}\frac{d^2R}{dz^2} - \left(\frac{1}{R}\frac{dR}{dz}\right)^2 \right] \sum_{i'} \sum_{mn'} V_{mn'}^{(i')} C_{(mn)(mn')}^{(i)(i')}. \tag{3.7}$$

$\beta_{\|mn}^{(i)}$ is the propagation constant and

$$\beta_{\|mn}^{(i)} = j k_{\|mn}^{(i)} \tag{3.8}$$

in which $k_{\|mn}^{(i)}$ is the axial wavenumber for the TM_{mn} mode (i=1) or the TE_{mn} mode (i=2). $Z_{mn}^{(i)}$ is the wave impedance and

$$Z_{mn}^{(1)} = \frac{\beta_{\|mn}^{(1)}}{j\omega\varepsilon} \tag{3.9a}$$

$$Z_{mn}^{(2)} = \frac{j\omega\sigma}{\beta_{\|mn}^{(2)}}. \tag{3.9b}$$

$\boldsymbol{J_t}(r,\varphi,z)$ is the transverse current density and

$$\boldsymbol{J_t}(r,\varphi,z) = \frac{1}{2\pi}\int_0^{2\pi} \boldsymbol{J_t}(r,\varphi,z,t)e^{-j\omega t}d(\omega t). \tag{3.10}$$

$C_{(mn)(mn')}^{(i)(i')}$ is the coupling coefficient between any two modes inside the cavity and

$$C_{(mn)(mn')}^{(i)(i')} = \begin{cases} -1 & i = i' = 1, n' = n \\ -\dfrac{m^2}{\mu_{mn}'^2 - m^2} & i = i' = 2, n' = n \\ \dfrac{2(-1)^{n+n'}\mu_{mn}^2}{\mu_{mn'}^2 - \mu_{mn}^2} & i = i' = 1, n' \neq n \\ -\dfrac{2\mu_{mn}'^2\mu_{mn'}'^2}{\mu_{mn}'^2 - \mu_{mn'}'^2} \cdot \dfrac{\left(1 - \dfrac{m^2}{\mu_{mn}'^2}\right)}{(\mu_{mn}'^2 - m^2)^{1/2}\left(\mu_{mn'}'^2 - m^2\right)^{1/2}} & i = i' = 2, n' = n \\ \dfrac{2m(-1)^{n+n'}}{\left(\mu_{mn'}'^2 - m^2\right)^{1/2}} & i = 1, i' = 2 \\ 0 & i = 2, i' = 1. \end{cases} \tag{3.11}$$

The current source in (3.7) represents the gyrating motion of the electrons. The relationship between the current density and the motions of the electron beam can be expressed as:

$$\boldsymbol{J} = \rho\boldsymbol{v} \tag{3.12}$$

where ρ is the charge density and $\boldsymbol{v}$ is the velocity of the electrons. And $\boldsymbol{J}$ can be decomposed as

$$\boldsymbol{J} = \boldsymbol{J_t} + \boldsymbol{J}_{\parallel} \tag{3.13}$$

, where $\boldsymbol{J}_{\parallel}$ is the longitudinal current density. The motion of the electrons in the EM field satisfies the Lorentz force equation:

$$\frac{d\boldsymbol{p}}{dt} = -e(\boldsymbol{E} + \boldsymbol{v} \times \boldsymbol{B}). \tag{3.14}$$

t represents the real time. $\boldsymbol{p}$ is the momentum of the electrons and

$$\boldsymbol{p} = m_e \gamma \boldsymbol{v}. \tag{3.15}$$

At the input end of the cavity where the EM wave is totally reflected, all the modes in the calculation should satisfy the evanescent wave condition [49-51]:

$$\left. \frac{dV_{mn}^{(i)}(z)}{dz} - j \cdot k_{\parallel mn}^{(i)}(z) \cdot V_{mn}^{(i)}(z) \right|_{z=0} = 0. \tag{3.16}$$

The input boundary condition can be used to determine the initial value of $V_{mn}^{(i)}$ that will be used for solving (3.7). By doing so, the boundary condition at the input end of the cavity is naturally fulfilled.

At the output end where the EM wave is coupled out of the cavity, the outgoing wave boundary condition should be satisfied [49-51]:

$$\sum_i \sum_{mn} \left| \frac{dV_{mn}^{(i)}(z)}{dz} + j \cdot k_{\parallel mn}^{(i)}(z) \cdot V_{mn}^{(i)}(z) \right|_{z=L} = 0. \tag{3.17}$$

The output boundary condition can be used as the criterion to judge whether the calculation of the oscillation frequency of the wave is true. The above equations form the self-consistent nonlinear theory of the gyrotrons in steady state. By solving the above equations self-consistently, the axial field distribution of the operation mode, the output power, the oscillation frequency can be obtained. The flow chart of solving the above self-consistent nonlinear problem is shown in Figure 3-1.

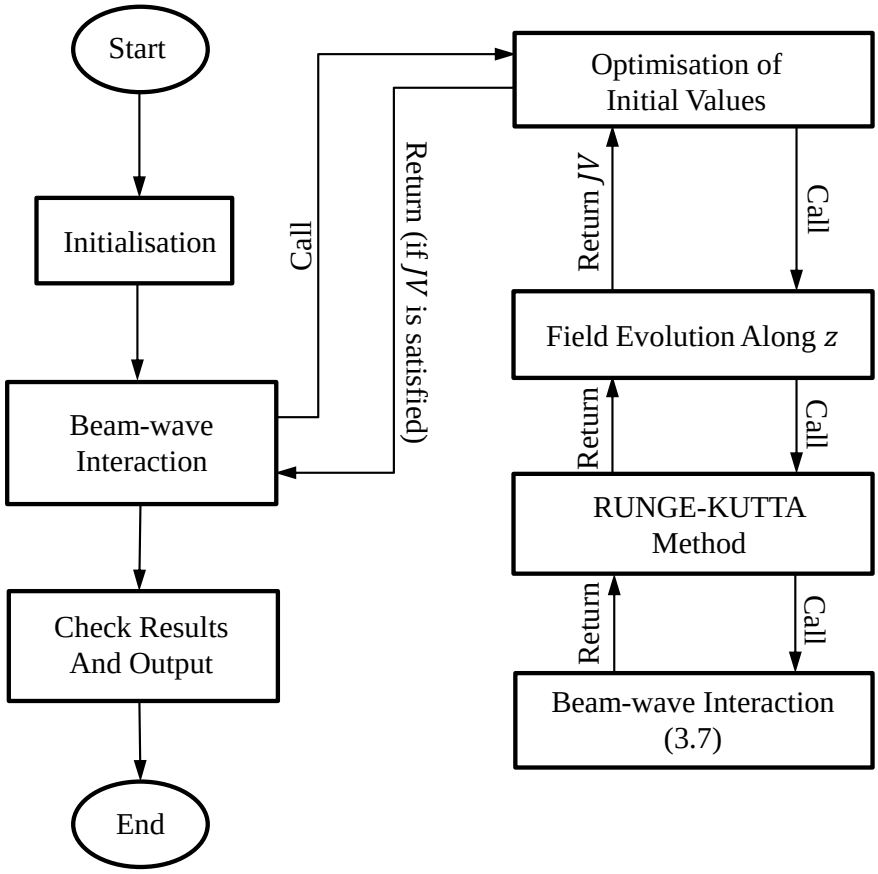

Figure 3-1: The flow chart of solving the self-consistent non-linear problem for the complex-cavity gyrotron. JV represents the criteria to judge if the boundary condition of (3.17) is fulfilled.

Based on the algorithm, a calculation code is developed in Fortran language to facilitate the prototype gyrotron design.

3.2 Numerical Simulations

To numerically verify the code, a simplified version of the gyro-multiplier scheme shown in Chapter 2 [65], namely a 342 GHz, large-orbit and complex-cavity gyrotron operating with $TE_{1,2}/TE_{1,3}$ modes is simulated. The gyrotron beam-wave interaction cavity profile is shown in Figure 3-2 with the structural parameters listed in Table 3-1. A 80 kV, 0.7 A helical electron beam at a velocity ratio of 1.4, as used in the gyro-multiplier simulation [65], is chosen in this study.

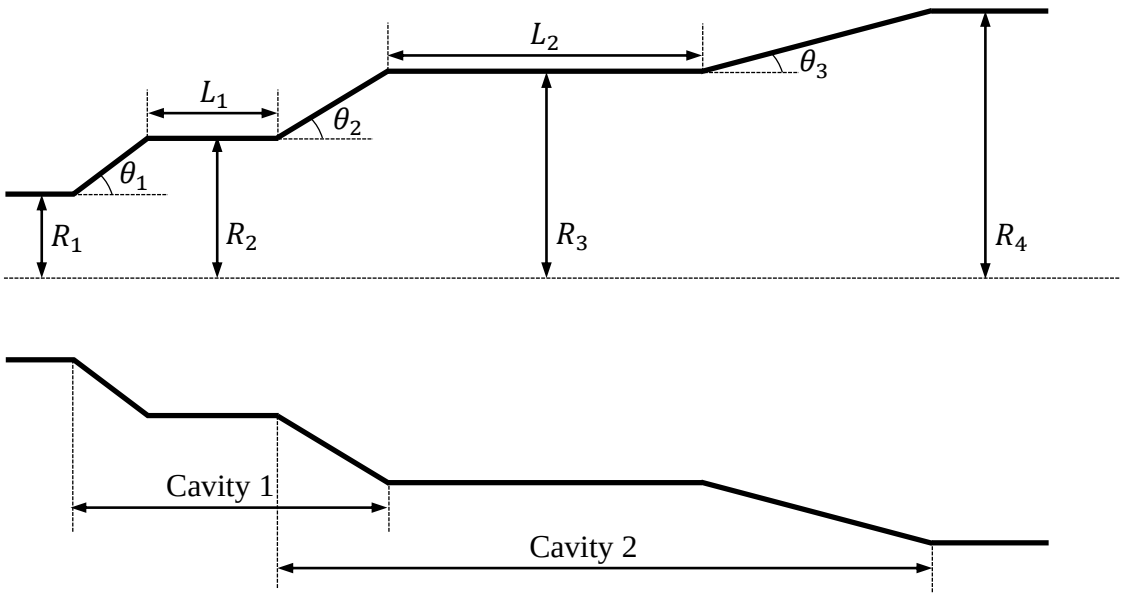

Figure 3-2: Schematic view of the complex-cavity configuration for beam-wave interaction.

Table 3-1: The structural parameters of the cavity.

R_1	0.25 mm	θ_1	26°
R_2	0.75 mm	θ_2	29°
R_3	1.2 mm	θ_3	12°
R_4	1.4 mm	L_1	1 mm
L_2	6.4 mm		

The numerical simulation results are shown in Figure 3-3. The electron beam is pre-bunched in the first cavity with $TE_{1,2}$ mode before entering the second cavity, where the main beam-wave interaction between $TE_{1,3}$ mode and the electron beam takes place. In the second cavity, the electrons firstly gain energy from the EM field. After that, most of them will loss energy to the field inside the cavity. The amplitude of $TE_{1,2}$ and $TE_{1,3}$ modes as well as the beam-wave interaction efficiency variation along the axis are shown. An output power of 6.72 kW corresponding to an efficiency of 12% and output frequency

of 341.96 GHz can be obtained with an external magnetic field of 13.7 T. The output mode is $TE_{1,3}$.

The gyrotron is then modelled with the same parameters in the commercial PIC code MAGIC. The output power variation with time is shown in Figure 3-4. It can be shown that the output power stabilised at 5 kW after a starting oscillation process of 8 *ns*.

The field amplitude variation at the output end of the cavity is recorded before a Fast Fourier Transformation (FFT) is applied. The spectrum of the oscillation is shown in Figure 3-5. The oscillation frequency is 341.76 GHz.

To verify the operation mode inside the gyrotron cavity, the axial electric and transverse magnetic field distributions are recorded at 9.7 ns, as shown in Figure 3-6 and Figure 3-7, respectively. It is confirmed that the output mode is $TE_{1,3}$.

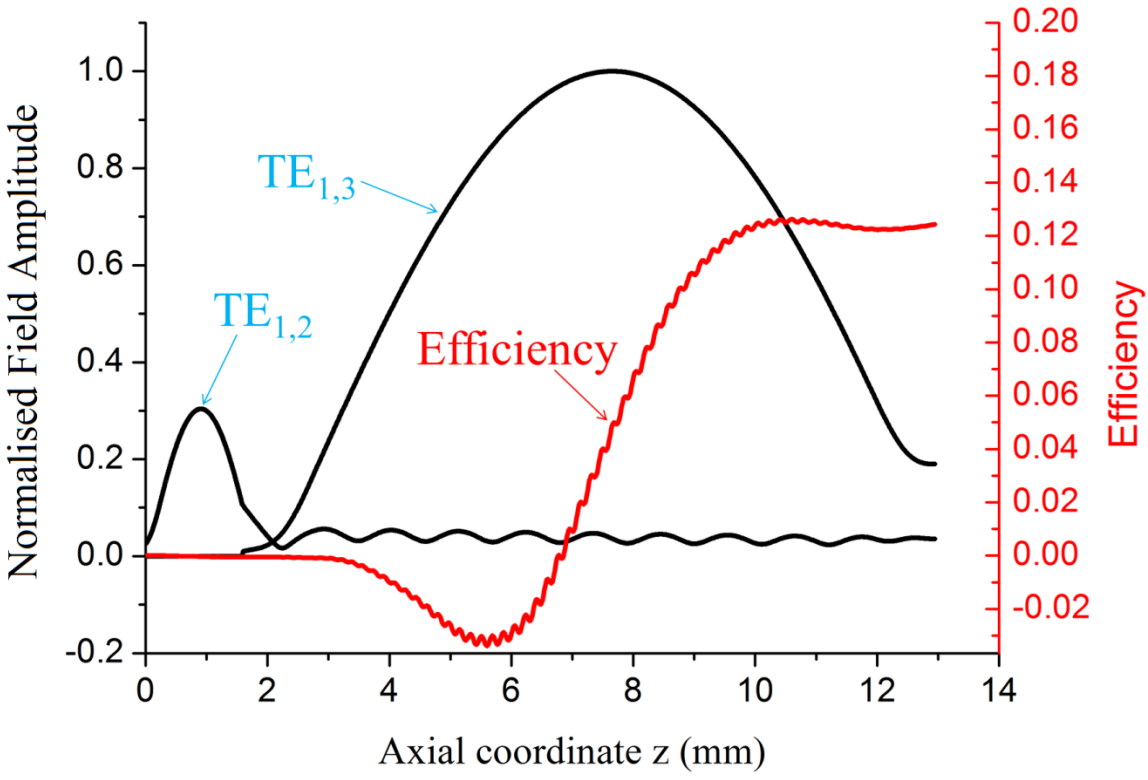

Figure 3-3: The numerical results from the calculation code.

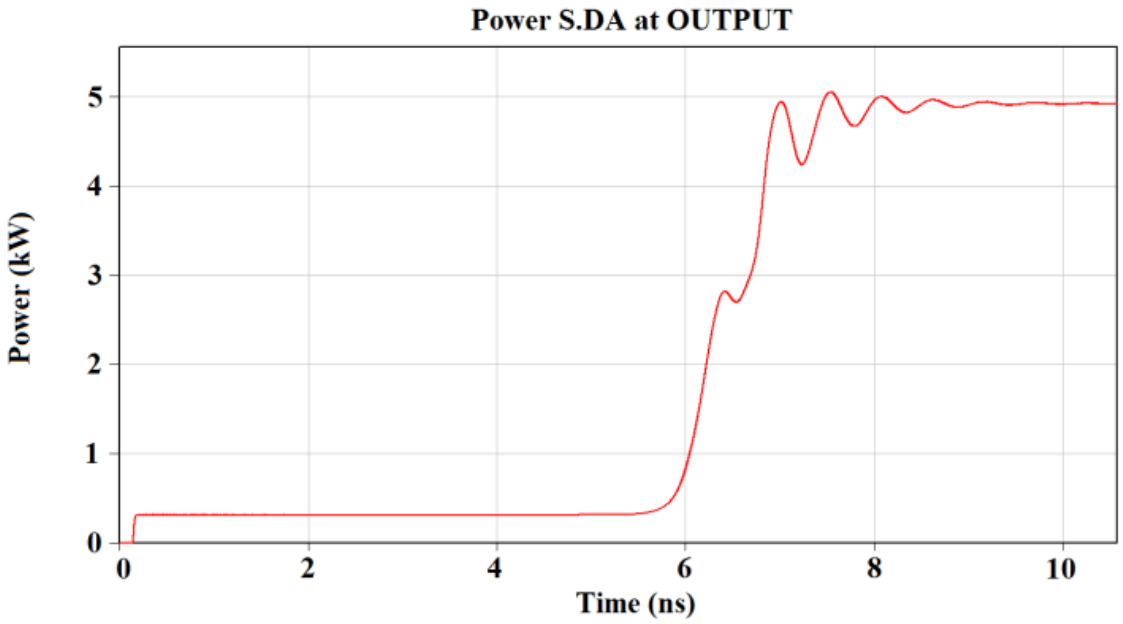

Figure 3-4: The output power variation with time from MAGIC simulation.

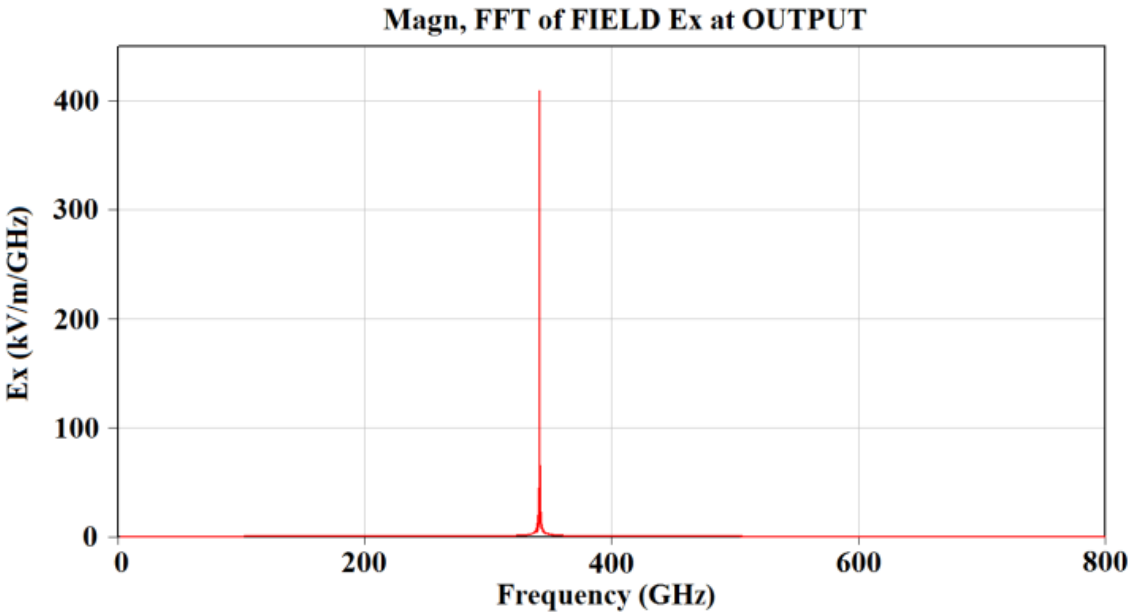

Figure 3-5: The spectrum of the recorded signal at the output end of the cavity from MAGIC simulation.

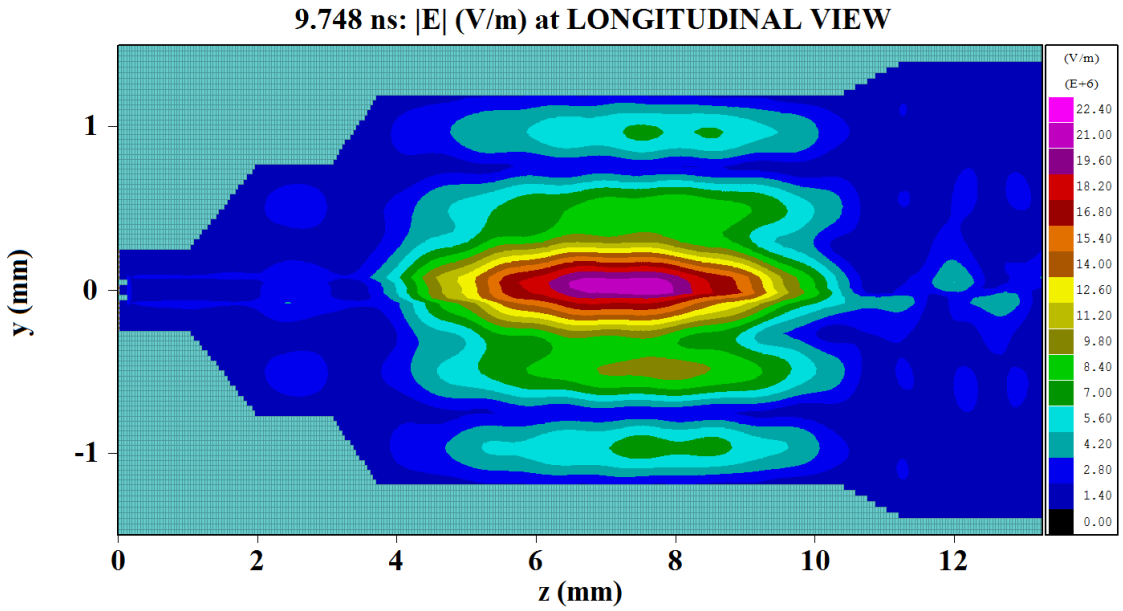

Figure 3-6: The E field distribution from the axial view.

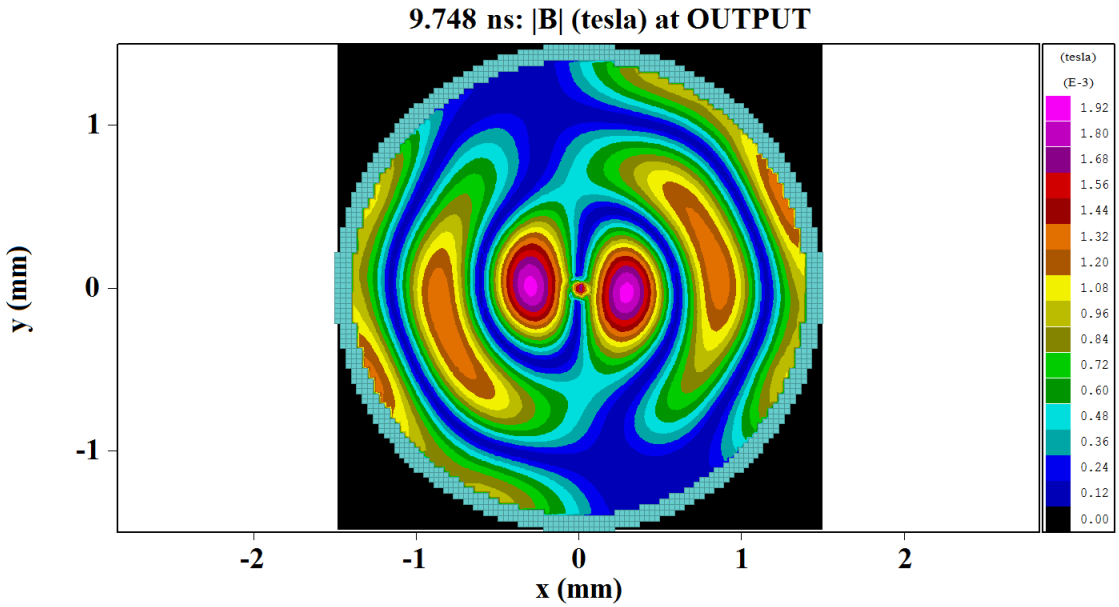

Figure 3-7: The B field distribution from the transverse view.

Figure 3-8 shows the comparison between the simulated output power from the in-house code and MAGIC. Within the external magnetic field range of 13.7 to 14.1 T, both numerical tools predict that the output power decreases with the increase of the external magnetic field. The peak output power can be obtained at 13.7 and 13.5 T, as predicted

by the in-house code and MAGIC, respectively. The difference can be explained by the simplifications used in the above steady-state non-linear theory as well as the limited meshing accuracy of MAGIC regarding the cavity radius.

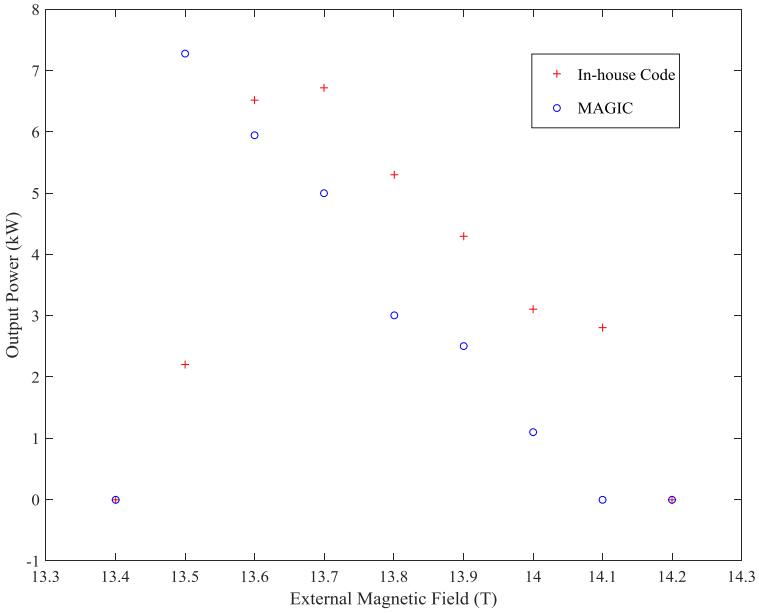

Figure 3-8: Comparison of the simulated output power from the in-house code and MAGIC.

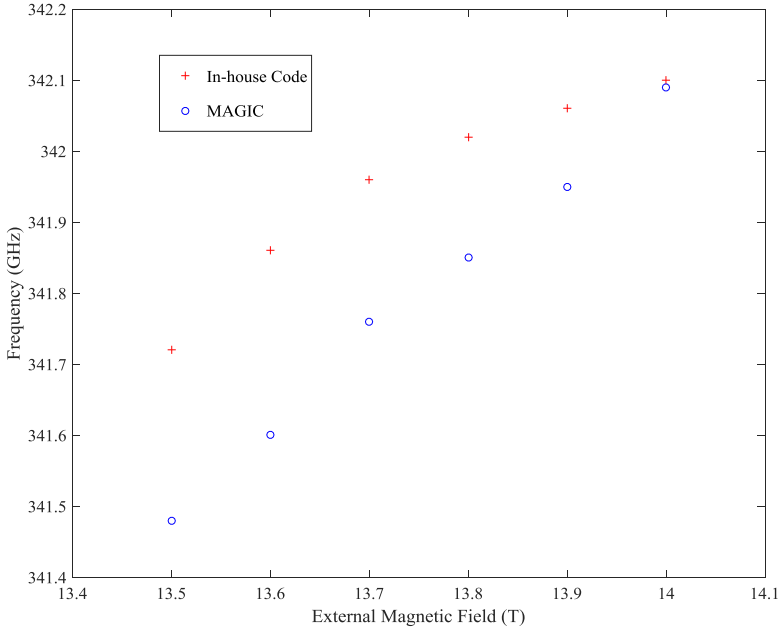

Figure 3-9: Comparison of the simulated oscillation frequency from the in-house code and MAGIC.

Figure 3-9 shows that as the external magnetic field increases, both tools predict increase of the oscillation frequency. The predicted oscillation frequency values from the in-house

code are higher than those from MAGIC. A number of factors may have induced the discrepancy, such as the different boundary condition algorithms used in the two tools, the simplification used in the self-consistent non-linear theory and the limited meshing accuracy of MAGIC regarding the radius of the beam-wave interaction cavity.

The PIC simulation result has shown reasonable agreement with that obtained using the in-house code. However, it is worth mentioning that on the same PC, the simulation time used by the self-developed code is about 10 minutes while that consumed by the PIC code is above 24 hours. Thus the self-developed code presented can be a useful fast analysis tool for the gyrotron oscillators.

The in-house code has also been successfully applied to the development of a 420 GHz complex-cavity gyrotron operating with the $TE_{17,3}/TE_{17,4}$ mode pair in the University of Electronic Science and Technology of China (UESTC) [134]. The experimental result has shown that the code can serve as an effective tool during the initial design stage of the beam-wave interaction structure.

The theory and analysis process in this chapter can be expanded into the study of a gyro-multiplier to generate a steady-state, nonlinear theory for the gyro-multiplier with sectioned cavity. This will facilitate the characterisation of the gyro-multiplier algorithm as well as the preliminary design of the device.

Chapter Summary

In this chapter, the steady-state non-linear theory of the gyrotrons has been summarised and an in-house simulation code has been developed. Due to a number of simplifications used in the non-linear theory, the code which focuses on the steady-state of the gyrotron operation, is more time efficient than MAGIC. To verify the code, a comparison has been made between the results generated by the two numerical tools. Reasonable agreements have been found. The in-house code can serve as a preliminary design tool for the gyrotrons.

Chapter 4 Numerical Investigation of a High-harmonic Gyrotron

In this chapter, a high-harmonic large-orbit gyrotron (LOG) operating with $TE_{m,1,1}$ modes is designed and theoretically analysed through the linear theory as well as the 3D PIC code. To fulfil the starting oscillation condition at the high harmonics, a 250 kV, 1 A electron beam is adopted with a pitch factor of 2. By careful choice of the external magnetic field, selective excitation of the oscillation from the fourth to the ninth harmonics of the electron cyclotron resonance can be achieved. Correspondingly, the radiation spans from 230 GHz to 465 GHz with kW-level output power. By enabling the high-harmonic operation, the required external magnetic field strengths are reduced to the range between 2.6 T to 3.1 T, which can be provided by a helium-free cryomagnet [135]. The study firstly focuses on the excitation and beam-wave interaction characterisation at the eighth harmonic. After that, a number of parameter variation studies are conducted to specify the influence of the external magnetic field, electron beam parameters as well as the structural parameters on the beam-wave interaction outcome. Finally, the multi-modes, multi-harmonics behaviour from the seventh to the ninth harmonic is also investigated.

4.1 Large-orbit Electron Beam Sources

One of the most vital parts in LOG development is the large-orbit gyrating electron beam source [24-27]. There are basically two categories of beam sources used in the previous experiments of LOGs: one is cusp electron type with beam voltage $U \leq 80$ kV and the other one is Pierce-kicker type or accelerator based type with beam voltage $U \geq 250$ kV. The reported LOG beam sources used in gyrotron oscillators are summarised in Table 4-1. One of the beam sources from Table 4-1 will be chosen in this study.

Table 4-1: Typical LOG beam sources.

Institution	U (kV)	I (A)	α	T	Modes	Frequency (GHz)
IAP [135]	15	0.3	≥2	N/A	$TE_{3,4}$	260
IAP [135]	30	1	1.5-2	CW	$TE_{m,1}$(m=2,4)	267, 394, 520
Fukui [59]	40	<2	2	1ms	$TE_{m,1}$(m =3,5)	89.3, 112.7, 138
Strathclyde [6]	40	1.5	1-3	1ms	$TE_{2,1}$	108-110
IAP [22, 136]	80	0.7	1.4-1.5	10us	$TE_{3,7}$	1000
IAP [58, 70, 137]	250	10	2	10us	$TE_{5,1}$	150
IAP [138]	250	≤4	1	10us	$TE_{3,9}$	414
IAP [139]	300-350	25-35	1.5	20ns	$TE_{m,1}$(m =1,5)	N/A
Maryland [140]	600	600-1000	2	75ns	$TE_{1,0}$*	0.65
Maryland [68]	600-750	1000	2.01	80ns	$TE_{1,1}$	0.65
Maryland [141]	2000	2000	1.83	5-25ns	$TE_{1,1}$	0.7-1.2

I denotes the maximum achievable beam current. $\alpha = v_\perp/v_\parallel$ is the pitch factor where $v_\perp$ and $v_\parallel$ are the electron beams transverse and axial velocities, respectively. T represents the reported pulse length of electron beam. The operation modes in the experiments are also listed in the last column.

*The study was conducted in a rectangular waveguide and thus with the mode $TE_{1,0}$.

IAP is short for the Institute of Applied Physics, Nizhny Novgorod, Russia; Fukui is the University of Fukui, Fukui, Japan; Strathclyde is the University of Strathclyde, Glasgow, UK; Maryland stands for the University of Maryland, College Park, USA.

However, not all of the electron beam sources shown above are suitable for the operation of LOGs at the eighth harmonic. For example, as shown by the authors in [142], a 40 kV, 1.5 A electron beam with a pitch factor of 3 can only support the first seven harmonics oscillation even when an extremely long cavity of 50 wavelengths is chosen. The reason can be interpreted from the linear theory of a gyrotron where the starting oscillation current of $TE_{m,n}$ mode is expressed by [135]

$$I_{st} \propto \frac{1}{G_{m,n}\beta_{\perp}^{2s}(L/\lambda)^2 Q}. \tag{4.1}$$

Here $\beta_{\perp}$ is the transverse electron beam velocity normalised to the speed of light c. Given a fixed value of α, $\beta_{\perp}$ is proportional to the beam voltage U [22, 58]. L/λ is the ratio between the cavity length and the wavelength of the operation mode. Q is the quality factor of the operation mode. In the aforementioned example where $\beta_{\perp} \approx 0.3$, I_{st} rises dramatically with s and exceeds the maximum beam current that can be provided when $s = 8$. Such strong dependence can be mitigated by increasing L and Q, or by using the electron beam sources with larger $\beta_{\perp}$. However, the former method is not only limited by the cavity wall loss in the THz band and the axial modes competition, but also complicated by the reabsorption of the wave energy by the electron beam which causes unstable output power levels [135, 142]. To maintain an acceptable I_{st} at the eighth harmonic, an electron beam with higher voltage and hence higher $\beta_{\perp}$ should be chosen.

Based on the above analysis, a high-voltage relativistic beam source should be chosen in our study to enable the operation of $TE_{8,1,1}$ mode at the eighth harmonic. It is also noteworthy that based on the 3D PIC simulation, the starting oscillation process of $TE_{8,1,1}$ mode in certain occasion takes over 50 ns. In this case, we should choose the high-voltage beam sources with sufficient pulse durations. Thus the beam with a voltage of 250 kV, a current of up to 10 A, a pitch factor of 2 and a pulse length of 1 μs is selected in this study.

4.2 Cold Cavity Analysis

A reasonable choice of the operation mode can greatly lower the risk of mode competition in gyrotron development. Although the adoption of axis-encircling electron beam has already greatly rarefied the competition modes spectrum by restricting the equality of operation harmonic number s and the corresponding modes' azimuthal index m, the high-harmonic LOG operation is still facing potential mode competition. On the one hand, within the same harmonic, the modes sharing the same azimuthal index can be excited. For example, the operation of $TE_{m,2}$ mode can be overtaken by $TE_{m,1}$ mode.

On the other hand, modes in the lower harmonics but with similar $\mu'_{m,n}/m$ can also be excited [22], such as $TE_{9,3}$ and $TE_{5,2}$ shown in Figure 4-1. One of the most effective way to suppress the above mode competition in high-harmonic LOGs is to use whispering gallery modes $TE_{m,1}$. By using such modes, all the corresponding $TE_{m,n}$ ($n > 1$) modes will be eliminated by the waveguides cut-off frequencies. For example, in a cavity designed for $TE_{8,1}$ mode, $TE_{8,2}$ mode will be cut-off. Besides, such modes have separated values of $\mu'_{m,n}/m$ from modes in the lower harmonics. In principle, given sufficient beam current and proper external magnetic field, sth harmonic operation with $TE_{m,1}$ ($m = s$) modes can be selectively excited. However, in order to maintain reasonable selectivity, s and m cannot be too large as the mode separation between $TE_{m+1,1}$ and $TE_{m,1}$ decreases as m increases, which can be interpreted from the left-hand part of Figure 4-1.

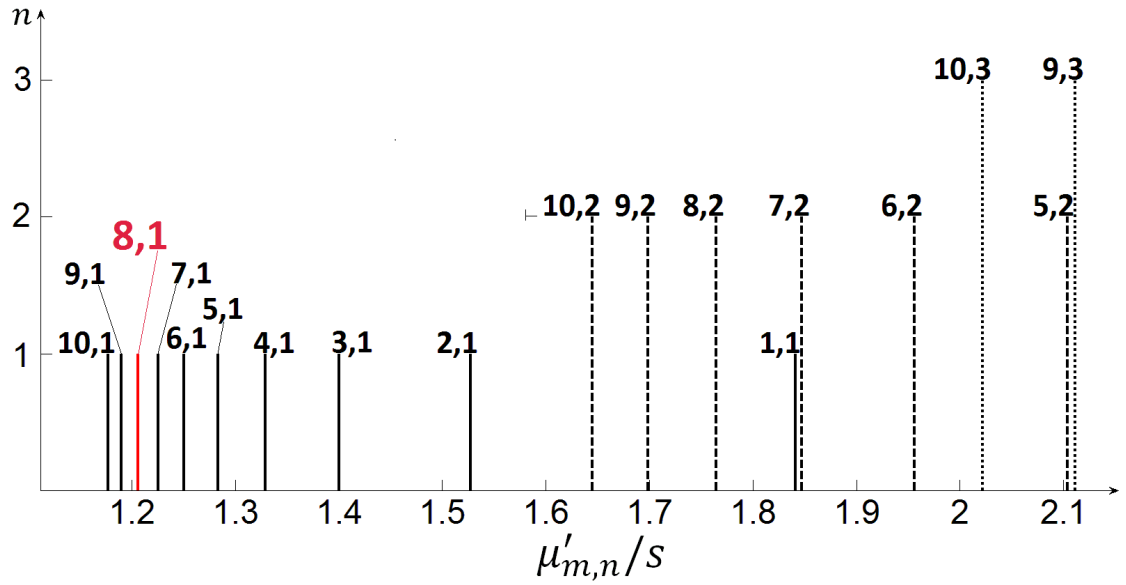

Figure 4-1: Mode spectrum of the candidate modes for high-harmonic operation.

Beside, as can be seen from Figure 4-2, the maxima of the radial electric field is located more and more close to the cavity wall as m increases, which will in turn induce higher Ohmic loss as well as require smaller distance between the electron beam and the cavity wall. Thus, this study firstly focuses on the eighth harmonic operation with $TE_{8,1,1}$ mode.

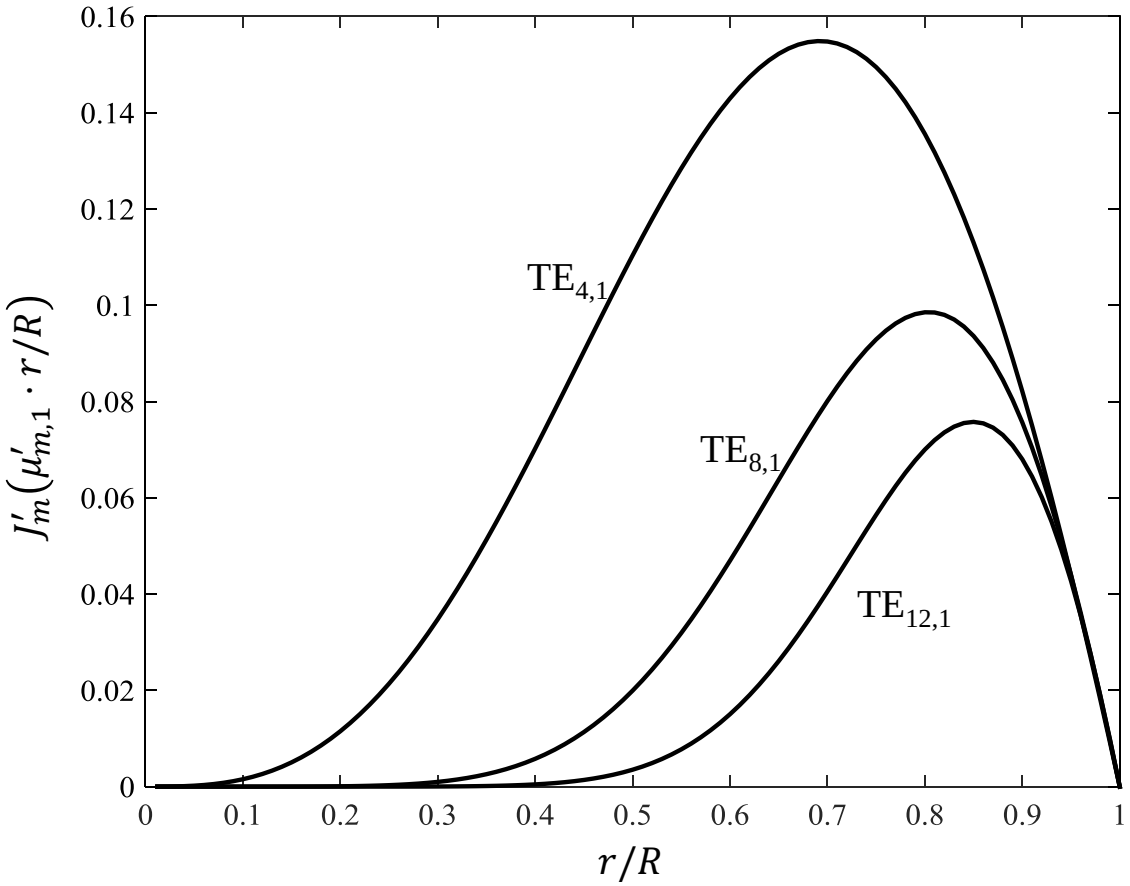

Figure 4-2: Radial distribution of the azimuthal electric field E_φ for $TE_{m,1}$ modes (m=4, 8 and 12). φ and r denotes the azimuthal and radial coordinate, respectively. J'_m is the first derivative of mth order Bessel function. $\mu'_{m,n}$ is the eigenvalue of $TE_{m,1}$ mode. R is the waveguide radius.

The beam-wave interaction cavity profile is shown in Figure 4-3. To maintain the cyclotron resonance condition between the gyrating electrons and the rotating wave, the oscillation frequency of $TE_{8,1}$ mode should be slightly higher than the cavity's cut-off frequency. Thus the cavity diameter is chosen to be 2.2 mm. Then, the Ohmic quality factor Q_Ω of the cavity when using oxygen-free copper as the cavity material can be calculated by [139]

$$Q_\Omega = (R/\delta)(1 - m^2/\mu'^2_{m,n}) \tag{4.2}$$

where R is the beam-wave interaction cavity radius and $\delta = \sqrt{2/\omega\sigma\varepsilon}$ is the skin depth, in which $\omega = 2\pi f$. $\sigma = 4\pi \times 10^{-7} H/m$ and $\varepsilon = 5.99 \times 10^7 S/m$ are the absolute permeability and the conductivity of the oxygen-free copper. Assuming that the

oscillation frequency is exactly 420 GHz, the Ohmic quality factor Q_Ω of this mode can be obtained from (4) as 3424.

The relatively low value of Q_Ω suggests that the Ohmic loss on the cavity wall is high due to the adoption of a whispering gallery mode where the field maxima is placed very close to the cavity wall [143]. To ensure that more power is coupled out of the cavity than being dissipated on the cavity wall, the diffraction quality factor Q_d should be smaller than Q_Ω. The code developed in Chapter 3 has predicted that a diffraction quality factor of 3051 corresponding to f = 420.1 GHz can be obtained by the geometric parameters listed in Table 4-2. The Ohmic quality factor Q_Ω is then modified to be 3425 given the oscillation frequency of 420.1 GHz. The total quality factor Q is calculated to be 1614 by

$$Q = Q_d \cdot Q_\Omega/(Q_d + Q_\Omega). \tag{4.3}$$

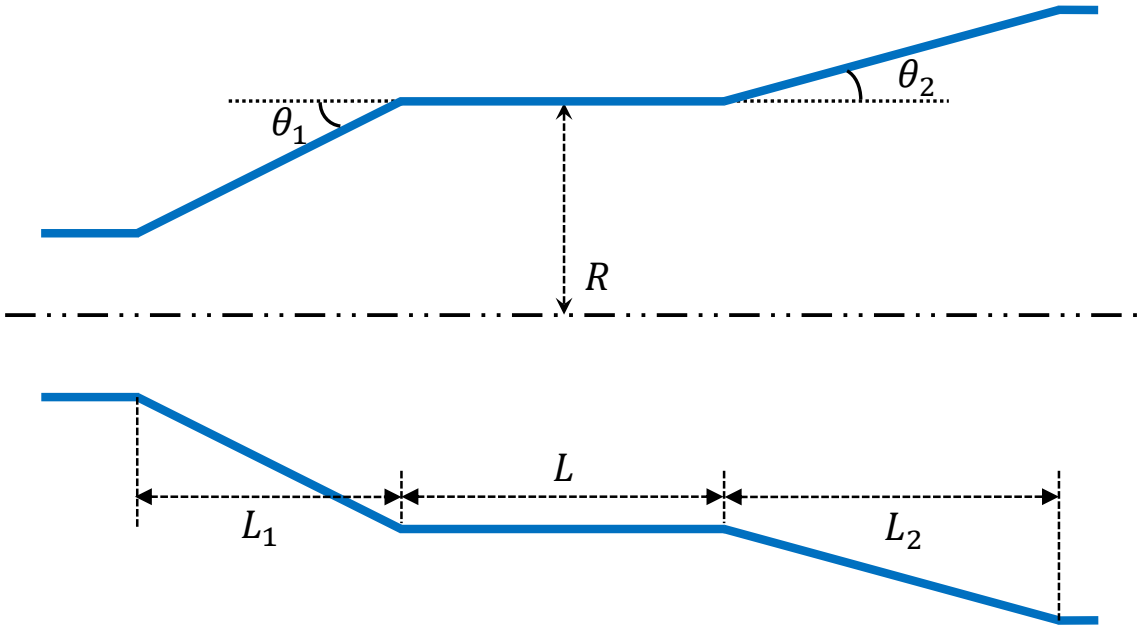

Figure 4-3: The gyrotron cavity profile from longitudinal view.

Table 4-2: The geometric parameters of the LOG cavity.

L_1	L_2	L	R	θ_1	θ_2
1.5 mm	2.5 mm	8 mm	1.1 mm	4.5°	5.6°

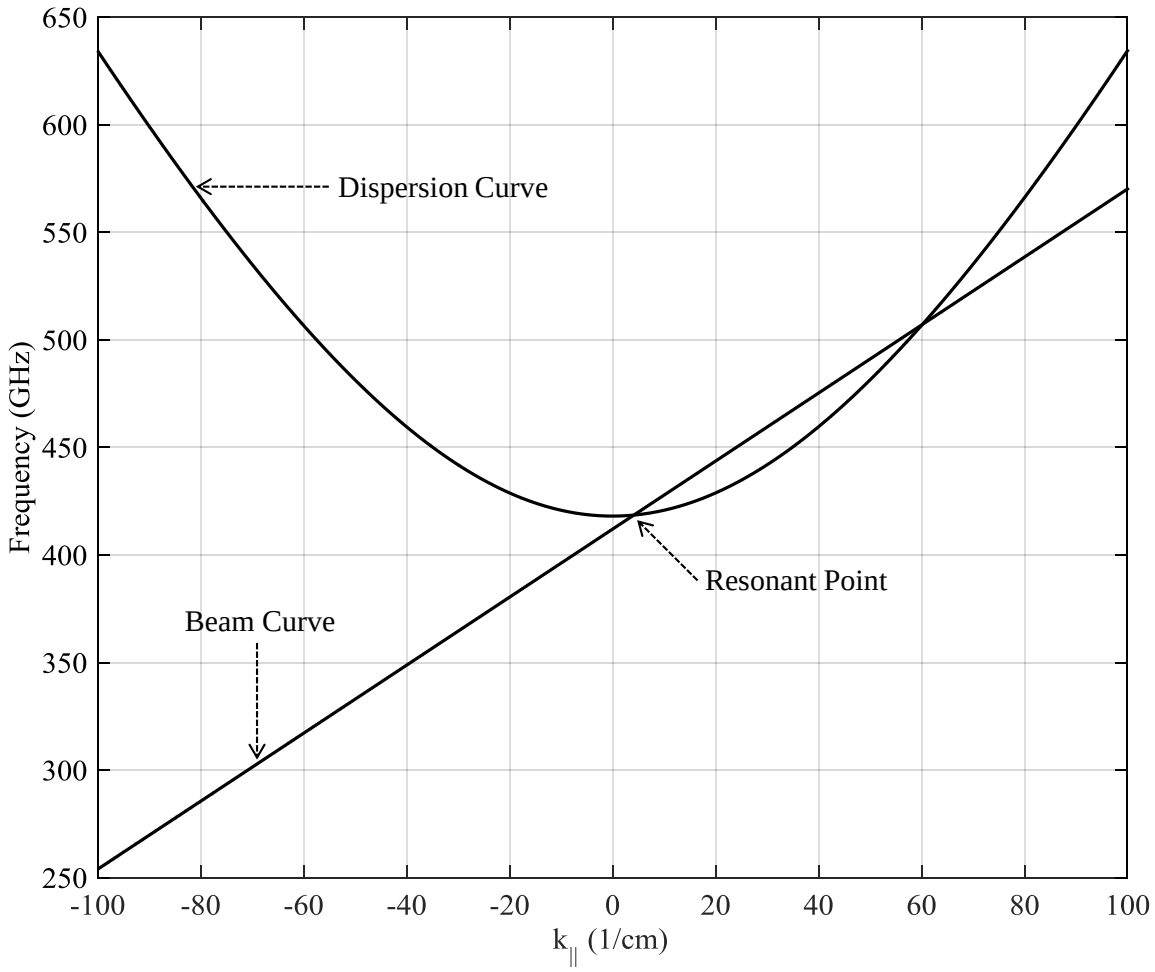

Figure 4-4: Dispersion diagram of the cylindrical waveguide $TE_{8,1,1}$ mode and the synchronism condition in straight line. The intersection between the two means the resonance interaction point.

The resonant interaction between the electron beam and the waveguide mode can be shown in Figure 4-4 [49-51]. The hyperbolic line is the dispersion curve of $TE_{8,1}$ mode in the cylindrical waveguide as shown in (4.4):

$$\omega^2 = k_{\parallel}^2 c^2 + \omega_c^2 \tag{4.4}$$

where ω_c is the cut-off frequency of the mode in the waveguide. The propagation constant $k_{\parallel}$ is restricted to a number of discrete values. The straight line represents the synchronism condition between the electrons and the $TE_{8,1}$ mode, as described in (1.1). A resonant interaction can take place at the intersection point between the two lines.

By using the above resonance condition and diagram, the external magnetic field amplitude and the pitch factor is chosen to be 2.75 T and 2, respectively. However, by

using the above parameters, the neighbouring modes of $TE_{8,1}$ might also be excited, such as $TE_{7,1}$ and $TE_{9,1}$ modes in Figure 4-1. To enable single mode operation, the cold cavity theory should be applied to analyse the starting oscillation currents of the potential competition modes.

The starting oscillation currents I_{st} of $TE_{8,1,1}$ mode and the neighbouring modes can be analysed by the linear theory as [53]:

$$I_{st} = -\left(\frac{I_A}{Q}\right)\left(\frac{\omega}{m\Omega}\right)\left(\frac{\gamma L\omega R_w^2 k_\parallel^2 \beta_\parallel^2}{16c}\right)\left(1-\frac{m^2}{\mu_{m,n}'^2}\right)\times\left(\frac{J_m(\mu_{m,n}')}{J_m'(\mu_{m,n}'\beta_\perp c/R_w/\Omega)}\right)^2 R(x)^{-1} \tag{4.5}$$

where

$$\begin{aligned} R(x) = \Bigg\{ & 2 - 2x\left(\frac{\beta_\perp^2}{\beta_\parallel}\right)\left(\frac{\omega}{m\Omega}\right)\left(\frac{k_\parallel c}{\omega}\right) + \left[\left(\frac{mR_w\Omega}{\beta_\perp c\mu_{m,n}'}\right)^2 - 1\right] \\ & \times\left(\frac{J_m(\mu_{m,n}'\beta_\perp c/R_w/\Omega)}{J_m'(\mu_{m,n}'\beta_\perp c/R_w/\Omega)}\right)^2 + \left(\frac{2\mu_{m,n}'\beta_\perp c}{R_w\Omega}\right) \\ & \times\left(\frac{2\mu_{m,n}'\beta_\perp c}{R_w\Omega}\right)\times\frac{J_m''(\mu_{m,n}'\beta_\perp c/R_w/\Omega)}{J_m'(\mu_{m,n}'\beta_\perp c/R_w/\Omega)}\Bigg\} G(x) \\ & + \left(\frac{\beta_\perp^2}{\beta_\parallel}\right)\left(\frac{\omega}{m\Omega}\right)\left[\left(\frac{\omega}{k_\parallel c}\right) - x^2\left(\frac{k_\parallel c}{\omega}\right)\right] G'(x) \end{aligned} \tag{4.6}$$

and I_A is the Alfven current and $I_A = 17$ kA. Q is the cavity quality factor. L is the cavity length. $\beta_\parallel = v_\parallel/c$ and $\beta_\perp = v_\perp/c$ are the axial and transverse electron beam velocity normalised to the speed of light, respectively. J_m is the mth order Bessel Function while J_m' and J_m'' is the first and second derivative of it, respectively. q is the axial wave number and

$$G(x) = [cos(\pi qx/2)/(1-x^2)]^2 \tag{4.7a}$$

for odd q and

$$G(x) = [sin(\pi qx/2)/(1-x^2)]^2 \tag{4.7b}$$

for even q in which.

$$x = (\omega - m\Omega)\gamma n/k_{\|}/p_{\|} \tag{4.8}$$

in which $p_{\|} = m_e \gamma v_{\|}$ is the axial momentum of the electrons. In this theory, the external magnetic field is assumed to be strictly uniform in the beam-wave interaction region. For the case where the external magnetic field varies in the beam-wave interaction region, numerical solution of I_{st} could be obtained instead of the analytical one.

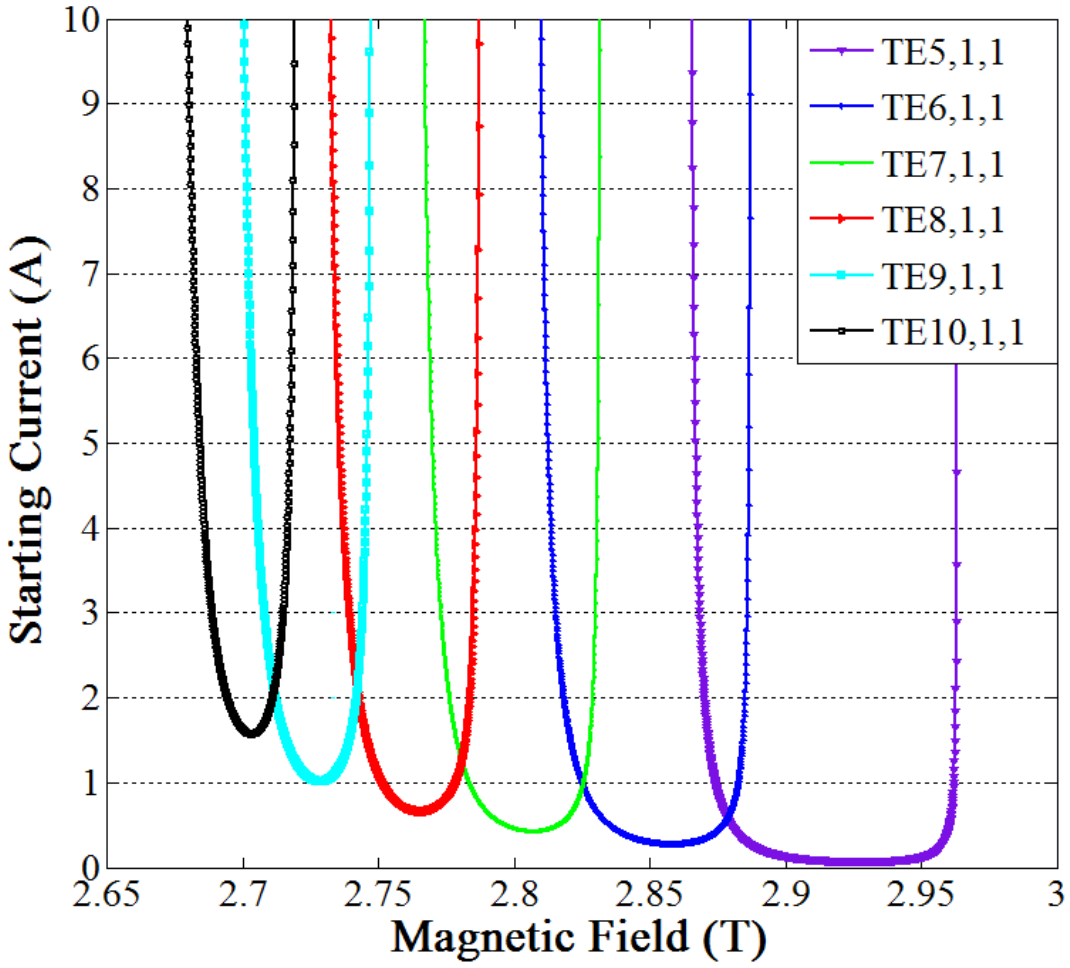

Figure 4-5: Starting oscillation currents of the potentially excited cavity modes.

Figure 4-5 gives the starting oscillation currents variation with the external magnetic field for a number of modes near $TE_{8,1,1}$. It can be seen that the starting oscillation current of $TE_{8,1,1}$ mode is the lowest of all the modes when the external magnetic field is between 2.74 T and 2.78 T. Within this magnetic field range, the $TE_{8,1,1}$ mode can be selectively excited when choosing the beam current to be lower than 1.3 A, by which only the starting oscillation condition at the eighth harmonic is fulfilled.

4.3 Hot Cavity Simulations

Based on the discussion in the previous part, the beam current should be properly chosen to optimise the operation of $TE_{8,1,1}$ mode. As can be seen in Figure 4-5, the starting oscillation current of $TE_{8,1,1}$ mode is the lowest of all the modes between 2.74 T and 2.78 T. To fulfil the excitation requirement of $TE_{8,1,1}$ as well as suppress the nearby competition modes, the beam current is chosen as 1 A. Using the parameters obtained in cold cavity analysis, a 3D model is built and simulated in the FDTD-PIC code MAGIC 2007 [144]. The Cartesian coordinate system is used in the representation of the structure by a number of small stair-cases. x and y denote the coordinate axes in the transverse direction while z is the coordinate axis in the axial direction. The oxygen-free copper as used in the above analysis is set as the material of the cavity wall when calculating the Ohmic loss by dynamically estimating the RF frequency and skin depth locally for each grid cell. In order to verify the hot simulation model as well as its agreement with the cold cavity analysis, one representative simulation result with an external magnetic field of 2.75 T is shown below.

The longitudinal and transverse trajectories of the large-orbit electron beam with a radius of 0.6 mm are shown at 5.715 ns in Figure 4-6 and Figure 4-12 (a), respectively.

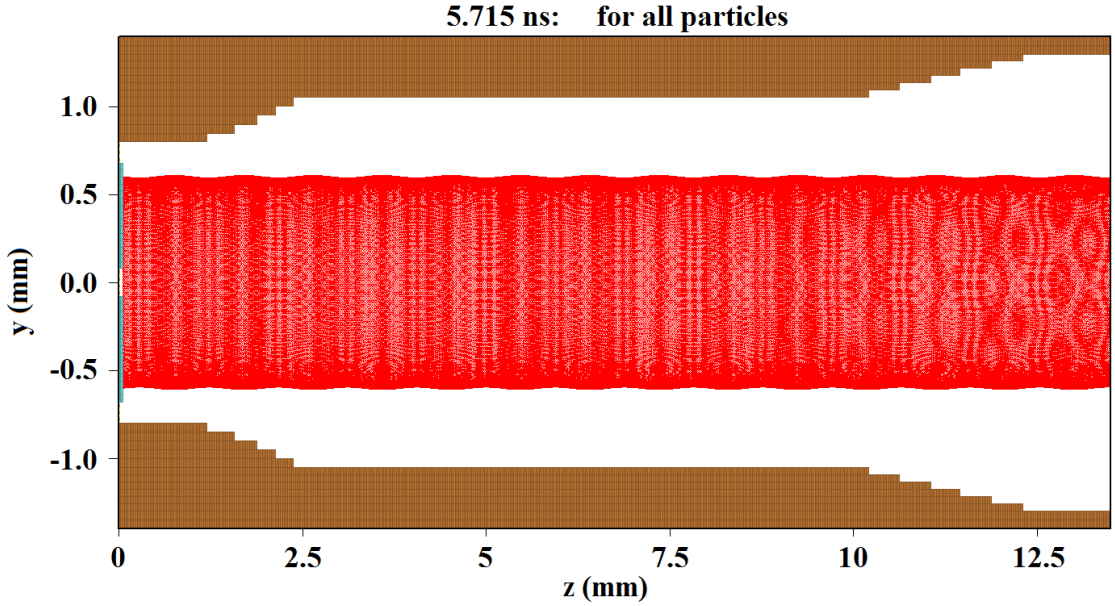

Figure 4-6: The longitudinal view of the electrons trajectory.

The starting oscillation process of $TE_{8,1,1}$ takes about 40 ns before the field amplitude settles down at a stable value, as shown in Figure 4-7. The E_x component, namely the electric field in x direction, is recorded at the output aperture of the beam-wave interaction cavity.

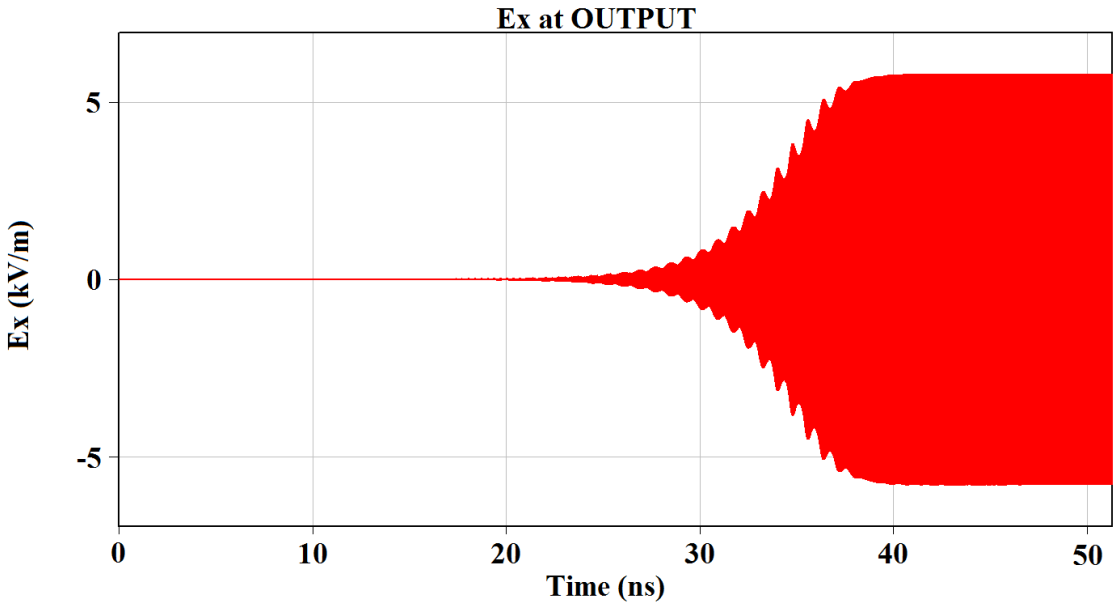

Figure 4-7: The evolution of the x component of the electric field with time.

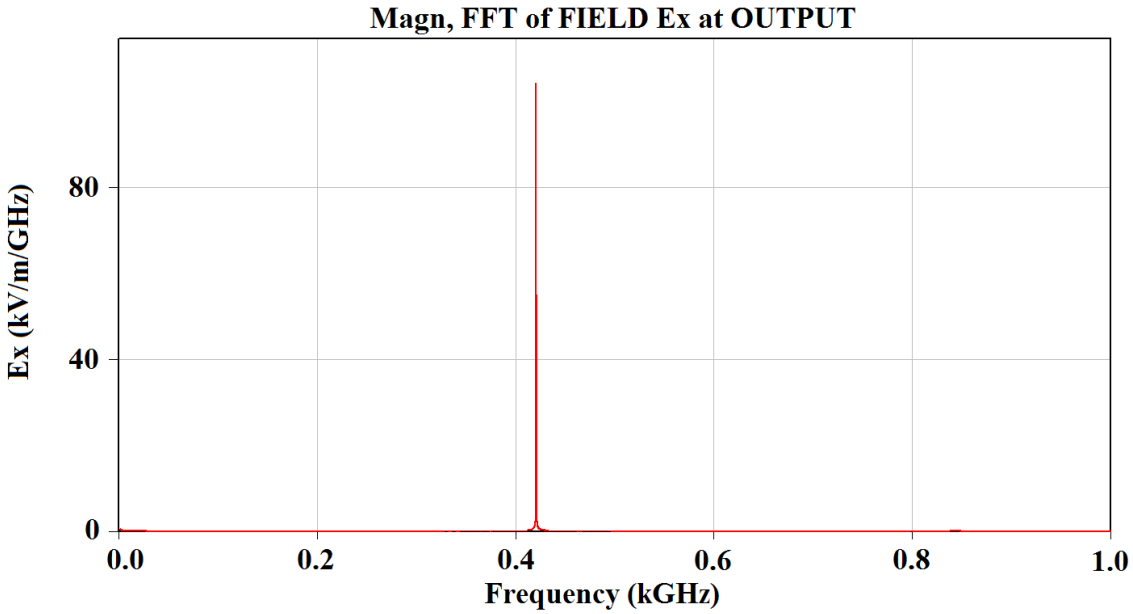

Figure 4-8: Fast Fourier Transformation (FFT) of the output time signal.

By the Fast Fourier Transformation (FFT) of the recorded time domain signal in Figure 4-7, the output frequency of the LOG can be obtained in frequency domain. The result in Figure 4-8 shows a pure frequency spectrum with only one peak at the point of 420.05 GHz, which is close to the initial design and cold cavity analysis.

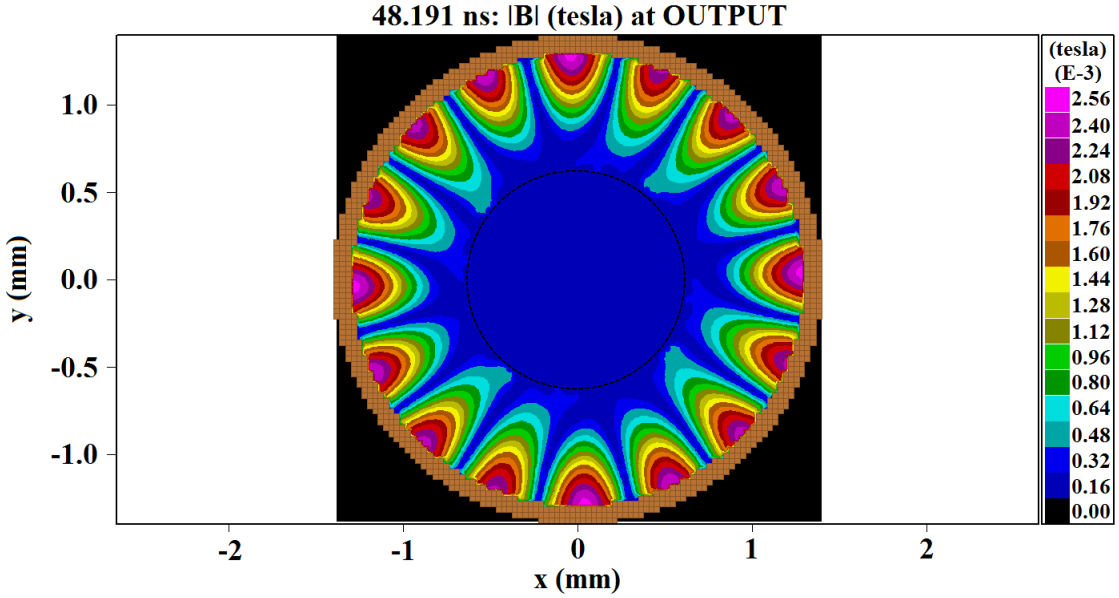

Figure 4-9: Transverse magnetic field distribution at the output end of the cavity. The trajectory of the electron beam is represented in black dotted curve.

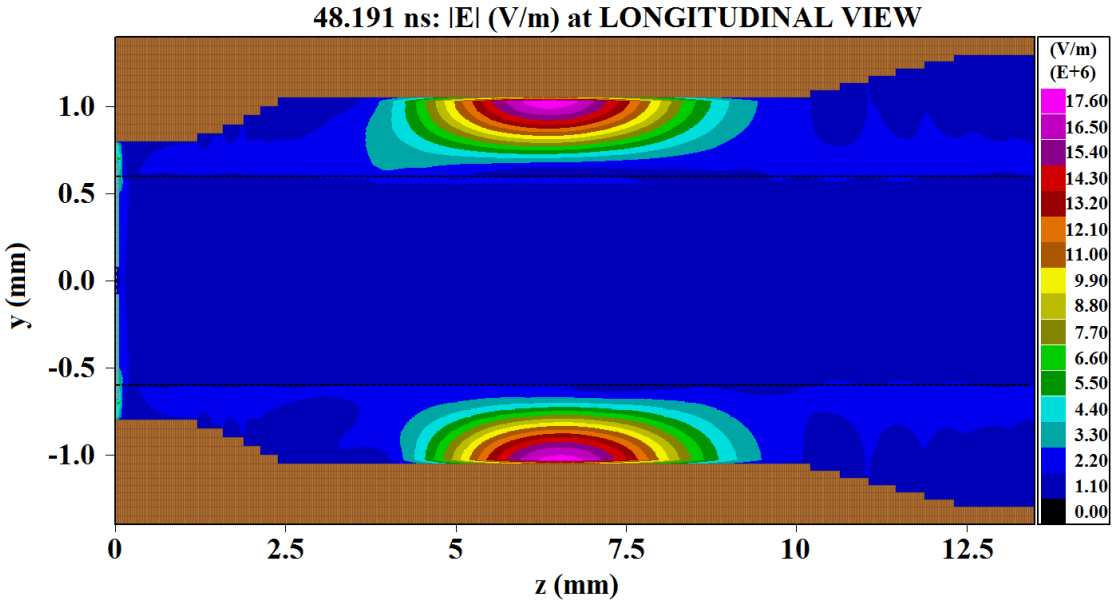

Figure 4-10: Axial electric field distribution in the cavity. The trajectory of the electron beam is represented in black dotted curve.

To further verify the operation mode of the LOG, the magnetic field distribution at the output end of the cavity is recorded at 48.191 ns, as shown in Figure 4-9. The transverse field distribution shows that the operation mode is $TE_{8,1}$ mode with 16 azimuthal peaks and only 1 radial peak.

Correspondingly, the axial electric field distribution is also recorded on a longitudinal cut-plane, as shown in Figure 4-10. Only one peak is observed in the axial direction at the time of 48.191 ns, meaning that the axial index of the operation mode is 1. By the combination of the observations in Figure 4-8, Figure 4-9 and Figure 4-10, a single mode operation of $TE_{8,1,1}$ at the eighth harmonic is verified. It can also be seen that the electron beam is placed away from the field maximum points of the $TE_{8,1}$ mode in the radial direction. The beam-wave interaction still takes place due to the fact that the synchronism condition as shown in (1.1) is exclusively fulfilled by the $TE_{8,1}$ mode at the eighth harmonic. For other modes, such condition is not fulfilled given the above parameters and thus no oscillation is observed.

The output power of the designed LOG recorded at the output aperture is shown in Figure 4-11. It can be seen that after the starting oscillation process of $TE_{8,1,1}$ mode for about 40 ns, the output power is stabilised at 3.8 kW. The stable output power level after 40 ns

suggests a single mode operation of $TE_{8,1,1}$. The variation of the Ohmic loss power with time is almost identical with that of the output power, except that it settles at 3.697 kW.

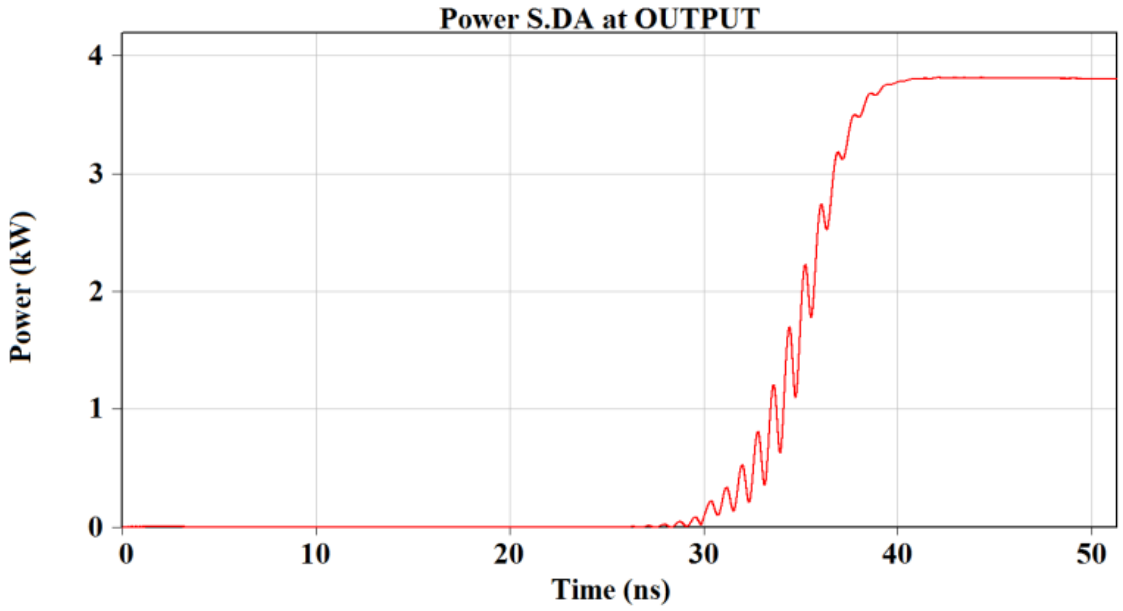

Figure 4-11: The output power variation with time of the LOG.

The above simulation results can be further verified by the agreement with the well-established fundamentals of CRM theory, as shown in Figure 4-12. Before the oscillation starts, the electron beam is evenly distributed in the azimuthal direction, as shown in Figure 4-12 (a). When the beam-wave interaction reaches the steady state at the eighth harmonic, where the wave frequency is about eight times the gyrating frequency of the electrons as governed by (7), there will be eight decelerating phase centres corresponding to eight electrons bunching centres in the azimuthal direction, as shown in Figure 4-12 (b). Such an observation is also described in the theory of conventional small orbit gyrotrons with harmonic operations [51]. It can also be interpreted that during the steady state of oscillation after 40 ns, most of the electrons are releasing energy to the RF field as the gyrating radii have decreased from the comparison between (a) and (b) in Figure 4-12.

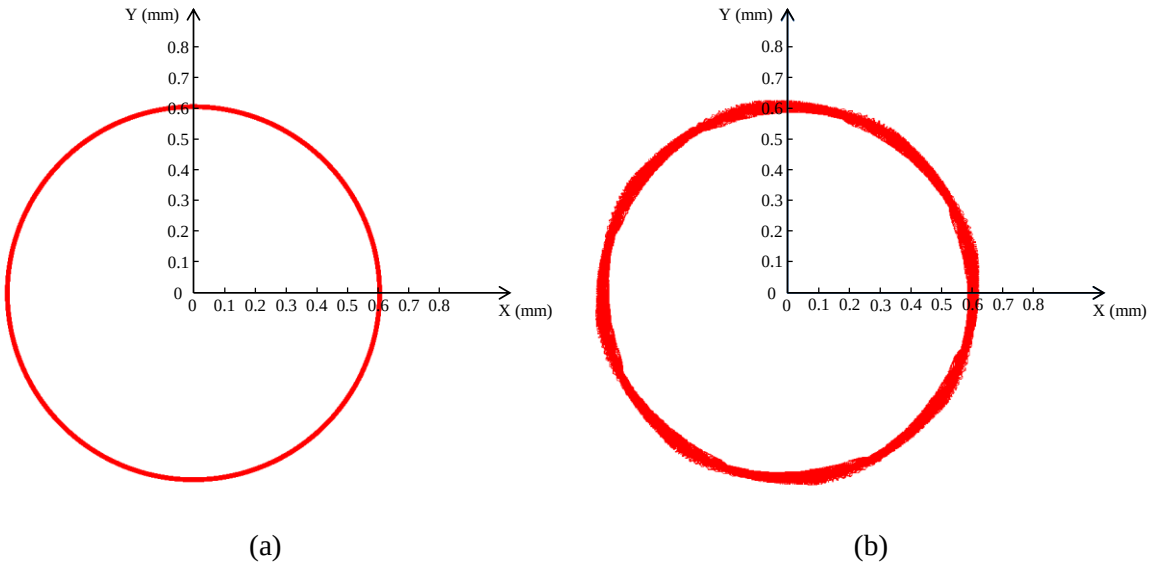

Figure 4-12: The electrons phase space in transverse direction observed at the output of the cavity: (a) At 5.715 ns before the excitation of $TE_{8,1,1}$ mode at the eighth harmonic; (b) At 48.191 ns when the oscillation of $TE_{8,1,1}$ mode is stable.

After the verification of the hot cavity model, a number of numerical parameter variation studies are conducted to characterise the operation of a LOG at very high harmonics. The influence of the external magnetic field, the electron beam parameters and the structural parameters will be examined.

The output power variation with the external magnetic field is shown in Figure 4-13. It can be seen that the external magnetic field range for the $TE_{8,1,1}$ mode is from 2.75 T to 2.77 T, which is smaller than the interval (2.74 T-2.78 T) predicted by the cold cavity analysis when the beam current is 1 A. The difference can be explained by the small signal approximations used in the cold cavity analysis [11]. Below 2.75 T, the oscillation of $TE_{8,1,1}$ fails to start and no output power is observed. Beyond 2.77 T, the operation mode becomes $TE_{7,1,1}$. It is also shown that the output power increases as the magnetic field decreases. As the external magnetic field decreases, the electron beam will become closer to the cavity wall as well as the field maxima of $TE_{8,1,1}$ mode (see Figure 4-10), which in turn enables more efficient energy exchange. The accurate control of the external magnetic field strength can be achieved by adopting auxiliary solenoids, in addition to the main solenoid of the superconducting magnet [145, 146].

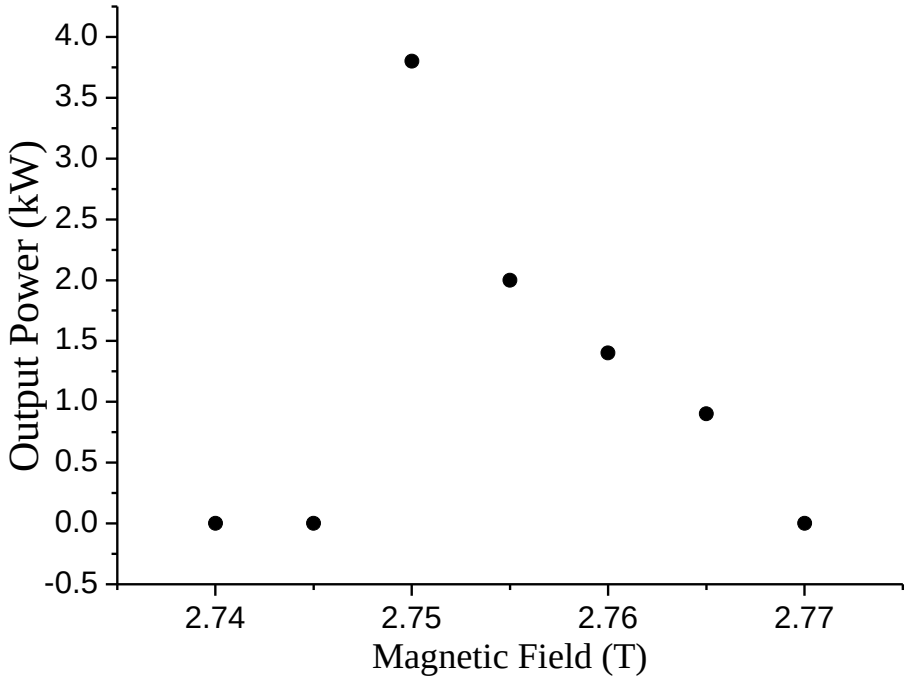

Figure 4-13: The output power variation with the external magnetic field ($I = 1\ A, \alpha = 2$).

The output power and output efficiency variation with the electron beam current from 1 A to 5 A is shown in Figure 4-14. As the beam current increases, the output power will increase as well. However, the output efficiency which is defined as the output power divided by the electron beam power, firstly rises with the increase of the beam current and then falls down. The maximum conversion efficiency is about 1.87 % at 3.5 A, where the beam-wave interaction saturates. Additional simulations have shown that no oscillation occurs at the beam current of 0.8 A or 0.9 A, which are lower than the starting oscillation current of $TE_{8,1,1}$ when the external magnetic field is 2.75 T.

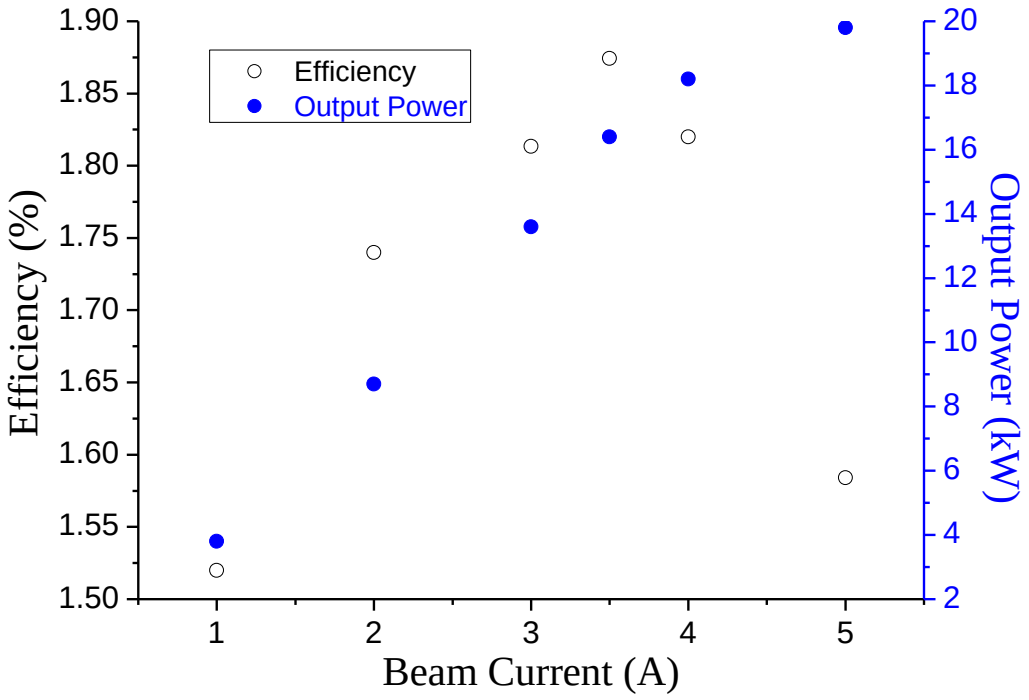

Figure 4-14: The output power and efficiency variation with the beam current ($B_0 = 2.75\ T, \alpha = 2$).

Figure 4-15 indicates the strong dependence of the output power on the transverse-axial velocity ratio α. As the value of α increases from 1.95 to 2.25, the output power increases from 2.21 kW to 9.04 kW. When α is chosen to be 2.3 or higher values, the competition from the $TE_{9,1,1}$ mode at the ninth harmonic and $TE_{7,1,1}$ mode at the seventh harmonic shows up. This is because when increasing the value of α from 2.3, the synchronism condition between the $TE_{8,1,1}$ mode at the eighth harmonic and the electron beam does not hold. When α=2.3, the final stable operation mode is found to be $TE_{7,1,1}$ at the seventh harmonic. The simulations have shown no signs of starting oscillation when α equals 1.9 or 1.8. This is because when α decreases, the transverse velocity of the electron beam will become smaller which in turn leads to higher starting oscillation current of $TE_{8,1,1}$ mode according to (4.1).

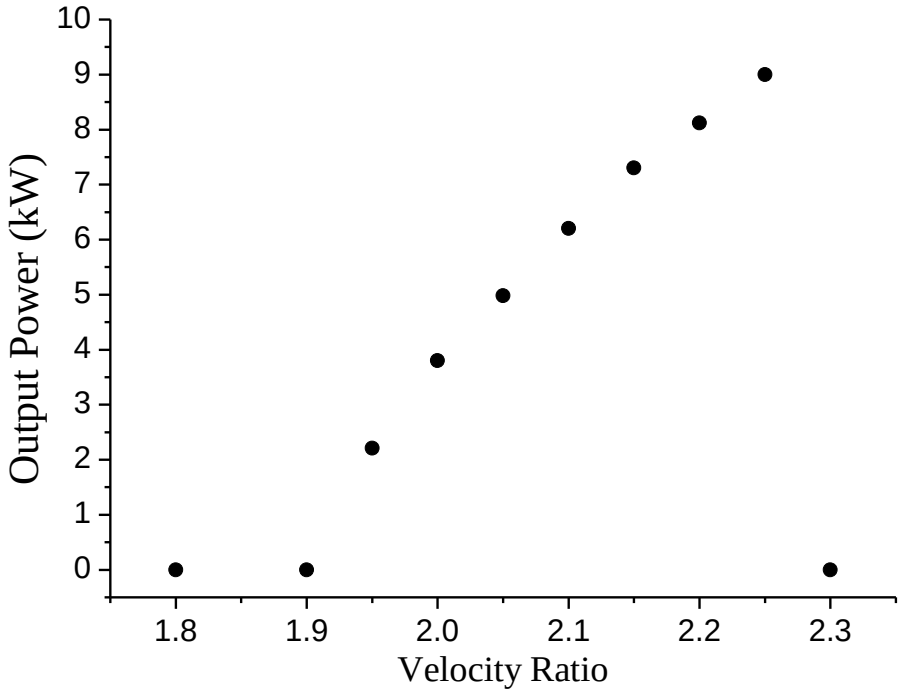

Figure 4-15: The output power variation with the transverse-axial velocity ratio ($\mathbf{I = 1\ A, B_0 = 2.75\ T}$).

In the LOG where the $TE_{m,1}$ modes are used, the Ohmic loss is significant because the field maxima is very close to the cavity wall. The total power (P) extracted from the electron beam will not only be coupled out of the cavity as output power (P_d), but also be dissipated as Ohmic loss power (P_Ω) on the cavity wall, meaning

$$P = P_d + P_\Omega. \tag{4.9}$$

There are three key parameters that essentially affect the total power, output power and Ohmic loss power, namely the beam-wave interaction cavity length L, the input taper angle θ_1 and the output taper angle θ_2. These parameters also have considerable impact on the oscillation frequency. The influence of these parameters on the beam-wave interaction behaviour should be discussed.

Figure 4-16 shows the variation of the total power, output power, Ohmic loss power and oscillation frequency with the cavity length. The total power represents the sum of the output and Ohmic loss power. The investigation of the cavity length L begins from 8 mm since the numerical simulation at $L = 7.5\ mm$ has shown no oscillation of $TE_{8,1,1}$ by requiring a starting oscillation current beyond 1 A. It can be seen that the output power,

the Ohmic loss power and the total power increase from $L = 8.0\,mm$ to $L = 10.5\,mm$. Since the beam current in this study is just slightly higher than the starting oscillation current of $TE_{8,1,1}$, and the beam-wave coupling coefficient is low [15, 19, 31], the beam-wave interaction will be more efficient by providing longer cavity within certain range. Within the range between 8.0 to 10.5 mm, the longer cavity will enable better energy exchange and hence higher total power. The lengthening of the cavity will enhance the energy storage capability as well as enlarge the inner surface area of the cavity, which in turn will cause the increase of the Ohmic loss power. Since the total power rises faster than the Ohmic loss power, the output power also goes up with increasing L.

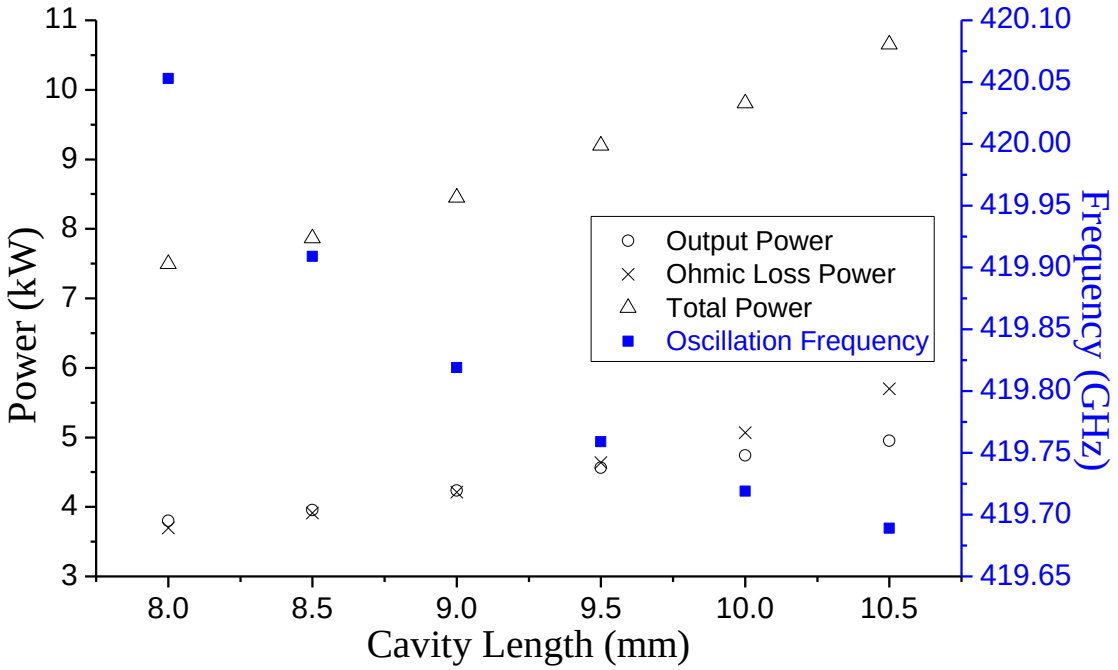

Figure 4-16: The variation of the output power, Ohmic loss power, total power and oscillation frequency with the cavity length ($\mathbf{I = 1\ A, B_0 = 2.75\ T, \alpha = 2, \theta_1 = 4.5^{\circ}, \theta_2 = 5.6^{\circ}}$).

Figure 4-16 also shows that as the cavity length increases, the Ohmic loss power, although being less than the output power at $L = 8.0\,mm$, eventually exceeds the later with increasing L. At $L = 9.25\,mm$, the two have approximately the same value. Considering the fact that the Ohmic loss power at $L = 10.5\,mm$ has already exceeded the output power, the adoption of even longer cavity, while being promising to provide higher output power, will cause even higher Ohmic loss. As L increases from 8 mm to 10.5 mm, the oscillation frequency drops from 420.053 GHz to 419.689 GHz.

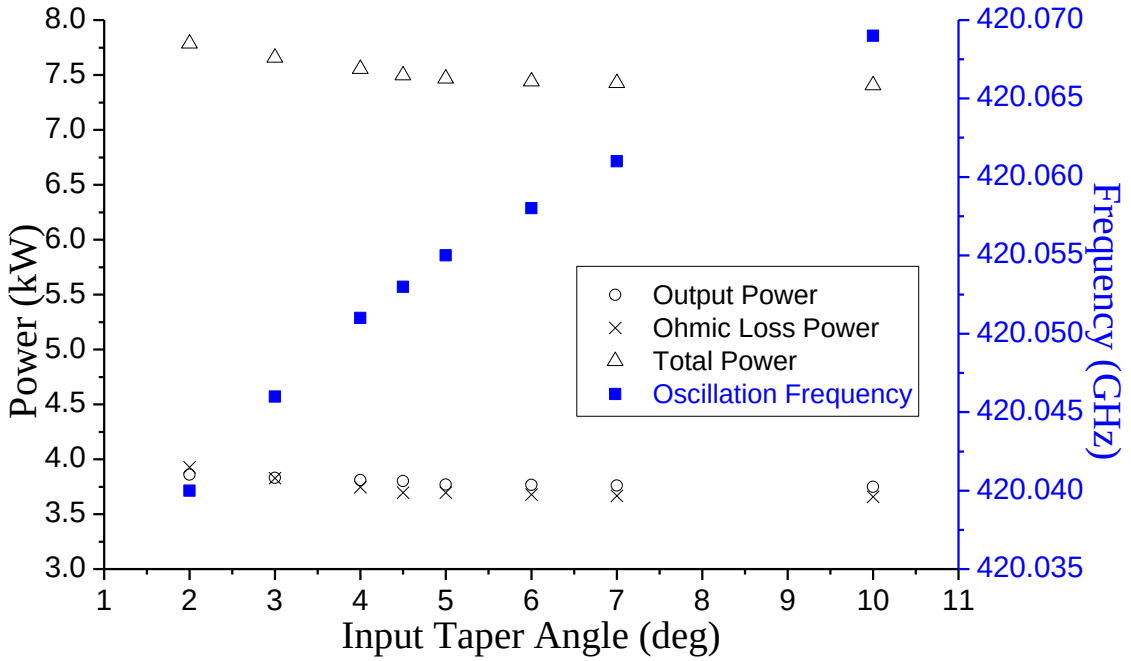

Figure 4-17: The variation of the output power, Ohmic loss power, total power and oscillation frequency with the input taper angle ($I = 1$ A, $B_0 = 2.75$ T, $\alpha = 2$, $L = 8$ mm, $\theta_2 = 5.6^{\circ}$).

To investigate the influence of the taper angles on the beam-wave interaction behaviour, all the structural parameters are kept constant except that L_1 and L_2 in Figure 4-3 are changed according to different values of the input and output taper angles, respectively. Figure 4-17 shows the influence of the input taper angle θ_1 on the beam-wave interaction behaviour. As θ_1 becomes larger, the total power, the output power and the Ohmic loss power go down gradually. Such trend can be interpreted by the influence of θ_1 on the diffraction quality factor Q_d. It is known from the cold cavity analysis that the value of Q_d drops with increasing θ_1 [38, 39]. Assuming that the Ohmic quality factor Q_Ω is constant as from (4), the total quality factor Q of the cavity will hence be reduced according to (5). As the beam current used in these studies is only slightly over the threshold starting current and the beam-wave coupling coefficient is low at the eighth harmonic, the drop of Q leads to lower beam-wave interaction efficiency [29-31,40] and hence lower total power. With the reduction of the beam-wave interaction efficiency, the field amplitude inside the cavity will become smaller, meaning the Ohmic loss power will also be reduced. Since the total power drops faster than the Ohmic loss power, the output power is also decreasing by examining (8). The oscillation frequency of $TE_{8,1,1}$ mode

goes up slightly from 420.040 GHz to 420.069 GHz when the input taper increases from 2 °to 10 °.

Figure 4-18 shows the influence of the output taper angle θ_2 on the beam-wave interaction performance. As θ_2 decreases, the total power, the output power and the Ohmic loss power drops. Since the decrease of θ_2 brings the reduction of Q_d, the drops of the total power, the output power and the Ohmic power can be explained in the same manner as shown in the previous case of increasing θ_1. The oscillation frequency of $TE_{8,1,1}$ mode increases slightly from 420.043 GHz to 420.057 GHz when the output taper angle varies from 3 °to 8 °.

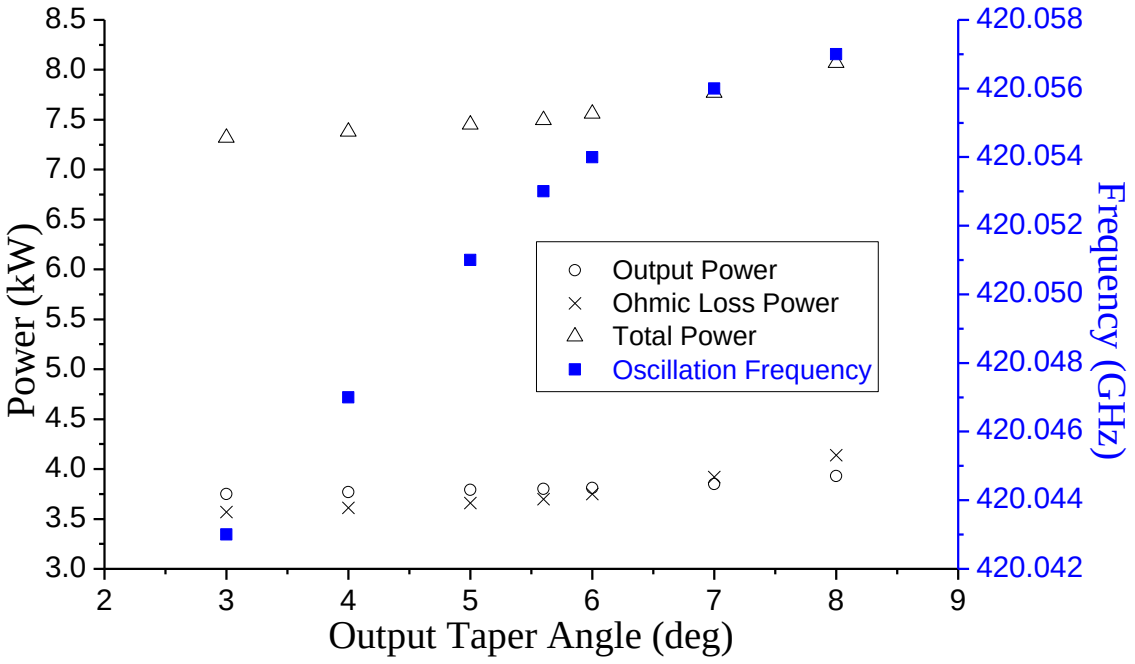

Figure 4-18: The variation of the output power, Ohmic loss power, total power and oscillation frequency with the output taper angle ($I = 1$ A, $B_0 = 2.75$ T, $\alpha = 2$, $L = 8$ mm, $\theta_1 = 4.5^{\circ}$).

While the decrease of θ_1 and the rise of θ_2 bear the potential to increase the total quality factor and hence the output power, even greater rise of the Ohmic loss power is observed at the same time. This is because as Q_d increases, the ratio between Q_d and Q_Ω will also go up, meaning the proportion of the total power that is converted to the Ohmic loss power will become larger. In THz LOG, it seems that the Ohmic loss has become a key constraint in obtaining high output power. On one hand, to access the high efficiency operation point when the beam-wave coupling coefficient is low, Q should be increased.

On the other hand, the increase of Q can only be achieved by raising the value of Q_d, which will then bring relatively larger Ohmic loss power compared to the output power.

Last but not the least, it is worth mentioning that for higher and higher harmonics operation, the mode spectrum becomes more and more crowded, as illustrated in Figure 4-1 and Figure 4-5. Under such situation, the velocity spread of the electron beam will have significant impact on the beam-wave interaction behaviour at high harmonics. In order to study the effect of the velocity spread in the PIC model, the beam current is increased from 1 A to 3 A to make sure that the starting oscillation condition of $TE_{8,1,1}$ mode is fulfilled even at high velocity spread values. In this study, one of the conventional models for considering the velocity spread is used, which approximates the transverse velocity distribution of the electrons with a Gaussian profile [41, 42].

Figure 4-19 shows the output power variation with time for different values of transverse velocity spread. It can be seen that as the transverse velocity spread goes up from 0 to 14.0%, it takes more time for the $TE_{8,1,1}$ to reach the steady oscillation state, the output power of which drops from 13.6 kW to 3.5 kW without the presence of competition modes. When the velocity spread is 16.0%, the electrons with the largest gyrating radius start to bombard on the drifting cavity wall. The above design is robust regarding the problem of mode competition with the presence of electron velocity spread from 0 to 14.0%.

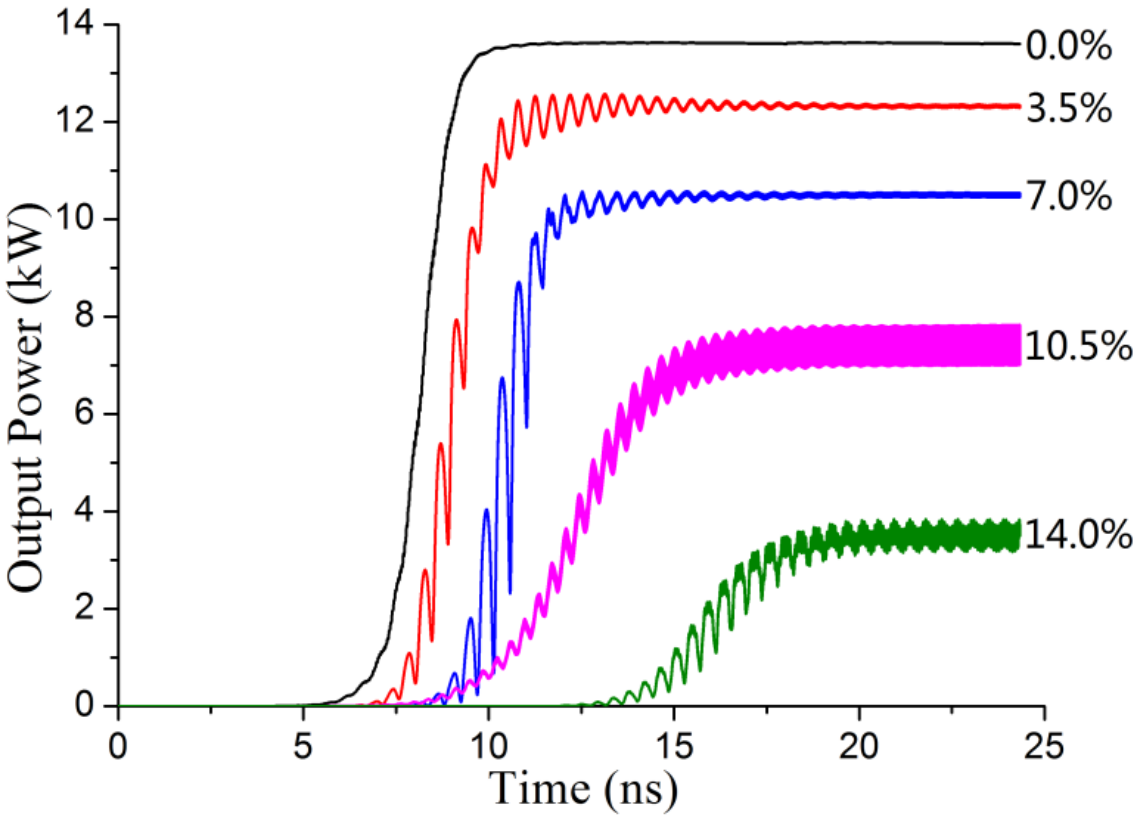

Figure 4-19: The variation of the output power with the velocity spread ($I = 3$ A, $B_0 = 2.75$ T, $\alpha = 2$, $L = 8$ mm, $\theta_1 = 4.5^\circ$, $\theta_2 = 5.6^\circ$). The numbers on the right-hand side of the curves indicate the corresponding values of velocity spread.

4.4 Multi-modes, Multi-harmonics Behaviour

It can be seen from Figure 4-5 that the neighbouring modes of the $TE_{8,1,1}$ mode are $TE_{7,1,1}$ and $TE_{9,1,1}$. The operation magnetic field range of the modes, while overlapping with each other, decreases as the harmonic number increases. Under this circumstance, the operation of $TE_{8,1,1}$ mode is influenced by both $TE_{7,1,1}$ and $TE_{9,1,1}$ modes, especially at the boundary of $TE_{8,1,1}$ mode's operation magnetic field range. The interference among these modes also represents the competition among the corresponding harmonics. Thus the multi-modes, multi-harmonics behaviour from the seventh to the ninth harmonic should be investigated to throw light on the mode competition dynamics as well as find the single mode operation regime.

Figure 4-20 shows the output power variation with time when $B_0 = 2.73$ T and $I = 3$ A, which indicates the existence of mode competition.

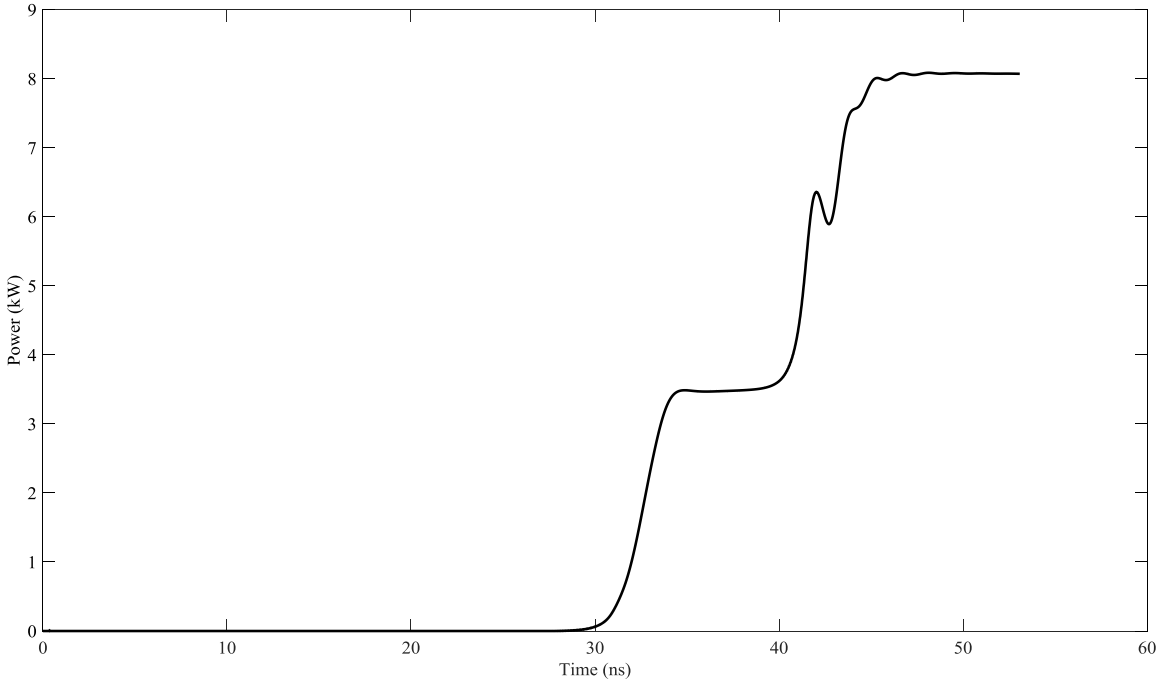

Figure 4-20: The output power variation with time when $B_0 = 2.73$ T, I = 3 A.

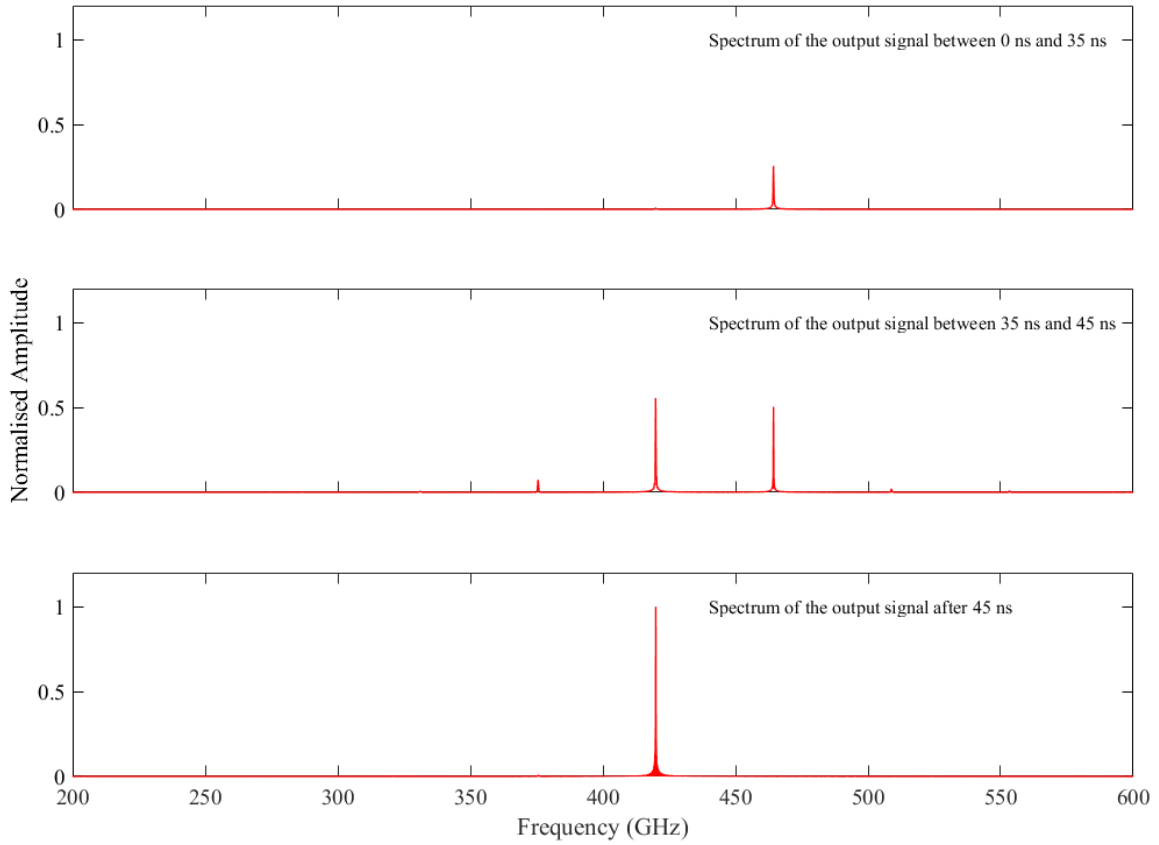

Figure 4-21: The spectrum of the output signal at different time slots for $B_0 = 2.73$ T, I = 3 A.

To identify the modes involved in the competition, the output signal within different instants of time are recorded and transformed into the frequency domain, as shown in Figure 4-21. The amplitude of the signals are normalised to the peak value at 419.93 GHz. It can be seen that before 35 ns, the spectrum of the output signal is pure with only one peak at 464.33 GHz. Such spectrum and the corresponding field distribution indicates single mode operation of the $TE_{9,1,1}$. Between 35 ns and 45 ns, the $TE_{8,1,1}$ mode at the eighth harmonic oscillates up and the $TE_{9,1,1}$ mode is gradually suppressed. After 45 ns, the output spectrum becomes pure again with single peak at 419.93 GHz. The spectrum and the corresponding field distribution indicate stable single mode operation of the $TE_{8,1,1}$ at the eighth harmonic. The stable output power is 8.1 kW.

A similar scenario of competition between $TE_{8,1,1}$ mode and $TE_{7,1,1}$ mode can also be observed. Figure 4-22 shows the output power variation with time when $B_0 = 2.78$ T and $I = 3$ A.

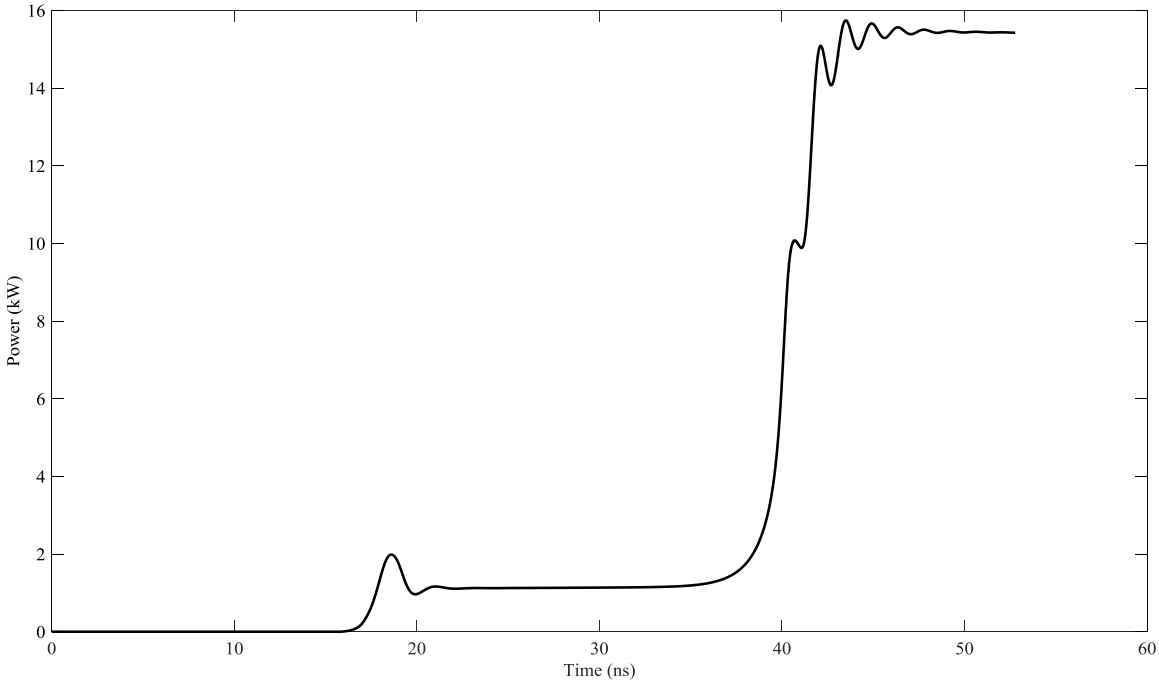

Figure 4-22: The output power variation with time when $B_0 = 2.78$ T, I = 3 A.

The output signal within different instants of time are recorded and transformed into the frequency domain, as shown in Figure 4-23. The amplitude of the signals are normalised to the peak value at 372.32 GHz. It can be seen that before 35 ns, the spectrum of the

output signal is pure with only one peak at 420.21 GHz. Such spectrum and the corresponding field distribution indicates single mode operation of the $TE_{8,1,1}$. Between 35 ns and 45 ns, the $TE_{7,1,1}$ mode oscillates up and the $TE_{8,1,1}$ mode at the eighth harmonic is gradually suppressed. After 45 ns, the output spectrum becomes pure again with single peak at 372.32 GHz. The spectrum and the corresponding field distribution indicate stable single mode operation of the $TE_{7,1,1}$ at the seventh harmonic. The stable output power is 15.4 kW.

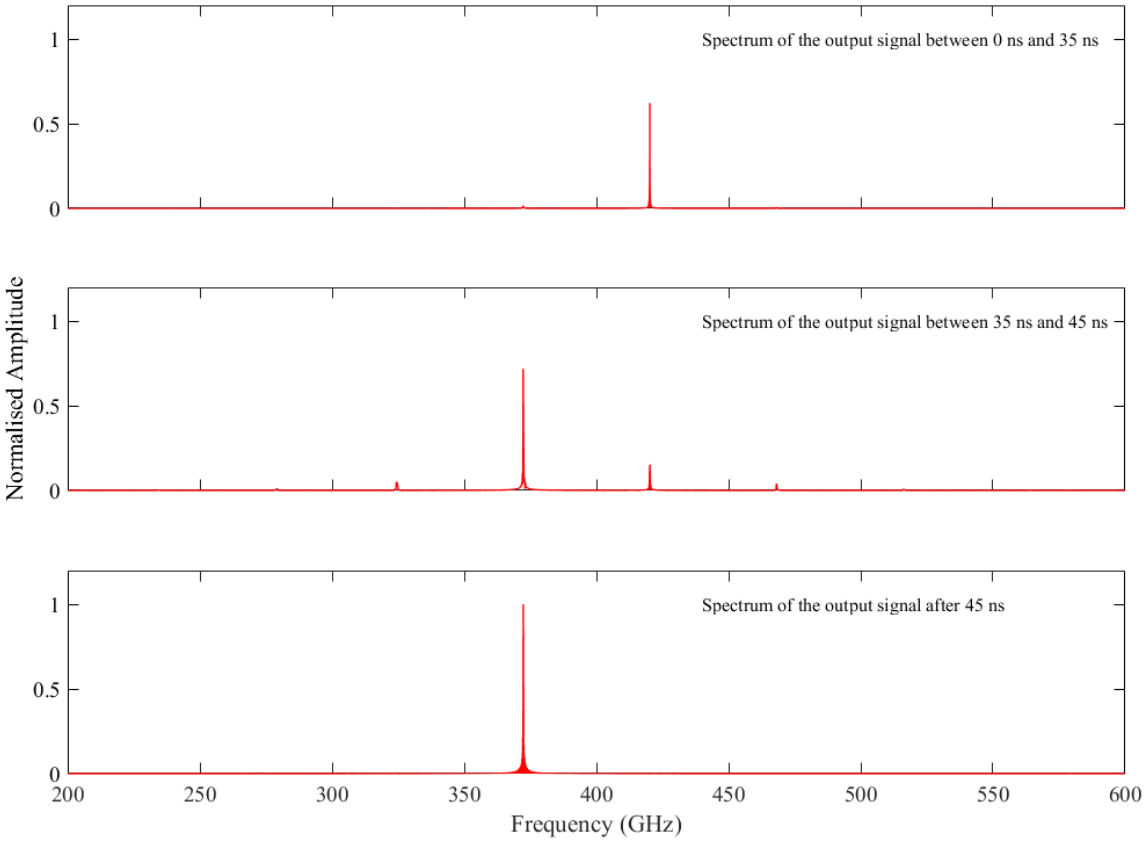

Figure 4-23: The spectrum of the output signal at different time slots for $B_0 = 2.78$ T, I = 3 A.

From the above analysis, it can be seen that it is feasible to operate the LOG at very high harmonics. However, special attention should be paid to the competition of the neighbouring modes at different harmonics. For $TE_{8,1,1}$, the single mode operation magnetic field range is from 2.75 T to 2.77 T when the beam current is chosen as 3 A. In the external magnetic field range between 2.78 T and 2.80 T, its operation tends to be replaced by the $TE_{7,1,1}$ mode at the seventh harmonic. In the range between 2.73 T and 2.74 T, its stable oscillation builds up after the competition with the $TE_{9,1,1}$ mode. The

mode competition scenario at lower harmonics (from the fourth to the sixth harmonic) can be studied in the same manner.

Chapter Summary

In this chapter, a high-harmonic large-orbit gyrotron is studied in detail. The designed LOG is capable of operation from the fourth to the ninth harmonic. By varying the external magnetic field strength and proper choice of the electron beam current, selective excitation of the $TE_{m,1,1}$ modes can be achieved. The designed LOG can generate kW-level output power at a number of discrete frequency points within the range from 230 GHz at the fourth harmonic to 465 GHz at the ninth harmonic. The high-harmonic operation of the device can significantly reduce the required external magnetic field. The multi-modes, multi-harmonics behaviour of the device is also characterised to determine the single-mode operation regime of the device.

Chapter 5 Output System Design for the Gyro-multiplier

In this chapter, the design of the output system for the fourth-harmonic gyro-multiplier is described. It begins with the examination of two possible configurations of the system, namely the Separation-Conversion scheme and the Conversion-Separation scheme. And the reason for choosing the latter is discussed. Then, the dual-harmonic quasi-optical mode converter (DQMC) is studied for the simultaneous conversion of the two high-order waveguide modes into quasi-Gaussian beams. Following that, a single disc window (SDW) is designed, which will be used to keep the vacuum seal and transmit both quasi-Gaussian beams with low insertion loss. For the separation of the two frequencies, a high-pass FSS is designed which is transparent at 1368 GHz while opaque at 342 GHz. The design and sensitivity test of the designed FSS are carried out with consideration of electric breakdown.

5.1 Methodology

There are basically two configurations that can be used in designing the output system of the gyro-multiplier. On the one hand, it seems applicable to put a FSS directly at the output end of the gyro-multiplier, which can separate the output $TE_{4,9}$ mode at 1368 GHz from the $TE_{1,3}$ mode at 342 GHz, before a quasi-optical system is applied to convert the former into a quasi-Gaussian beam. Such configuration can be called the Separation-Conversion scheme. On the other hand, the quasi-optical mode conversion of the two modes can be applied first and followed by the FSS to separate the two frequencies, which can be called the Conversion-Separation scheme.

5.1.1 Scheme One: Separation-Conversion

The Separation-Conversion scheme can be illustrated in Figure 5-1. To apply the FSS at the output end of the truncated waveguide of the gyro-multiplier, the electrons needs to

be collected before the generated wave is radiated. Such configuration is found to be problematic because the gyro-multiplier operates with high-order cylindrical waveguide modes exhibiting complicated field distribution and polarisation. As a periodic structure, the performance of the FSS can only be ideal and predictable when the incident wave is a plane wave or Gaussian beam. When the incident wave of the FSS is consisted of high-order waveguide modes, the performance of the FSS will be degraded or even malfunctioned.

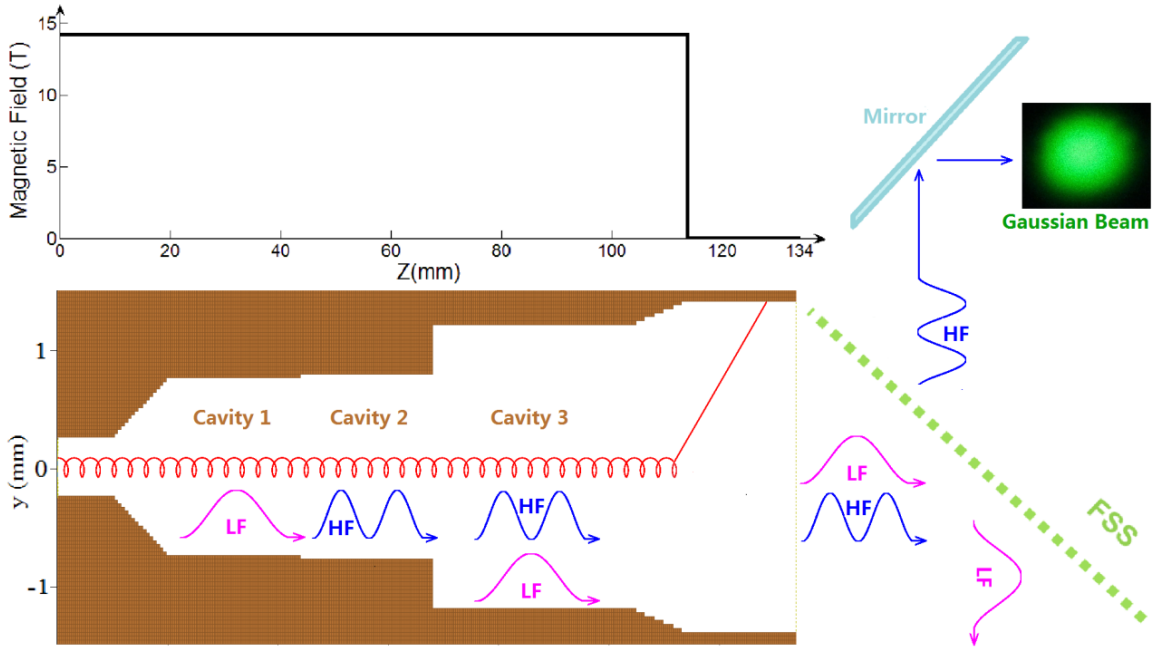

Figure 5-1: The transverse view of the Separation-Conversion scheme.

To study the performance of a FSS with the direct radiation from a truncated waveguide, a model is built in CST Microwave Studio. In the numerical simulation, when the generated $TE_{1,3}$ and $TE_{4,9}$ modes are coupled out directly from the truncated waveguide with a circular aperture, most of the radiated power will spread into a relatively broad circularly symmetric hollow cone with a rather complex polarisation and poor directivity, as shown in Figure 5-2 for the case of $TE_{4,9}$ mode excitation. A high-pass FSS which is designed to be transparent at 1368 GHz is placed in front of the output aperture.

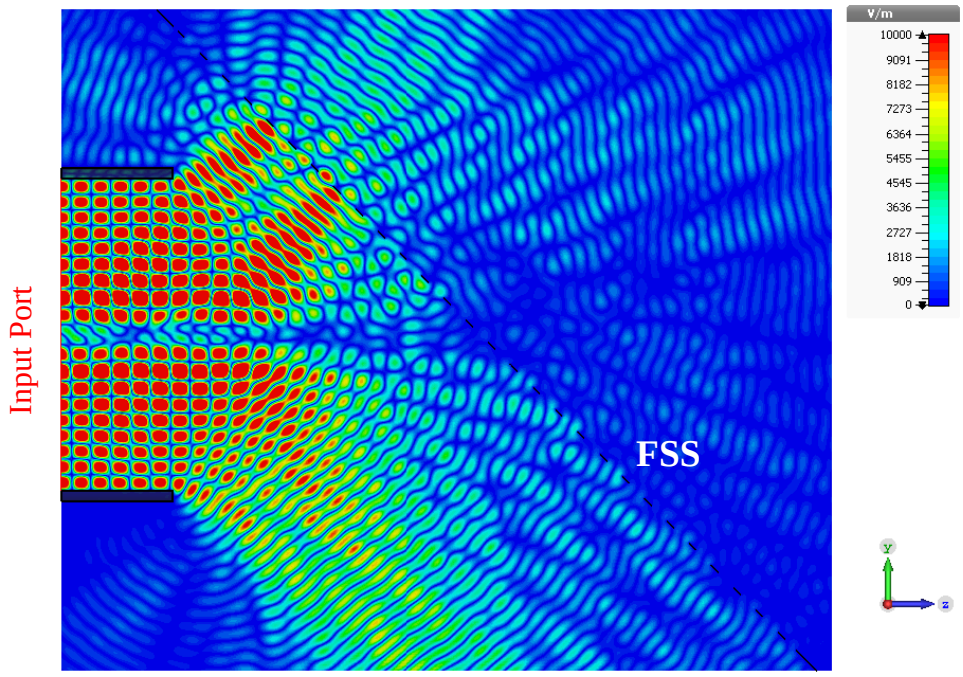

Figure 5-2: Propagation of the wave radiated directly from a waveguide aperture and its interaction with the designed FSS.

In this case, the adoption of a FSS at the output end of the cavity is facing several difficulties：

After leaving the output aperture of the gyro-multiplier cavity, the radiated field instantly spread into space with different propagation directions at different locations. If a FSS is place directly in front of the spreading wave at the output aperture, as shown in Figure 5-2, the angle of incident wave will be different at different locations on the FSS. The incident angle of the wave might be any value from 0 degree to near 90 degree. For large angle of incident, the operating of FSS will be greatly degraded, meaning the two frequencies cannot be separated effectively. As a matter of fact, the insertion loss of the FSS in this case is more than 10 dB at 1368 GHz, which does not satisfy the design requirement.

And to minimise the reflection of the wave, the FSS has to be placed at certain distance from the output aperture of the waveguide. This means the radiated wave will have to propagate for a certain distance before being separated by the FSS. However, the high-

order waveguide modes are unsuitable for power transmission in free space because of the strong transmission and diffraction loss.

Based on the above analysis, the FSS is unsuitable for operating with the high-order waveguide modes directly. To design a proper gyro-multiplier output system, the high-order modes should be converted into quasi-Gaussian beams before being illuminated on the FSS.

5.1.2 Scheme Two: Conversion-Separation

The Conversion-Separation scheme is shown in Figure 5-3, in which a dual-harmonic quasi-optical mode converter (DQMC) and a FSS are employed. As the magnetic confined electrons passes through the beam-wave interaction cavity, both the high-order modes as specified in Table 1-1 can be generated. The spent electrons are then collected by the collector. A DQMC consisting of a launcher and two subsequent mirrors is connected to the output end of the gyro-multiplier beam-wave interaction cavity directly. The launcher is used to radiate the high-order waveguide modes into free space with designed directivity. And the subsequent mirrors are adopted to adjust the phase and amplitude distribution of the radiated wave beams to form two quasi-Gaussian beams at certain distance away from the DQMC. The red lines represent the path of the converted wave beams. Apart from enabling the effective operation of the subsequent FSS, the adoption of the DQMC makes the output system of the gyro-multiplier more compact, which is a favourable choice to reduce the transmission and Ohmic loss in the THz frequency range.

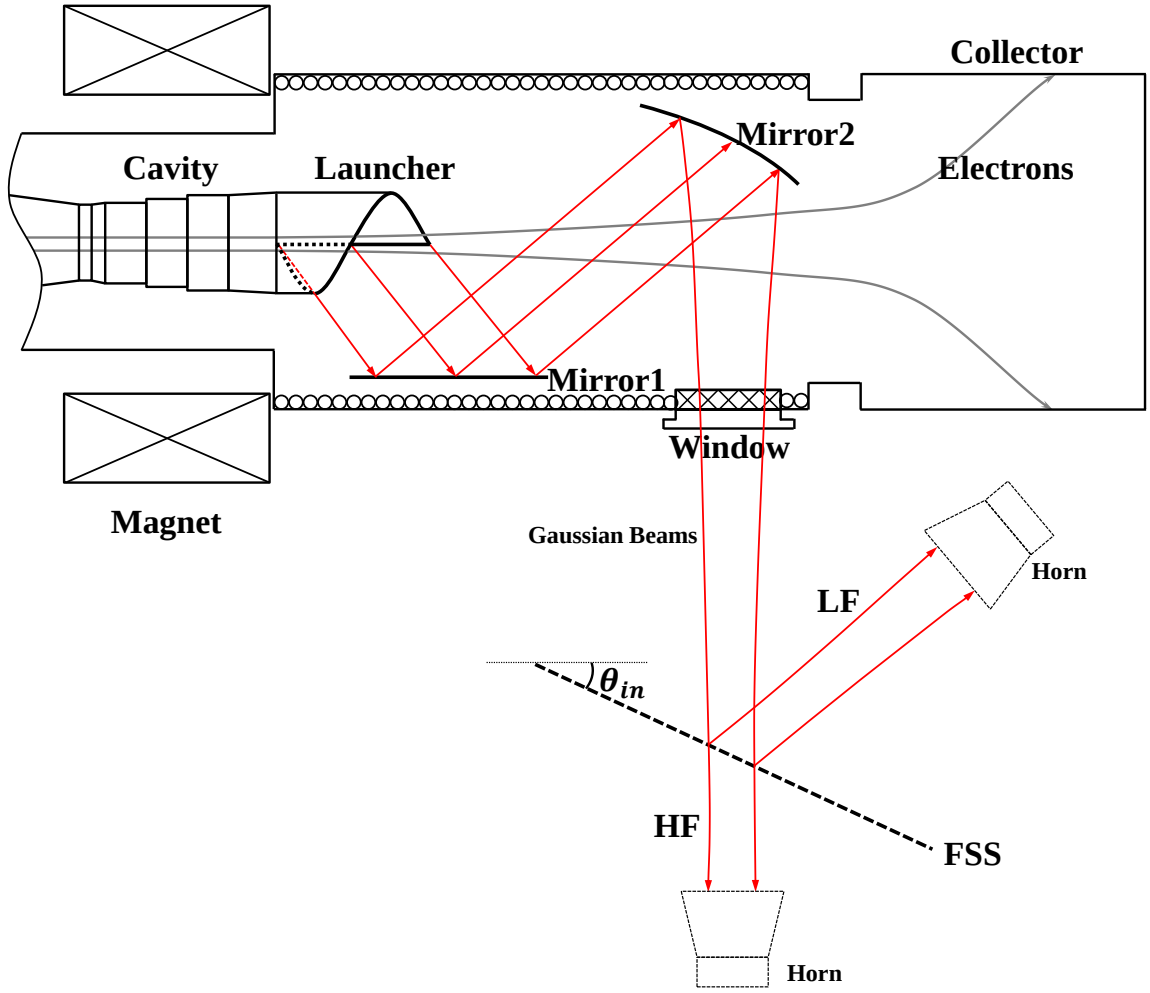

Figure 5-3: Transverse view of the Conversion-Separation scheme with transverse output.

At the waists of the converted quasi-Gaussian beams, a FSS can be applied to separate the two frequencies. To avoid reflecting the wave back into the beam-wave interaction system, the FSS is designed for oblique incidence with an incident angle of θ_{in}. In Figure 5-3, a high-pass FSS is shown where the low frequency content is reflected while the high frequency counterpart is transmitted. After the separation, the two beams can be received by two horns, separately.

5.2 Quasi-optical Mode Converter Development

The quasi-optical mode converter (QMC) has been demonstrated successfully in the gyrotrons to transform the high-order waveguide modes into quasi-Gaussian beams. A QMC is usually composed of a launcher to directionally radiate the high-order waveguide

modes into free space and several subsequent reflectors to adjust the amplitude and phase of the radiated wave beams to form quasi-Gaussian field distributions. A launcher is basically an asymmetrically cut waveguide that is capable of radiating the high-order waveguide mode with chosen directivity and polarisation. The original Vlasov launcher with the standard mirrors was proposed and demonstrated in 1975 [76, 95]. To improve the radiation efficiency of the output system, several improved versions of the Vlasov launcher have been proposed and reported in the literature [94, 97, 98, 147-151]. The standard mirrors are also in some applications replaced by the irregular phase-correcting mirrors to improve the beam forming property [90, 103, 152].

Although the improved versions of the Vlasov-type launcher and the phase-correcting mirrors are proved to be more efficient, additional complexity in the design, fabrication and alignment will be considerable when operating at 342 and 1368 GHz. For example, the estimated fabrication precision required by a Denisov launcher at 1368 GHz will be as high as 1 micron [153]. As the first effort to develop an output system for the gyro-multiplier in the THz frequency range, the consideration of simplicity in design and fabrication outweighs that of the efficiency. Thus the original Vlasov launcher and the standard mirrors are chosen in the designed DQMC for the proof-of-principle study.

In this section, the geometric optics (GO) for the high-order waveguide modes propagation as well as the synthesis of the Vlasov launcher and the subsequent mirrors will be described in detail. The geometric optics will be used as a preliminary tool of designing the DQMC for the output modes of the gyro-multiplier. To verify and optimise the design, a 3-D full electromagnetic simulation with Feko 7.0 [154] is conducted. The efficiency of power transmission and the Gaussian content of the converted beam at the output window area will also be extracted from the results of the simulation.

5.2.1 Design and Simulation of the Vlasov Launcher

The design of a qualified DQMC requires that, not only the angles of radiation for the two modes when leaving the launcher should be close enough, to make sure that the subsequent mirrors operate properly for both, but also the Vlasov launcher should launch

both modes effectively. It will be shown in the following that, although these two modes are different in the field pattern and distantly separated in the spectrum, the above requirements can be fulfilled.

On the one hand, the difference between the angles of radiation for the two modes, can be defined as

$$\Delta\theta_B = \frac{|\theta_{BLF} - \theta_{BHF}|}{\theta_{BHF}} \times 100\% \tag{5.1}$$

in which θ_{BLF} and θ_{BHF} are the Brillouin angles for the $TE_{1,3}$ mode at 342 GHz and $TE_{4,9}$ mode at 1368 GHz, respectively. It can be seen from (2.29) that, given the operation modes and the corresponding frequencies, $\Delta\theta_B$ varies smoothly with R. By the combination of (2.29) and (5.1), the variation of $\Delta\theta_B$ with R is shown in Figure 5-4.

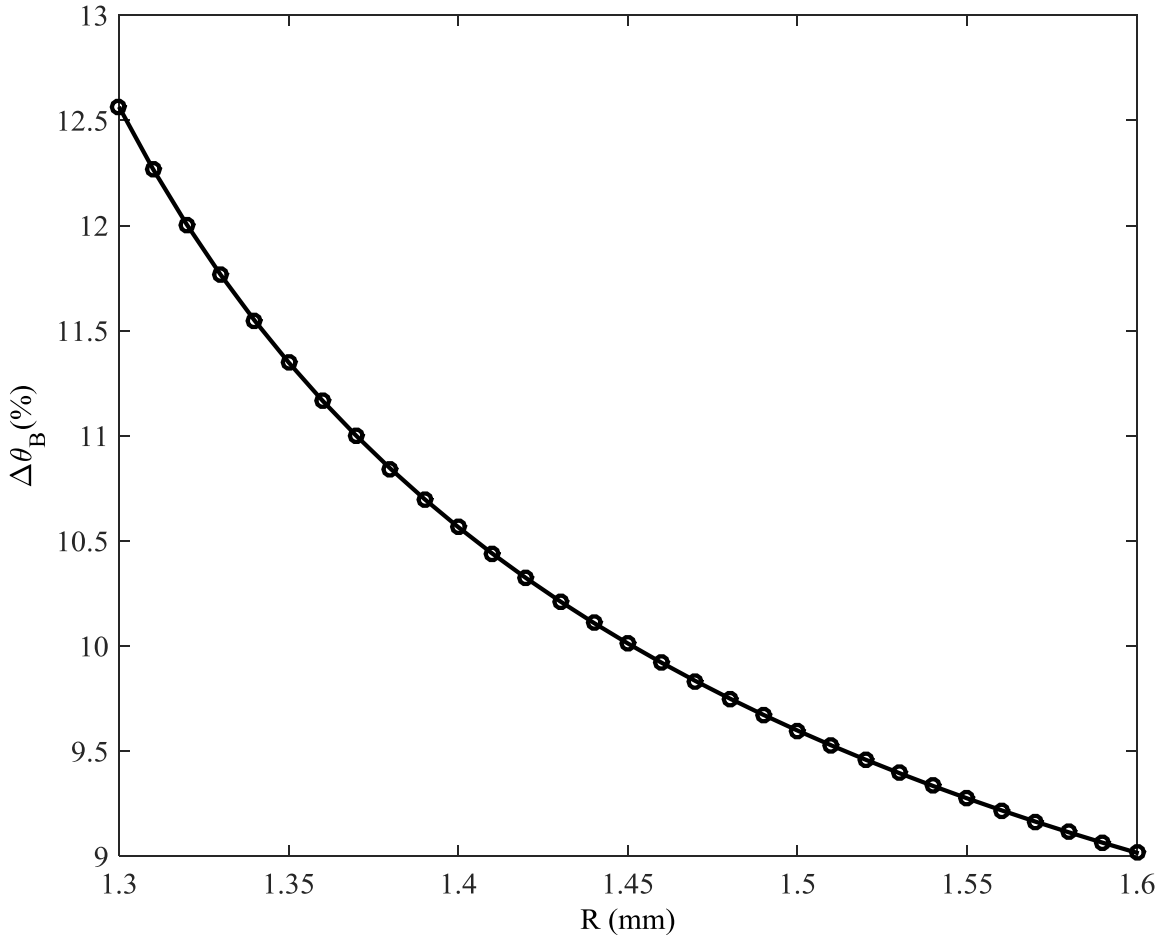

Figure 5-4: Variation of $\Delta\theta_B$ with the radius of the Vlasov launcher.

Figure 5-4 has shown that $\Delta\theta_B$, while being relatively small, decreases with the increase of R. Thus the choice of the waveguide radius of the Vlasov launcher is based on trade-off. In order to maintain a relatively small value of $\Delta\theta_B$, the value of R should be as large as possible. While the upper limit of the value of R is restricted by the design of the beam-wave interaction cavity of the gyro-multiplier and the concern of unwanted mode transformation. Considering these factors, the radius of the waveguide at the input end of the Vlasov launcher is designed as 1.4 mm, at which θ_{BLF} and θ_{BHF} are determined by (2.29) as $58.3°$and $52.8°$, respectively .

On the other hand, the helical cut of the Vlasov launcher should cover the Brillouin regions of both modes. For $TE_{1,3}$ mode, the Brillouin region can be explicitly defined by the axial length L_{LF}, the azimuthal length L_{aLF} and the inclination angle Φ_{LF}. And the Brillouin region for $TE_{4,9}$ mode is determined by the axial length L_{HF}, the azimuthal length L_{aHF} and the inclination angle Φ_{HF}. These values as listed in Table 5-1, are determined by (2.34), (2.35) and (2.37).

Table 5-1: The dimensional parameters of the Brillouin regions of the two modes at different frequencies.

L_{LF}	L_{HF}	L_{aLF}	L_{aHF}	Φ_{LF}	Φ_{HF}
3.70 mm	4.59 mm	4.07 mm	4.05 mm	67.2°	62.5°

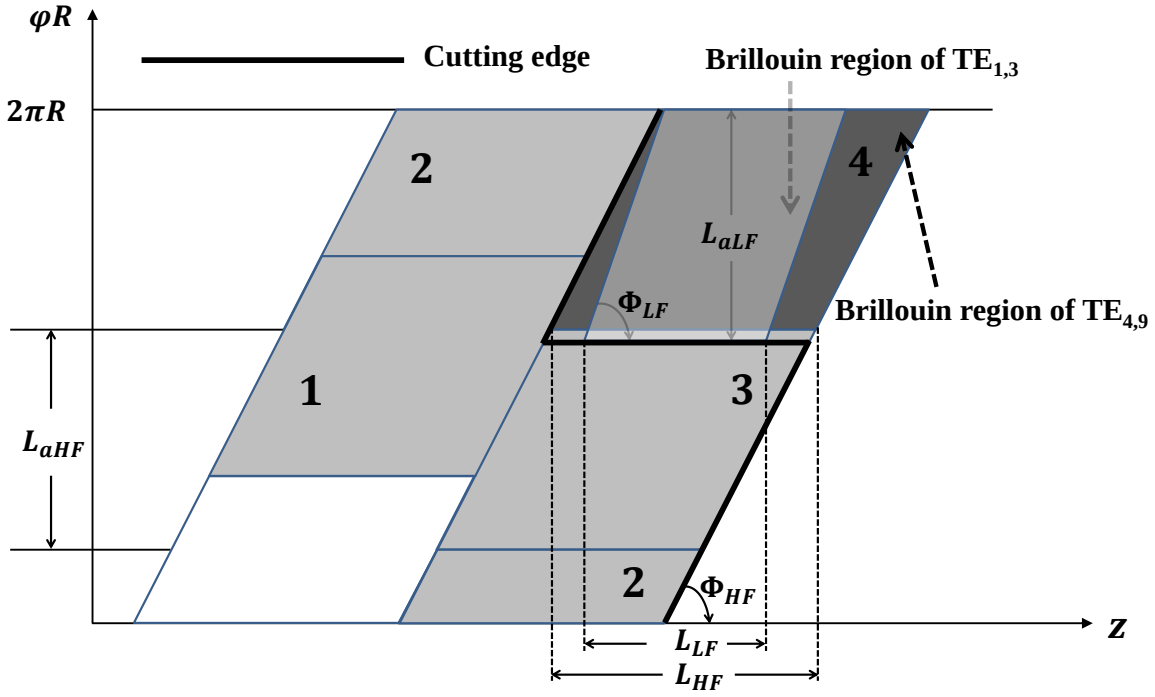

Figure 5-5: The unfolded view of the modified Vlasov launcher. The helical cut of the launcher embraces the Brillouin regions of the two modes, such that the launcher can radiate the two modes effectively.

The Brillouin regions of the two modes are then shown in Figure 5-5. It can be seen that, the axial length of the Brillouin region for $TE_{1,3}$ mode is shorter than that for the $TE_{4,9}$ mode, while the azimuthal length of the former is longer than that of the latter. To enclose both Brillouin regions, the traditional helical cut of the Vlasov launcher should be modified accordingly. That is, the azimuthal and the axial lengths should be chosen as L_{aLF} and L_{HF}, respectively. And the new cut is show as the bolded line in Figure 5-5. In such way, the launcher will be capable of launching the two modes effectively. Thus the length of the helical cut of the modified Vlasov launcher is 4.59 mm in the axial direction and 4.07 mm in the azimuthal direction, which will be sufficient for the directional radiation of both modes into free space. Given the lengths and the radius, the simulation model of the modified Vlasov launcher in Feko 7.0 is determined and shown in Figure 5-6.

The above model is then excited by $TE_{1,3}$ mode at 342 GHz with power of 2 kW and $TE_{4,9}$ mode at 1368 GHz with power of 120 W, respectively. The field distribution of the $TE_{1,3}$ mode and $TE_{4,9}$ mode are shown in Figure 5-7 (a) and (b), respectively.

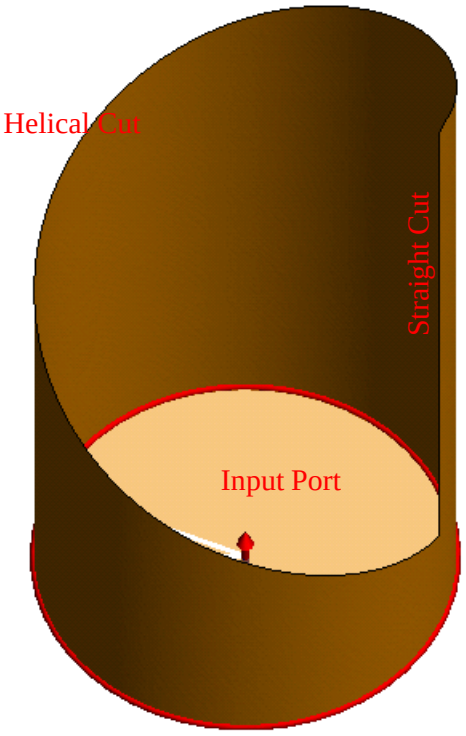

Figure 5-6: Details of the modified Vlasov launcher with a helical and straight cut.

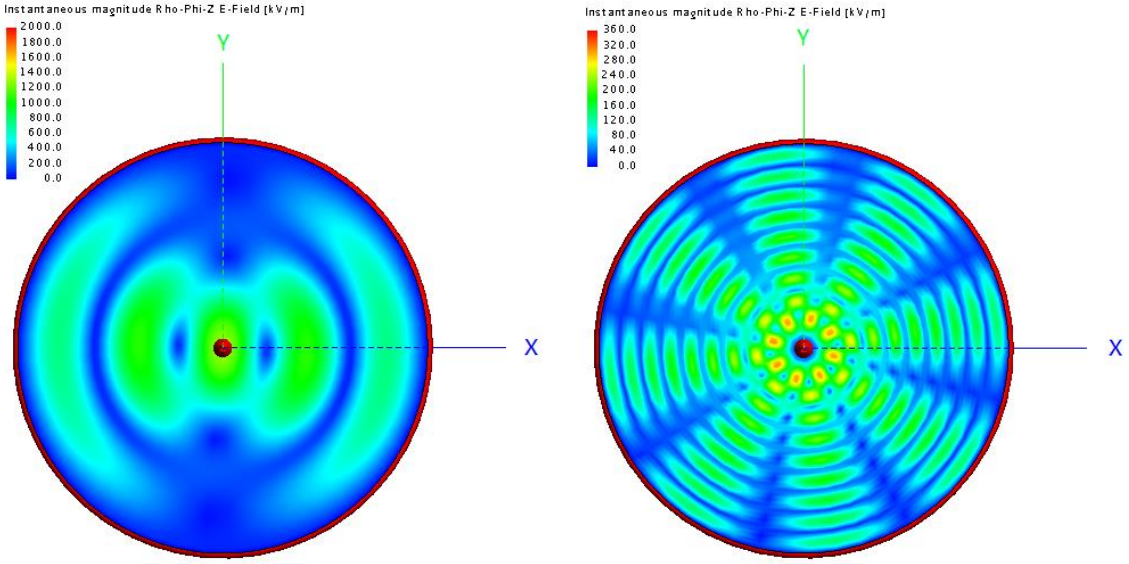

(a) (b)

Figure 5-7: Field distribution on the input port for: (a) $TE_{1,3}$ mode; (b) $TE_{4,9}$ mode.

The surface current distributions on the launcher wall for the case of $TE_{1,3}$ mode and $TE_{4,9}$ mode excitation are also shown in Figure 5-8 (a) and (b), respectively. The azimuthal direction of the current flow is the same as that of the helical cut.

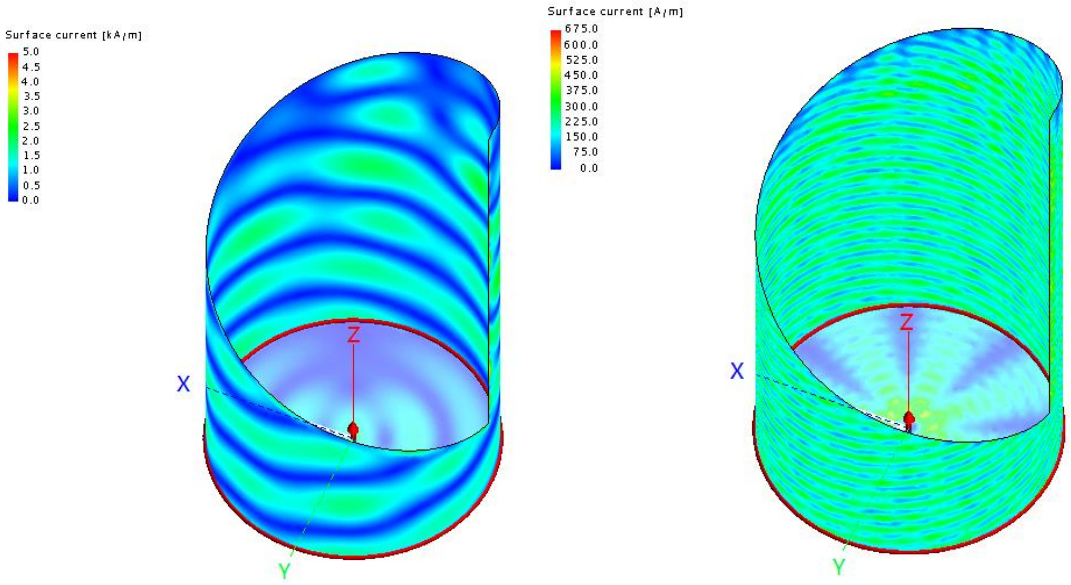

(a) (b)

Figure 5-8: Current distribution on the modified Vlasov launcher with a helical cut when being excited by: (a) $TE_{1,3}$ mode; (b) $TE_{4,9}$ mode.

The radiated near-field at the output aperture of the modified Vlasov launcher can be observed on the unfolded cylindrical waveguide surface for the case of $TE_{1,3}$ mode and $TE_{4,9}$ mode excitation, respectively, as shown in Figure 5-9. In Figure 5-9, the horizontal and vertical axes correspond to the longitudinal and azimuthal coordinates of the Vlasov launcher, respectively. It can be seen that the field distribution at the aperture of the modified Vlasov launcher is concentrated within the removed helical area. And the power is radiated towards the y axis, which is also the direction of the opening of the aperture. The field radiated toward the $-y$ axis is negligible. The electric field distribution as shown in Figure 5-9 also resembles the results of the Brillouin regions analysis in the geometrical optics, as shown in Figure 5-5. The difference is caused by the diffraction of the wave beam, which is not taken into consideration by the geometrical optics analysis. It can also be seen from Figure 5-9 that the electric fields at $\phi = \pi$, which corresponds to the straight cut of the modified Vlasov launcher, are stronger than the neighbouring areas. This is caused by the obstruction of the wall currents by the straight cut, as shown in Figure 5-8.

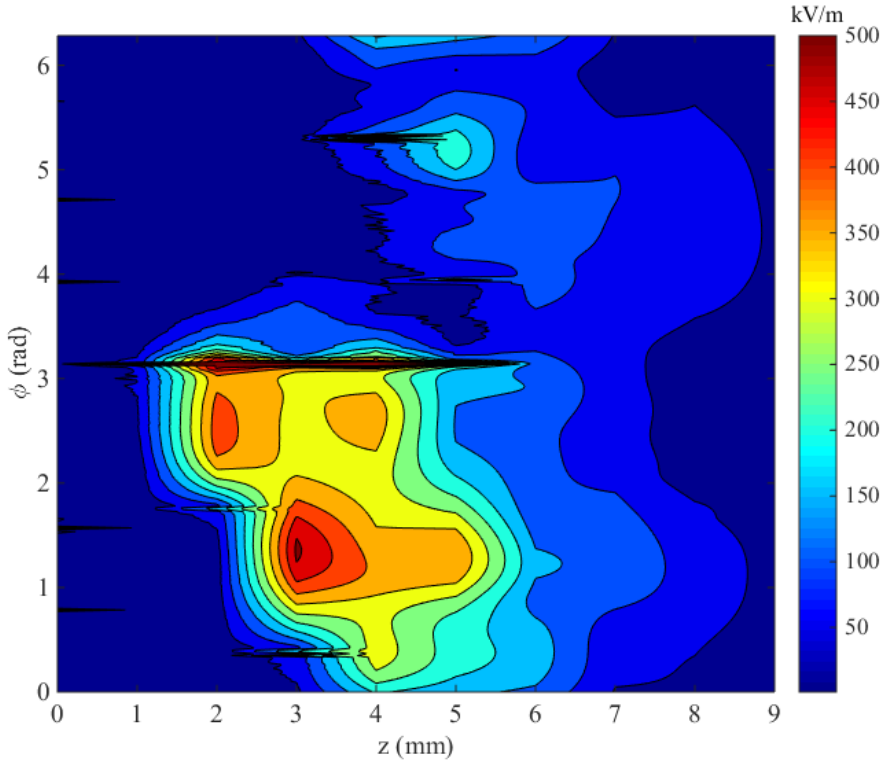

(a)

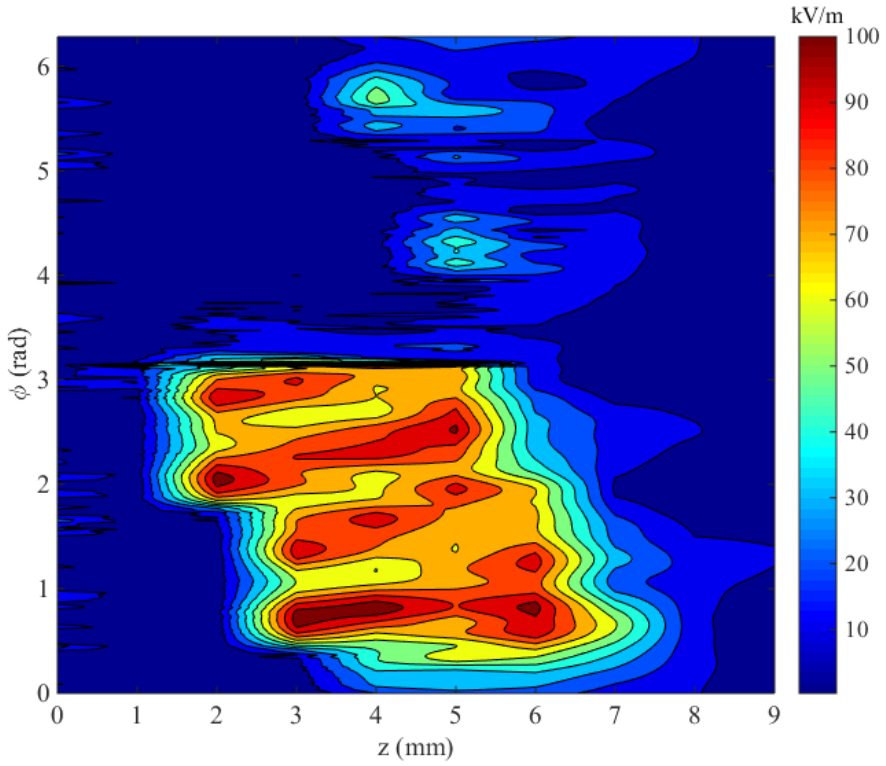

(b)

Figure 5-9: E-field distribution on the unfolded waveguide surface when being excited by: (a) $TE_{1,3}$ mode; (b) $TE_{4,9}$ mode. The unit of the field value is kV/m.

5.2.2 Mirror Synthesis

The radiated rays of the modified Vlasov launcher are parallel in the $y-z$ plane and spread an angle of 2θ in the $x-y$ plane, which can be converted to have Gaussian-like distributions by two-dimensionally adjusting the amplitude and phase. To do so, two types of mirror system can be utilised.

The first type is shown in Figure 5-10. The path of the wave beam in the DQMC is represented by the red lines. The quasi-elliptical cylinder mirror is used to focus the rays in the $x-y$ plane. Then, the parabolic cylinder mirror is placed at half way of the ray propagation, to reflect and focus the beam in $y-z$ plane. The radiated beam is finally directed to the focal point F.

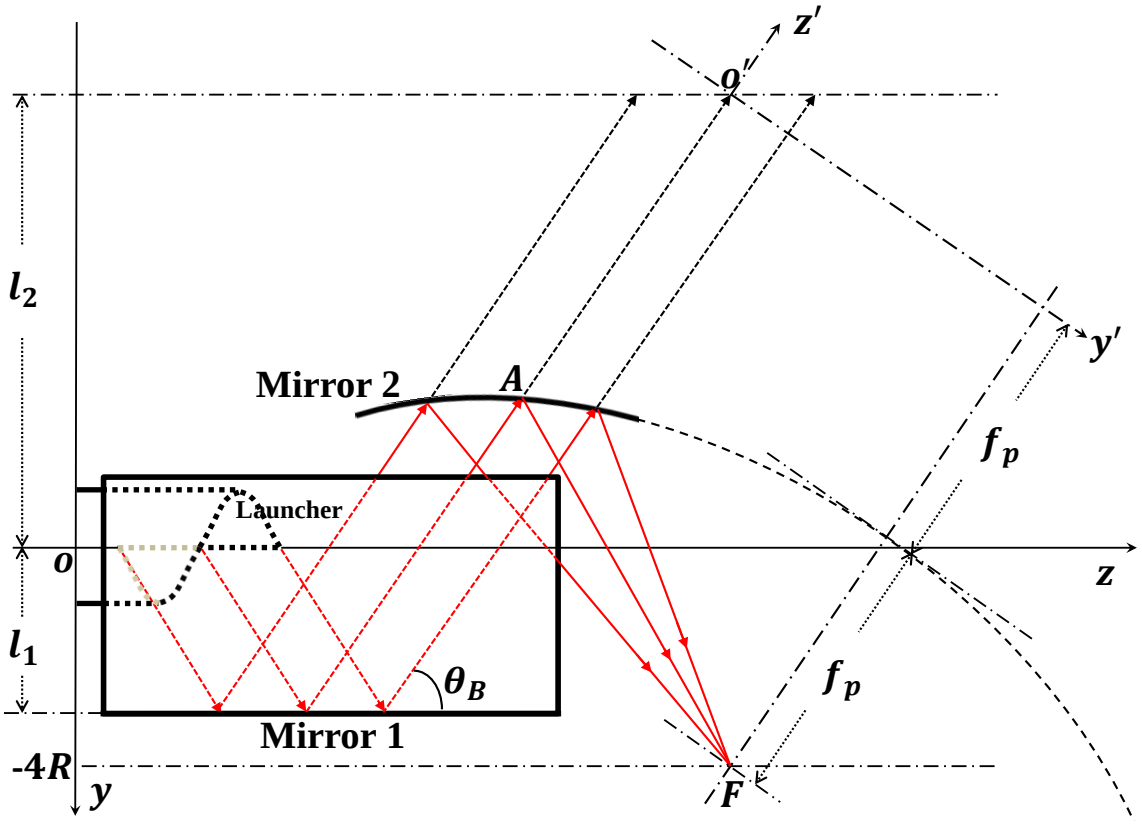

Figure 5-10: The reflection of the rays by a quasi-elliptical cylinder mirror and a parabolic cylinder mirror.

This mirror system has been proven to be effective when operating with the TE_{0n} modes [155] where the radiated field from the Vlasov launcher and the first mirror is symmetrical regarding the $y-z$ plane. In this study where the reflected field from the

first mirror is asymmetrical, the parabolic cylinder mirror whose shape does not vary along the x direction, will not be effective in reflecting and focusing the electric field in the $y-z$ plane.

The second type of mirror synthesis is shown in Figure 5-11. The path of the wave beam in the DQMC is represented by the red lines. A quasi-parabolic cylinder mirror can be used to parallelise the rays in the $x-y$ plane. After the adjustment of the first mirror, the rays are parallel in both $x-y$ and $y-z$ planes. Then, if an elliptic-paraboloid mirror is placed in such a way that its axis is parallel with the propagation directions of the rays, they will all be reflected to and two-dimensionally focused at the focal point of the mirror. The two-dimensionally focusing mirror is suitable for reshaping the field with asymmetrical distribution.

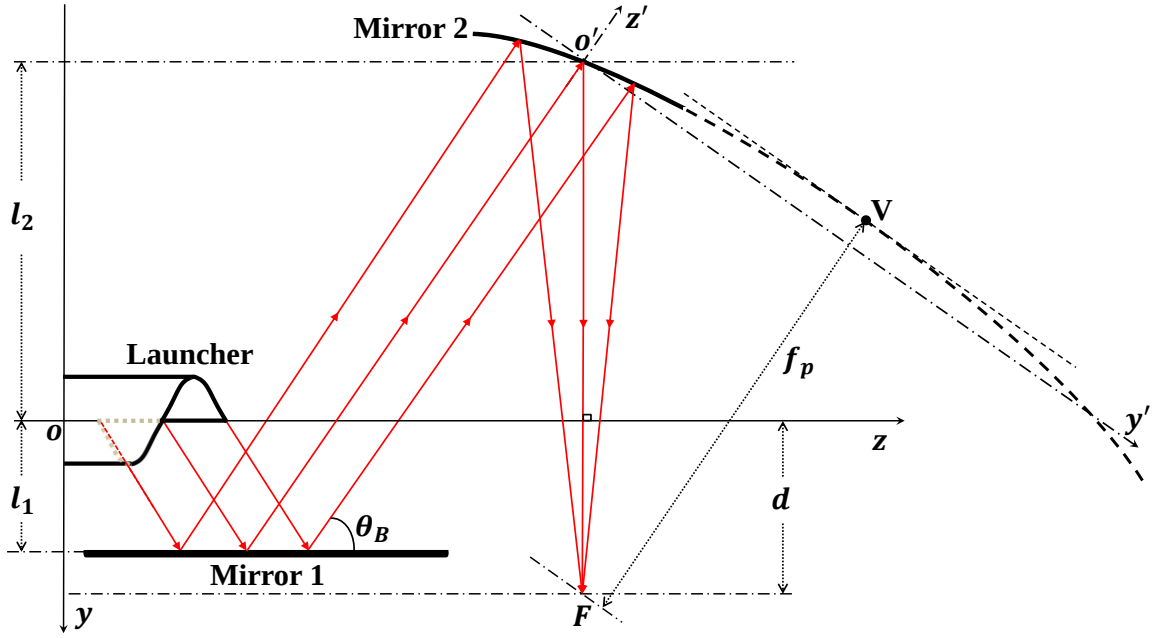

Figure 5-11: The reflection of the rays by a quasi-parabolic cylinder mirror and an elliptic-paraboloid mirror.

The dimension of the quasi-parabolic cylinder mirror in the $x-y$ plane is governed by [51]

$$x(\phi) = R_c + \pi R_c cot\left(\frac{\phi}{2}\right) - R_c \phi cot\left(\frac{\phi}{2}\right) - 2l_1 cot\left(\frac{\phi}{2}\right) \qquad (5.2)$$

$$y(\phi) = R_c cot\left(\frac{\phi}{2}\right) + \left(\pi\frac{R_c}{2} - R_c\frac{\phi}{2} - l_1\right)\left(cot^2\left(\frac{\phi}{2}\right) - 1\right) \tag{5.3}$$

in which l_1 is the distance between the vertex of the quasi-parabolic cylinder mirror and the z axis. ϕ represents the azimuthal angle between the radiated rays and the y axis in the $x-y$ plane [51]. R_c is the caustic radius of the mode to be transformed. The shape of the quasi-parabolic cylinder mirror is consistent along the z direction.

The original point of the local coordinate system for the elliptic-paraboloid mirror is O'. The distance between O' and O is l_2 in the y direction and L_Z in the z direction. To avoid the interference between the reflected wave beams from the elliptic-paraboloid mirror and the quasi-parabolic cylinder mirror, the following relationship should be fulfilled:

$$L_Z \geq l_0 + L/2 + (2l_1 + l_2)/tan\theta_B \tag{5.4}$$

where l_0 is the length of the unperturbed waveguide section at the input end of the launcher.

By setting the focusing point F being right below O' and having a distance of d from the z axis, the axis z' forms an angle of θ_B with the z axis. The distance between F and O' is

$$l_{FO'} = l_2 + d. \tag{5.5}$$

The coordinates of F in the (y', z') plane are $(l_{FO'} \cdot cos\theta_B, -l_{FO'} \cdot sin\theta_B)$. In the (x', y', z') coordinate system, the equation of the elliptic-paraboloid mirror can be written as

$$z' = -\frac{(y' - l_{FO'} \cdot cos\theta_B)^2}{4f_{py}} - \frac{(x')^2}{4f_{px}} + \frac{(l_{FO'} \cdot cos\theta_B)^2}{4f_{py}}. \tag{5.6}$$

In the (y', z') plane, the equation of the elliptic-paraboloid mirror can be simplified to represent a parabolic line,

$$z' = -\frac{(y' - l_{FO'} \cdot cos\theta_B)^2}{4f_{py}} + \frac{(l_{FO'} \cdot cos\theta_B)^2}{4f_{py}}. \tag{5.7}$$

The directrix of this parabolic line can be written as:

$$z' = f_{py} + \frac{(l_{FO'} \cdot cos\theta_B)^2}{4f_{py}}. \tag{5.8}$$

Since the original point $(0,0)$ in the (y', z') plane is also on the parabolic line, its distance to the focusing point F is identical with that to the directix, which gives

$$l_{FO'} = f_{py} + \frac{(l_{FO'} \cdot cos\theta_B)^2}{4f_{py}}. \tag{5.9}$$

Thus it can be derived that

$$f_{py} = \frac{l_{FO'}}{2}(1 + sin\theta_B). \tag{5.10}$$

And from the geometrical optics, it can be derived that

$$f_{py} = f_{px} \tag{5.11}$$

when the focal length in the $y - z$ and $x - z$ planes are chosen to be the same. The chosen values of the variables used in (5.2)-(5.11) are listed in Table 5-2.

Table 5-2: The designed parameters for the mirror synthesis.

R_c	l_1	l_2	l_0	θ_B	d
0.18 mm	4.2 mm	14.0 mm	1.0 mm	52.8°	22.4 mm

Here the values of R_c and θ_B are calculated according to the parameters of the $TE_{4,9}$ mode at 1368 GHz. This is because the two modes share similar values of R_c as well as θ_B and the $TE_{1,3}$ mode at 342 GHz is less sensitive to the parameter variations.

To verify the above design, a 3-D full electromagnetic simulation using Feko 7.0 is conducted. The model is shown in Figure 5-12. Apart from the launcher and the two reflectors, a virtual observation window is located in parallel with the $y = -22.4\,mm$ plane, to record the field distribution of the converted wave beams at the waists.

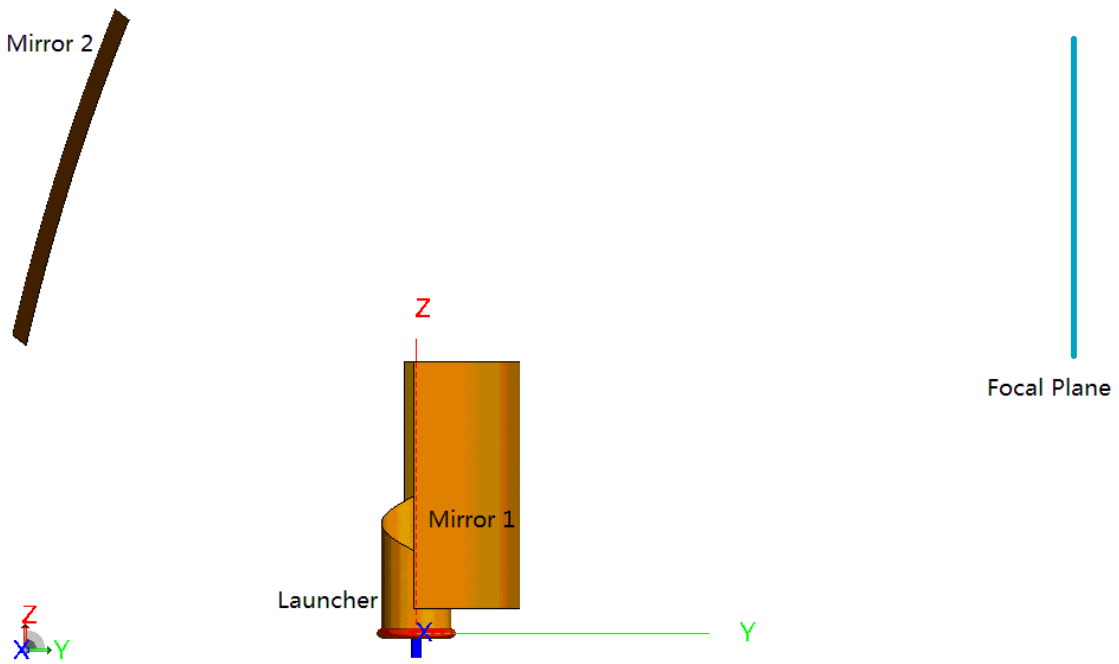

Figure 5-12: The 3D model of the DQMC built in Feko 7.0. The virtual observation plane is placed at the designed focal plane.

The above model is simulated with rotating TE_{13} excitation at 342 GHz and TE_{49} input at 1368 GHz, respectively. The rotation direction of the input waveguide modes is chosen to be the same as the helical cut of the modified Vlasov launcher.

The current distribution on the quasi-parabolic cylinder mirror when the system is excited by $TE_{1,3}$ mode at 342 GHz and $TE_{4,9}$ mode at 1368 GHz are shown in Figure 5-13 and Figure 5-14, respectively. It can be seen that the radiated field of the modified Vlasov launcher can be effectively collected by the quasi-parabolic mirror. The induced surface current by the $TE_{1,3}$ mode at 342 GHz is higher than its counterpart at 1368 GHz, as the input power of the former is much higher than the later.

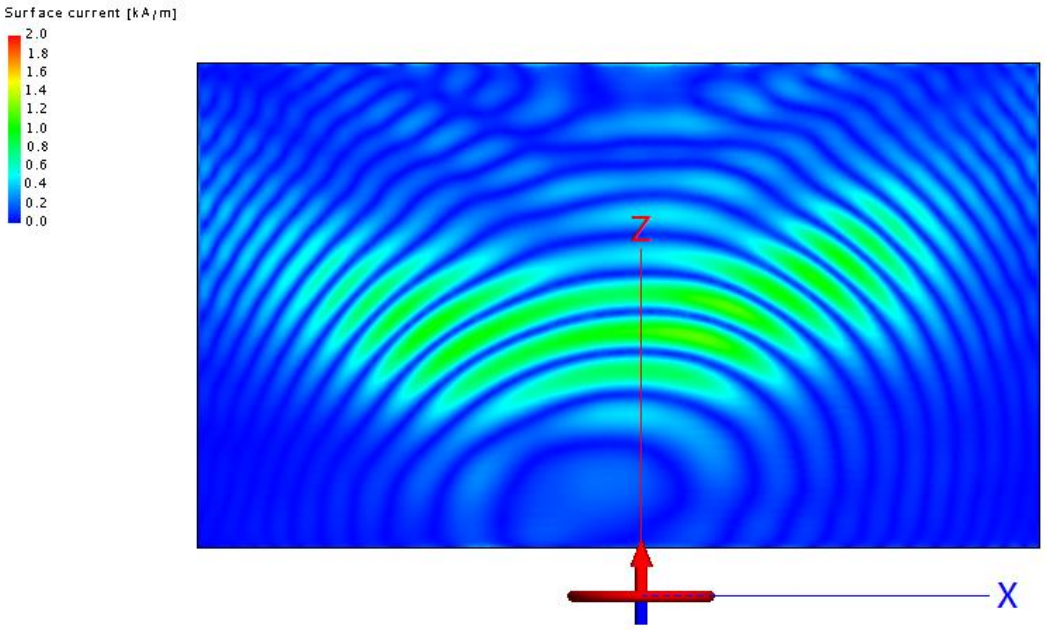

Figure 5-13: The current distribution on the quasi-parabolic cylinder mirror when the launcher is excited at 342 GHz with TE_{13} mode.

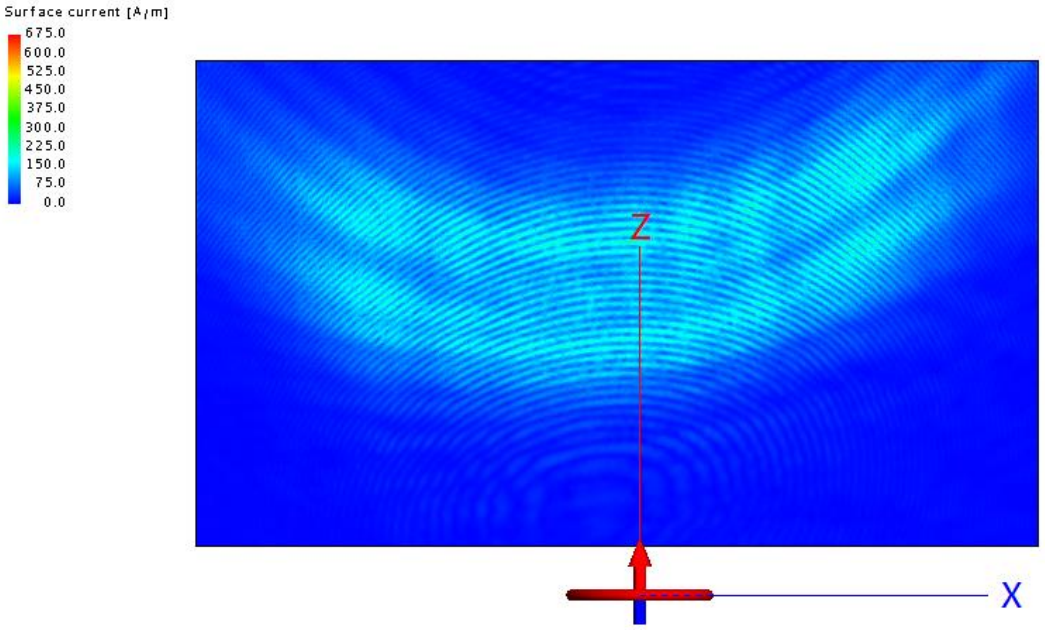

Figure 5-14: The current distribution on the quasi-parabolic cylinder mirror when the launcher is excited at 1368 GHz with TE_{49} mode.

The reflected wave beam is then directed to the elliptic-paraboloid mirror. And the current distributions on this mirror when being excited by $TE_{1,3}$ mode at 342 GHz and $TE_{4,9}$ mode at 1368 GHz are shown in Figure 5-15 and Figure 5-16, respectively. After

been reflected by the elliptic-paraboloid mirror, the wave beam will be focused in both $x-y$ and $y-z$ planes.

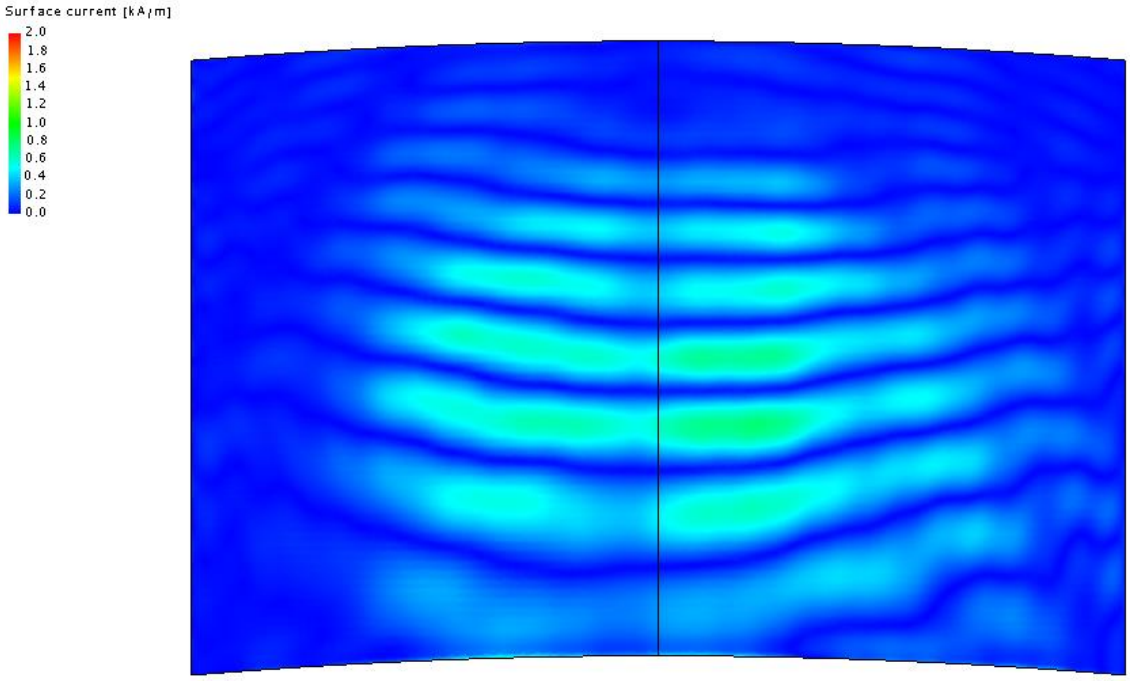

Figure 5-15: The current distribution on the elliptic-paraboloid mirror when the launcher is excited at 342 GHz with TE_{13} mode.

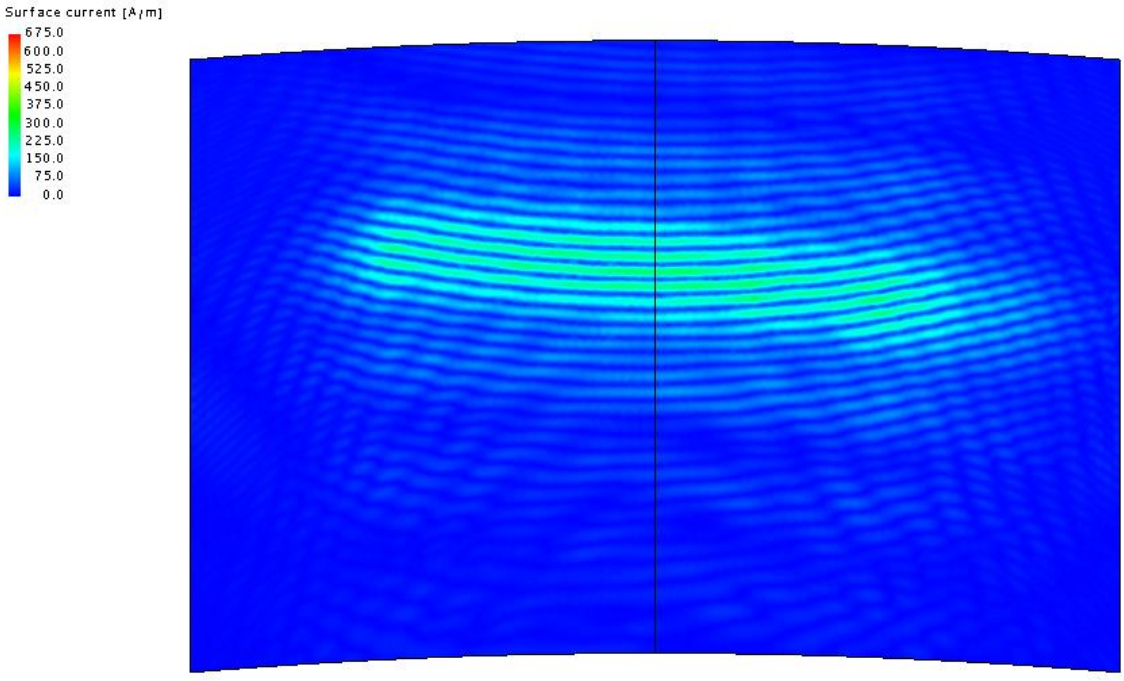

Figure 5-16: The current distribution on the elliptic-paraboloid mirror when the launcher is excited at 1368 GHz with TE_{49} mode.

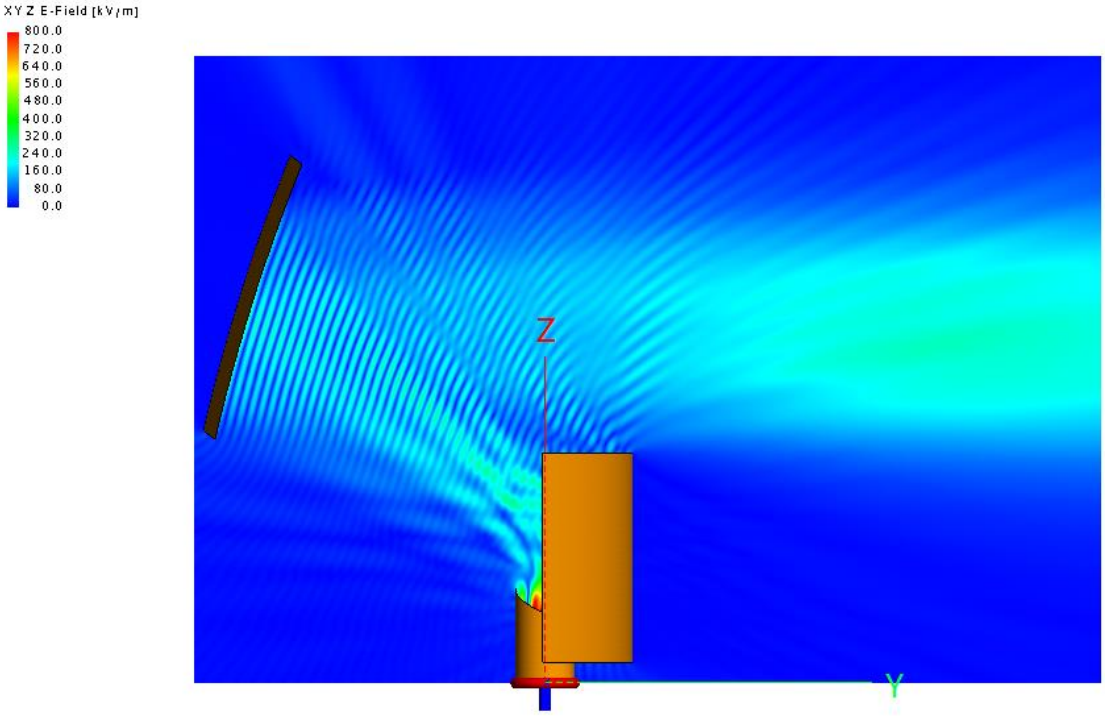

Figure 5-17: The path of the wave beam propagation in the designed DQMC from the side view when the launcher is excited at 342 GHz with TE_{13} mode.

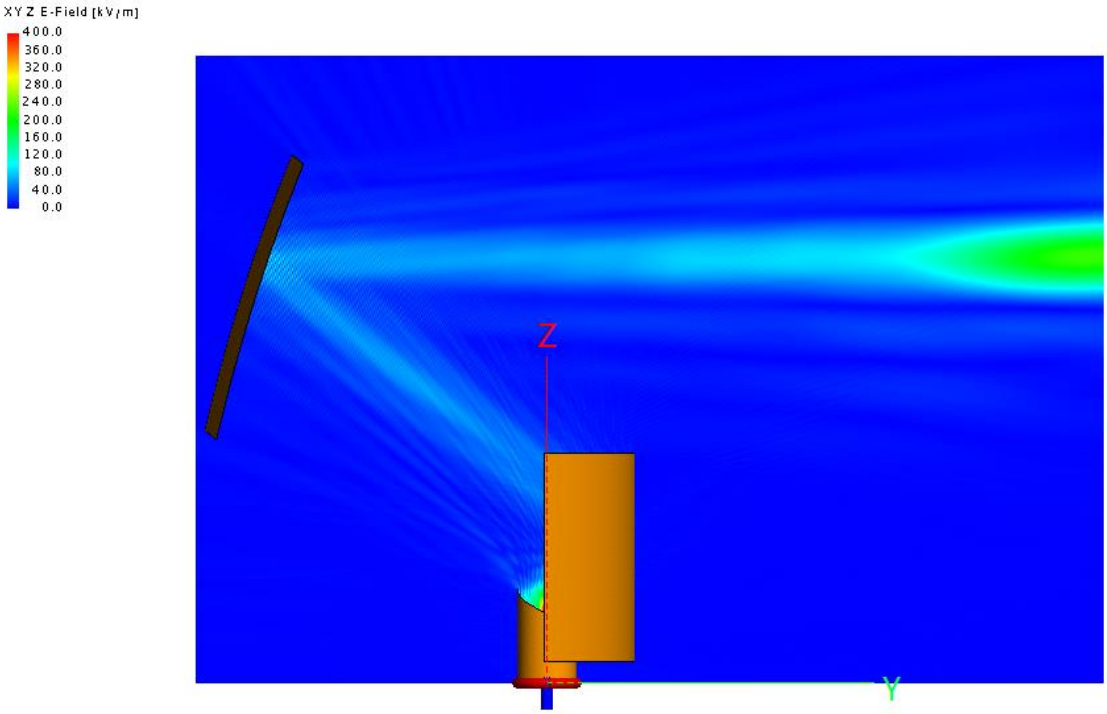

Figure 5-18: The path of the wave beam propagation in the designed DQMC from the side view when the launcher is excited at 1368 GHz with TE_{49} mode.

Figure 5-17 and Figure 5-18 shows the path of the wave beams propagation in the designed DQMC when the system is excited by $TE_{1,3}$ mode at 342 GHz and $TE_{4,9}$ mode at 1368 GHz, respectively. It can be seen that both wave beams are properly focused at a given distance from the elliptic-paraboloid mirror. And the converted wave beams are propagating in the y direction. The simulation results agree with the geometrical optics analysis. The effect of diffraction during the propagation of the wave beams is also shown.

The distributions of the total electric field (E) as well as the corresponding x component (E_x), y component (E_y) and z component (E_z) on the focal plane, for the case of TE_{13} excitation at 342 GHz, are shown in Figure 5-19. The distributions of E, E_x, E_y and E_z are shown in dB contour with normalisations to the maximum total electric field value, which is denoted as E_{LF}^{in}. And from the result of the numerical simulation, $E_{LF}^{in} = 2.25 \times 10^5\ V/m$ when the incident power is 2 kW.

And the distribution of E, E_x, E_y, E_z on the focal plane for the case of TE_{49} excitation at 1368 GHz are shown in Figure 5-20. The distributions of E, E_x, E_y and E_z are shown in dB contour with normalisation to the maximum total electric field value, which is denoted as E_{HF}^{in}. From the result of the numerical simulation, $E_{HF}^{in} = 2.38 \times 10^5\ V/m$, when the incident power is 0.12 kW.

From Figure 5-19 (a) and Figure 5-20 (a), it can be seen that both the high-order modes at the fundamental and the fourth harmonic can be converted into quasi-Gaussian beams. And the side lobes of the converted quasi-Gaussian beams are lower than -20 dB at 342 GHz and lower than -15 dB at 1368 GHz. Figure 5-19 and Figure 5-20 suggest that both quasi-Gaussian beams are linearly polarised in the x direction. It is also shown that after the transformation of the DQMC, the converted quasi-Gaussian beam at 342 GHz is larger in size than that at 1368 GHz.

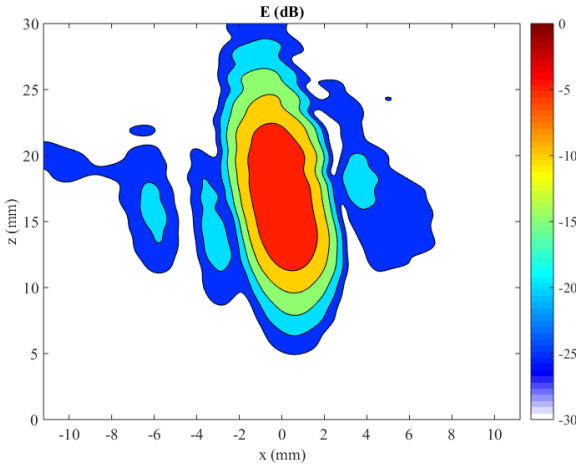

(a)

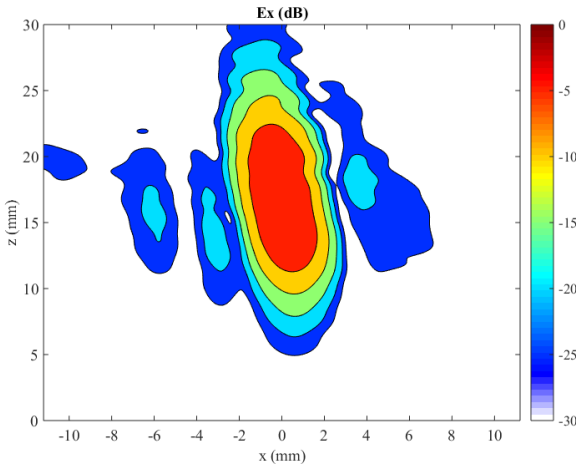

(b)

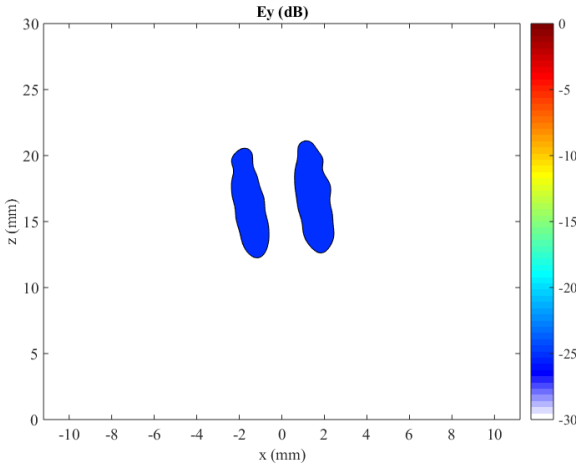

(c)

Figure 5-19: The dB contour of the electric field distribution on the observation window for $TE_{1,3}$ mode incidence at 342 GHz: (a) The total electric field distribution; (b) The distribution of the E_x component; (c) The distribution of the E_y component. The dB values of the E_z component are all below -30 dB in the plotted area.

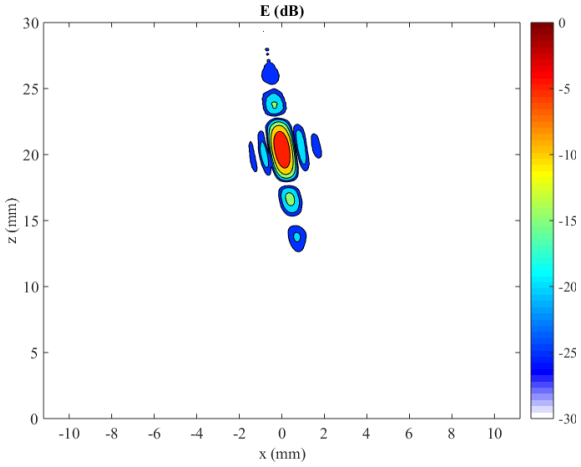

(a)

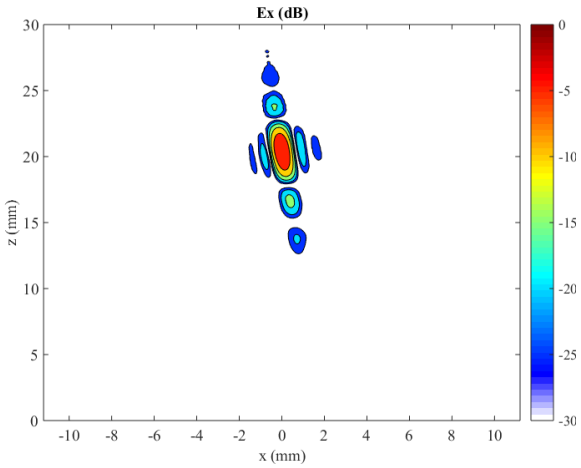

(b)

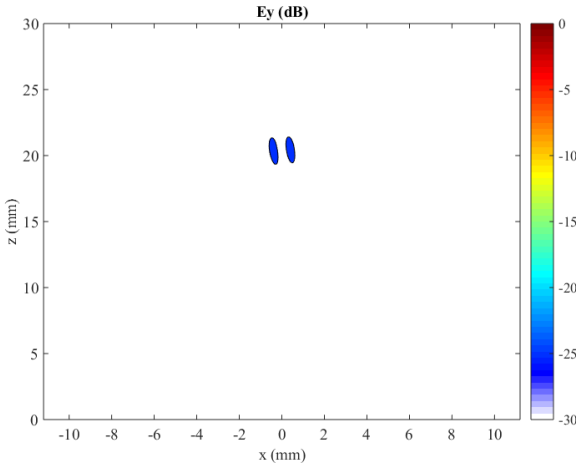

(c)

Figure 5-20: The dB contour of the electric field distribution on the observation window for $TE_{4,9}$ mode incidence at 1368 GHz: (a) The total electric field distribution; (b) The distribution of the E_x component; (c) The distribution of the E_y component. The dB values of the E_z component are all below -30 dB in the plotted area.

The Gaussian content of the converted wave beam can be calculated as [156]:

$$C_s = \frac{(\iint |u_1| \cdot |u_2| dS)^2}{\iint |u_1|^2 \, dS \cdot \iint |u_2|^2 dS} \tag{5.12}$$

in which $|u_1|$ and $|u_2|$ are the amplitude distributions of the converted quasi-Gaussian beam and the fundamental Gaussian beam, respectively. S denotes the plane of observation. And from definition of the standard Gaussian beam,

$$u_2(x, y, z) = \left(\frac{2}{\pi \omega_x \omega_z}\right)^{0.5} \cdot \exp\left[-\frac{(x - x_0)^2}{\omega_x^2} - \frac{(z - z_0)^2}{\omega_z^2}\right] \tag{5.13}$$

in which

$$\omega_x = \omega_{0x}\left[1 + \left(\frac{\lambda(y - y_0)}{\pi \omega_{0x}^2}\right)^2\right]^{0.5} \tag{5.14a}$$

$$\omega_z = \omega_{0z}\left[1 + \left(\frac{\lambda(y - y_0)}{\pi \omega_{0z}^2}\right)^2\right]^{0.5}. \tag{5.14b}$$

ω_{0x} and ω_{0z} are the beam waists in the x and z directions, respectively. λ is the wavelength. (x_0, y_0, z_0) is the coordinate of the center point of the beam waist.

The power being collected on the virtual observation window can be determined by the Poynting vector integration [103]:

$$P = \frac{1}{2}\iint Re\left[\vec{E} \times \vec{H}^*\right] \cdot \vec{n} dS \tag{5.15}$$

where $\vec{E}$ and $\vec{H}$are the electric and magnetic field vectors, respectively. $\vec{H}^*$ represents the conjugate of $\vec{H}$. And $\vec{n}$ is the unit normal vector of the observation plane.

Since the electric and magnetic field can be decomposed as:

$$\vec{E} = \vec{\imath} \cdot E_x + \vec{j} \cdot E_y + \vec{k} \cdot E_z \tag{5.16a}$$

$$\vec{H}^* = \vec{\imath} \cdot {H_x}^* + \vec{\jmath} \cdot {H_y}^* + \vec{k} \cdot {H_z}^* \tag{5.16b}$$

the converted power can be expressed as:

$$\mathrm{P} = \frac{1}{2} \iint Re\left[\left(\vec{\imath} \cdot E_x + \vec{\jmath} \cdot E_y + \vec{k} \cdot E_z\right) \times \left(\vec{\imath} \cdot {H_x}^* + \vec{\jmath} \cdot {H_y}^* + \vec{k} \cdot {H_z}^*\right)\right] \cdot \vec{n} dS \tag{5.17}$$

which yields:

$$P = \frac{1}{2} \iint Re \begin{bmatrix} \vec{\imath} \cdot \left(E_y \cdot {H_z}^* - E_z \cdot {H_y}^*\right) + \vec{\jmath} \cdot \left(E_z \cdot {H_x}^* - E_x \cdot {H_z}^*\right) \\ + \vec{k}\left(E_x \cdot {H_y}^* - E_y \cdot {H_x}^*\right) \end{bmatrix} \cdot \vec{n} dS. \tag{5.18}$$

${H_x}^*$, ${H_y}^*$ and ${H_z}^*$ are the conjugates of H_x, H_y and H_z, respectively. In the above simulation model, the observation plane is parallel with the $x - z$ plane. Thus $\vec{n} = \vec{\jmath}$ and (5.18) becomes

$$P = \frac{1}{2} \iint Re[E_z \cdot {H_x}^* - E_x \cdot {H_z}^*] \cdot dS. \tag{5.19}$$

By recording the x, y, z components of the electric and magnetic field, the power that has been transmitted to the observation plane can be calculated by piecewise integration. Then the power transmission coefficient can be calculated as

$$\eta = \frac{P}{P_0} \tag{5.20}$$

where the values of P_0 for the two modes are listed in Table 1-1. The polarisation characteristics of the converted quasi-Gaussian beam are of critical importance for the application of the FSS. The fraction of depolarised power can be defined as [157]

$$XP = \frac{\iint S_z dS}{\iint S_z dS + \iint S_x dS} \tag{5.21}$$

in which S_x and S_z are the y component of the Poynting vector associated with the electric field in the x and z directions, respectively. And

$$S_x = \left|Re\left[E_x^0 \cdot H_z^{0^*}\right]\right| \tag{5.22a}$$

$$S_z = \left|Re\left[E_z^0 \cdot H_x^{0^*}\right]\right|. \tag{5.22b}$$

By recording the electric and magnetic field distributions at the two frequencies, the values of C_s, η and XP are calculated and summarised in Table 5-3.

Table 5-3: The Gaussian contents, the power transmission coefficients and the fractions of depolarised power for the two modes.

	342 GHz	1368 GHz
C_s	94.6%	89.6%
$P\ (kW)$	1.628	0.109
η	81.4%	90.6%
XP	0.8%	0.8%

A number of important conclusions can be drawn from Table 5-3. Firstly, by using the DQMC, both TE_{13} mode at the fundamental harmonic and the $TE_{4,9}$ mode at the fourth harmonic can be transformed into quasi-Gaussian beams. Secondly, for both modes, the Gaussian contents and the power transmissions coefficient of the converted wave beams have shown comparable values with some of the previous work in the single mode QMC [158, 159], which in turn validates the above approach of DQMC design. Thirdly, the converted wave beams are linearly polarised in the x direction with very low fraction of depolarised power in the z direction. The linearly polarised quasi-Gaussian beams can be properly separated by the FSS.

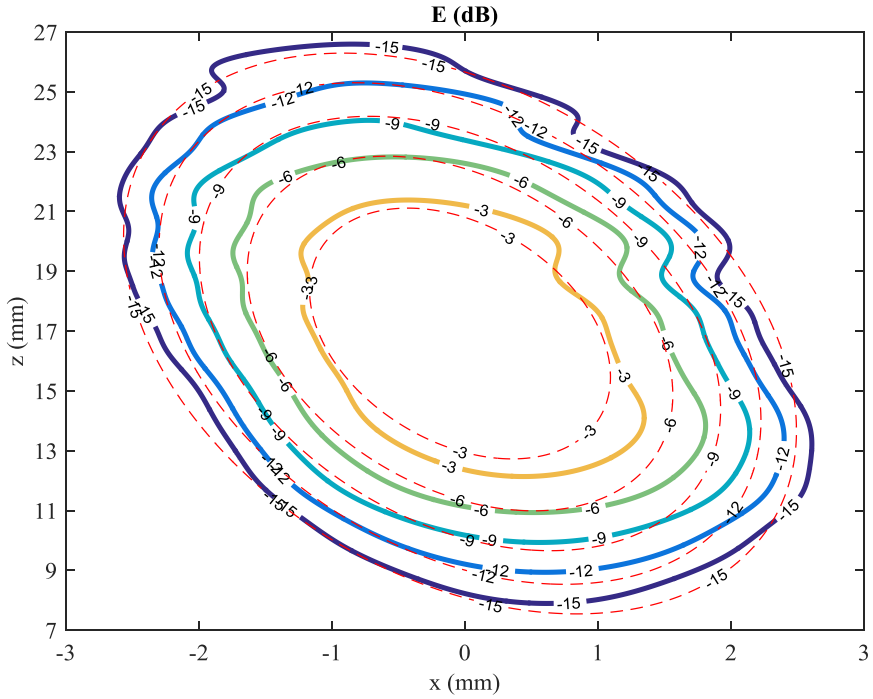

(a)

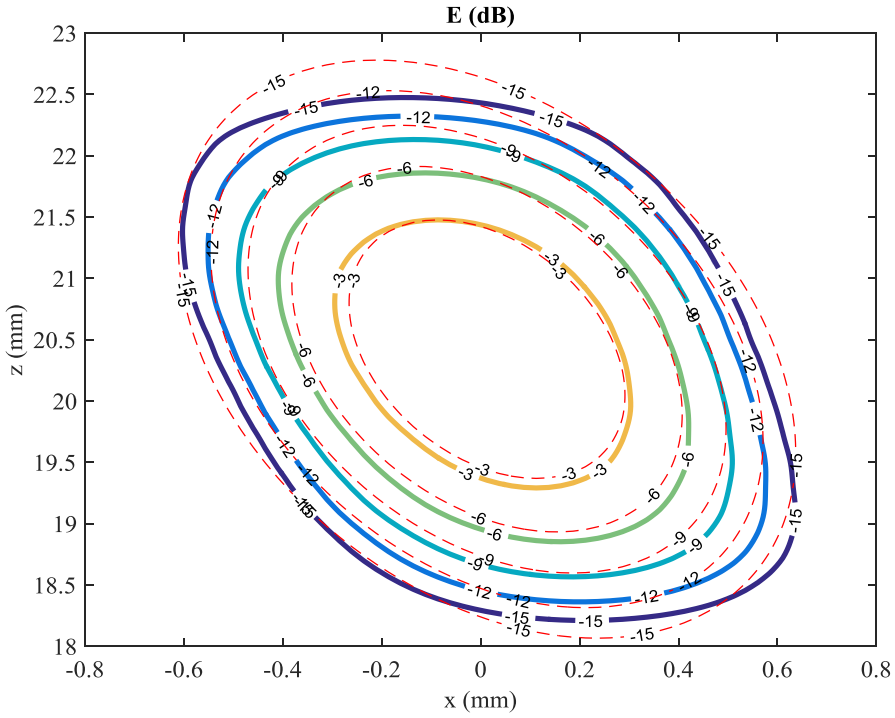

(b)

Figure 5-21: The dB contour comparison between the standard Gaussian distribution and the electric field distribution on the window area when the launcher is excited at (a) 342 GHz with TE_{13} mode; (b) 1368 GHz with TE_{49} mode. The red dotted line is a standard Gaussian beam distribution.

Figure 5-21 shows the comparison between the converted quasi-Gaussian beams and the standard Gaussian beams for the cases of TE_{13} mode and TE_{49} mode excitation of the DQMC, respectively. It can be seen that the converted quasi-Gaussian beams show similar field patterns as the tilted standard Gaussian beams. This implies that with the above designed DQMC, both high-order asymmetric waveguide modes can be effectively converted into quasi-Gaussian beams.

It should be noticed that the similar propagation properties of the two modes in the DQMC is essential to the success of the design. As seen from the mode selection criteria and the operation principle of the gyro-multiplier [62-64], the k_0, k_z, $k_\perp$, m, $\mu'_{m,n}$ and ω values of $TE_{4,9}$ mode are nearly four times the values of their counterparts of $TE_{1,3}$ mode, which in turn lead to similar values of θ_B, L, L_a and Φ for the two modes. That is to say, the particular mode selection criteria and operation principle of the gyro-multiplier have facilitated a successful design of the DQMC. It is also predictable that the above algorithm can be generalised to apply to other gyro-devices with frequency multiplication.

5.3 Single Disc Window Design

After the quasi-optical mode conversion system, the converted dual-frequency wave beam should be transmitted through an output window, which is widely used in the vacuum electronic devices to hold the ultra-high vacuum environment. There are traditionally two types of vacuum windows in the development of gyrotrons: the double disk window [160] and the single disk window [161]. The double disk windows with the coolant flowing between the two discs are usually used in the gyrotrons with ultra-high power. In the case of a gyro-multiplier where the generated power is relatively low, a single disc window is more preferable for the simplicity of design as well as fabrication. Besides, the single disc window can naturally solve the challenge of transmitting two frequencies simultaneously.

It is known that for a single disc window, the disc thickness, d, should be chosen as [162]

$$d = N \cdot \frac{\lambda}{2\sqrt{\varepsilon'_r}} \tag{5.23}$$

to minimise the reflection. Here N is an integer and λ is the wavelength of the transmitted wave. ε_r' is the relative permittivity of the window material. Suppose the disc thickness for the wave at 342 GHz is d_1 and that for the wave at 1368 GHz is d_2, we have

$$d_1 = N_1 \cdot \frac{\lambda_1}{2\sqrt{\varepsilon_r'}} \tag{5.24}$$

$$d_2 = N_2 \cdot \frac{\lambda_2}{2\sqrt{\varepsilon_r'}} \tag{5.25}$$

where λ_1 and λ_2 are the wavelength at 342 GHz and 1368 GHz, respectively. By assuming that the two frequencies share the same window thickness and the difference of ε_r' values at the two wavelengths is negligible [163], we have

$$d_1 = d_2 \tag{5.26}$$

and thus

$$\frac{N_1}{N_2} = \frac{\lambda_2}{\lambda_1} = \frac{1}{4}. \tag{5.27}$$

By choosing $N_2 = 4N_1$, the thickness of the window for both frequencies are the same. That is, the window designed in this way can transmit both wave beams, one at the fundamental frequency and the other one at the fourth harmonic.

To verify the possibility of transmitting the two frequencies simultaneously, the designed single disc window is modelled in CST MWS, as shown in Figure 5-22. The disc material is chosen as Sapphire with $\varepsilon_r' = 9.41$. The window is designed to be able to transmit waves at two frequencies, 342 GHz and 1368 GHz. The incident mode is set as TE_{11} waveguide mode. The incident mode is launched from Port 1. Both Port 1 and Port 2 are adopted to record the transmitted and reflected signals, from which the S-parameters of the window are calculated. Based on (5.23)-(5.26), the thickness of the window disc is calculated to be 143 μm when $N_1 = 1$.

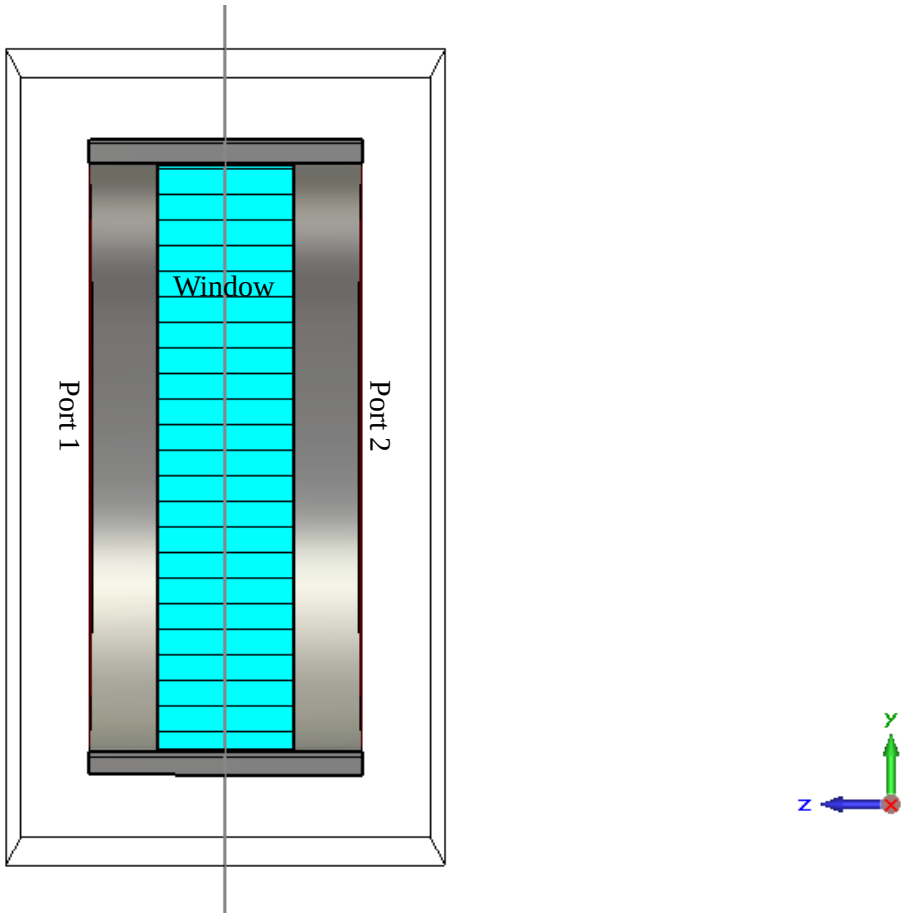

Figure 5-22: The cutting-plane view of the single disc window modelled in CST MWS. The incident wave is launched at Port 1. Both Port 1 and 2 are used to record the transmitted and reflected signals.

The S-parameter performance of the designed window is shown in Figure 5-23. The S_{21} parameters at 342 GHz and 1368 GHz are -0.39 dB and -0.13 dB, respectively. Thus the transmission of the wave beam at the fundamental frequency as well as its fourth harmonic can be achieved with a single disc vacuum window. The thickness of the window can also be increased by chosen larger N_1 values, to better fulfil the mechanical strength or thermal dissipation requirement of the gyro-multiplier.

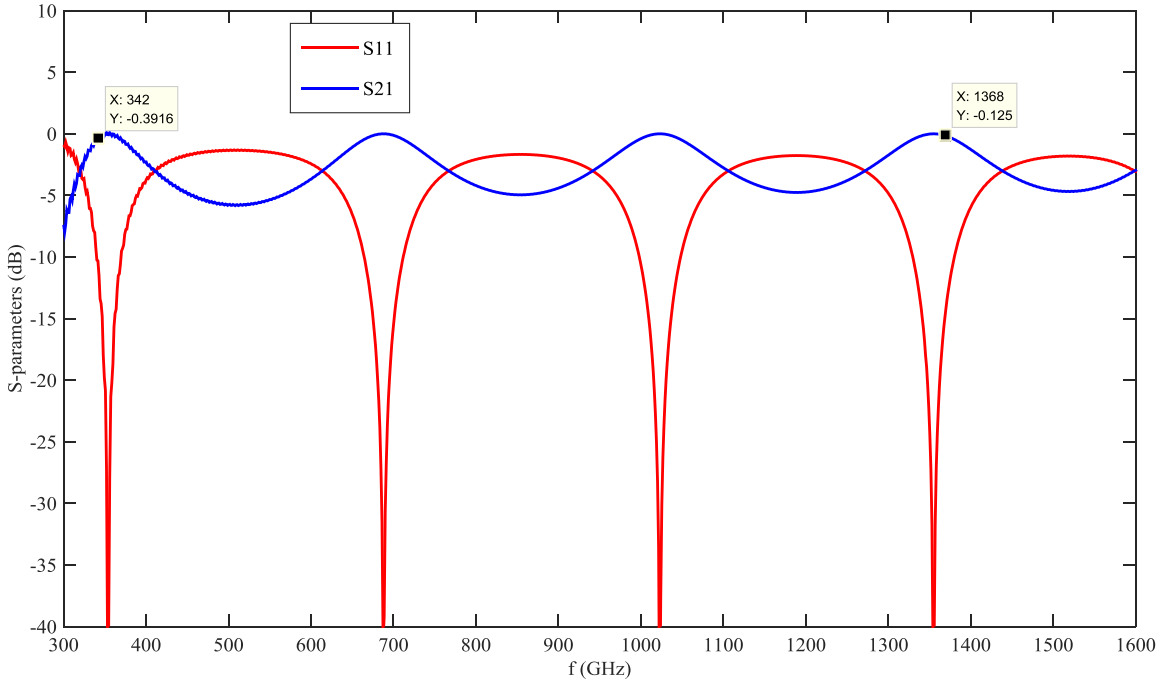

Figure 5-23: The S-parameter performance of the designed single disc window.

5.4 Frequency Selective Surface Design

Having shown the capability of the DQMC in transforming the high-order waveguide modes into linearly polarised Gaussian beams, the next step would be the design of the FSS which separates the high frequency wave from the low frequency one.

Considering the unusually high output power in the gyro-multiplier case, the dielectric materials will induce high level of power loss and heat deformation since the heat dissipation ability of the dielectric materials is limited. Thus a metal FSS with high conductivity as well as heat dissipation ability should be considered in this application. This leads to the choice of an all-metal structure of the FSS, which is formed by employing periodic perforations on a brass plate. Such kind of configuration can alleviate the challenges of fabricating and aligning the very slim wires at high frequency that are indispensible in the FSSs of centre connected type and the loop type. The FSSs formed by the periodic perforations on the metal plate usually show high-pass property where the frequencies below the cut-off of the perforations will be reflected.

5.4.1 FSS Design and Simulation

Based on the above analysis, the designed FSS is shown in Figure 5-24. The lengths of the unit cell in both directions are L_u. The diameter of the circular perforation is D. The values of L_u and D are designed as 0.19 mm and 0.15 mm, respectively. And the thickness (H) of the brass plate is 0.10 mm. The designed angle of incidence for the FSS is 15°, which has been shown in Figure 5-3 as θ_{in}.

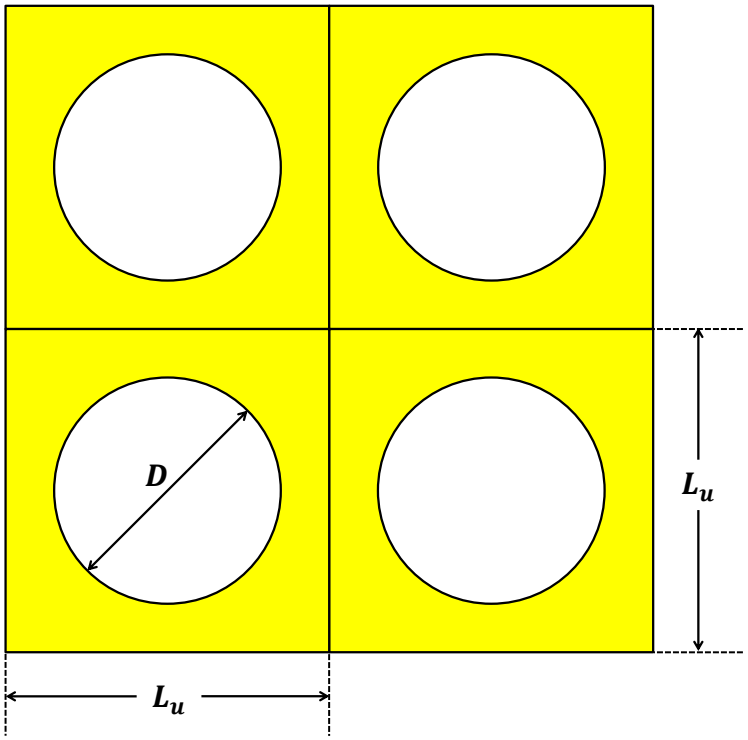

Figure 5-24: Unit cell of FSS.

The above design is modelled in CST MWS to evaluate the performance of the FSS. The incident field is set as a plane wave excited by the Floquet port. An additional Floquet port is applied at the other side to record the S_{21} parameter. The periodic boundary condition is adopted on the four edges of the unit cell, to emulate an infinitely sized FSS.

The S_{21} parameter of the designed FSS is shown in Figure 5-25. The simulation result has shown a S_{21} value of -34.01 dB at 342 GHz and that of -0.52 dB at 1368 GHz, indicating that the low frequency content will be reflected while the high frequency content will be transmitted. Thus the two frequencies can be separated by the designed FSS with good isolation.

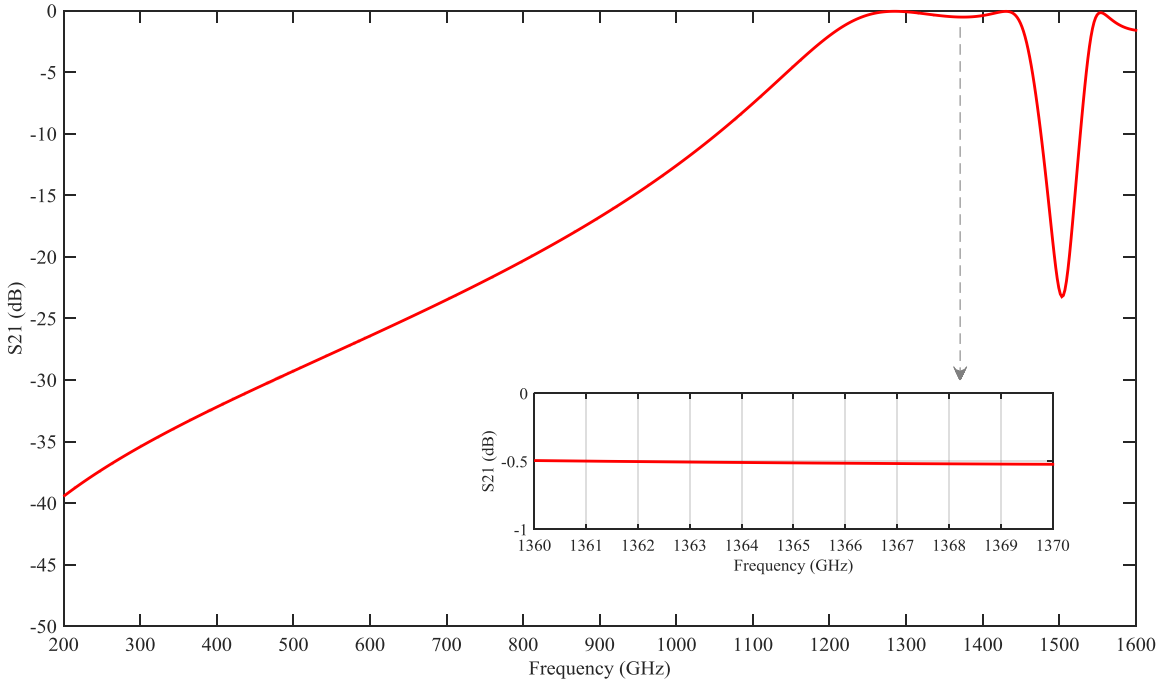

Figure 5-25: The S_{21} parameters of the designed FSS.

Figure 5-26 (a) shows that as the diameter of the perforation varies from 0.13 mm to 0.17 mm, the insertion loss at 342 GHz remains higher than 27.66 dB while that at 1368 GHz stays below 0.52 dB. Figure 5-26 (b) shows that as the thickness of the brass slab varies from 0.08 mm to 0.12 mm, the insertion loss at 342 GHz remains higher than 29.94 dB while that at 1368 GHz keeps lower than 0.74 dB. And as the angle of incidence varies from 13° to 17°, the insertion loss at 342 GHz stays higher than 33.94 dB while that at 1368 GHz remains lower than 0.54 dB. From the above analysis, the designed FSS can tolerate fabrication error of 0.02 mm regarding the diameter of the circular perforations as well as the thickness of the FSS slab. The insertion loss can be maintained as below 1 dB given the above fabrication error. Such accuracy can be provided by the traditional etching technology. And it can tolerate an alignment error of 2° regarding the angle of incidence.

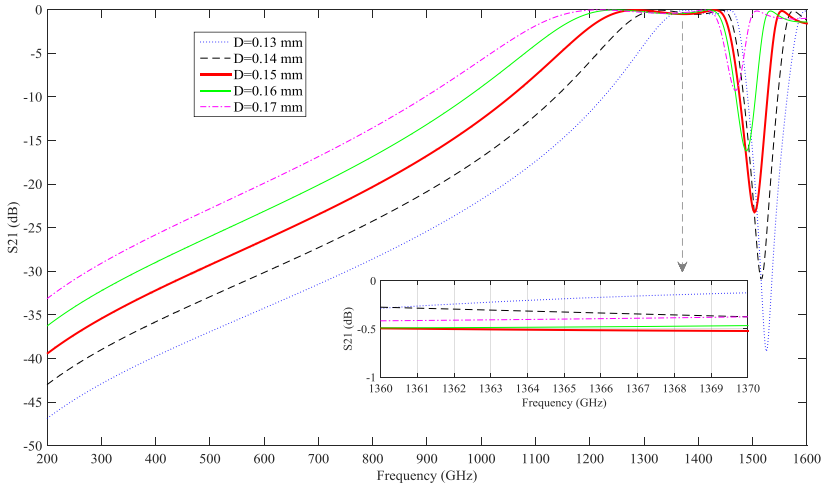

(b)

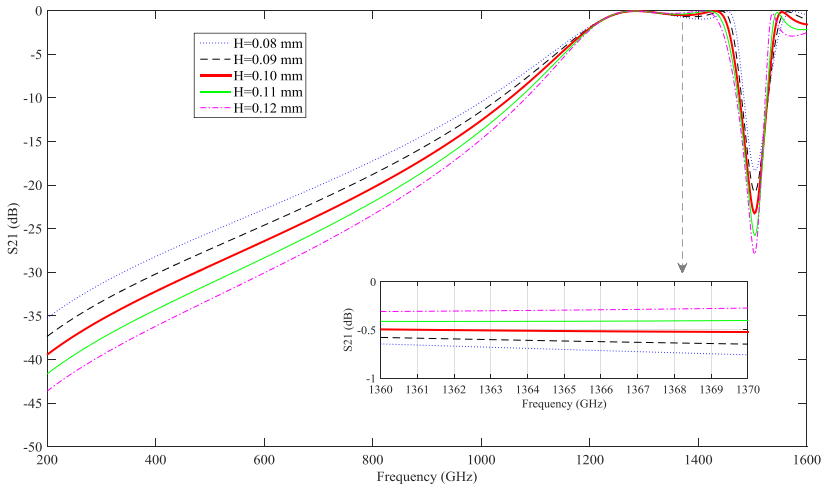

(c)

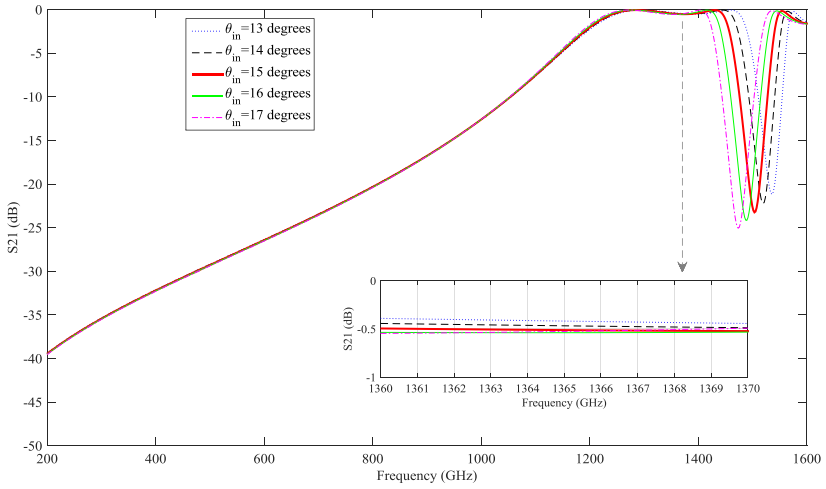

(d)

Figure 5-26: The S_{21} parameters of the designed FSS and the sensitivity test regarding D, H and θ_{in} with CST Microwave Studio. (a) The S_{21} parameters of the designed FSS; (b) The sensitivity test regarding D; (c) The sensitivity test regarding H; (d) The sensitivity test regarding θ_{in}.

Figure 5-26 (b) shows that as the diameter of the perforation varies from 0.13 mm to 0.17 mm, the insertion loss at 342 GHz remains higher than 27.66 dB while that at 1368 GHz stays below 0.52 dB. Figure 5-26 (c) shows that as the thickness of the brass slab varies from 0.08 mm to 0.12 mm, the insertion loss at 342 GHz remains higher than 29.94 dB while that at 1368 GHz keeps lower than 0.74 dB. And as the angle of incidence varies from 13° to 17°, the insertion loss at 342 GHz stays higher than 33.94 dB while that at 1368 GHz remains lower than 0.54 dB. From the above analysis, the designed FSS can tolerate fabrication error of 0.02 mm regarding the diameter of the circular perforations as well as the thickness of the FSS slab. The insertion loss can be maintained as below 1 dB given the above fabrication error. Such accuracy can be provided by the traditional etching technology. And it can tolerate an alignment error of 2° regarding the angle of incidence.

5.4.2 Possibility of Breakdown for the Designed FSS

For consideration of the electric breakdown problem, the maximum electric field (E_{max}) induced on the surface of the designed FSS by the incidence of the quasi-Gaussian beams should be examined. Since the FSS will be radiated by the two quasi-Gaussian beams simultaneously, E_{max} can be calculated as

$$E_{max} = E_{maxLF} + E_{maxHF} \tag{5.28}$$

where E_{maxLF} and E_{maxHF} are the maximum electric field induced on the FSS by the LF and the HF incidence, respectively. The electric breakdown will occur when

$$E_{max} > E_a \tag{5.29}$$

in which E_a is the breakdown electric field strength of the material around the FSS. In the design where a freestanding FSS is exposed to the air [117],

$$E_a = 3 \times 10^6\ V/m. \tag{5.30}$$

Since the incident waves on the FSS at 342 GHz and 1368 GHz are quasi-Gaussian beams with the maximum electric field amplitude of $E_{LF}^{in} = 2.25 \times 10^5\ V/m$ and

$E_{HF}^{in} = 2.38 \times 10^5\ V/m$, respectively, the determination of the E_{maxLF} and E_{maxHF} values is difficult. However, another set of variables can be defined to estimate the upper limit of the E_{maxLF} and E_{maxHF} values, which are denoted as E'_{maxLF} and E'_{maxHF}. E'_{maxLF} is the maximum electric field strength induced on the designed FSS when the incident field is a plane wave at 342 GHz with an uniform electric field amplitude of E_{LF}^{in}. And E'_{maxHF} denotes the maximum electric field strength induced on the FSS when the incident field is a plane wave at 1368 GHz with an uniform electric field amplitude of E_{HF}^{in}. Thus it can be interpreted that

$$E'_{maxLF} > E_{maxLF} \tag{5.31a}$$

$$E'_{maxHF} > E_{maxHF}. \tag{5.31b}$$

And the values of E'_{maxLF} and E'_{maxHF} can be calculated by [120]

$$E'_{maxLF} = E_{LF}^{in} \cdot MFEF_{LF} \tag{5.32a}$$

$$E'_{maxHF} = E_{HF}^{in} \cdot MFEF_{HF}. \tag{5.32b}$$

The maximum field enhancement factor (MFEF) is defined as the ratio between the maximum electric field amplitude inside the FSS and the incident electric field strength [120]. $MFEF_{LF}$ and $MFEF_{HF}$ are the MFEF factors at 342 GHz and 1368 GHz, respectively. And the values of $MFEF_{LF}$ and $MFEF_{HF}$ can be obtained from the full-wave EM simulation with CST MWS as 1.19 at 342 GHz and 3.28 at 1368 GHz, respectively. Thus it can be derived from (5.32) that

$$E'_{maxLF} = 0.27 \times 10^6\ V/m \tag{5.33a}$$

$$E'_{maxHF} = 0.78 \times 10^6\ V/m. \tag{5.33b}$$

By combining (5.30)-(5.33), it can be derived that

$$E_{max} < 1.05 \times 10^6\ V/m < E_a. \tag{5.34}$$

It can be seen that when being radiated by the high-power output from the DQMC, the induced maximum electric field on the FSS, while being considerably high, does not exceed the breakdown limit of the air. This implies that the above designed FSS is capable of handling the high-power THz output from the gyro-multiplier.

Chapter Summary

In this chapter, the design of the dual-harmonic quasi-optical mode converter (DQMC), the single disc window (SDW) and the frequency selective surface (FSS) are described. The study has shown that the high-order output modes from the gyro-multiplier can be effectively converted and separated by the designed output system into two quasi-Gaussian beams. The sensitivity test of the designed high-pass FSS is also conducted as the basis of the fabrication.

Chapter 6 Experimental Study of the FSS

This chapter focuses on the experimental study of the designed FSSs. It begins by introducing the experimental set-up of the THz-TDS test bench and its operation principle. Then, the measured results of the designed high-pass FSSs are summarised with comparison with the simulated ones. Finally, this chapter proposes and experimentally verifies some methods to improve the performance of the FSS.

6.1 Experimental Set-up

There are traditionally two types of system that can be used in the experimental characterisation of the FSS: the vector network analyser with testing frequency range up to 1.1 THz [164] and the THz-TDS system [13] with that typically between 0.1 THz and 3 THz. Since the FSSs to be used in the designed output system will operate at frequencies as high as 1368 GHz, the THz-TDS system is chosen for the experimental characterisation.

Figure 6-1 shows the THz-TDS system used to test the fabricated FSS. The system is developed in the Antenna Lab of Queen Mary University of London. Its effectiveness and accuracy have been demonstrated in a number of previous literatures [165-167].

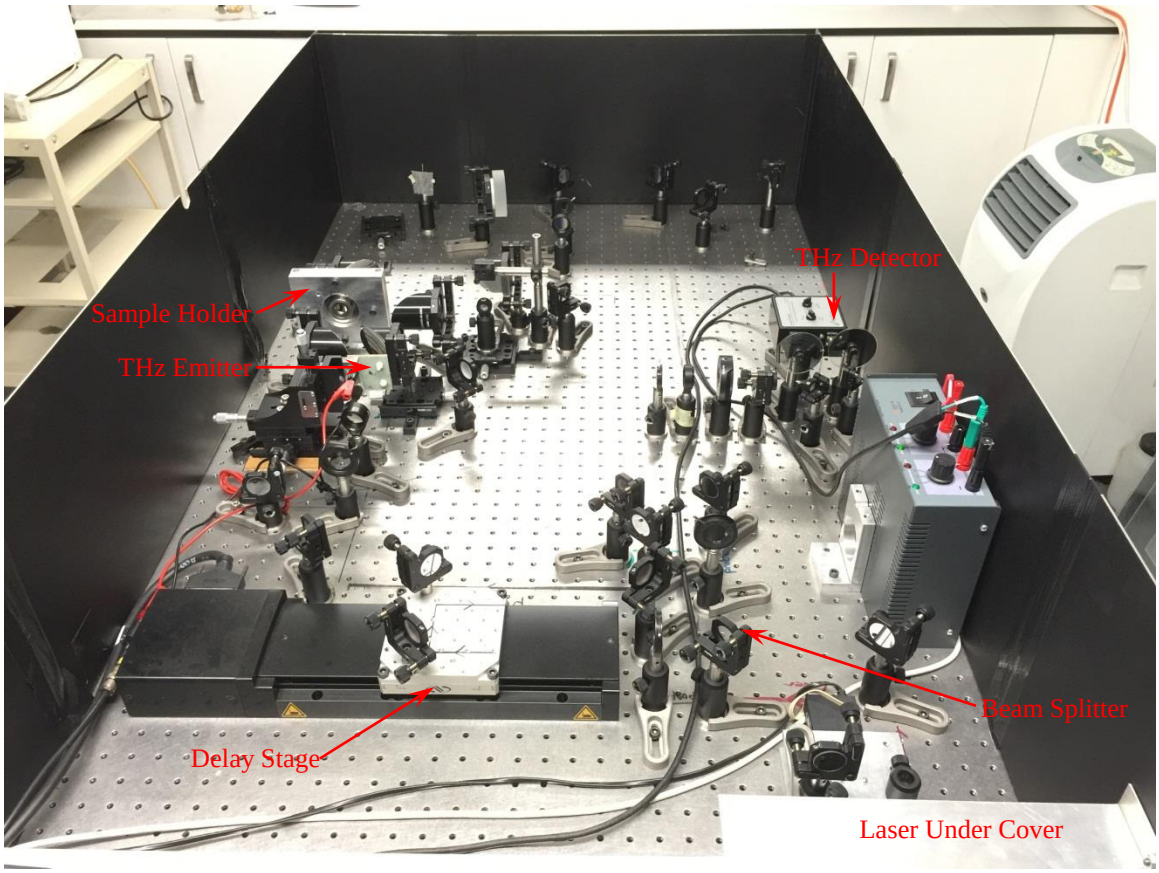

Figure 6-1: The THz-TDS bench used for the experimental test of the FSS.

Figure 6-2 shows the operation principle of the THz-TDS system. A femtosecond laser beam is generated from a Ti:Sapphire laser, which is then split into a pump and probe laser beam. The pump laser beam, after passing the delay stage, is used for excitation of the photoconductive antenna to generate THz radiation. The radiation is then guided by a number of mirrors along a beam path to go through the sample. After going through the sample, the transmitted THz signal can be detected by the probe laser beam by electro-optical sampling. The electro-optical sampling is based on the <110> ZnTe crystal which becomes birefringent when being exposed to the THz radiation. The polarisation of the probe laser beam, which is also directed through this crystal, will be rotated with an angle proportional to the electric field magnitude of the THz radiation. Then, by measuring the rotation angle, the electric field amplitude variation of the THz radiation as a function of the time delay induced by the delay stage, can be obtained. By applying the Fourier Transformation, the equivalent frequency domain spectrum can be generated.

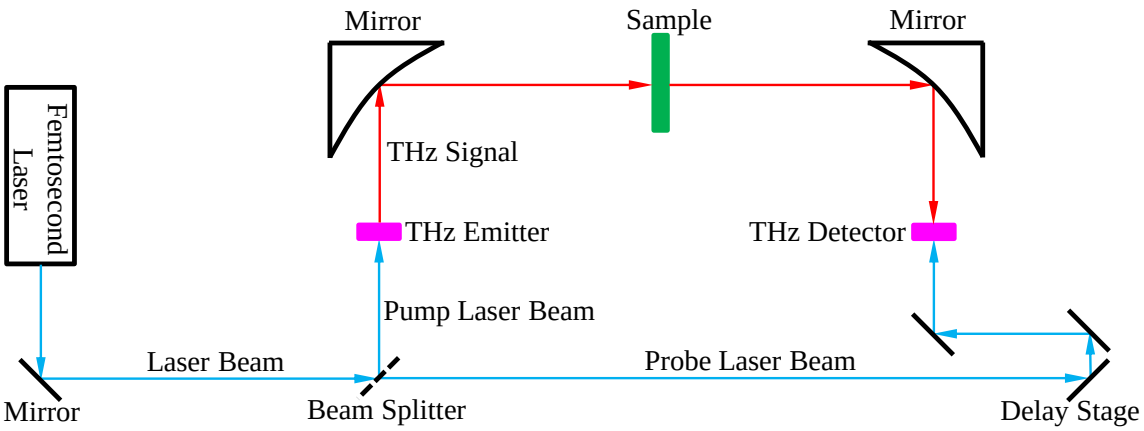

Figure 6-2: The schematic view of the THz-TDS system.

In the actual experiments with the THz-TDS system, the test should be conducted by two steps. Firstly, the sample measurement is conducted with the sample placed on the optical path of the THz radiation. The Fourier Transformation is performed to the received signal to retrieve the spectrum. Then, the same procedure is applied after removing the sample from the optical path of the THz signal. And a reference spectrum can be derived from the measurement. The ratio between the two spectra reveals the interaction between the sample and the THz signal, and can be used to calculate the S_{21} parameter of the designed FSS.

6.2 The FSS Experimental Results

Based on the parameters described in Section 5.4.1, two samples of the designed FSS are fabricated by perforations on a brass slab. And they are numbered as Sample 1 and Sample 2, respectively. Both samples are formed by arrays of 105×105 circular perforations.

Figure 6-3 shows the fabricated Sample 1 as a whole view. The detail of the array is too small to be distinguished by naked eyes. To identify the accuracy of the fabrication, a microscopic image of it is shown in Figure 6-4. Good alignment of the holes can be observed. Sample 2 is fabricated under the same condition and show similar images.

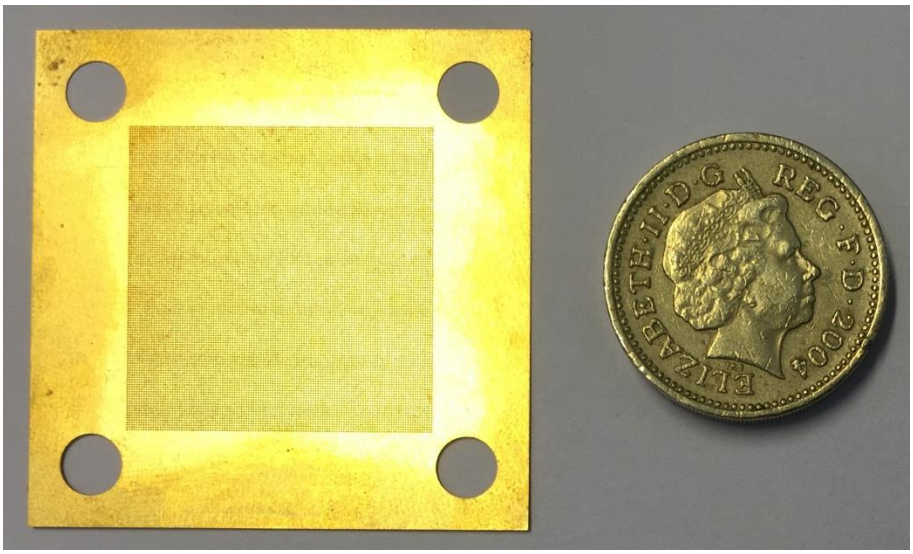

Figure 6-3: The fabricated FSS Sample 1.

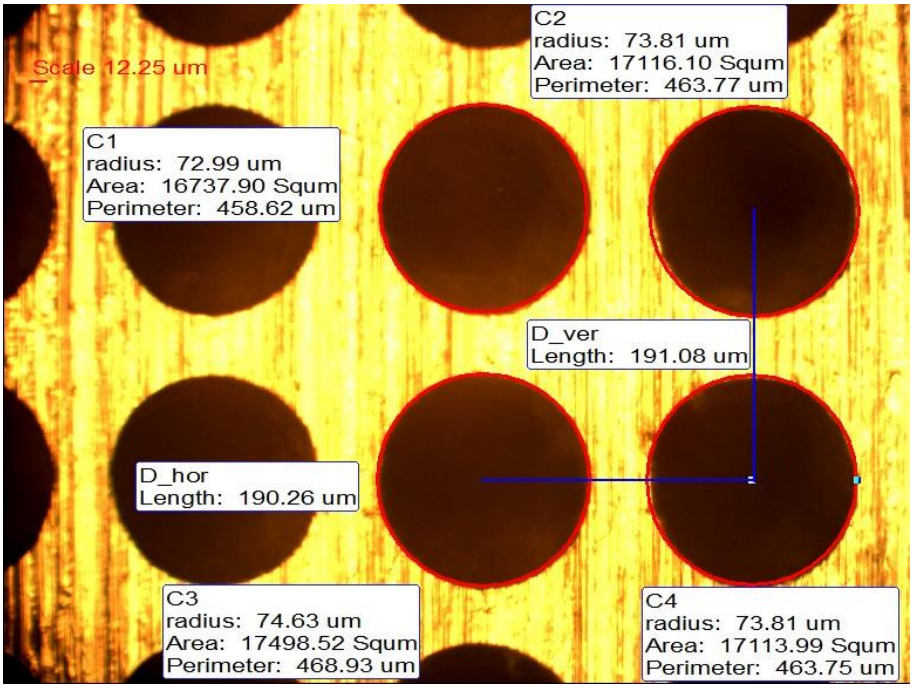

Figure 6-4: The microscopic view of FSS Sample 1.

The comparison between the designed parameters and the averaged fabricated sizes of the two samples are shown in Table 6-1. To obtain the averaged values of L_u, D and H, 10 measurements at different locations are taken for both samples. The values of the 20 measurements are then averaged. It is found that the diameters of the individual perforations vary from 144 um to 152 um. The fabricated thickness of the FSS slab is also in good agreement with the designed value.

Table 6-1: The comparison between the designed parameters and averaged fabricated sizes.

	$L_u\ (mm)$	$D\ (mm)$	$H\ (mm)$
Designed	0.190	0.150	0.100
Fabricated	0.187	0.149	0.097
Relative Error	1.6%	0.7%	3%

Having verified the accuracy of the fabrication, the designed FSS is then tested in the aforementioned THz-TDS system to experimentally characterise the S_{21} performances. Firstly, by scanning the delay stage in Figure 6-2 without the FSS sample, the 100 fs probe laser beam can sample the reference THz signal in the time domain. Then, the same process is repeated with the FSS placed in the path of the THz signal, to record the sample pulse. The recorded reference and sample pulses are shown by the red and blue curves in Figure 6-5, respectively. In the test, the step width d of the delay stage is set as 10 μm. By moving the delay stage by one step, the increased length of the optical path is $2d$. Thus each step of the delay stage represents a time delay of $2d/c$, where c is the speed of light in free space.

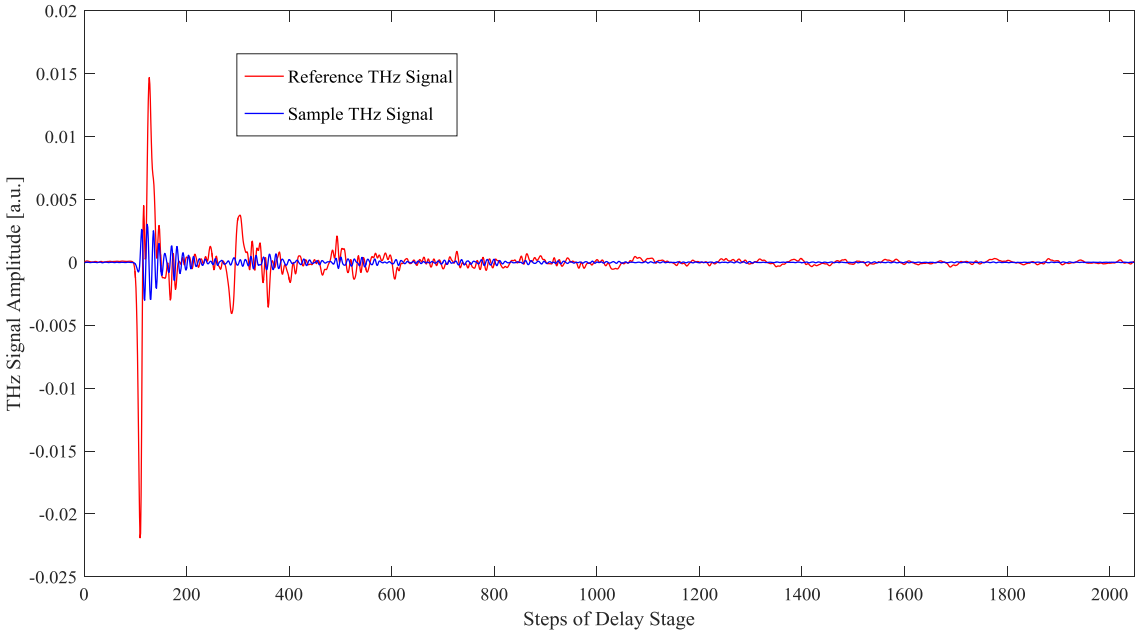

Figure 6-5: The experimental recorded time domain variation of the reference and test THz signal for Sample 1.

By Fourier Transformation of both signals from time domain to frequency domain, the spectrum of the reference and sample signals are shown in Figure 6-6. As the dynamic range of the THz-TDS system is from 0.1 THz to 3 THz, only the spectrum within this frequency range is shown.

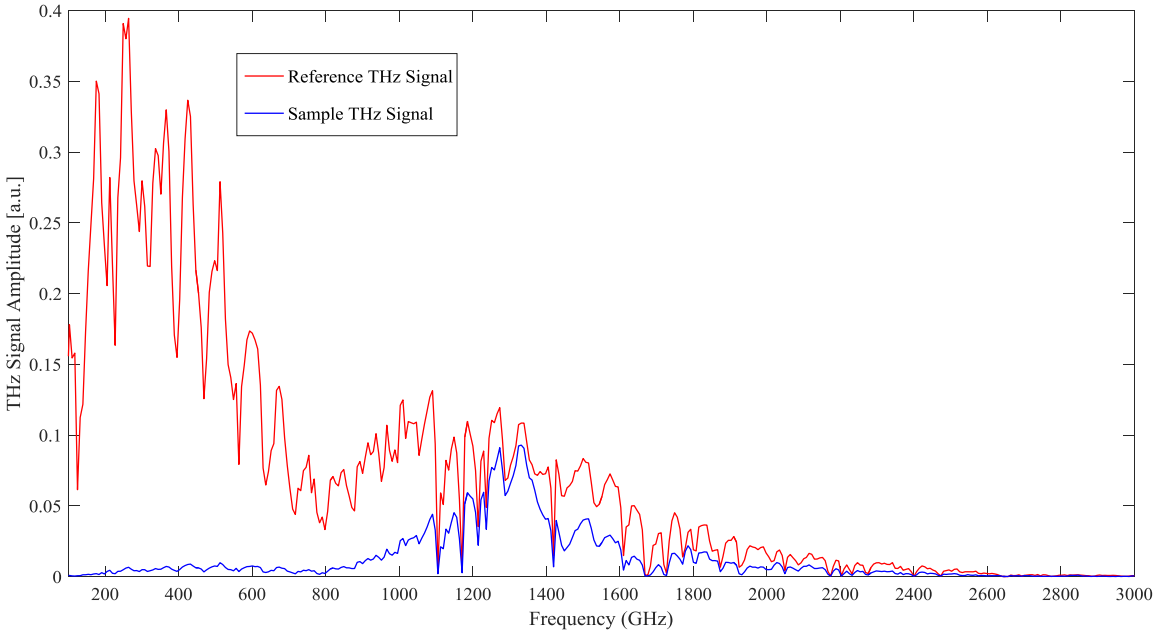

Figure 6-6: The frequency domain spectrum of the reference and test THz signal for Sample 1.

Assuming that the amplitudes of the reference signal and the test THz signal at a given frequency point are E_{ref} and E_{sam}, respectively, the S_{21} parameter at this frequency can be calculated as

$$S_{21} = 20log\frac{E_{sam}}{E_{ref}}. \tag{6.1}$$

Figure 6-7 shows the comparison between the simulated and the measured results of the S_{21} performance for the two samples. In the simulation with the unit cell model and periodic boundary condition, the two fundamental Floquet modes are considered [73]. Simulation with more Floquet port modes will generate more accurate results, while taking more time. The black curve is the simulated S_{21} variation with frequency using the averaged fabricated parameters as listed in Table 6-1. The red-circle and blue-square curves are the experimental S_{21} when either side of the FSS is placed facing the incoming THz wave of the test system. It can be seen that both samples show similar S_{21}

performance within the frequency range between 200 GHz and 1600 GHz. And both the simulation and the experimental results show similar variation trend of the S_{21} parameters regarding the frequency.

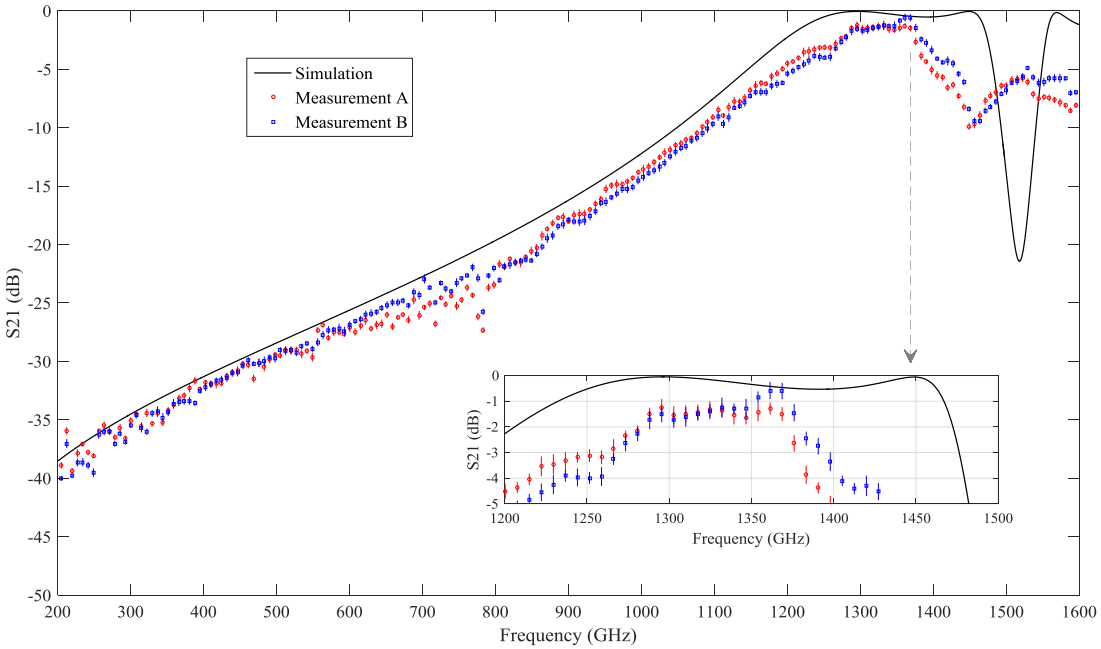

(a)

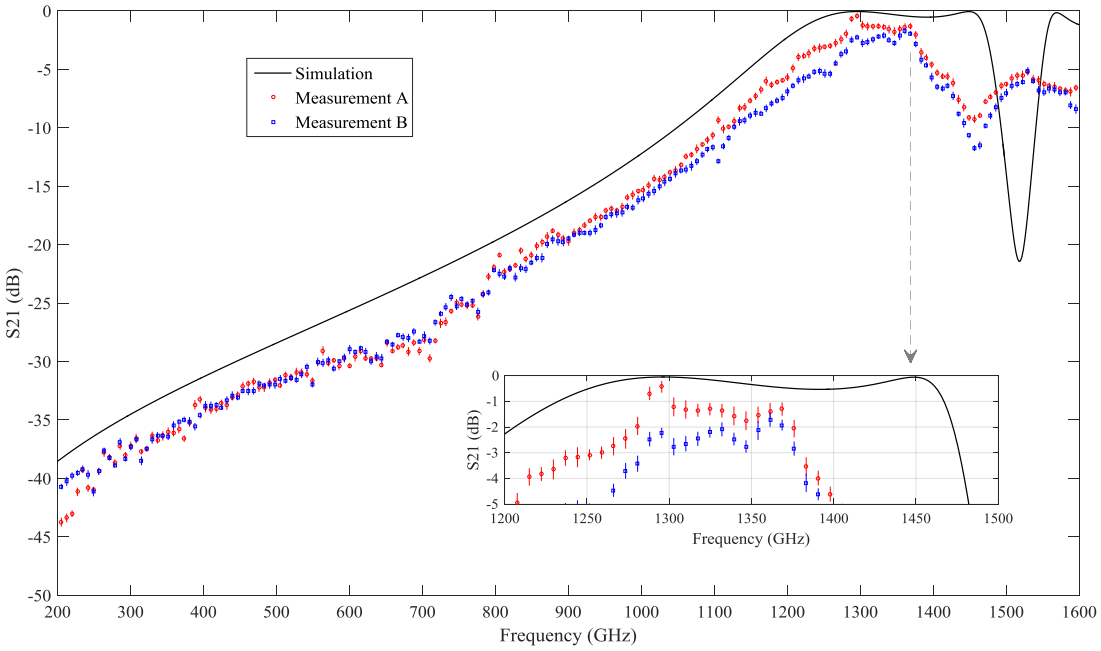

(b)

Figure 6-7: The comparison between the simulation and experimental results for: (a) Sample 1; (b) Sample 2. The black curve is the simulated S_{21} performance with the measured sizes listed in Table 6-1. The red-circle and blue-square curves are the measured S_{21} performance when the two sides of the FSS sample are facing the incoming test beam, respectively.

Based on the results shown in Figure 6-7, the averaged experimental S_{21} values at 342 GHz and 1368 GHz for the two samples are summarised in Table 6-2. It can be seen that the insertion loss values of the two samples at 342 GHz are higher than 34.85 dB, showing satisfactory rejecting property at this frequency. The insertion loss values at 1368 GHz for the two samples are 1.05 dB and 1.61 dB, respectively. The -3 dB transmission bandwidths in the experiments are narrower than their counterparts in the simulations, which can be attributed to the surface roughness, the flatness of the slab, and the diameter variation of each hole at different depths.

Table 6-2: Summary of the transmission performance of the fabricated samples.

	S_{21} at 342 GHz	S_{21} at 1368 GHz	Maximum S_{21}	Frequency point with maximum S_{21}
Sample 1	-34.85 dB	-1.05 dB	-0.94 dB	1361 GHz
Sample 2	-36.41dB	-1.61 dB	-1.35 dB	1295 GHz

Table 6-2 also summarises the highest values of the S_{21} parameters of the two FSS samples and the frequency points at which they are reached. It can be seen that the lowest insertion loss values of the FSSs are reached at frequencies lower than 1368 GHz.

The above analysis naturally leads to two methods to increase the transmission performance at 1368 GHz. On the one hand, fabrication technologies other than the etching process can be used for improved precision, such as the computer numerically controlled (CNC) milling machining [168] process. On the other hand, given the limited fabrication precision in the THz range, the FSS design can be modified to enable better transmission performance at 1368 GHz. For example, the diameter of the perforations can be reduced to around 0.14 mm, which will help to increase the frequency at which the maximum S_{21} is obtained. And the hexagonal array instead of the square array is also worth looking into for its potential to reduce the diffraction loss of the FSS at 1368 GHz.

6.3 The Designs for Improvement

Several methods to increase the transmission coefficient of the high-pass FSS at 1368 GHz have been proposed in the previous section. In this section, the effort of employing smaller perforation diameter, smaller inter-element spacing and a hexagonal array are carried out. It should be noted that due to the availability issue, the copper plates are used in the following fabrication, instead of the previously used brass ones.

6.3.1 FSSs with Smaller Perforation Diameter

It can be interpreted from Figure 6-7 that by reducing the perforation diameter of the FSS, the S_{21} curve will have its peak located at frequencies around 1368 GHz. This section will be dedicated to utilise such algorithm.

Table 6-3 shows the comparison between the original design parameters used for the previous samples and the new ones. Compared with Sample 1 and 2, Sample 3 has the same inter-element spacing but smaller perforation diameter. Sample 4 utilise both smaller L_u and D values. The designed thickness of the FSS slab is kept the same.

Table 6-3: The comparison between the design of Sample 1&2 and the proposed new designs.

	$L_u(mm)$	$D(mm)$	$H(mm)$
Design of Sample 1&2	0.190	0.150	0.100
Design of Sample 3	0.190	0.140	0.100
Design of Sample 4	0.180	0.140	0.100

Figure 6-8 shows the comparison between the S_{21} of the design for Sample 1&2 and the new designs. It can be seen that the transmission bands of the new designs are located in relative higher frequency range than the original design.

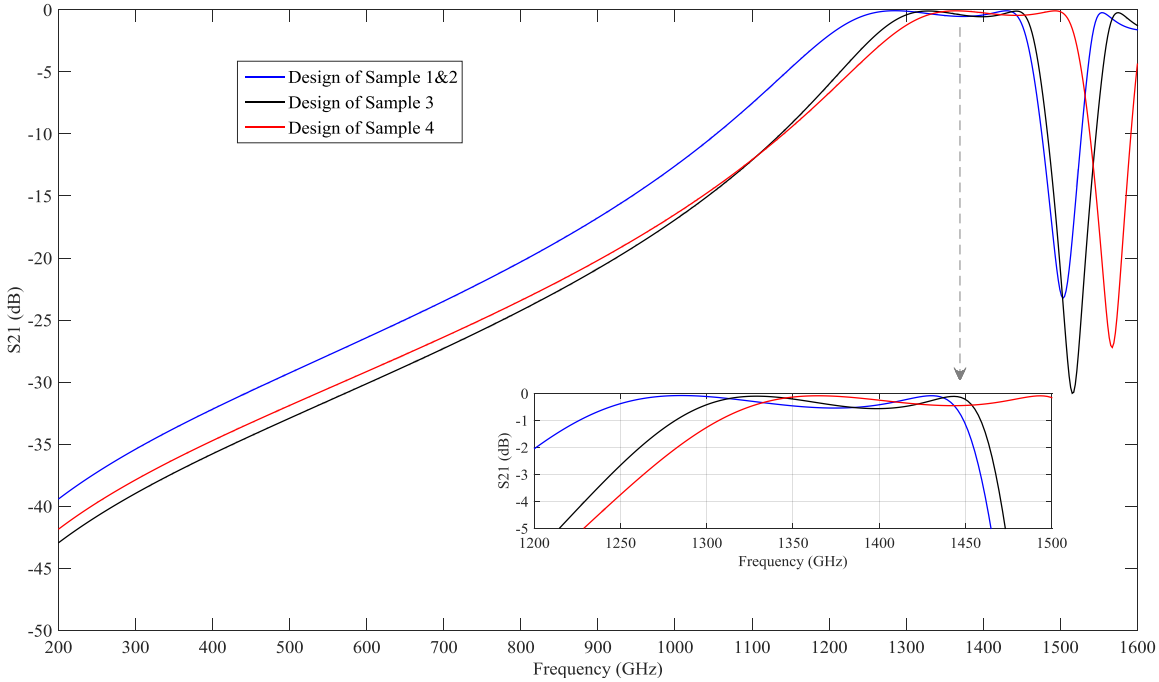

Figure 6-8: The comparison between the S_{21} performance of the design for Sample 1&2 and the new designs.

Figure 6-9 shows the fabricated Sample 3 as a whole view. To assess the quality of the fabrication, a microscopic image of it is shown in Figure 6-10. Good alignment of the holes can be observed. It is however noted that the quality of the circular perforation is generally poorer than that of Sample 1 as shown in Figure 6-4. The is because to achieve perforations with diameters below 0.15 mm is beyond the upper limit of the etching technology used in the fabrication [169]. The concentration of the chemical drugs and the exposure time during the etching process may also affect the quality of fabrication.

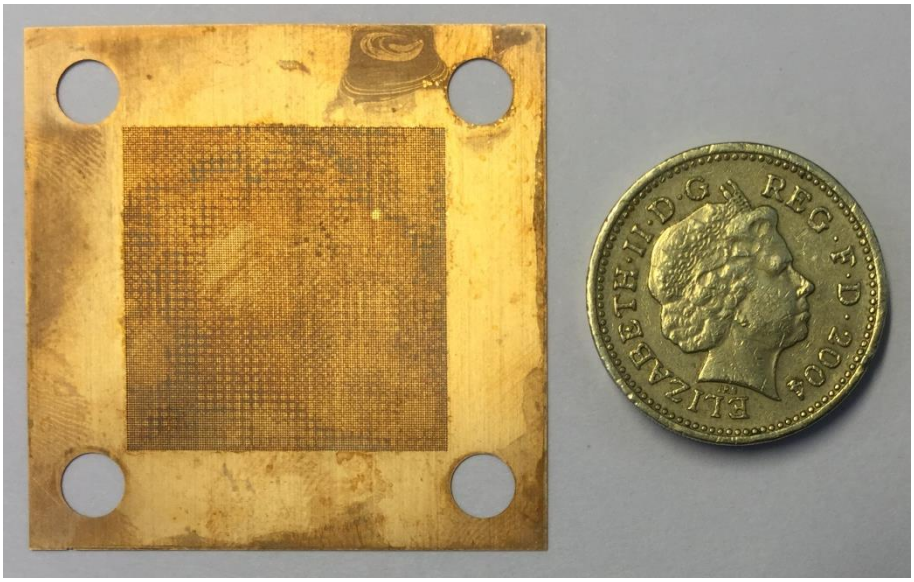

Figure 6-9: The fabricated Sample 3 with copper. Sample 4 shares the same arrangement but is of different sizes.

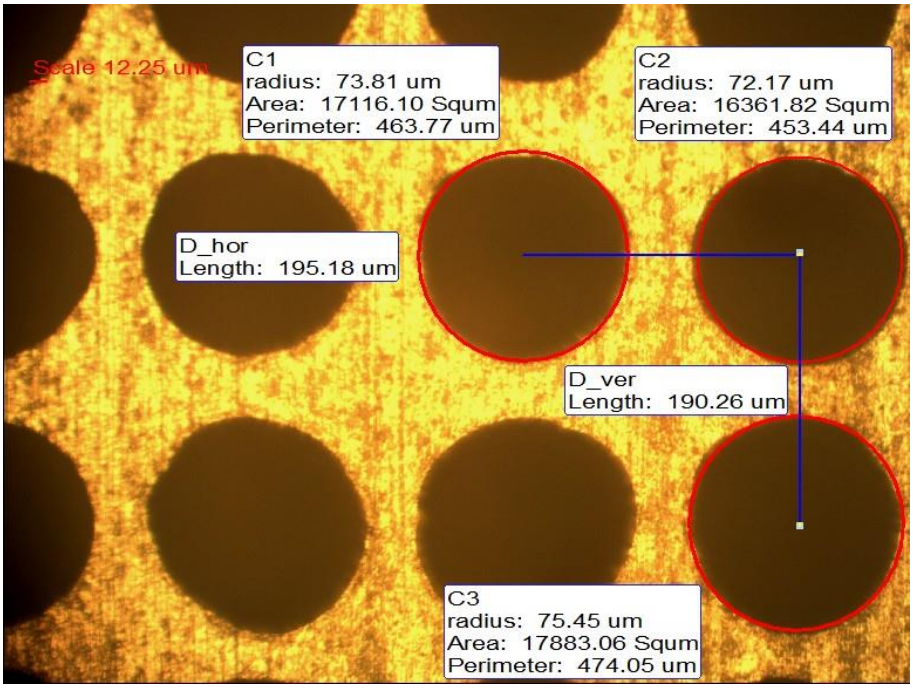

Figure 6-10: The microscopic view of FSS Sample 3. The quality of the perforations are generally worse than that of Sample 1, as shown in Figure 6-4.

Similar degradation of fabrication accuracy can be observed from the microscopic view of Sample 4, as shown in Figure 6-11.

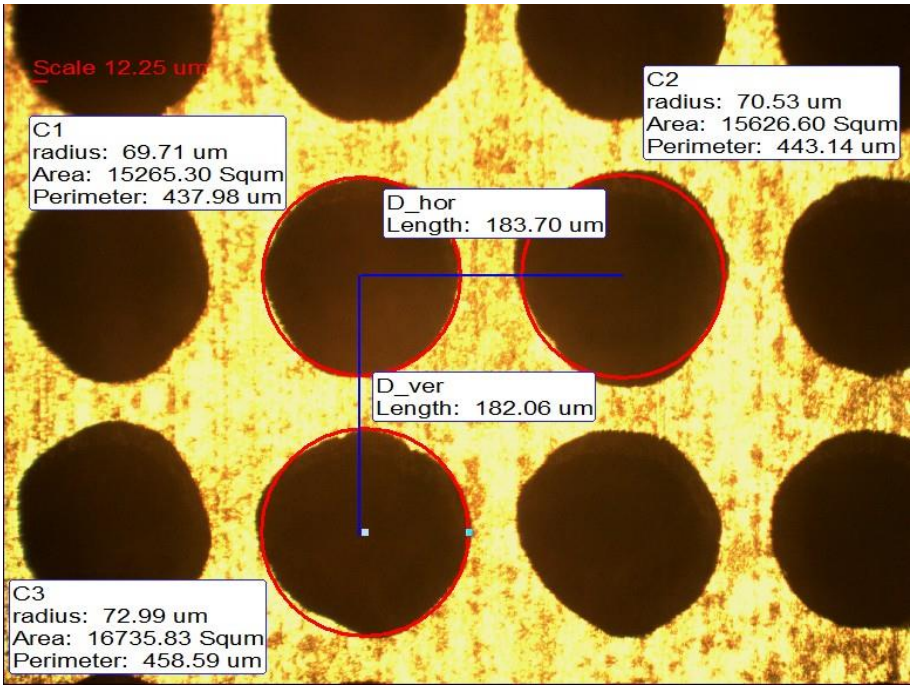

Figure 6-11: The microscopic view of FSS Sample 4.

The comparison between the designed and averaged fabrication sizes for Sample 3 and 4 can be seen in Table 6-4. The averaged fabricated sizes are obtained by 10 sample measurements.

Table 6-4: The comparison between the design and averaged fabricated sizes for Sample 3 and 4.

	$L_u(mm)$	$D(mm)$	$H(mm)$
Design of Sample 3	0.190	0.140	0.100
Fabricated of Sample 3	0.193	0.147	0.097
Relative Error	1.6%	5%	3%
Design of Sample 4	0.180	0.140	0.100
Fabricated of Sample 4	0.182	0.142	0.098
Relative Error	1.1%	1.4%	2%

Figure 6-12 shows the comparison between the simulation results using the fabricated parameters in Table 6-4 and the experimental outcomes for Sample 3 and 4. It can be

seen that due to the limited fabrication precision, the transmission bandwidths in the experiment are narrower than those in the simulation.

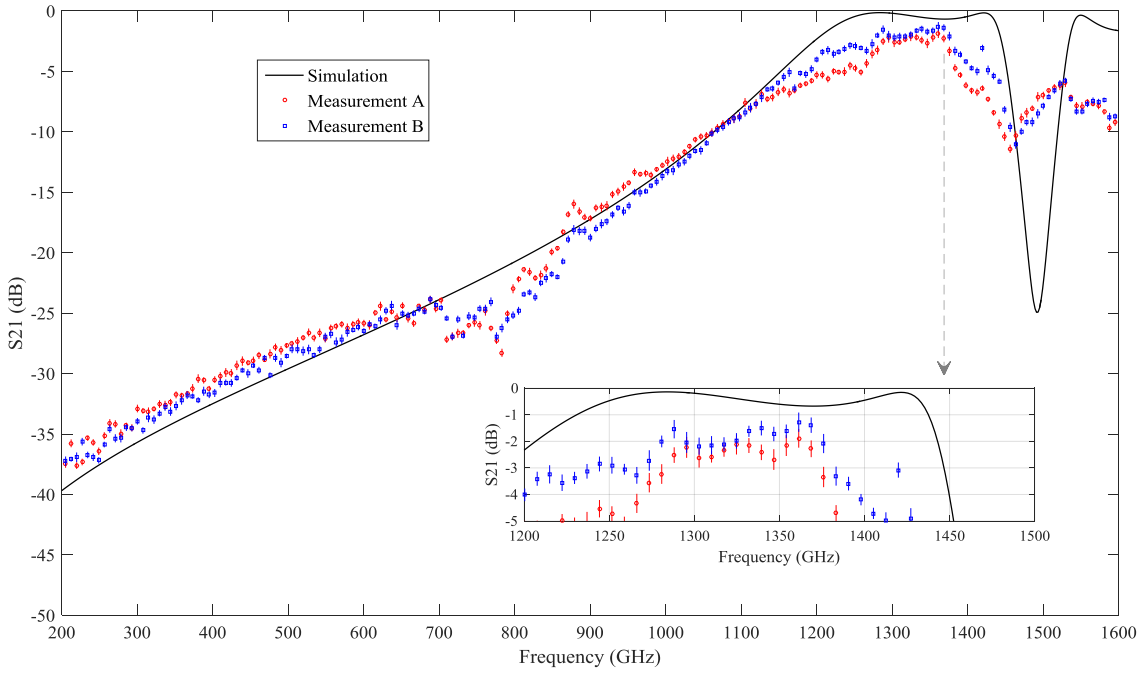

(a)

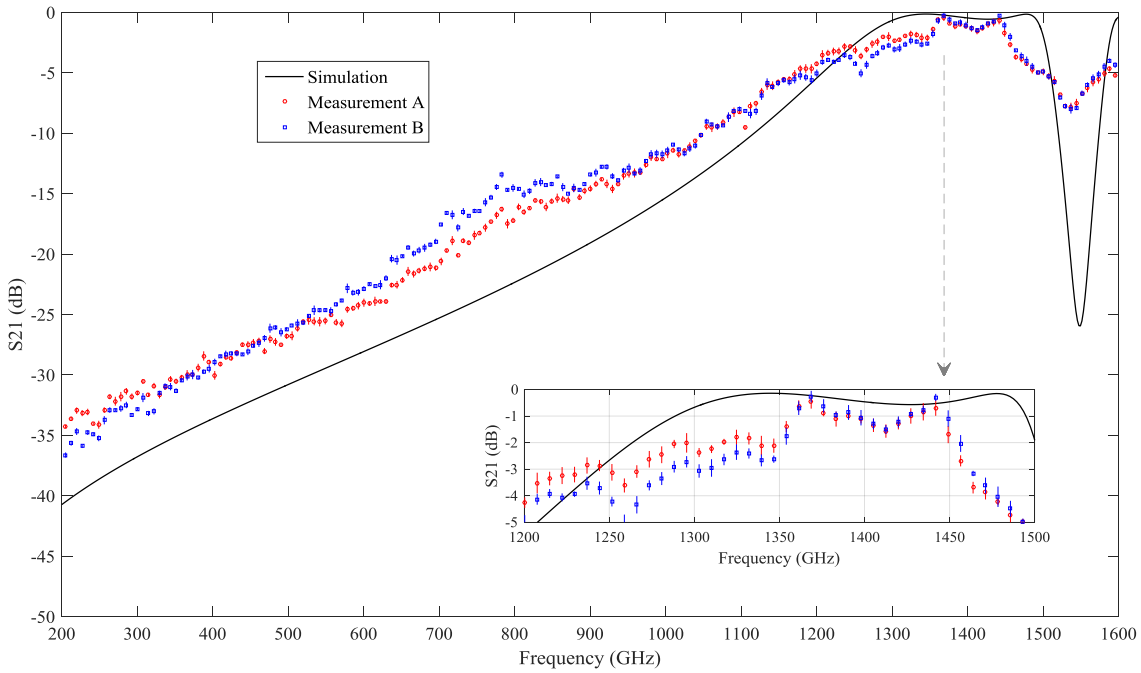

(b)

Figure 6-12: The comparison between the simulation and experimental results for: (a) Sample 3; (b) Sample 4. The black curve is the simulated S_{21} performance with the designed sizes listed in Table 6-4. The red and blue curves are the measured S_{21} performance when the two sides of the FSS sample are facing the incoming test beam, respectively.

Table 6-5 summarises the S_{21} performance comparison between Sample 1, 3 and 4. It can be seen that all the three FSSs have high reflectivity at 342 GHz. Since Sample 3 and Sample 4 are fabricated at the same time and under the same condition, a fair comparison can be made between the two. The fact that the insertion loss of Sample 4 at 1368 GHz is much lower than that of Sample 3 suggests that the inter-element spacing is an essential parameter in determining the performance of the FSS. This is because the diffraction loss can be reduced by adopting smaller inter-element spacing [170]. Further reduction of the insertion loss at 1368 GHz by decreasing L_u is restricted by the capability of the etching technique.

Table 6-5: The S_{21} performance comparison among Sample 1, 3 and 4.

	S_{21} at 342 GHz	S_{21} at 1368 GHz
Sample 1	-34.85 dB	-1.05 dB
Sample 3	-32.75 dB	-1.81 dB
Sample 4	-30.76 dB	-0.40 dB

6.3.2 FSS of Hexagonal Array

The hexagonal array is shown in Figure 6-13. In such arrangement, each perforation is surrounded by six neighbouring units. And the distances between the central unit and the neighbouring units are the same.

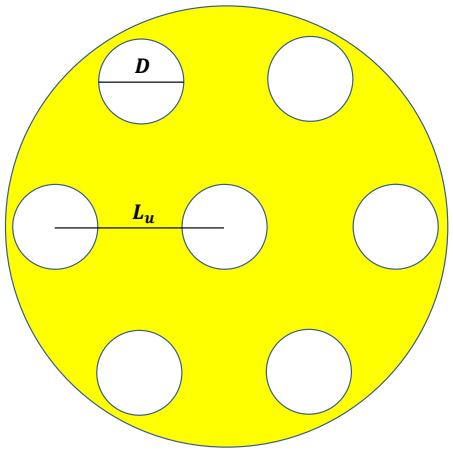

Figure 6-13: The schematic view of the hexagonal array.

The reason for looking into the hexagonal arrangement is its potential to employ larger inter-element spacing, L_u. The diffraction limit for the FSS with periodic perforations can be expressed as [171]

$$\left(\frac{L_u}{\lambda}\right)_{max} = \frac{1}{A(1+sin\theta_{in})} \tag{6.2}$$

for an air-dielectric environment. λ is the wavelength and

$$A = \begin{cases} 1 & for\ squrare\ array \\ 0.5\sqrt{3} & for\ hexagonal\ array. \end{cases} \tag{6.3}$$

When the ratio between L_u and λ exceeds this limit, the transmission diffraction will occur and the transmission coefficient of the FSS will decrease. It can be seen from (6.2) and (6.3) that the hexagonal array generally has higher diffraction limit, meaning that relatively larger value of L_u can be used without degrading the S_{21} performance.

Table 6-6 summarised the design parameters of Sample 1 and 5. Also presented are the theoretical diffraction limits for the two designs. It can be seen that the design of Sample 1 has exceeded the diffraction limit of the square array. And the design of Sample 5 stays within the diffraction limit of the hexagonal array even when L_u is chosen as 0.20 mm.

Figure 6-14 shows the comparison between the S_{21} curve of the design for Sample 1&2 and that of the new design. It can be seen that while both designs show good transmission performance at 1368 GHz, the transmission band of the new design is located at relative higher frequencies than the original design.

Table 6-6: The design parameters as well as the diffraction limit comparison between the original design and the design used for Sample 5. Here $\lambda = 0.22\ mm$ corresponding to 1368 GHz.

	$L_u(mm)$	$D(mm)$	$H(mm)$	$\left(\frac{L_u}{\lambda}\right)_{max}$	$\frac{L_u}{\lambda}$
Sample 1	0.19	0.15	0.10	0.79	0.86
Sample 5	0.20	0.14	0.10	0.92	0.91

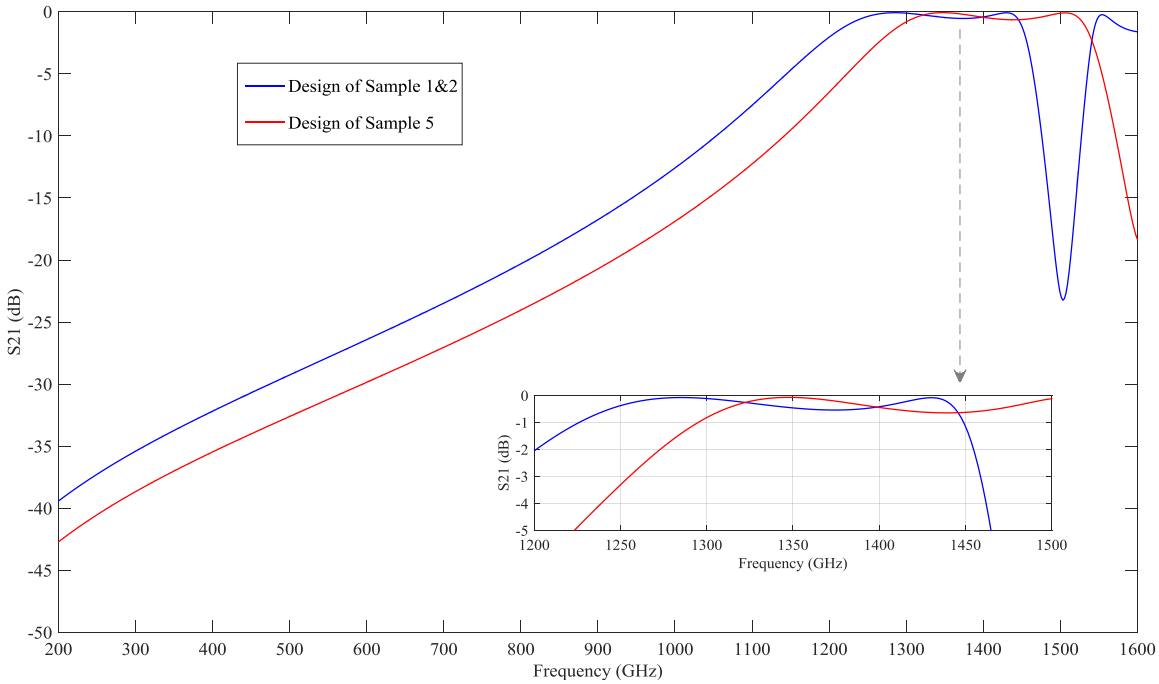

Figure 6-14: The comparison between the S_{21} performance of the original design and the design of the hexagonal array.

Figure 6-15 and Figure 6-16 show the whole and microscopic views of the fabricated Sample 5, respectively. Good alignment of the hexagonally arranged holes can be observed. It is also noted that the quality of the circular perforation is generally worse than that of Sample 1 as shown in Figure 6-4, the reason of which has been discussed earlier.

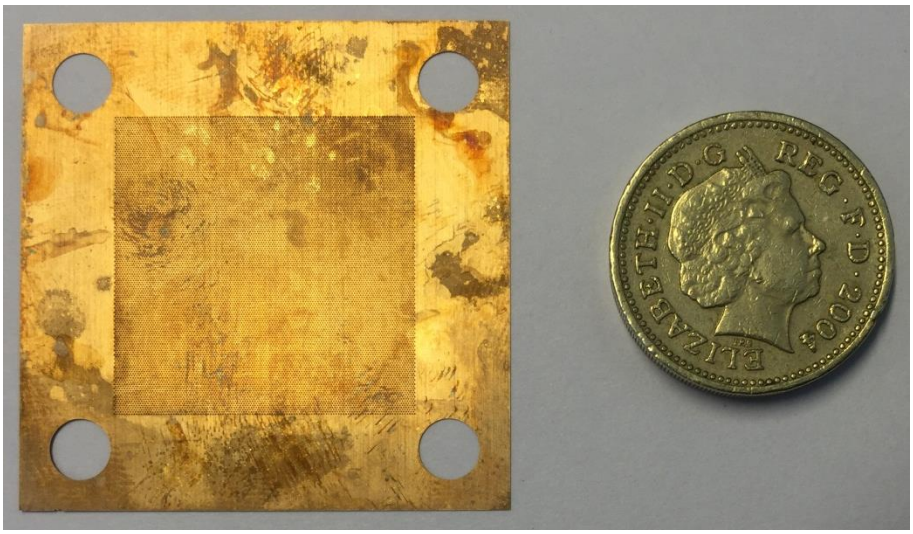

Figure 6-15: Fabricated Sample 5 with copper.

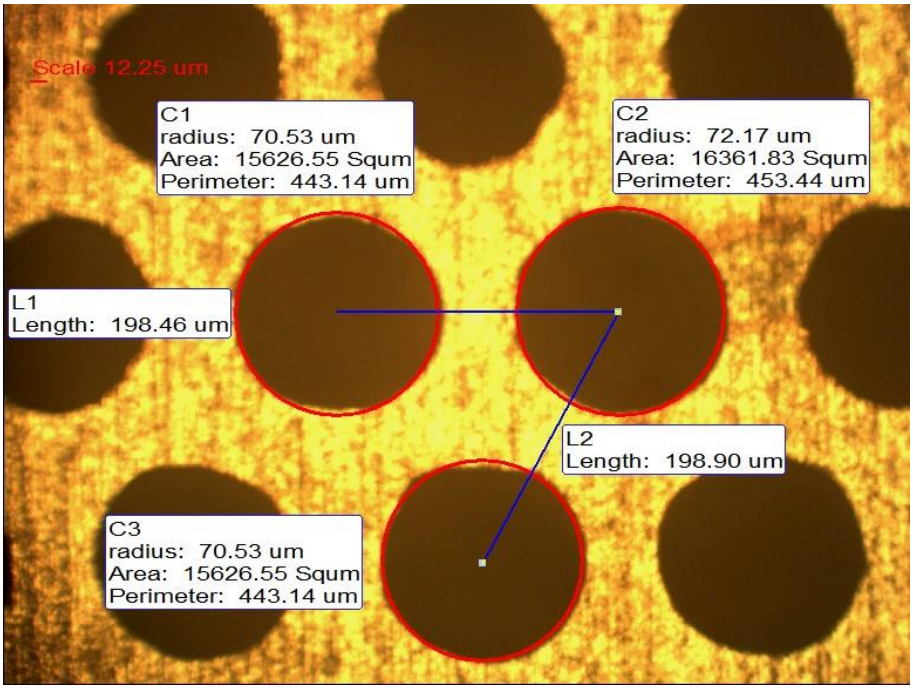

Figure 6-16: The microscopic view of FSS Sample 5.

Table 6-7 compares the designed and the averaged fabricated sizes of Sample 5. The averaged fabricated sizes are obtained by 10 sample measurements.

Table 6-7: The comparison between the design and averaged fabricated sizes for Sample 5.

	$L_u(mm)$	$D(mm)$	$H(mm)$
Design	0.200	0.140	0.100
Fabricated	0.199	0.144	0.099
Relative Error	0.5%	2.9%	1%

Figure 6-17 shows the comparison between the simulation results of Sample 5 using the fabricated sizes in Table 6-7 and the experimental results. It can be seen that the two reasonably agrees with each other. The narrower transmission bandwidth of the experimental result can be attributed to the fabrication errors, as discussed earlier.

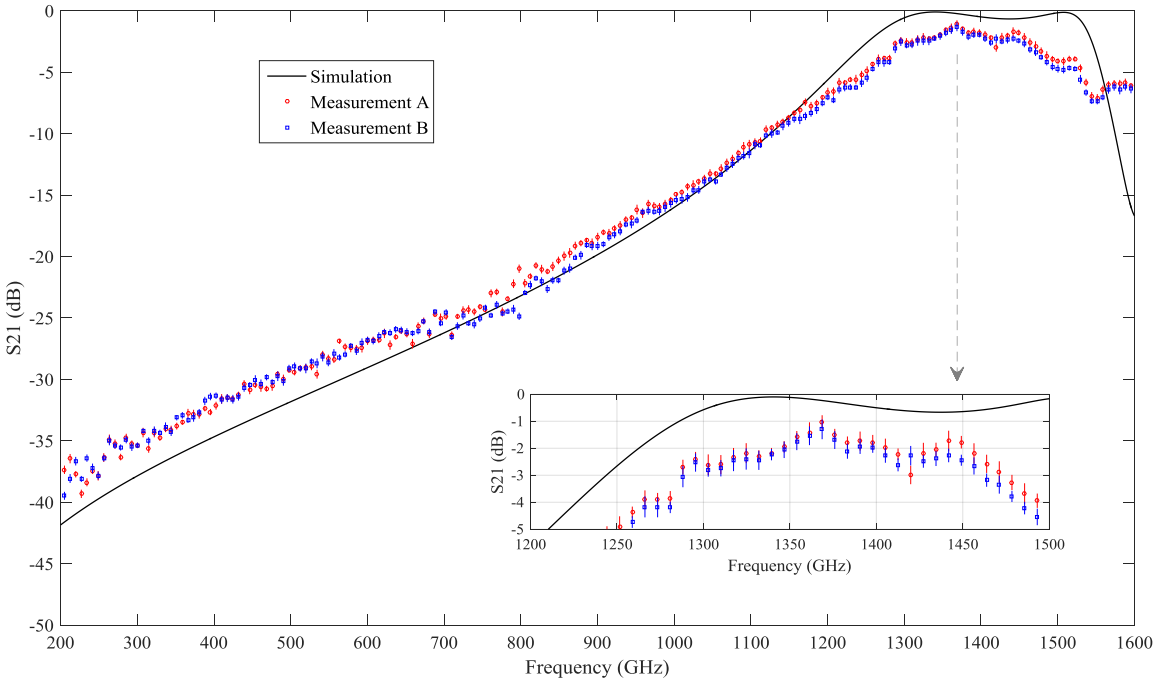

Figure 6-17: The comparison between the simulation and experimental results for Sample 5. The black curve is the simulated S_{21} performance with the designed sizes listed in Table 6-7. The red and blue curves are the measured S_{21} performance when the two sides of the FSS sample are facing the incoming test beam, respectively.

Table 6-8 summarised the comparison between the S_{21} values of Sample 1 and Sample 5. Both have similar performance at the two designed frequencies, while the latter enables the adoption of the larger inter-element spacing, which is a favourable factor to alleviate the fabrication difficulties.

Table 6-8: The comparison between the experimental S_{21} performance of Sample 1 and 5.

	S_{21} at 342 GHz	S_{21} at 1368 GHz
Sample 1	-34.85 dB	-1.05 dB
Sample 5	-34.11 dB	-1.19 dB

By measuring the fabricated FSS samples, the root-mean-squared (rms) values of the fabrication error regarding the perforation diameter are calculated to be 2 μm, 2 μm, 7 μm, 5 μm and 5 μm for Sample 1 to 5, respectively. The fabrication error is mainly determined by the metal used for the fabrication, the expertise of the operator, the concentration of the chemical solution and exposure time of the sample.

It can be seen from the above experimental results and analysis that without utilising the fabrication technologies with higher precision, such as the nano-CNC technology [172] which is typically more time-consuming and expensive, the performances of some of the fabricated FSSs are satisfactory. The trade-off of using the traditional etching technique in this study is that due to the limited precision, the surface roughness property and the non-uniformity of the perforations, the transmission bandwidth is narrowed, which is however an unnecessary concern in this study as the gyro-multiplier is an oscillator with very narrow operation frequency bands. It is also foreseeable that even larger angles of incidence can also be realised with sacrifice of the transmission bandwidth.

Chapter Summary

In this chapter, the fabrication and experimental test of the high-pass FSSs are described in detail. The experimental results have confirmed the validity of the design procedure in Chapter 5. It is shown that by the original design, the insertion loss of the fabricated FSS at 1368 GHz is 1.05 dB while that at 342 GHz is 34.85 dB. To reduce the insertion loss at 1368 GHz, several methods have been utilised, namely the adoption of smaller perforation diameters, reduced inter-element spacing and hexagonal array. Sample 4 which employs smaller inter-element spacing and perforations has shown the lowest insertion loss of 0.4 dB among all the samples. Sample 5 of hexagonal type shows similar S_{21} value at 1368 as the original design, but enables larger inter-element spacing. The performances of Sample 1, 4 and 5 will be sufficient to fulfil the requirement of the gyro-multiplier output system. The error analysis regarding the fabrication of the FSSs has also been done.

Chapter 7 Conclusions

This chapter concludes the thesis, highlights the key contributions and suggests the future work. The author's publications during the doctoral study are also listed.

7.1 Summary of Previous Work

This thesis focuses on the high-harmonic operation of the gyro-devices in the THz range, which has great potential of reducing the required external magnetic field. Specifically, it involves the numerical tool development for the gyrotrons, the study of high-harmonic beam-wave interaction in a large-orbit gyrotron (LOG) and the investigation of the output system for a fourth-harmonic gyro-multiplier.

Firstly, the steady-state non-linear theory has been adopted in the development of a complex-cavity large-orbit gyrotron, which also serves as the basis for the sectioned-cavity gyro-multiplier. The cold-cavity code generated from this theory can be adopted in the analysis of high-harmonic gyro-devices. The corresponding hot-cavity simulation code has been verified by comparing its result with that from the 3D PIC software. Such code can be further upgraded and used in the analysis of the sectioned-cavity gyro-multiplier in the steady-state.

Secondly, a high-harmonic LOG operating with the $TE_{m,1,1}$ modes (m=4-9) has been designed and characterised in the THz band. The operation of the designed LOG at the eighth harmonic with the $TE_{8,1,1}$ modes is investigated in detail to give an overview of the beam-wave interaction dynamics, starting oscillation process and the Ohmic loss at very high harmonics. The parameter variation study is also performed to provide a general conclusion of the high-harmonic LOGs operation. The study is then extended to show that by proper choice of the operation parameters, selective excitation of oscillation from the fourth to the ninth harmonic of the electron cyclotron resonance can be achieved with kW-level output power from 230 GHz to 465 GHz. By enabling the high-harmonics operation, the required external magnetic field strengths are reduced to the range between

2.6 T to 3.1 T. Upon verification of the model, the multi-modes, multi-harmonics behaviour of the designed LOG is studied by looking into the mode competition scenario between neighbouring harmonics. The operation points at which the single mode operation can be enabled are also discussed.

Thirdly, the investigation of a quasi-optical output system for the fourth-harmonic gyro-multiplier in the THz band has been conducted. To solve the challenges in conversion and separation of the dual-harmonic output from the gyro-multiplier, a dual-harmonic quasi-optical mode converter (DQMC) and a frequency selective surface (FSS) are integrated within this system. The design of the DQMC is based on the consideration of the transmission characteristics of both high-order waveguide modes. It is shown that the optimal design of the DQMC is enabled by the special mode selection criteria of the gyro-multiplier. The converted quasi-Gaussian beams show Gaussian contents of 94.6 % and 89.6% at 342 GHz and 1368 GHz, respectively. The high-pass FSS is designed, fabricated and experimentally verified by a THz-TDS system. Reasonable agreement between the simulated results and experimental ones has been achieved. After demonstrating that the designed FSS is capable of handling the high-power output from the gyro-multiplier, several methods of improving its performance have been proposed and experimentally tested. Of all the fabricated FSSs, the one with the best performance has shown insertion loss values of 30.76 dB at 342 GHz and 0.4 dB at 1368 GHz, which can well satisfy the requirement of the output system.

7.2 Key Contributions

The key contributions to knowledge from this thesis are summarised as follows:

A nonlinear steady-state simulation code has been developed as an in-house tool for the analysis of gyro-devices. This tool is verified by comparison of the generated results with that from the 3D PIC software and proved to be efficient at the design stage of the gyro-devices.

A comprehensive study of the high-harmonic operation of a LOG with the $TE_{m,1,1}$ modes (m=4-9) is conducted in the THz band with the assistant of 3D PIC simulation. Based on

the model, the multi-modes, multi-harmonics behaviour of the device is characterised, the results from which will be beneficial to the future experimental work.

An original investigation on the output system for the fourth-harmonic gyro-multiplier is carried out. The combination of a DQMC and a FSS in the system is proposed and verified numerically. The design of a DQMC is carried out by geometrical optics analysis and verified by numerical simulations.

The design of a single disc window for the simultaneous transmission of two waves at 342 GHz and 1368 GHz has been done. The numerical investigation has shown satisfactory transmission property at both frequencies.

By the combination of theoretical analysis, numerical simulation and experimental testing, the operation of the high-pass FSS at 1368 GHz is verified and the performance is greatly improved in a cost effective way. Only traditional etching technology is required to achieve satisfactory performance of the designed FSS. All the fabricated FSSs show good reflectivity at 342 GHz. One of them with the best performance shows an insertion loss as low as 0.4 dB at 1368 GHz.

7.3 Future Work

Since most of the previous study on the beam-wave interaction of the gyro-multiplier is conducted by the time-consuming 3D PIC simulation, a highly-specialised computer code will be helpful for the characterisation and preliminary development of the device. As the sectioned-cavity gyro-multiplier is actually based on the complex-cavity gyrotron scheme, the existing non-linear theory of the latter can be extended for studying the beam-wave interaction and frequency-multiplication of the former. Thus one of the future tasks will be the development of a self-consistent, steady-state nonlinear code for the gyro-multiplier.

It is found in the study of the high-harmonic LOG that, by varying the external magnetic field, selective excitation of a series of modes at different harmonics and with different axial index can be achieved. Thus such kind of LOG has the potential to provide coherent

radiation with broadband frequency step-tunability by enable the beam-wave interaction from the fourth to the ninth harmonic. Apart from studying the frequency step-tunability of the LOG scheme developed in this thesis, the future work includes the demonstration of LOGs with even higher harmonic operation ($s \geq 10$) to boost the operation frequency to 1 THz as well as the incorporation of $TE_{m,n}$ ($n > 1$) modes in these LOGs operation to both increase the power capacity and decrease the Ohmic loss of the cavity.

Besides, after characterisation of the high-voltage LOG scheme, a low-voltage LOG will be designed and studied based on an 80 kV, 0.7 A electron beam with an velocity ratio of 1.4. By lowering the operation beam voltage, the existing electron beam source for the designed gyro-multiplier is ready to be used in the experimental verification of the theory and design of the high-harmonic LOG.

The design of the output system for the fourth harmonic gyro-multiplier will also be improved and optimised. Although the modified Vlasov launcher has showing acceptable results in terms of the power transmission efficiencies and Gaussian mode contents of the converted wave beams, further improvements of the performance is still possible. For example, the adoption and optimisation of a Denisov launcher for both high-order modes will be intriguing.

The fabricated FSS have shown satisfactory performances, but the influences of using smaller perforations and hexagonal arrays are not determined. It can only be achieved by fabricating more samples of different sizes as well as configurations but under the same fabrication conditions. As for the electric breakdown problem, the configurations with lower MFEF values can be investigated to increase the power capacity. Also, the low-pass FSS with the resonant transmission peak at around 342 GHz is worth looking into, which can help to reduce the fabrication precision requirement.

7.4 List of Publications

Journal papers (5 in total)

1. **Xiang Li**, Xiaoming Liu, Yasir Alfadhl, Kevin Ronald, Wenlong He, Adrian Cross, Xiaodong Chen, 'A dual-frequency quasi-optical output system for a THz gyro-multiplier', IEEE Transactions on Terahertz Science and Technology, Volume 6, Issue 5, pp. 674-681, September 2016.

2. **Xiang Li**, Jiandong Lang, Yasir Alfadhl and Xiaodong Chen, 'Study of an Eighth-Harmonic Large-Orbit Gyrotron in the Terahertz Band', IEEE Transactions on Plasma Science, Volume 43, Issue 2, pp. 506-514, February 2015.

3. **Xiang Li**, Jiandong Lang, Yasir Alfadhl and Xiaodong Chen, 'A high harmonic large orbit gyrotron in THz range', International Journal of Terahertz Science and Technology, Volume 7, Issue 4, pp. 181-187, December 2014.

4. Jiandong Lang, **Xiang Li**, Yasir Alfadhl and Xiaodong Chen, 'Investigation of a 0.2 THz magnetron using 3D particle simulation', International Journal of Terahertz Science and Technology, Volume 7, Issue 3, pp. 139-144, September 2014.

5. **Xiang Li**, Xiaodong Chen. 'Design and simulation of a 0.42 THz complex-cavity gyrotron', International Journal of Terahertz Science and Technology, Volume 5, Issue 4, pp. 196-200, December 2012.

Conference papers (17 in total)

1. **Xiang Li**, Xiaoming Liu, Yasir Alfadhl, Kevin Ronald, Wenlong He, Adrian Cross, Xiaodong Chen, 'Design of Frequency Selective Surfaces for a Gyro-multiplier output system', 17th International Vacuum Electronics Conference (IVEC2016), California, United States, 19-21 April, 2016.

2. Monika C. Balk, Maryam Kiyani, **Xiang Li**, Yasir Alfadhl, Xiaodong Chen. '3D Gyrotron Simulation with CST STUDIO SUITE', National Vacuum Electronics Conference 2015 (NVEC2015), Technology and Innovation Centre (TiC), University of Strathclyde, Glasgow, United Kingdom, 18 November 2015.

3. Jiandong Lang, **Xiang Li**, Yasir Alfadhl and Xiaodong Chen. 'Simulation of Millimetre-wave Spatial Harmonic Magnetrons', National Vacuum Electronics

Conference 2015 (NVEC2015), Technology and Innovation Centre (TiC), University of Strathclyde, Glasgow, United Kingdom, 18 November 2015.

4. **Xiang Li**, Yasir Alfadhl, Xiaodong Chen, Wenlong He, Kevin Ronald, Adrian Cross. 'Design of the output system for a gyro-multiplier', 8th Europe/UK-China Workshop on Millimeter Waves and Terahertz Technologies (UCMMT2015). Cardiff, United Kingdom, 14-16 September, 2015.

5. **Xiang Li**, Jiandong Lang, Yasir Alfadhl and Xiaodong Chen. 'Study of the multi-mode behavior in a high harmonic large orbit gyrotron', 42nd IEEE International Conference on Plasma Science (ICOPS2015), Belek, Turkey, 24-28 May, 2015.

6. **Xiang Li**, Jiandong Lang, Yasir Alfadhl and Xiaodong Chen. 'Numerical Study of a high harmonic gyrotron using an axis-encircling electron beam', 16th International Vacuum Electronics Conference (IVEC2015), Beijing, China, 27-29 April, 2015.

7. Monika C. Balk, Cier-Siang Chua, **Xiang Li**, Yasir Alfadhl, Xiaodong Chen. '3D Gyrotron Simulation with CST STUDIO SUITE™', 16th International Vacuum Electronics Conference (IVEC2015), Beijing, China, 27-29 April, 2015.

8. **Xiang Li**, Jiandong Lang, Yasir Alfadhl and Xiaodong Chen. 'Study of A 0.42 THz Fourth-Harmonic Large Orbit Gyrotron', 39th International Conference on Infrared, Millimeter and Terahertz Waves (IRMMW2014). Tucson, United States, 14-19 September 2014.

9. **Xiang Li**, Jiandong Lang, Yasir Alfadhl and Xiaodong Chen. 'A high harmonic large orbit gyrotron in THz range', 7th Europe/UK-China Workshop on Millimeter Waves and Terahertz Technologies (UCMMT2014). Chengdu, China, 2-4 September 2014.

10. Jiandong Lang, **Xiang Li**, Yasir Alfadhl and Xiaodong Chen. 'Investigation of a 0.2-THz Magnetron Using 3D Particle Simulation', 7th Europe/UK-China Workshop on Millimeter Waves and Terahertz Technologies (UCMMT2014). Chengdu, China, 2-4 September 2014.

11. **Xiang Li**, Jiandong Lang, Yasir Alfadhl and Xiaodong Chen. 'Design and Simulation of a Large Orbit Gyrotron in THz Range', National Vacuum Electronic Conference 2014 (NVEC2014). Warrington, United Kingdom, 05 June 2014.

12. **Xiang Li**, Yasir Alfadhl, Xiaodong Chen, Sheng Yu, Qixiang Zhao and Yanyan Zhang. 'A computational efficient simulation tool for gyrotrons', 41st IEEE International Conference on Plasma Science (ICOPS2014) and the 20th International Conference on High-Power Particle Beams (Beams 2014). Washington DC, United States, 25-29 May 2014.

13. Jiandong Lang, **Xiang Li**, Yasir Alfadhl and Xiaodong Chen. '3D simulation of a 200GHz Magnetron', IET Colloquium on Millimetre-wave and Terahertz Engineering & Technology, Liverpool, United Kingdom, 05 March 2014.

14. **Xiang Li**, Jiandong Lang, Yasir Alfadhl and Xiaodong Chen. 'Magic 3D simulation of starting process of oscillation in a 42 GHz gyrotron', IET 1st Annual Active and Passive RF Devices Seminar. Glasgow, United Kingdom, 29 October 2013.

15. **Xiang Li**, Jiandong Lang, Yasir Alfadhl and Xiaodong Chen. '3D PIC simulation of starting process of oscillation in a 42 GHz gyrotron', 6th UK, Europe, China Millimeter Waves and Terahertz Technology Workshop (UCMMT2013). Rome, Italy, 9-11 September 2013.

16. **Xiang Li**, Jiandong Lang, Yasir Alfadhl and Xiaodong Chen. 'Study of starting process of oscillation in a gyrotron using 3D PIC simulation', National Vacuum Electronic Conference 2013 (NVEC2013). London, United Kingdom, 25 June 2013.

17. Jiandong Lang, **Xiang Li**, Yasir Alfadhl and Xiaodong Chen. '3D spatial harmonic magnetron-a contender for compact high power THz source', National Vacuum Electronic Conference 2013 (NVEC2013). London, United Kingdom, 25 June 2013.

Appendix-I

The cyclotron resonance condition as shown in (1.1) can be derived in a number of ways [80, 173, 174]. Here the quantum model of a gyrating electron in a homogenous static external magnetic field will be briefly revisited [174].

From the quantum viewpoint, the different gyrating status of the electron represents a number of discrete Landau energy levels. The distant between two adjacent Landau levels is $\hbar\Omega$, where $\hbar$ is the Planck constant and Ω is the electron cyclotron frequency in the external magnetic field. Due to the interaction with the alternating electromagnetic field, the electron can emit a photon with and jump to the nearest lower Landau level, or absorb a photon and transit to a nearest upper level.

The classical electron-electromagnetic interaction can be viewed as electron-photon energy exchange. When an electron emits the photon, it loses both its gyrating energy and longitudinal momentum. Thus the energy loss of the electron can be expressed by:

$$\Delta\Pi = \Delta\Pi_{\parallel} + \Delta\Pi_{\perp} \tag{A1.1}$$

in which $\Delta\Pi_{\parallel}$ and $\Delta\Pi_{\perp}$ are the energy loss values corresponding to the longitudinal momentum change and gyration motion, respectively.

Assuming that the electron jumps down by s Landau level, $\Delta\Pi_{\perp}$ can be expressed by

$$\Delta\Pi_{\perp} = s\hbar\Omega. \tag{A1.2}$$

The part of energy lost due to the reduction of the electron's longitudinal momentum can be expressed by

$$\Delta\Pi_{\parallel} = \frac{\partial\Pi}{\partial p_{\parallel}}\Delta p_{\parallel} = v_{\parallel}\Delta p_{\parallel} \tag{A1.3}$$

where $\Delta p_{\parallel}$ is the amount of the reduced longitudinal momentum and $v_{\parallel}$ is the longitudinal velocity of the electron's motion. The lost energy and longitudinal momentum of the electron should be transferred into the energy and momentum of the emitted photon. The

energy of the photon can be expressed as $\hbar\omega$ with ω denoting the classical oscillation frequency of the wave. The longitudinal momentum of the photon can be expressed as $\hbar k_{\parallel}$ where $k_{\parallel}$ is the longitudinal wavenumber of the photon. Thus is can be obtained that

$$\Delta\Pi = \hbar\omega \tag{A1.4}$$

and

$$\Delta p_{\parallel} = \hbar k_{\parallel}. \tag{A1.5}$$

From (A1.1) to (A1.5), it can be seen that

$$\omega - v_{\parallel} k_{\parallel} = s\Omega \tag{A1.6}$$

which is also the same as (1.1).

References

[1] E. Nichols and J. Tear, "Joining the infra-red and electric wave spectra," *The Astrophysical Journal*, vol. 61, p. 17, 1925.

[2] P. H. Siegel, "Terahertz technology," *IEEE Transactions on microwave theory and techniques*, vol. 50, pp. 910-928, 2002.

[3] G. P. Williams, "Filling the THz gap—high power sources and applications," *Reports on Progress in Physics*, vol. 69, p. 301, 2005.

[4] E. R. Mueller, "Terahertz radiation source for imaging and sensing technologies," *Photonics Spectra*, 2006.

[5] X. Zhang, "Terahertz wave imaging: horizons and hurdles," *Physics in Medicine and Biology*, vol. 47, p. 3667, 2002.

[6] F. Li, "Design and operation of a harmonic gyrotron based on a cusp electron gun," Ph.D., Department of Physics, University of Strathclyde, Scotland, 2010.

[7] M. K. Hornstein, "A continuous-wave second harmonic gyrotron oscilltor at 460 GHz," Doctor of Philosophy, Department of Electrical Engineering and Computer Science, Massachusetts Institute of Technology, Massachusetts Institute of Technology, 2005.

[8] T. Globus, D. Woolard, T. W. Crowe, T. Khromova, B. Gelmont, and J. Hesler, "Terahertz Fourier transform characterization of biological materials in a liquid phase," *Journal of Physics D: Applied Physics*, vol. 39, p. 3405, 2006.

[9] C. J. Strachan, T. Rades, D. A. Newnham, K. C. Gordon, M. Pepper, and P. F. Taday, "Using terahertz pulsed spectroscopy to study crystallinity of pharmaceutical materials," *Chemical Physics Letters*, vol. 390, pp. 20-24, 2004.

[10] R. Juanola-Parramon, D. Fenech, and G. Savini, "Architecture and performance of the space-based Far-Infrared Interferometer Instrument Simulator," *Monthly Notices of the Royal Astronomical Society*, vol. 457, pp. 3457-3469, 2016.

[11] M. Tonouchi, "Cutting-edge terahertz technology," *Nature photonics*, vol. 1, pp. 97-105, 2007.

[12] M. C. Gaidis, "Space-based applications of far-infrared systems," DTIC Document2000.

[13] P. U. Jepsen, D. G. Cooke, and M. Koch, "Terahertz spectroscopy and imaging–Modern techniques and applications," *Laser & Photonics Reviews*, vol. 5, pp. 124-166, 2011.

[14] Y. A. Min Zhou, Xiaodong Chen, "Study on terahertz holography system at 220 GHz," presented at the 7th Europe/UK-China Workshop on Millimeter Waves and Terahertz Technologies, Chengdu, China, 2014.

[15] Q. Wu, T. Hewitt, and X. C. Zhang, "Two‐dimensional electro‐optic imaging of THz beams," *Applied Physics Letters*, vol. 69, pp. 1026-1028, 1996.

[16] Q. Chen, Z. Jiang, G. Xu, and X.-C. Zhang, "Near-field terahertz imaging with a dynamic aperture," *Optics Letters*, vol. 25, pp. 1122-1124, 2000.

[17] T. Löffler, T. Bauer, K. Siebert, H. G. Roskos, A. Fitzgerald, and S. Czasch, "Terahertz dark-field imaging of biomedical tissue," *Optics Express*, vol. 9, pp. 616-621, 2001.

[18] D. M. Sheen, D. L. McMakin, T. E. Hall, and R. H. Severtsen, "Active millimeter-wave standoff and portal imaging techniques for personnel screening," in *Technologies for Homeland Security, 2009. HST'09. IEEE Conference on*, 2009, pp. 440-447.

[19] *http://www.sds.l-3com.com/products/advancedimagingtech.htm*.

[20] E. A. Nanni, A. B. Barnes, R. G. Griffin, and R. J. Temkin, "THz dynamic nuclear polarization NMR," *Terahertz Science and Technology, IEEE Transactions on*, vol. 1, pp. 145-163, 2011.

[21] C. Darbos, F. Albajar, T. Bonicelli, G. Carannante, M. Cavinato, F. Cismondi, *et al.*, "Status of the ITER Electron Cyclotron Heating and Current Drive System," *Journal of Infrared, Millimeter, and Terahertz Waves,* vol. 37, pp. 4-20, 2016.

[22] V. Bratman, M. Glyavin, T. Idehara, Y. Kalynov, A. Luchinin, V. Manuilov, *et al.*, "Review of subterahertz and terahertz gyrodevices at IAP RAS and FIR FU," *Plasma Science, IEEE Transactions on,* vol. 37, pp. 36-43, 2009.

[23] P. H. Siegel, "Terahertz technology in biology and medicine," in *Microwave Symposium Digest, 2004 IEEE MTT-S International*, 2004, pp. 1575-1578.

[24] B. Breitenstein, M. Scheller, M. K. Shakfa, T. Kinder, T. Müller-Wirts, M. Koch, *et al.*, "Introducing terahertz technology into plant biology: A novel method to monitor changes in leaf water status," *Journal of Applied Botany and Food Quality,* vol. 84, p. 158, 2012.

[25] H.-J. Song and T. Nagatsuma, "Present and future of terahertz communications," *Terahertz Science and Technology, IEEE Transactions on,* vol. 1, pp. 256-263, 2011.

[26] T. Kleine-Ostmann and T. Nagatsuma, "A review on terahertz communications research," *Journal of Infrared, Millimeter, and Terahertz Waves,* vol. 32, pp. 143-171, 2011.

[27] J. Federici and L. Moeller, "Review of terahertz and subterahertz wireless communications," *Journal of Applied Physics,* vol. 107, p. 111101, 2010.

[28] J. H. Booske, "Plasma physics and related challenges of millimeter-wave-to-terahertz and high power microwave generation," *Physics of Plasmas,* vol. 15, p. 055502, 2008.

[29] G. Chattopadhyay, "Technology, capabilities, and performance of low power terahertz sources," *Terahertz Science and Technology, IEEE Transactions on,* vol. 1, pp. 33-53, 2011.

[30] V. L. Granatstein, R. K. Parker, and C. M. Armstrong, "Vacuum electronics at the dawn of the twenty-first century," *Proceedings of the IEEE,* vol. 87, pp. 702-716, 1999.

[31] P. Mukherjee and B. Gupta, "Terahertz (THz) frequency sources and antennas-A brief review," *International Journal of Infrared and Millimeter Waves,* vol. 29, pp. 1091-1102, 2008.

[32] M. Tonouchi, "Galore new applications of terahertz science and technology," *Terahertz Sci. Technol,* vol. 2, pp. 90-101, 2009.

[33] A. C. T. d. Sousa, "Frequency-Tunable Second-Harmonic Submillimeter-Wave Gyrotron Oscillators," Doctor of Philosophy, Department of Electrical Engineering and Computer Science, Massachusetts Institute of Technology, Massachusetts Institute of Technology, 2010.

[34] M. Y. Glyavin, A. Luchinin, and G. Y. Golubiatnikov, "Generation of 1.5-kW, 1-THz coherent radiation from a gyrotron with a pulsed magnetic field," *Physical review letters,* vol. 100, p. 015101, 2008.

[35] G. S. Nusinovich, M. K. Thumm, and M. I. Petelin, "The Gyrotron at 50: Historical Overview," *Journal of Infrared, Millimeter, and Terahertz Waves,* vol. 35, pp. 325-381, 2014.

[36] J. Faist, F. Capasso, D. L. Sivco, C. Sirtori, A. L. Hutchinson, and A. Y. Cho, "Quantum cascade laser," *Science,* vol. 264, pp. 553-556, 1994.

[37] L. A. Samoska, "An overview of solid-state integrated circuit amplifiers in the submillimeter-wave and THz regime," *Terahertz Science and Technology, IEEE Transactions on,* vol. 1, pp. 9-24, 2011.

[38] G. Gallerano and S. Biedron, "Overview of terahertz radiation sources," in *Proceedings of the 2004 FEL Conference*, 2004, pp. 216-221.

[39] W. He, L. Zhang, D. Bowes, H. Yin, K. Ronald, A. Phelps, *et al.*, "Generation of broadband terahertz radiation using a backward wave oscillator and pseudospark-sourced electron beam," *Applied Physics Letters,* vol. 107, p. 133501, 2015.

[40] C. Paoloni, M. Mineo, M. Henry, and P. G. Huggard, "Double Corrugated Waveguide for Ka-Band Traveling Wave Tube," *Electron Devices, IEEE Transactions on,* vol. 62, pp. 3851-3856, 2015.

[41] H. T. Tran, G. Lankford, M. E. Read, R. L. Ives, K. Reppert, K. Cline, *et al.*, "Optimization of klystron designs using deterministic sampling methods," *IEEE Transactions on Electron Devices,* vol. 62, pp. 1032-1036, 2015.

[42] F. B. Taheri, I. Konoplev, G. Doucas, P. Baddoo, R. Bartolini, J. Cowley, *et al.*, "Electron bunch profile reconstruction based on phase-constrained iterative algorithm," *Physical Review Accelerators and Beams,* vol. 19, p. 032801, 2016.

[43] J. Lang, X. Li, Y. Alfadhl, and X. Chen, "Study of a THz spatial harmonic magnetron," in *Vacuum Electronics Conference (IVEC), 2015 IEEE International*, 2015, pp. 1-2.

[44] A. Marinelli, D. Ratner, A. Lutman, J. Turner, J. Welch, F.-J. Decker, *et al.*, "High-intensity double-pulse X-ray free-electron laser," *Nature communications,* vol. 6, 2015.

[45] K. Chu, "Some recent progresses on electron cyclotron maser research," in *Vacuum Electronics Conference (IVEC), 2015 IEEE International*, 2015, pp. 1-2.

[46] A. C. Sousa, "Frequency-tunable second-harmonic submillimeter-wave gyrotron oscillators," Massachusetts Institute of Technology, 2010.

[47] T. Idehara, S. Mitsudo, M. Ui, I. Ogawa, M. Sato, and K. Kawahata, "Development of frequency tunable gyrotrons in millimeter to submillimeter wave range for plasma diagnostics," *J. Plasma Fusion Res. Series,* vol. 3, pp. 407-410, 2000.

[48] S. Mitsudo, T. Shirai, T. Matsuda, T. Kanemaki, and T. Idehara, "High power, frequency tunable, submillimeter wave ESR device using a gyrotron as a radiation source," *International Journal of Infrared and Millimeter Waves,* vol. 21, pp. 661-676, 2000.

[49] G. S. Nusinovich, *Introduction to the Physics of Gyrotrons*: JHU Press, 2004.

[50] M. V. Kartikeyan, E. Borie, and M. Thumm, *Gyrotrons: High-Power Microwave and Millimeter Wave Technology*: Springer, 2004.

[51] C. J. Edgcombe, *Gyrotron Oscillators: Their Principles and Practice.* London, UK: Taylor & Francis, 1993.

[52] Y. Lau and L. Barnett, "Theory of a low magnetic field gyrotron (gyromagnetron)," *International Journal of Infrared and Millimeter Waves,* vol. 3, pp. 619-644, 1982.

[53] D. McDermott, N. Luhmann Jr, A. Kupiszewski, and H. Jory, "Small‐signal theory of a large‐orbit electron‐cyclotron harmonic maser," *Physics of Fluids (1958-1988),* vol. 26, pp. 1936-1941, 1983.

[54] K. Chu and D. Dialetis, "Theory of harmonic gyrotron oscillator with slotted resonant structure," *International Journal of Infrared and Millimeter Waves,* vol. 5, pp. 37-56, 1984.

[55] W. Lawson, W. W. Destler, and C. D. Striffler, "High-power microwave generation from a large-orbit gyrotron in vane and hole-and-slot conducting wall geometries," *Plasma Science, IEEE Transactions on,* vol. 13, pp. 444-453, 1985.

[56] S.-C. ZHANG and S. LIU, "Large-orbit gyrotron with an assistant radial electrostatic focusing-field," *International Journal of Electronics Theoretical and Experimental,* vol. 61, pp. 1091-1098, 1986.

[57] G. Nusinovich, "Non-linear theory of a large-orbit gyrotron," *International journal of electronics,* vol. 72, pp. 959-967, 1992.

[58] V. L. Bratman, A. E. Fedotov, Y. K. Kalynov, V. N. Manuilov, M. M. Ofitserov, S. V. Samsonov, *et al.*, "Moderately relativistic high-harmonic gyrotrons for millimeter/submillimeter wavelength band: Special Issue on Cyclotron Resonance Masers and Gyrotrons," *IEEE transactions on plasma science,* vol. 27, pp. 456-461, 1999.

[59] T. Idehara, I. Ogawa, S. Mitsudo, Y. Iwata, S. Watanabe, Y. Itakura, *et al.*, "A high harmonic gyrotron with an axis-encircling electron beam and a permanent magnet," *Plasma Science, IEEE Transactions on,* vol. 32, pp. 903-909, 2004.

[60] I. Bandurkin, V. Bratman, G. Denisov, Y. K. Kalynov, A. Savilov, A. Cross, *et al.*, "Single-cavity Gyromultipliers," *Terahertz Science and Technology,* vol. 1, pp. 169-188, 2008.

[61] I. V. Bandurkin, V. L. Bratman, Y. K. Kalynov, V. N. Manuilov, S. V. Samsonov, and A. V. Savilov, "Terahertz high-harmonic gyrotrons and gyro-multipliers," in *Infrared, Millimeter and Terahertz Waves, 2008. IRMMW-THz 2008. 33rd International Conference on*, 2008, pp. 1-2.

[62] I. Bandurkin, V. Bratman, A. Savilov, S. Samsonov, and A. Volkov, "Experimental study of a fourth-harmonic gyromultiplier," *Physics of Plasmas,* vol. 16, p. 070701, 2009.

[63] I. Bandurkin and S. Mishakin, "Gyromultiplier with sectioned cavity," *Physics of Plasmas,* vol. 17, p. 110706, 2010.

[64] D. Constable, K. Ronald, W. He, A. Phelps, A. Cross, A. Savilov, *et al.*, "Numerical simulations of a co-harmonic gyrotron," *Journal of Physics D: Applied Physics,* vol. 45, p. 065105, 2012.

[65] D. A. Constable, "The Numerical and Experimental Investigation of Gyro-Multiplier Configurations," *PhD Thesis,* 2013.

[66] N. Ginzburg, I. Zotova, A. Sergeev, V. Y. Zaslavsky, and I. Zheleznov, "High-power terahertz-range planar gyrotrons with transverse energy extraction," *Physical review letters,* vol. 108, p. 105101, 2012.

[67] M. Schmid, J. Franck, P. Kalaria, K. Avramidis, G. Gantenbein, S. Illy, *et al.*, "Gyrotron development at KIT: FULGOR test facility and gyrotron concepts for DEMO," *Fusion Engineering and Design,* vol. 96, pp. 589-592, 2015.

[68] K. Irwin, W. Destler, W. Lawson, J. Rodgers, E. Scannell, and S. Spang, "Second generation, high‐power, fundamental mode large‐orbit gyrotron experiments," *Journal of applied physics,* vol. 69, pp. 627-631, 1991.

[69] W. Destler, E. Chojnacki, R. Hoeberling, W. Lawson, A. Singh, and C. Striffler, "High-power microwave generation from large-orbit devices," *Plasma Science, IEEE Transactions on,* vol. 16, pp. 71-89, 1988.

[70] Y. Bratman, Y. K. Kalynov, N. Kolganov, Y. Manuilov, M. Ofitserov, S. Samsonov, *et al.*, "High-harmonic relativistic gyrotron as an alternative to FEL," in *High-Power Particle Beams, 1996 11th International Conference on*, 1996, pp. 401-404.

[71] I. Bandurkin, V. Bratman, and A. Savilov, "Frequency multiplication in gyrotron autooscillators," *Technical Physics Letters,* vol. 32, pp. 84-87, 2006.

[72] I. Bandurkin and A. Savilov, "Cyclotron resonance maser operating in a nonresonant electron bunching regime," *Technical Physics Letters,* vol. 32, pp. 6-9, 2006.

[73] CST, "CST Studio Suite Help Document," 2015.

[74] HFSS, "HFSS Online Help," 2015.

[75] MAGIC, "MAGIC Help Manual," 2007.

[76] S. N. Vlasov and I. Orlova, "Quasioptical transformer which transforms the waves in a waveguide having a circular cross section into a highly directional wave beam," *Radiophysics and Quantum Electronics,* vol. 17, pp. 115-119, 1974.

[77] O. Prinz, A. Arnold, G. Gantenbein, Y.-h. Liu, M. Thumm, and D. Wagner, "Highly efficient quasi-optical mode converter for a multifrequency high-power gyrotron," *Electron Devices, IEEE Transactions on,* vol. 56, pp. 828-834, 2009.

[78] Y. Wang, B. Yang, Y. Tian, R. S. Donnan, and M. J. Lancaster, "Micromachined thick mesh filters for millimeter-wave and terahertz applications," *Terahertz Science and Technology, IEEE Transactions on,* vol. 4, pp. 247-253, 2014.

[79] M. Li and N. Behdad, "Frequency selective surfaces for pulsed high-power microwave applications," *Antennas and Propagation, IEEE Transactions on,* vol. 61, pp. 677-687, 2013.
[80] K. Chu, "The electron cyclotron maser," *Reviews of modern physics,* vol. 76, p. 489, 2004.
[81] A. Balkcum, D. McDermott, K. Leou, F. Hartemann, and N. Luhmann Jr, "Theory and design of a high-harmonic gyrofrequency multiplier," *Plasma Science, IEEE Transactions on,* vol. 22, pp. 913-919, 1994.
[82] G. Nusinovich and O. Dumbrajs, "Two‐harmonic prebunching of electrons in multicavity gyrodevices," *Physics of Plasmas,* vol. 2, p. 568, 1995.
[83] C. Wang, J. Hirshfield, and A. Ganguly, "Efficient co-generation of seventh-harmonic radiation in cyclotron autoresonance acceleration," *Physical review letters,* vol. 77, p. 3819, 1996.
[84] I. Bandurkin, V. Bratman, G. Denisov, I. Gachev, Y. K. Kalynov, and A. Savilov, "New schemes of high-harmonic gyro-devices with frequency multiplication," in *Infrared Millimeter Waves and 14th International Conference on Teraherz Electronics, 2006. IRMMW-THz 2006. Joint 31st International Conference on*, 2006, pp. 83-83.
[85] I. Bandurkin, V. L. Bratman, G. G. Denisov, I. G. Gachev, Y. K. Kalynov, and A. V. Savilov, "High-harmonic gyrodevices with frequency multiplication," in *Infrared and Millimeter Waves, 2007 and the 2007 15th International Conference on Terahertz Electronics. IRMMW-THz. Joint 32nd International Conference on*, 2007, pp. 321-322.
[86] D. Constable, W. He, A. Cross, K. Ronald, I. Bandurkin, A. Savilov, *et al.*, "3-D numerical simulation of novel gyro-multiplier schemes," in *Plasma Science (ICOPS), 2012 Abstracts IEEE International Conference on*, 2012, pp. 1P-14-1P-14.
[87] D. A. Constable, I. V. Bandurkin, W. He, A. W. Cross, A. V. Savilov, A. D. Phelps, *et al.*, "Numerical investigation of gyro-multiplier schemes," in *Vacuum Electronics Conference (IVEC), 2012 IEEE Thirteenth International*, 2012, pp. 529-530.
[88] D. A. Constable, I. V. Bandurkin, W. He, A. W. Cross, A. V. Savilov, A. D. Phelps, *et al.*, "Numerical simulation of a 1.37 THz gyro-multiplier," in *Vacuum Electronics Conference (IVEC), 2013 IEEE 14th International*, 2013, pp. 1-2.
[89] B. Ruth, R. Dahlstrom, C. Schlesiger, and L. Libelo, "Design and low-power testing of a microwave Vlasov mode converter," in *Microwave Symposium Digest, 1989., IEEE MTT-S International*, 1989, pp. 1277-1280.
[90] J. Liu, J. Jin, M. Thumm, J. Jelonnek, H. Li, and Q. Zhao, "Vector Method for Synthesis of Adapted Phase-Correcting Mirrors for Gyrotron Output Couplers," *Plasma Science, IEEE Transactions on,* vol. 41, pp. 2489-2495, 2013.
[91] J. A. Lorbeck and R. Vernon, "Singly curved dual-reflector synthesis technique applied to a quasi-optical antenna for a gyrotron with a whispering-gallery mode output," *Antennas and Propagation, IEEE Transactions on,* vol. 39, pp. 1733-1741, 1991.
[92] M. Thumm, H. Kumric, and H. Stickel, "TE03 to TE01 mode converters for use with a 150 GHz gyrotron," *International journal of infrared and millimeter waves,* vol. 8, pp. 227-240, 1987.
[93] J. Trulsen, P. Woskoboinikow, and R. J. Temkin, "Circular waveguide mode converters at 140 GHz," *NASA STI/Recon Technical Report N,* vol. 86, p. 30953, 1986.
[94] M. K. Thumm and W. Kasparek, "Passive high-power microwave components," *Plasma Science, IEEE Transactions on,* vol. 30, pp. 755-786, 2002.
[95] L. I. Z. S. N. Vlasov, M. I. Petelin, "Transformation of a whispering gallery mode, propagating in a circular waveguide, into a beam of waves," *Radio Eng. Electron. Phys.,* vol. 21, p. 4, 1975.
[96] S. Vlasov, M. Shapiro, and E. Sheinina, "Wave beam shaping on diffraction of a whispering gallery wave at a convex cylindrical surface," *Radiophysics and Quantum Electronics,* vol. 31, pp. 1070-1075, 1988.

[97] S. Vlasov, M. Shapiro, and K. Likin, "Geometrical optics of waveguide mode converters," *Optics Communications,* vol. 88, pp. 455-463, 1992.
[98] G. Denisov, A. Kuftin, V. Malygin, N. Venediktov, D. Vinogradov, and V. Zapevalov, "110 GHz gyrotron with a built-in high-efficiency converter," *International journal of electronics,* vol. 72, pp. 1079-1091, 1992.
[99] V. A. Fliagin and G. S. Nusinovich, "Gyrotron oscillators," in *IEEE Proceedings*, 1988, pp. 644-656.
[100] B. G. Danly, K. Kreischer, W. Mulligan, and R. Temkin, "Whispering-gallery-mode gyrotron operation with a quasi-optical antenna," *Plasma Science, IEEE Transactions on,* vol. 13, pp. 383-388, 1985.
[101] G. Ling, B. Piosczyk, and M. K. Thumm, "A new approach for a multistage depressed collector for gyrotrons," *Plasma Science, IEEE Transactions on,* vol. 28, pp. 606-613, 2000.
[102] A. Roy Choudhury, S. Kern, and M. Thumm, "Study of Dynamic After Cavity Interaction in Gyrotrons—Part I: Adiabatic Approximation," *Electron Devices, IEEE Transactions on,* vol. 62, pp. 184-191, 2015.
[103] J. Jin, "Quasi-optical mode converter for a coaxial cavity gyrotron," PhD Thesis, Institute for Pulsed Power and Microwave Technology, Karlsruhe Institute of Technology, 2007.
[104] E. Choi, M. Shapiro, J. Sirigiri, and R. Temkin, "Calculation of radiation from a helically cut waveguide for a gyrotron mode converter in the quasi-optical approximation," *Journal of Infrared, Millimeter, and Terahertz Waves,* vol. 30, pp. 8-25, 2009.
[105] I. Ogawa, T. Idehara, M. Pereyaslavets, and W. Kasparek, "Design of a quasi-optical system converting the TE06 output mode of a gyrotron into a Gaussian-like beam," *International journal of infrared and millimeter waves,* vol. 20, pp. 543-558, 1999.
[106] E. Pelton and B. Munk, "A streamlined metallic radome," *Antennas and Propagation, IEEE Transactions on,* vol. 22, pp. 799-803, 1974.
[107] P. Franchi and R. J. Mailloux, "Theoretical and experimental study of metal grid angular filters for sidelobe suppression," *Antennas and Propagation, IEEE Transactions on,* vol. 31, pp. 445-450, 1983.
[108] A. Saleh and R. Semplak, "A quasi-optical polarization-independent diplexer for use in the beam feed system of millimeter-wave antennas," *Antennas and Propagation, IEEE Transactions on,* vol. 24, pp. 780-785, 1976.
[109] M. Gingrich and D. Werner, "Synthesis of low/zero index of refraction metamaterials from frequency selective surfaces using genetic algorithms," *Electronics Letters,* vol. 41, pp. 1266-1267, 2005.
[110] J. A. Bossard, X. Liang, L. Li, S. Yun, D. H. Werner, B. Weiner, *et al.*, "Tunable frequency selective surfaces and negative-zero-positive index metamaterials based on liquid crystals," *Antennas and Propagation, IEEE Transactions on,* vol. 56, pp. 1308-1320, 2008.
[111] O. Paul, B. Reinhard, B. Krolla, R. Beigang, and M. Rahm, "Gradient index metamaterial based on slot elements," *Applied Physics Letters,* vol. 96, p. 241110, 2010.
[112] J. A. Encinar, "Design of two-layer printed reflectarrays using patches of variable size," *Antennas and Propagation, IEEE Transactions on,* vol. 49, pp. 1403-1410, 2001.
[113] X. Chen, H. F. Ma, X. Y. Zou, W. X. Jiang, and T. J. Cui, "Three-dimensional broadband and high-directivity lens antenna made of metamaterials," *Journal of Applied Physics,* vol. 110, p. 044904, 2011.
[114] N. Gagnon, A. Petosa, and D. McNamara, "Thin microwave phase-shifting surface lens antenna made of square elements," *Electronics letters,* vol. 46, pp. 327-329, 2010.
[115] V. Agrawal and W. A. Imbriale, "Design of a dichroic Cassegrain subreflector," *Antennas and Propagation, IEEE Transactions on,* vol. 27, pp. 466-473, 1979.

[116] A. K. Rashid, B. Li, and Z. Shen, "An overview of three-dimensional frequency-selective structures," *Antennas and Propagation Magazine, IEEE*, vol. 56, pp. 43-67, 2014.
[117] B. A. Munk, *Frequency Selective Surfaces: Theory and Design*. New York: Wiley, 2000.
[118] J. C. Vardaxoglou, *Frequency selective surfaces: analysis and design* vol. 997: Research Studies Press London, 1997.
[119] T.-K. Wu, *Frequency Selective Surfaces*: Wiley Online Library, 1995.
[120] M. Li and N. Behdad, "Frequency selective surfaces for high-power microwave (HPM) applications," in *Antennas and Propagation Society International Symposium (APSURSI), 2012 IEEE*, 2012, pp. 1-2.
[121] M. Li and N. Behdad, "Fluidically tunable frequency selective/phase shifting surfaces for high-power microwave applications," *Antennas and Propagation, IEEE Transactions on*, vol. 60, pp. 2748-2759, 2012.
[122] C.-H. Liu and N. Behdad, "Tunneling and filtering characteristics of cascaded ε-negative metamaterial layers sandwiched by double-positive layers," *Journal of Applied Physics*, vol. 111, p. 014906, 2012.
[123] C.-H. Liu and N. Behdad, "High-power microwave filters and frequency selective surfaces exploiting electromagnetic wave tunneling through ϵ-negative layers," *Journal of Applied Physics*, vol. 113, p. 064909, 2013.
[124] C.-H. Liu and N. Behdad, "Investigating the impact of microwave breakdown on the responses of high-power microwave metamaterials," *Plasma Science, IEEE Transactions on*, vol. 41, pp. 2992-3000, 2013.
[125] C.-H. Liu, J. D. Neher, J. H. Booske, and N. Behdad, "Investigating the Physics of Simultaneous Breakdown Events in High-Power-Microwave (HPM) Metamaterials With Multiresonant Unit Cells and Discrete Nonlinear Responses," 2014.
[126] S. Pugh, "Investigating the Use of Frequency Selective Surfaces in High Power Microwave Applications," DTIC Document2010.
[127] C. R. G. J. H. Barton, E. A. Berry, R. G. May, D. T. Gray, R. C. Rumpf, "All-Dielectric Frequency Selective Surface for High Power Microwaves," *IEEE TRANSACTIONS ON ANTENNAS AND PROPAGATION*, vol. 62, pp. 3652-3656, 2014.
[128] A. T. O. (ATK), *Magic Tool Suite User Help Document*, 2007.
[129] C. S. Technology, "CST Studio Suite Help 2013."
[130] T.-X. Corporation, "Vsim User Help Document 2014."
[131] M. Botton, T. M. Antonsen, B. Levush, K. T. Nguyen, and A. N. Vlasov, "MAGY: A time-dependent code for simulation of slow and fast microwave sources," *Plasma Science, IEEE Transactions on*, vol. 26, pp. 882-892, 1998.
[132] A. Fliflet, M. Read, K. Chu, and R. Seeley, "A self-consistent field theory for gyrotron oscillators: application to a low Q gyromonotron," *International Journal of Electronics Theoretical and Experimental*, vol. 53, pp. 505-521, 1982.
[133] H. Li, Z.-L. Xie, W. Wang, Y. Luo, P. Du, X. Den, *et al.*, "A 35-GHz low-voltage third-harmonic gyrotron with a permanent magnet system," *Plasma Science, IEEE Transactions on*, vol. 31, pp. 264-271, 2003.
[134] T. Zhang, Q. Zhao, S. Yu, Y. Yang, Y. Zhang, and X. Li, "The nonlinear simulation, design and experiments on 0.42 THz gyrotron with gradually tapered complex cavity," *Vacuum*, vol. 125, pp. 85-92, 2016.
[135] V. Bratman, Y. K. Kalynov, P. Makhalov, and A. Fedotov, "New Versions of Terahertz Radiation Sources for Dynamic Nuclear Polarization in Nuclear Magnetic Resonance Spectroscopy," *Radiophysics and Quantum Electronics*, vol. 56, pp. 532-541, 2014.
[136] V. Bratman, Y. K. Kalynov, and V. Manuilov, "Large-orbit subterahertz and terahertz gyrotrons," *Radiophysics and Quantum Electronics*, vol. 52, pp. 472-481, 2009.
[137] V. Bratman, Y. D. Grom, Y. K. Kalynov, V. Manuilov, M. Ofitserov, and S. Samsonov, "Relativistic gyrotron at the 5th cyclotron harmonic," in *Physics and Engineering of*

Millimeter and Submillimeter Waves, 1998. MSMW'98. Third International Kharkov Symposium, 1998, pp. 191-193.
[138] V. Bratman, Y. K. Kalynov, V. Manuilov, and S. Samsonov, "Submillimeter-wave large-orbit gyrotron," *Radiophysics and Quantum Electronics*, vol. 48, pp. 731-736, 2005.
[139] V. Bratman, Y. K. Kalynov, and A. Fedotov, "Theory of gyro devices with thin electron beams (large-orbit gyrotrons)," *Technical Physics*, vol. 43, pp. 1219-1225, 1998.
[140] D. Radack, K. Ramaswamy, W. Destler, and J. Rodgers, "A fundamental mode, high‐power, large‐orbit gyrotron using a rectangular interaction region," *Journal of applied physics*, vol. 73, pp. 8139-8145, 1993.
[141] W. Destler, K. Irwin, W. Lawson, J. Rodgers, Z. Segalov, E. Scannell, *et al.*, "Intense beam fundamental mode large‐orbit gyrotron studies," *Journal of applied physics*, vol. 66, pp. 4089-4094, 1989.
[142] F. Li, W. He, A. W. Cross, C. R. Donaldson, L. Zhang, A. D. Phelps, *et al.*, "Design and simulation of a~ 390 GHz seventh harmonic gyrotron using a large orbit electron beam," *Journal of Physics D: Applied Physics*, vol. 43, p. 155204, 2010.
[143] D. McDermott, N. Luhmann Jr, D. Furuno, A. Kupiszewski, and H. Jory, "Operation of a millimeter-wave harmonic gyrotron," *International Journal of Infrared and Millimeter Waves*, vol. 4, pp. 639-664, 1983.
[144] ATK, *Magic Tool Suite User Help Document*, 2007.
[145] O. Dumbrajs, E. Khutoryan, and T. Idehara, "Hysteresis and Frequency Tunability of Gyrotrons," *Journal of Infrared, Millimeter, and Terahertz Waves*, vol. 37, pp. 551-560, 2016.
[146] P. Kalaria, K. Avramidis, J. Franck, G. Gantenbein, S. Illy, I. G. Pagonakis, *et al.*, "A fast frequency step-tunable 236 GHz gyrotron design for DEMO," in *2016 German Microwave Conference (GeMiC)*, 2016, pp. 377-380.
[147] J. Lorbeck and R. Vernon, "Dual-shaped dual-reflector antenna for a whispering-gallery-mode gyrotron," in *Antennas and Propagation Society International Symposium, 1991. AP-S. Digest*, 1991, pp. 452-455.
[148] T. Idehara, T. Tatsukawa, G. Brand, P. Fekete, and K. Moore, "A two‐dimensionally focusing, quasi‐optical antenna for millimeter‐wave scattering in plasmas," *Journal of Applied Physics*, vol. 67, pp. 7086-7091, 1990.
[149] M. N. Osami Wada, "A Beam Focusing Antenna for the TE0n Mode High-Power Millimeter Wave," *Memoirs of the Faculty of Engineering*, vol. 26, pp. 77-92, March 1992.
[150] I. Ogawa, T. Idehara, S. Maekawa, W. Kasparek, and G. Brand, "Conversion of gyrotron output into a gaussian beam using the far-field," *International journal of infrared and millimeter waves*, vol. 20, pp. 801-821, 1999.
[151] I. Ogawa, T. Idehara, M. Pereyaslavets, and W. Kasparek, "Design of quasi-optical systems converting a gyrotron output into a Gaussian-like beam," *International journal of electronics*, vol. 87, pp. 865-877, 2000.
[152] S. Liao, "Multi-frequency beam-shaping mirror system design for high-power gyrotrons: theory, algorithms and methods," Doctor of Philosophy, Electrical Engineering, ProQuest, 2008.
[153] J. Jin, M. Thumm, B. Piosczyk, S. Kern, J. Flamm, and T. Rzesnicki, "Novel numerical method for the analysis and synthesis of the fields in highly oversized waveguide mode converters," *Microwave Theory and Techniques, IEEE Transactions on*, vol. 57, pp. 1661-1668, 2009.
[154] FEKO, "FEKO User Help Document," 2014.

[155] I. Ogawa, T. Idehara, S. Maekawa, and W. Kasparek, "Design of a quasi-optical system with variable output beam size," *International journal of electronics,* vol. 87, pp. 1095-1104, 2000.
[156] J. H. Flamm, "Diffraction and scattering in launchers of quasi-optical mode converters for gyrotrons," PhD Thesis, Electrical and Computer Engineering, KIT Scientific Publishing, Karlsruhe Institute of Technology, 2012.
[157] J.-P. Hogge, T. Tran, P. Paris, and M. Tran, "Operation of a quasi‐optical gyrotron with a Gaussian output coupler," *Physics of Plasmas (1994-present),* vol. 3, pp. 3492-3500, 1996.
[158] M. Blank, "High efficiency quasi-optical mode converters for overmoded gyrotrons," Doctor of Philosophy, Department of Electrical Engineering and Computer Science, Massachusetts Institute of Technology, September, 1994.
[159] B. Rock and A. W. Fliflet, "Analysis and Design of a Quasi-Optical Mode Converter for a 1-kW, 550-GHz,-Mode Gyrotron," *Terahertz Science and Technology, IEEE Transactions on,,* vol. 3, 2013.
[160] M. Thumm, "Development of output windows for high-power long-pulse gyrotrons and EC wave applications," *International Journal of Infrared and Millimeter Waves,* vol. 19, pp. 3-14, 1998.
[161] X. Yang, D. Wagner, B. Piosczyk, K. Koppenberg, E. Borie, R. Heidinger, *et al.*, "Analysis of transmission characteristics for single and double disk windows," *International Journal of Infrared and Millimeter Waves,* vol. 24, pp. 619-628, 2003.
[162] M. Thumm, "MPACVD-diamond windows for high-power and long-pulse millimeter wave transmission," *Diamond and Related Materials,* vol. 10, pp. 1692-1699, 2001.
[163] K. Z. Rajab, M. Naftaly, E. H. Linfield, J. C. Nino, D. Arenas, D. Tanner, *et al.*, "Broadband Dielectric Characterization of Aluminum Oxide (Al2O3)," *Journal of Microelectronics and Electronic Packaging,* vol. 5, pp. 2-7, 2008.
[164] *http://www.keysight.com/en/pcx-x2015001/network-analyzers?nid=-32503.0&cc=GB&lc=eng*.
[165] A. I. McIntosh, B. Yang, S. M. Goldup, M. Watkinson, and R. S. Donnan, "Terahertz spectroscopy: a powerful new tool for the chemical sciences?," *Chemical Society Reviews,* vol. 41, pp. 2072-2082, 2012.
[166] O. Sushko, "Terahertz dielectric study of bio-molecules using time-domain spectrometry and molecular dynamics simulations," PhD, School of Electronic Engineering and Computer Science, Queen Mary Univeristy of London, London, 2014.
[167] A. I. McIntosh, B. Yang, S. M. Goldup, M. Watkinson, and R. S. Donnan, "Crystallization of amorphous lactose at high humidity studied by terahertz time domain spectroscopy," *Chemical Physics Letters,* vol. 558, pp. 104-108, 2013.
[168] C. Winnewisser, F. Lewen, J. Weinzierl, and H. Helm, "Transmission features of frequency-selective components in the far infrared determined by terahertz time-domain spectroscopy," *Applied optics,* vol. 38, pp. 3961-3967, 1999.
[169] *http://www.micromesh.com.cn/shike*.
[170] J. W. Archer, "A novel quasi-optical frequency multiplier design for millimeter and submillimeter wavelengths," *Microwave Theory and Techniques, IEEE Transactions on,* vol. 32, pp. 421-427, 1984.
[171] L. A. ROBINSON, "ELECTRICAL PROPERTIES OF METAL-LOADED RADOMES," DTIC Document1960.
[172] A. Baig, Y.-M. Shin, L. R. Barnett, D. Gamzina, R. Barchfeld, C. W. Domier, *et al.*, "Design, fabrication and RF testing of near-THz sheet beam TWTA," *Terahertz Sci. Technol,* vol. 4, pp. 181-207, 2011.
[173] J. Hirshfield and V. Granatstein, "The electron cyclotron maser-an historical survey," *IEEE Transactions on Microwave Theory and Techniques,* vol. 25, pp. 522-527, 1977.

[174] M. I. Petelin, "One century of cyclotron radiation: Special Issue on Cyclotron Resonance Masers and Gyrotrons," *IEEE transactions on plasma science*, vol. 27, pp. 294-302, 1999.